Universitat de les Illes Balears
Departament de Física

Fast Magnetohydrodynamic Waves in Line-tied Solar Coronal Flux Tubes

Memoria presentada por Antonio Jesús Díaz Medina para optar al Grado de Doctor en Física por la Universitat de les Illes Balears.

Directores: Prof. J. L. Ballester y Dr. R. Oliver

Para *Esther*
Para mi familia

Agradecimientos

Esta tesis es el fruto de los años de trabajo en el Grupo de Física Solar del Departament de Física de la UIB. En primer lugar querría agradecer a mis directores de tesis, el Dr. Ramón Oliver i el Prof. Josep Lluís Ballester, por haberme introducido en el mundo de la física solar y en el grupo de investigación y haberme ayudado en todo momento durante la realización del trabajo. Gracias a ellos, esta tesis ha llegado a buen puerto y sigue apasionándome la astronomía en general, y la física solar en particular. Además, con su experiencia me han permitido relacionarme con muchos otros miembros de la comunidad científica y desenvolverme con mayor soltura en el mundo de la investigación. También agradezco las orientaciones que me han proporcionado en el periodo de la realización de esta tesis doctoral, seleccionando las ideas y temas más relevantes durante nuestras sesiones de "brainstorm" y ayudándome a mejorar la presentación y el lenguaje de los trabajos. Sin lugar a dudas puedo afirmar que el ambiente de estudio y el trato directo han sido los puntos fuertes del grupo, amén de los amplios conocimientos en la materia.

También querría expresar mi gratitud al resto de miembros del grupo, a Marc Carbonell, por alegrar y amenizar cualquier reunión, y a mis "hermanos mayores" Jaume Terradas e Iñigo Arregui, perfectos compañeros tanto en la universidad como en los viajes, por ayudarme en estos años de estudios compartidos y orientarme en la utilización de las herramientas informáticas a nuestra disposición. Del mismo modo, hago extensivo el agradecimiento al resto de miembros del departamento por haber contribuido con una atmósfera abierta, así como al resto de estudiantes de doctorado que me han acompañado estos años y finalmente, a mis compañeros de promoción, con los que he podido "desconectar" en mi tiempo libre.

También debo agradecer la ayuda prestada al estado español en forma de las becas y ayudas siguientes, sin las que este trabajo no se hubiera podido llevar a cabo. He podido disfrutar de las ayudas enumeradas a continuación: Beca de formación de profesorado universitario FPU AP99-43090617 sobre el tema "Ondas magnetohidrodinámicas en la corona solar", beca de formación de personal investigador FPI BFM2000-0627 con el proyecto de investigación "Sismología de la corona solar y actividad solar", beca de prelicenciatura 1998-15100 al proyecto de colaboración "Ecuaciones diferenciales estocásticas". La Universitat de les Illes Balears me ha apoyado con ayudas extraordinarias para viajes y me ha proporcionado el entorno y material necesario para la investigación, ofreciéndome una ayudantía, durante la cual he podido compartir conocimientos y experiencias con los alumnos de la universidad, a los cuales animo a seguir con sus estudios. Del mismo modo, agradezco a los organizadores de los congresos a los que he asistido (Guildford, Santiago de Compostela, Cambridge, Palma, Santorini, Praga y Palma de nuevo) su labor y esfuerzo.

I would like to thank Prof. Robert Erdélyi (Applied Mathematics Dept., University of Sheffield) for helping with the mathematics and for his encouragement and discussions about solar physics. I also thank Prof. Bernard Roberts (School of Mathematics and Statistics, University of St. Andrews) for his comments and suggestions during all the work. I am really gratefull to them for their kind hospitality during my stays in their institutions and I am also indebted to all the members of the solar physics groups of both universities for their hospitality, discussions and cheerful company.

Por último, pero no menos importante, debo reconocer el apoyo que toda mi familia en general me ha prestado en mi decisión de continuar mis estudios. Agradezco sinceramente a mis padres la oportunidad de haber cursado los estudios de doctorado y haber apoyado incondicionalmente desde siempre mi carrera en investigación. Agradezco también su paciencia, dedicación y abnegación, así como agradezco a mis hermanos, Juan Manuel y Sergio, haber sido grandes compañeros durante toda mi vida y haber despertado en mi la curiosidad por el mundo que nos rodea. Finalmente, quiero agradecer a Esther, auténtica musa inspiradora de este trabajo, haberme apoyado en mis decisiones y haberme dado inumerables momentos de felicidad durante todos estos años.

Antonio J. Díaz Medina

25-III-2004

Contents

Chapter 1

Introduction

One thing I have learned in a long life: that all our science, measured against reality, is primitive and childlike - and yet it is the most precious thing we have.

Albert Einstein

Sunshine is one of the most enjoyable experiences in life, specially in bright sunny days in Mallorca. From the beginning of time mankind has been interested in our source of energy, usually associating it with a deity, many times the most powerful one, and besides we can understand it when realizing how important this body is for us. That was the first motivation I had for investigating a bit more about this intriguing object, an investigation which has resulted in the work presented in this Thesis.

Since our aim in this Thesis is to study some of the standing oscillatory modes of solar prominence fibrils and coronal loops, first of all it is convenient to have an overlook of our star, specially focused on the Sun's atmosphere. In this introductory Chapter we start describing the main features of the solar atmosphere, which supports a lot of intriguing structures. We are interested in coronal loops and prominences, so we proceed to describe some of their properties and configurations based on observations. Finally, we concentrate on the observations of waves in these structures, setting the background of our theoretical study.

1.1 The Sun and its atmosphere

Our Sun is a self-gravitating yellow star (spectral type G2 V) of radius 696,000 km that radiates energy to feed all the solar system. This solar energy is produced by nuclear fusion at the inner region, where the temperature (about 15,000,000 K from models) and pressure are so intense that nuclear reactions take place. The composition is basically hydrogen (91.2 %) and helium (7.8 %), plus other heavier elements in a very small proportion, specially O, C, N, Ne, Fe among others. Almost all the matter is in a plasma state, in which almost all the electrons are not bounded to the nuclei. Therefore, a plasma is an ionised gas that can be affected by electric and magnetic fields.

The overall structure of the Sun (see Fig. 1.1) is made of concentric layers. The interior

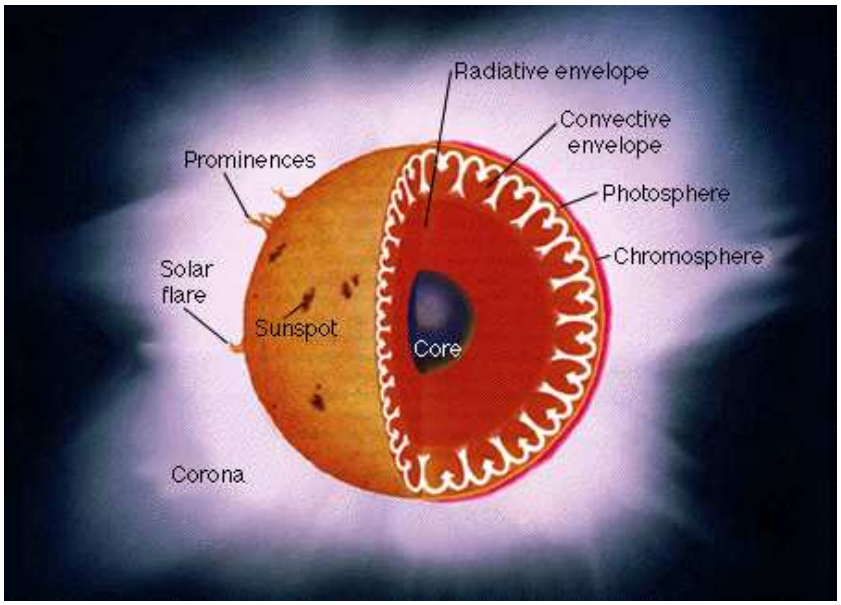

Figure 1.1: A sketch of the Sun showing its overall internal structure and its atmosphere. Also represented there are several forms of activity such as sunspots, flares and prominences, in the atmospheric layers.

is divided in three regions, the *core*, the *radiative zone* and the *convection zone*. The *core*, which extends up to $0.25R_\odot$, is like a furnace where the nuclear reactions take place. The energy generated there is slowly transferred outwards by radiative diffusion up to $0.7R_\odot$ and by convection thereafter. It is at the base of this final region where the solar magnetic field is generated. The solar interior is optically thick, so the original *γ-rays* coming from the nuclear fusion take 10^7 years on average to reach the surface and the typical wavelength is increased to that of visible light in the process. All this structure cannot be observed directly and must be inferred from theoretical models and other tools, like helioseismology (the study of the internal oscillations of the Sun) or neutrino detection. Outside these layers there is a visible *solar atmosphere*, which consists of three regions with different physical properties: the *photosphere*, the *chromosphere* and the *corona*. Finally, coronal material is continuously flowing away from the Sun to form the *solar wind*, that travels through the solar system and eventually reaches the Earth and beyond. Auroras and geomagnetic storms in the Earth are caused by strong perturbations of the solar wind.

The lowest part of the solar atmosphere (the *photosphere*) is the extremely thin (500 km) visible surface layer were most of the Sun's emission takes place. Therefore, the photosphere glows in visible light, except for dark areas called sunspots. Anyway, the photosphere does not only emit in the visible range, but it emits in a continuous spectrum in all frequencies, nearly like a black-body at a temperature of 5800 K, with emission and absorption lines superimposed. This layer has a mottled appearance when it is observed with more detail due to the turbulent plasma motions and eruptions of energy just below the surface.

Above the photosphere, the temperature has a minimum in the *chromosphere* and then

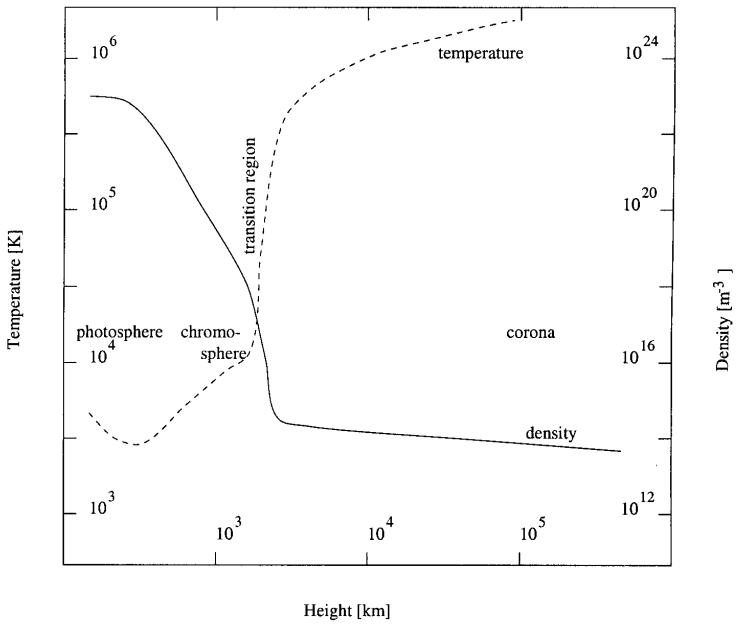

Figure 1.2: Schematic drawing showing the density (solid line, right-hand axis) and temperature (dashed line, left-hand axis) as a function of height in the solar atmosphere. The temperature decreases monotonically from the 15×10^6 K at the Sun's centre to about 6000 K at the surface, along a distance of some 700,000 km (not shown). Surprisingly, it only takes a few thousand km for the plasma to reach 10^6 K again. The heating of the solar corona to such a high temperature constitutes one of the great open questions of solar physics. The outer part of the corona is flowing continuously forming the solar wind (neither shown).

raises until it reaches millions of degrees in the outer part of the atmosphere, the *corona* (see Fig. 1.2). It is at this region were some of the emission and absorption lines are produced. The *chromosphere* is not only a static highly symmetric region, but it is also highly non-uniform, somehow reflecting the convective transport of energy in the outer layer of the Sun. This shell receives its name because it is so faint that it was directly seen for first time in solar eclipses as a colourful band at the limb of the Sun.

The solar corona

The *corona* cannot normally be seen in visible light because of the dazzling light of the photosphere, except in eclipses or with coronagraphs (in which a disk is used to eliminate the photospheric emission). Early observations of the visible spectrum of the corona revealed bright emission lines at wavelengths that did not correspond to any known materials. The true nature of the corona remained a mystery until it was determined that coronal gases are heated to temperatures greater than 1,000,000 K. At these high temperatures both hydrogen and helium (the two dominant elements) are completely stripped of their electrons and even minor elements like carbon, nitrogen and oxygen are stripped down to bare nuclei. Only the heavier trace elements

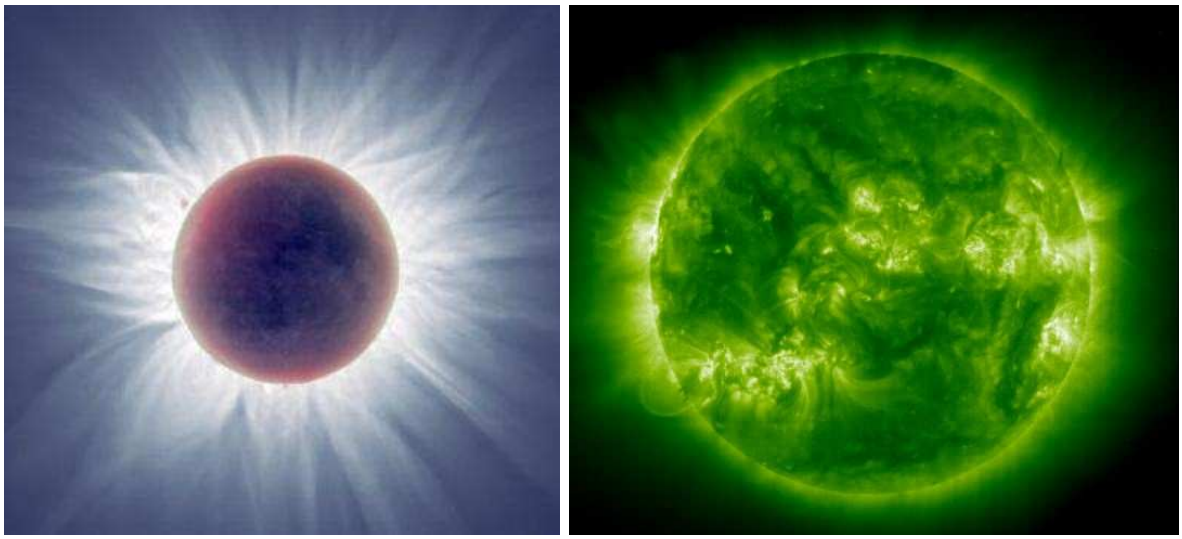

Figure 1.3: Two views of the solar corona. The first image was taken from a small ground telescope during the total eclipse of 2001 June 21 (credit by F. Espernak). The second one is an image taken by the EIT instrument of the *SOHO* spacecraft in the FeXII 195A line.

like iron and calcium are able to retain a few of their electrons in this high temperature. It is the emission from these highly ionised elements that produces the spectral emission lines that were so mysterious to nineteenth century astronomers. The nature of the processes that heat the corona, maintain it at these high temperatures and accelerate the solar wind is still unknown. Usually temperatures fall as you move away from a heat source. This is true in the Sun's interior right up to the visible surface, but then, over a relatively small distance, the temperature suddenly rises to extremely high values (Fig. 1.2). Thermal energy must be continually supplied to maintain such temperature against radiative cooling, so several mechanisms have been suggested as the source of this heating, mainly wave dissipation and electric current dissipation, although there is no consensus on which physical process, or combination, is actually responsible. In fact, the *coronal heating problem* remains one of the most challenging questions in solar physics (Priest & Hood 1991; Priest 2000).

The emitted intensity of the corona is about a millionth of the photospheric one, so it is not surprising that the corona only becomes visible to the naked eye during a total eclipse. Despite this, the solar corona is a very active research topic nowadays and many space missions have been sent out of the Earth's atmosphere to study the properties and fenomena that it displays. In *soft X-rays* the corona emits thermally and may be viewed directly from space, which is difficult for ground based telescopes due to the high absorption by the Earth's atmosphere at these wavelengths) and tones of useful information can be obtained by taking "radiographs" of the Sun at different wavelengths. Probably, the most outstanding missions have been the *Yohkoh* spacecraft (*sunbeam* in Japanese), the *Solar and Heliospheric Observatory (SOHO)* and the *Transition Region and Coronal Explorer (TRACE)*, but there are some others scheduled for the next years, so thanks to the efforts of the space agencies over the world the observations will become more detailed an precise in a short time.

The corona is a high temperature, low density region, in which the *magnetic field* determines the structure and in fact, under coronal conditions, the behaviour of the plasma is dominated by the magnetic field. Space observations in *soft X-rays* can be very detailed, so the magnetic structuring can be distinguished. There are two types of regions, depending on whether the magnetic field lines are open and connect to the interplanetary field (coronal holes) or closed over the surface, so that field lines form arches with their two endpoints in the photosphere), with small-scale energetic features (*X-ray* bright points) scattered over all the Sun's surface. Closed regions are in fact composed of myriads of coronal loops, with a wide range of dimensions, densities and temperatures. There are lots of other amazing structures supported in the highly structured corona (like active regions, prominences, streamers, plumes and so on). In this work we are interested in oscillations in coronal loops and solar prominences and we will focus on describing them.

Finally, far away from the static model in the 50s, the corona is a highly dynamical region, which is one of the first striking properties that we have learnt from space observations. There are many transient features and even the overall structure is changing in a high variety of time scales. All these forms of activity are due to the existence of the magnetic field and simply represent different ways in which the coronal plasma reacts to its variations. For example, the overall magnetic field follows the 22-year periodicity (the *solar cycle*), while a typical prominence can last for over 200 days, a coronal loop evolves in a matter of days and a coronal bright point or a flare evolve in hours or minutes. Even if we use static models to describe these objects and phenomena we should always keep in mind this fact.

1.2 Coronal loops

In 1973, the first *EUV* and *X-ray* images from Skylab revolutioned the scientific understanding of the solar corona by revealing that, far from a spatially homogeneous atmosphere, the coronal plasma is contained in closed, bright, looplike structures which outline the magnetic field. These structures, which are called coronal loops, are both dynamically and energetically independent (Vaiana, Krieger & Timothy 1973). Coronal loops have their footpoints in the photosphere and undergo only a slow evolution (apart from transient fenomena such as flares) over a time scale of weeks. However, this is the time scale of a loop system not influenced by other transients, since a single loop lasts about a day. It is also remarkable that loops have been detected in the atmospheres of other stars, pointing out that these are common features in stellar physics.

Coronal loops are classified in many ways, depending on what property is considered. They display a large range of temperatures (Fig. 1.4), densities and lengths. The main distinction is that some loops are associated with active regions while others are in quieter regions. The first ones are highly dynamical, and often hotter and shorter than the "quiet" ones, which connect different active regions or just different photospheric regions. In this work we concentrate on the "quiet" loops, whose range of temperatures is roughly 1–5 MK, particle density of 10^{14}–10^{15} m^{-3} and lengths of 20–1000 Mm. Some beautiful examples are shown in Fig. 1.5.

Regarding the structure of these coronal loops, observations point out that hot loops ($T \sim$ 3–5 MK, observed in soft *X-rays*) behave different than cool loops ($T \sim$ 1-2 MK, observed in *EUV*), which seem to be isothermal, while the hot ones obey scaling laws for plasma parameters

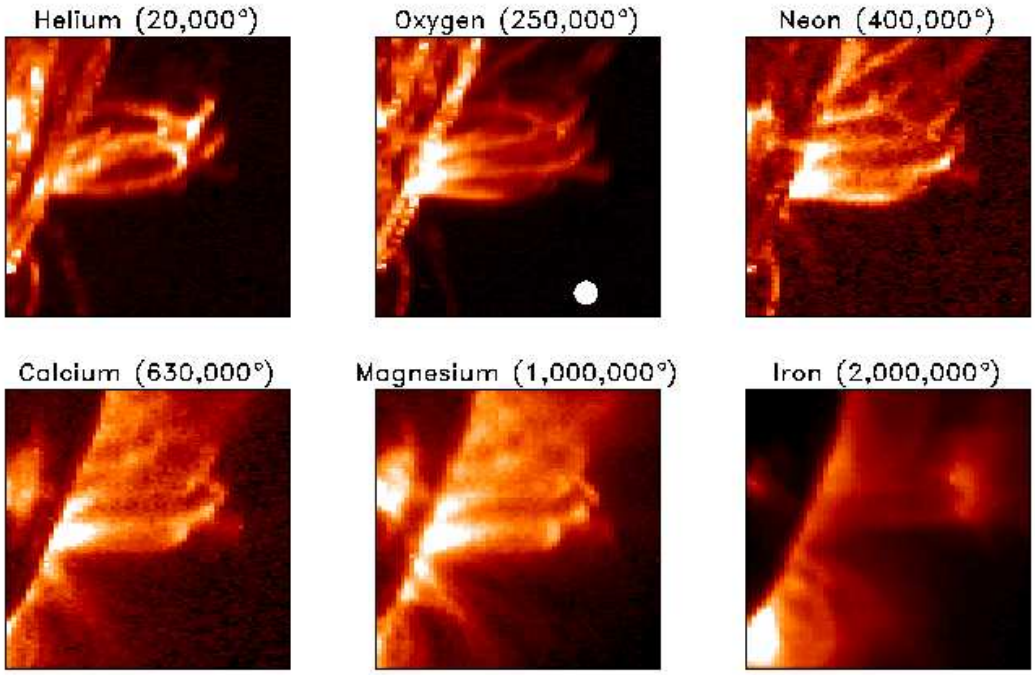

Figure 1.4: Coronal loops observed by CDS on the *SOHO* spacecraft above the solar limb (the edge of the Sun) at different temperatures.

such as density or temperature (Testa et al. 2002; Nagata et al. 2003; Winebarger, Warren & Mariska 2003). Detailed observational profiles of equilibrium parameters are obtained from instruments on spacecrafts and the equilibrium of these structures is a subject of intense research nowadays, with implications in the physics of plasma confinement. Here it must be remarked that coronal magnetic fields, which play a relevant role in the equilibrium and evolution of these structures, cannot be directly measured and only extrapolations from photospheric fields are available. Finally, observations at ever-increasing angular resolution have shown the presence of plasma structuring at every spatial scale so far resolved. Current theories and models tend to represent the structure of a bunch of fibrils as a single coronal loop, but some works have been published with the aim of studying the internal structure and the properties of single fibrils (see for example Testa et al. 2002).

One may wonder how it is possible that solar coronal loops are so hot. The nature of the energy source remains a long-standing fundamental problem in the physics of solar and stellar coronae. Theories for coronal heating fall mainly into three different types, namely small-scale heating (small explosive events, for example triggered by local reconnection), wave heating (phase mixing of Alfvén waves or resonant absorption) or turbulent current sheet heating (reconnection driven by changes in the configuration of the magnetic field due to footpoint motions). However, there is no closed explanation of this challenging question and every new detailed observation reveal new features, so in all probability, different mechanisms are acting

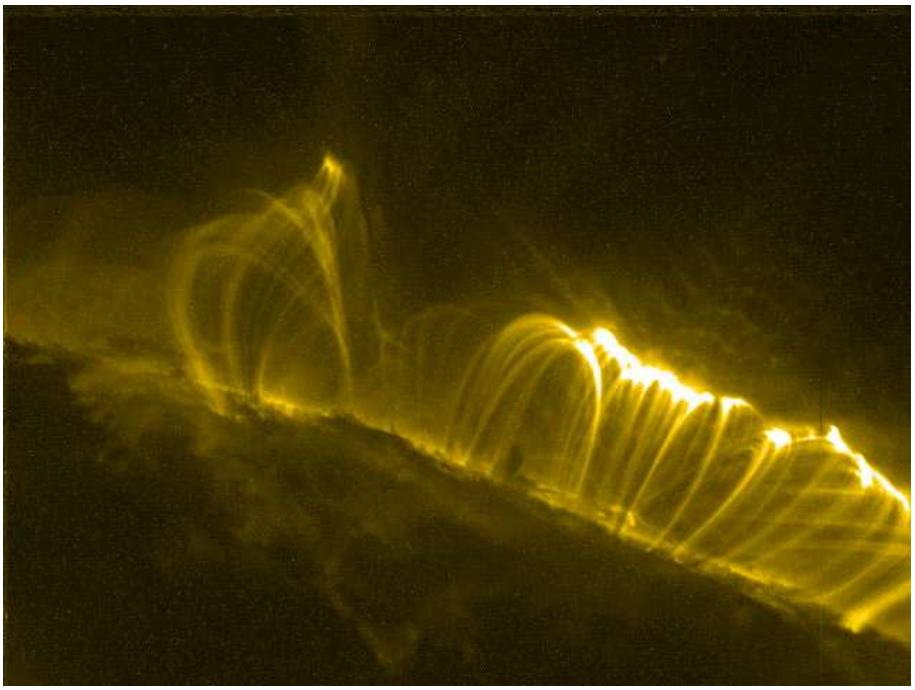

Figure 1.5: An arcade of coronal loops observed from *TRACE*.

Table 1.1: Typical parameter values in quiescent prominences.

particle density	10^{17} m^{-3},
temperature	7000 K,
magnetic field strength	5–10 G,
length	200,000 km,
height	50,000 km,
width	6000 km.

depending on the local circumstances.

1.3 Prominences: overall and fine structure

Prominences are intriguing objects. They are located in the corona, but possess temperatures a hundred times lower and densities a hundred or a thousand times greater than typical coronal values (see Table 1.1). Prominences are classified mainly in two types: active and quiescent. Active prominences appear over active regions (regions in which magnetic flux is emerging) and are short-lived, highly dynamical structures, with higher temperatures and magnetic fields than the ones in Table 1.1. On the other hand, quiescent prominences are quite stable structures that can last for several months until they gradually fade and disappear or become unstable and erupt. In eclipses or coronagraphs these features appear bright above the limb and can also

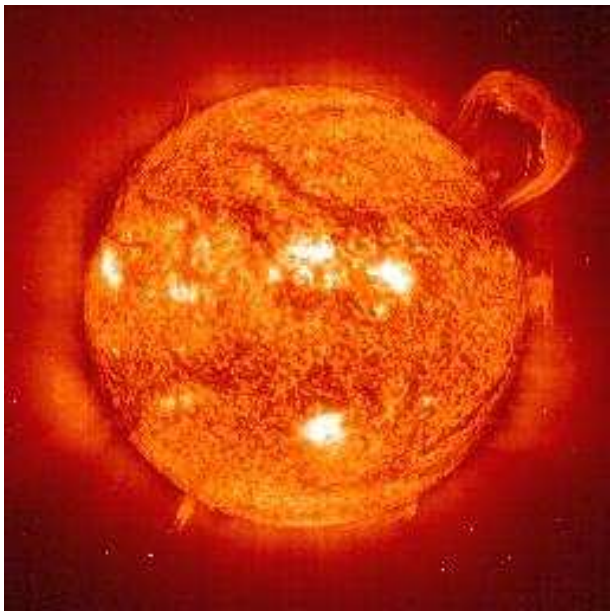

Figure 1.6: This *SOHO* spacecraft full Sun image taken in the He II emission line shows the upper chromosphere at a temperature of about 60,000 K. The bright features are called active regions. Prominences can be seen at the limb and as dark filaments in the disc. A huge erupting prominence escaping from the Sun can be seen in the upper right corner. If an eruption like this is directed toward the Earth it can cause a significant amount of geomagnetic activity in the Earth's environment with a following spectacular aurora.

be seen in Hα photographs (which show the lower *chromosphere*) as thin dark ribbons called filaments (see Figs. 1.6 and 1.7). Therefore, prominences can be described as cold dense vertical sheets of plasma embedded in the corona, with typical dimensions of Table 1.1, that can remain stable for many solar rotations. They are probably supported against gravity by the magnetic field, even though it is difficult for us to keep a similar laboratory plasma stable for a second (see Tandberg-Hanssen (1995) for a thorough description of prominence observations, physical parameter values and current theories).

Many models have been developed to explain how these cold clouds of dense plasma are supported against gravity and why they are not heated by the surrounding coronal material. Although it is not the aim of this work, we can briefly explain the main points. The key ingredient is the magnetic field structure, which shields the prominence from the coronal medium and supports it in the corona. Thermal conduction is directed mainly along magnetic field lines and hence any temperature inhomogeneity is along the field, but maintained across it. The magnetic field also exerts forces on the plasma, which in certain configurations can counteract gravity. There are also attempts to explain the formation, support, stability and disappearance of these intriguing objects, although no consensus about these issues has been reached yet (Webb, Schmieder & Rust 1998). Theoretical models have been put forward considering prominences as an infinite slab of plasma having a small thickness in comparison with coronal dimensions (Tandberg-Hanssen 1995; Priest 2000), as sketched in Fig. 1.8.

Observations also suggest that solar prominences are composed by small-scale threads of length 5000–10,000 km and width about 300 km (Tandberg-Hanssen 1995) called *fibrils* (see for example Figs. 1.9 and 1.10). However, these threads may be thinner, since the smallest observed widths are of the same size as the instrumental resolution limit. In a perfectly conducting plasma, magnetic field lines behave as if they were frozen to the plasma (see Appendix A), so probably this fine structure is determined by the magnetic arcades that support the prominence. These fibrils are stacked up one after another in both the vertical and horizontal directions to form the sheet of plasma of the prominence, each of them consisting in a magnetic loop with accumulated

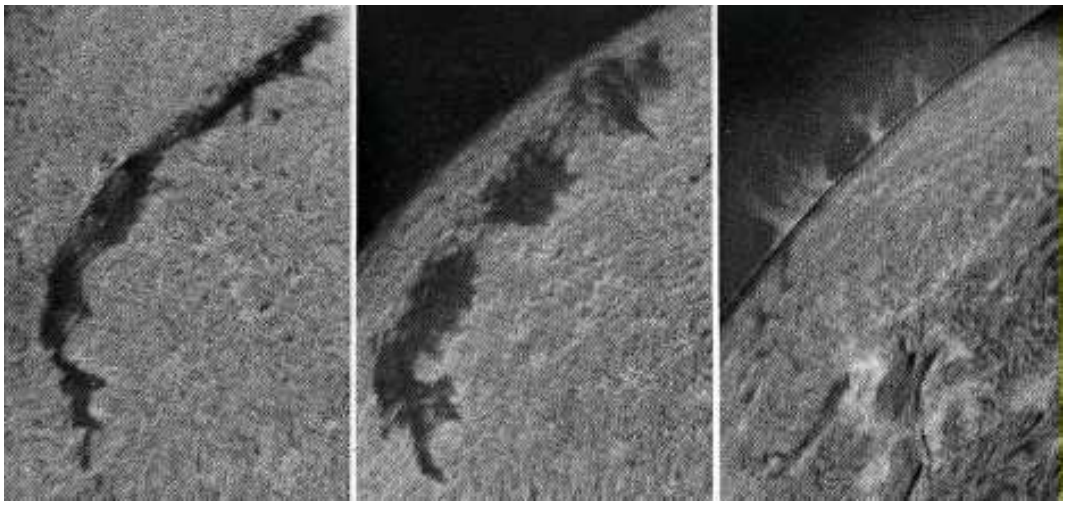

Figure 1.7: A prominence seen in different moments of solar rotation. In the first image it is clearly a dark filament on the disk, while in the last one the same structure is seen as a bright prominence at the limb.

material on the top, while the rest of the loop, which is rooted in the photosphere, has coronal properties. The existence of this internal structure in prominences was already suggested by Menzel & Evans (1953) and was clarified with the improvement of observational capabilities (Engvold 1976; Engvold et al. 1987). Although vertical filamentary structures can be seen in limb prominences, as in Fig. 1.10 (Dunn 1960), there is also evidence for the existence of horizontal fine structures within prominences, as in Fig. 1.9 (Schmieder & Mein 1989; Schmieder, Raadu & Wijk 1991, Engvold 2001). Demoulin et al. (1987) deduced statistical sizes of 10^3 km and 10^4 km for the thickness and length of the threads which form a filament, respectively. Engvold et al. (1987) studied a quiescent prominence seen in projection against the disk and, from the study of the prominence-corona interface, deduced that the fine structure of the cool core of the prominence may consist of thin magnetic flux ropes oriented at an angle of 20^o with the prominence long axis, as later confirmed in Engvold (2001). Taking into account the observational evidence that solar prominences can be composed of small-scale loops, magnetostatic equilibrium models for prominence fibrils have been constructed by Ballester & Priest (1989), Degenhardt & Deinzer (1993) and Schmitt & Degenhardt (1996). These models represent a prominence fibril by means of a hot-cool loop modeled using the thin flux tube approximation. A different approach was used by Hood, Priest & Anzer (1992), Steele & Priest (1992) and Steele (1996), who modeled prominences as a vertical set of cold fibrils in the hotter corona, with ad hoc temperature profiles.

1.4 Observations of coronal loop oscillations

Many types of oscillations have been observed in coronal loops and, generally, standing modes are distinguished from propagating ones. Propagating slow waves have been clearly observed both with the EIT instrument on the *SOHO* (Berghmans & Clette 1999) and *TRACE* (De

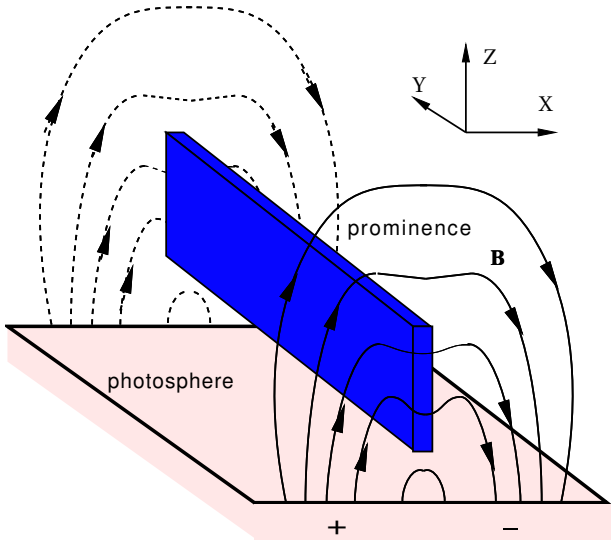

Figure 1.8: Sketch of the supporting magnetic field for a straight unlimited prominence(represented as a blue slab) modeled as a plasma sheet lying above the photosphere.

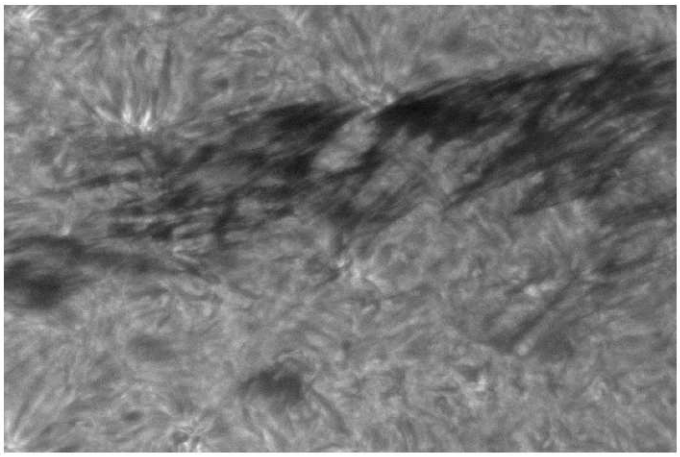

Figure 1.9: A large filament observed on 19 June 1998 in the Hα 6563A line using the tunable filter of Lockheed mounted in the Swedish Vacuum Solar Telescope at La Palma. Notice the thread like structures that form the filament when observed with more resolution (after Lin et al. 2002).

Moortel et al. 2002a, 2002b). These waves are triggered at the footpoints, propagate upwards and are attenuated as they travel. Another interesting feature is that this phenomenon of waves being excited and dissipating in the way upwards is stable and long-term remaining. The periods are in the range 10–15 min, while the velocity of propagation lies in the range 75–125 km/s. In fact, theoretical models have been put forward and reproduce quite well the phase velocity, the periods and damping lengths, so these waves are currently identified as propagating slow modes. It is also remarkable that there are also ground observations during eclipses of propagating waves with periods of 6 s and phase velocities of 2100 km/s (Solar Eclipse Coronal Imaging System, Williams et al. 2002; Katsiyannis et al. 2003); these oscillations seem to be impulsive fast modes, but they are still being investigated.

These impulsive modes are outside the scope of this Thesis, which is devoted to standing modes. These sort of modes have also been observed in coronal loops as transverse displacements and also in the Doppler shift and line intensity. There are reports of many observations of temporal oscillations of coronal loops in the radio band (see table 1 in Aschwanden et al. (1999)

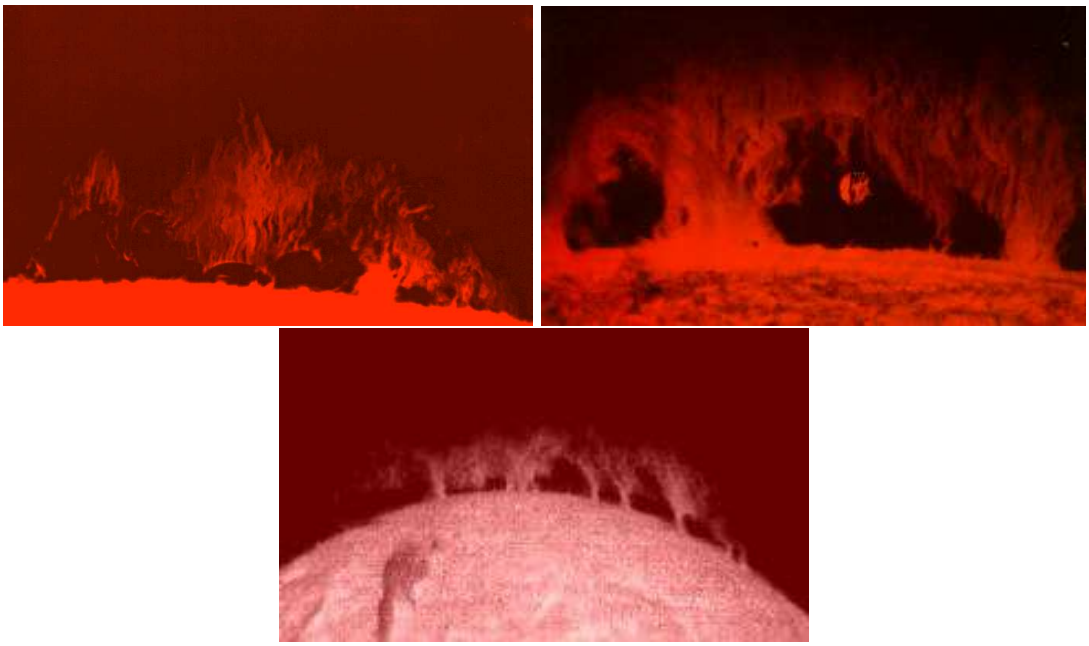

Figure 1.10: Three prominences seen in Hα at the limb. The fibril structure can be clearly appreciated in these images. Most of the fibrils are vertical and so they do not seem to correspond to the horizontal ones in Fig. 1.9.

for a review), but the observations made from *TRACE* are the ones that have stunned the solar community. Spatial displacement oscillations of coronal loops have been clearly observed by this spacecraft (Aschwanden et al. 1999, 2002; Schrijver, Aschwanden & Title 2002), with periods in the order of 5 min; these modes have been identified as the standing kink modes (Nakariakov & Ofman 2001, Aschwanden et al. 2002).

Other type of detected standing modes are those seen in the line intensity and Doppler shift simultaneously by *SOHO* instruments (Wang et al. 2002, 2003a, 2003b). These oscillations have periods of the order of 14–18 min and phase velocities in the range 240–360 km/s, which matches the sound speed of the loop, making possible to identify these waves as standing slow modes. It is important to remark that a clue to label them as standing is that there is a quarter period phase difference between the Doppler velocity and the line intensity (Fig. 1.11), a fact that is also discussed later in this work.

Finally, another recently reported kind of standing mode supported by loops is the global sausage mode, detected by ground telescopes. The period is in the 6–20 s range and it is under investigation right now (Nakariakov, Melnikov & Reznikova 2003; Aschwanden, Nakariakov & Melnikov 2004).

In this Thesis we are interested in the standing kink (and also sausage) modes, so we proceed to describe these modes in more detail. A carefully obtained sample of events is presented and discussed in Schrijver et al. (2002) and Aschwanden et al. (2002). First of all, these transverse oscillations are detected by movement of the bright loops in the images. Then, the loops are characterized by their geometrical properties and finally the properties of the oscillations are

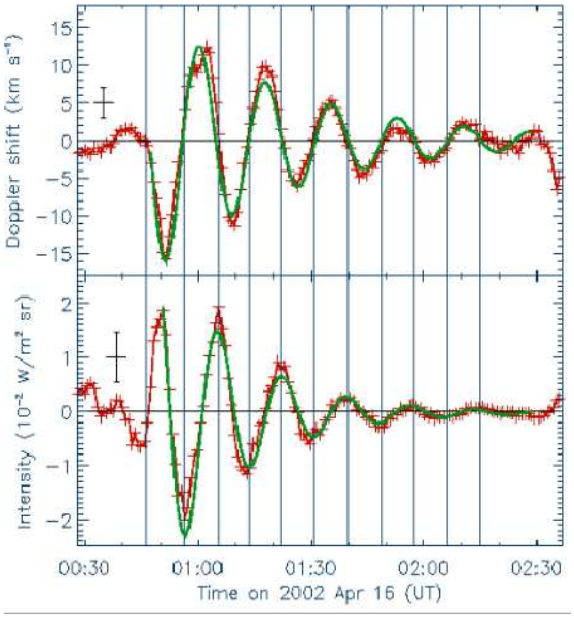

Figure 1.11: Evolution of the Doppler shift and of the line-integrated intensity in the Fe XIX line. The thick solid curves are the best fits with a damped sine function. The background shift has been removed in the first panel, while the background intensity has also been removed in the second. Notice the 1/4-period phase difference between velocity and line intensity (after Wang et al. 2003b).

obtained. The resulting periods are in the range 3–18 min. These modes are identified as kink modes because the loop center is also displaced and their period matches the one predicted for the fast magnetohydrodynamic mode. However, there are many other features still lacking explanation, such as how these modes are modified by the inhomogeneities, why these modes are so rarely excited or what the mechanism is responsible for the damping these oscillations.

1.5 Observations of prominence oscillations

The study of prominence oscillations goes back to the 1950s and 1960s. Since that time, considerable advances have been made in the field thanks to the use of sophisticated observational techniques and tools for analysing the data. Furthermore, the theoretical side has experienced an enormous progress since plenty of studies on the propagation of magnetohydrodynamic (MHD) waves in simple prominence equilibria have been undertaken (see Oliver & Ballester (2002), Engvold (2001) and Ballester (2003) for thorough reviews on prominence oscillations observations and theory).

From the observational point of view, prominence oscillations can be grossly classified in two groups according to the amplitude of periodic variations: large amplitude and small amplitude oscillations. The first ones arise when the whole prominence is shaken by a wave propagating on the Sun's surface. In this category falls the so called "winking filament", which refers to the optical effect of an event in which the line of sight velocity is large enough to make the emission of the material fall outside the sensitivity range of the instrument at the maxima of the oscillatory movement. The second class is frequently observed (specially in the last twenty years) and may show spatial structure (can be even confined to a small region or a fibril). The amplitude is smaller, sometimes near the noise level, and seems to be related to proper modes of the structure. There is evidence of a given prominence that has been observed over a few consecutive days and the outcome is that the same period seems to be recovered (Bashkirtsev &

Table 1.2: Some relevant reports in which the oscillatory region is just a small part of a prominence. The value of the period found in some consecutive points is given, along with the size of this region. In the last column 'Slit' is used to specify that oscillations have been detected using a spectrograph slit, whereas 'Fibril' or 'Region' indicate that individual fibrils or an extense region in a two-dimensional field of view display an oscillatory character (After Oliver & Ballester 2001).

Reference	Period (min)	Size (km)	Slit/Fibril
Tsubaki & Takeuchi (1986)	3.5	20,000	Slit
Suematsu et al. (1990)	~ 60	2800	Slit
Thompson & Schmieder (1991)	4.4	84,000	Fibril
Yi et al. (1991)	5.3, 8.6, 15.8	21,000	Fibril
	5.3, 7.9, 10.6	7000	Fibril
Balthasar et al. (1993)	0.5–20	1000–37,000	Slit
Balthasar & Wiehr (1994)	5.3–60	1000–2000	Slit
Sütterlin et al. (1997)	3.5-62	2100–7700	Slit
Molowny-Horas et al. (1997)	4–12	1400–7300	Slit
Terradas et al. (2002)	~ 80	$\sim 30{,}000$	Region
Lin & Engvold (2002)	14-19	~ 5000	Fibril

Mashnich 1984; Mashnich & Bashkirtsev 1990; Sütterlin et al. 1997). This seems to indicate that each prominence has its own characteristic period, or periods, of oscillation, such as expected for an object whose overall properties do not change much over this time interval. In addition, Tsubaki et al. (1988) obtained successively two time series of spectra by placing the spectrograph slit first at a height of 30,000 km above the solar limb and next 40,000 km above the limb. A group of vertical threads detached from the prominence main body displayed 10.7 min periodic variations at both heights, which points to the "one prominence (or one fibril), one period (or set of periods)" interpretation. A similar picture emerges from two-dimensional analyses of filaments (Thompson & Schmieder 1991; Yi, Engvold & Keil 1991) and limb prominences (Terradas et al. 2002). However, two-dimensional spatially resolved observations are required, since the actual Doppler and line intensity observations may be simply noise in most of the samples (the signal to noise ratio is very low and often there is only one detectable period or less) and it is difficult to track one position to make accurate measurements. If fact, in some of the observations the different reported periods may be only a problem of coherence lengths (Wiehr 2003).

The existence of small amplitude, periodic velocity oscillations in quiescent solar prominences is a well-known phenomenon and many theoretical investigations have been undertaken to explain them. Periods of oscillation are classified as short ($T < 10$ min), intermediate (10 min $< T < 40$ min) and long ($T > 40$ min) although this classification does not seem to reflect the origin of the prominence exciter. In addition, it appears to be well established that small amplitude, periodic changes in solar prominences are of local nature, affecting only restricted prominence areas. Some recent observations of periods in prominence structures are summarized in Table 1.2. Two-dimensional, high-resolution observations (Yi et al. 1991; Yi & Engvold 1991) have even revealed that individual fibrils or groups of fibrils may oscillate independently with their own periods, which range between 3 and 20 minutes. Hence, one of the basic questions in prominence seismology that remains unanswered nowadays is whether periodic changes in prominences are always associated with their fibril structure or not. But at least, in previous references there is some evidence of these structures supporting their own

modes. Obviously, in real prominence fibrils there is some kind of damping of these stationary modes (see for example Nakariakov et al. (1999) and Terradas et al. (2002)), but this simple description provides physical insight into the nature of the modes and also will serve as a useful guide to calculations in more complicated situations.

1.6 Outlook of the Thesis

After having presented the current observational background in this Chapter, it is clear that the topic of oscillations in the corona is of great interest. However, theoretical models are still in development, so the aim of this Thesis is to contribute to improve the theoretical understanding. In particular, we focus in the effects produced by the addition of inhomogeneities along the structure in the oscillatory modes. To achieve this objective, the Thesis is divided in the following Chapters.

First of all, in Chapter 2 we introduce the equations of Magnetohydrodynamics. Then, we proceed to the wave equations and the description of the array of modes that are obtained. We end this Chapter by reviewing some classical results about oscillations in simple structures with inhomogeneities. In Chapter 3 we present the equilibrium models that we use in the rest of the Thesis, with a brief introduction about the aims of coronal seismology and its relation with the modelling of coronal structures. Two types of models are detailed: those for coronal loops and those for prominence fibrils. In Chapter 4 the procedure to find analytical solutions is presented, starting with the description of wave equations specific for the kind of problems described in Chapter 3 and following with the mathematical tools employed to find dispersion relations. Here we distinguish between two different geometries, the Cartesian and the cylindrical ones, and find dispersion relations for each of them carefully applying the suitable boundary conditions.

In Chapter 5 the topic of coronal loop oscillations is addressed. The Chapter is divided in two parts, one describing the differences introduced by the line-tying condition in previous unbounded models, while in the second part the effect of inhomogeneities along the loop is studied. The first part is a starting point not only for this Chapter, since it presents the most simple model that we use, but it is also a linking point with other developments. The second part is more focused on coronal loop modelling, in the sense that it is a first step towards a more accurate description of the modes of coronal loops with observed density profiles. Here we also consider the topic of evanescent modes, which provides some interesting conclusions about the leakage of energy towards the coronal medium and the lack of detection of some of the modes.

After having explained the results for coronal loops, we turn our attention to prominence fibrils. In Chapter 6 we present the first model: a single Cartesian prominence fibril without and with longitudinal propagation and the results are compared with the observed data. However, prominence fibrils are expected to be closely packed and vibrating together, so in Chapter 7 the problem of multifibril Cartesian systems is studied, departing from the results obtained in Chapter 6. However, these models lack an important ingredient: prominence fibrils are better modelled as cylindrically symmetric structures, and hence we study a single cylindrical fibril in Chapter 8.

Finally, in Chapter 9 the results and conclusions of this work are presented, and a brief discussion of future developments and applications of these results is carried out.

Chapter 2

Magnetohydrodynamics

How can it be that mathematics, being after all a product of human thought independent of experience, is so admirably adapted to the objects of reality?

Albert Einstein

It has been stated that the matter in the conditions present in the Sun is in a plasma state, that is, a ionised gas in which free charges are abundant enough to influence the physical properties of the medium. Under these conditions the plasma is reasonably well described by the equations of Magnetohydrodynamics (MHD for short). This theory can be introduced as reasonable equations from fundamental theories in Physics or can be derived directly from the kinetic equations taking into account certain approximations and properties of the plasma state.

MHD describes a single fluid (although a plasma contains different components, like ions and electrons, that behave differently), so the length scales of variations need to be much larger than the typical kinetic plasma lengths. This is not the most general description of a plasma, although it has been capable to explain the major facts in solar physics. In fact no *quantum effects* are taken into account, neither are *relativistic corrections* considered (speeds are usually very small compared with the speed of light), *kinetic effects* are removed (only thermodynamic equilibrium is used and the equations can be cast without statistical effects) and even the *displacement current* is neglected in Maxwell equations (no electromagnetic waves). The whole field could have been studied more than 140 years ago if observations had been available. But even having removed nearly all modern physics, MHD is the simplest relevant theory that explains many facts in solar Physics and also has a coherent structure and respects the main physical conservation laws (see Goedbloed (1983) for a deeper discussion about this interesting topic), although for studying some effects it is necessary to include some of this "modern" physics.

In spite of all the simplifications made, the resulting system is still very complex because it is a description in terms of coupled non-linear partial differential equations. More assumptions and simplifications are currently used to obtain analytical solutions, or for studying the behaviour under solar conditions. Dissipative terms can be neglected, leading to ideal MHD. It is also very useful to consider small deviations from a given equilibrium, leading to linearized perturbation equations, used for small perturbations that lead to stability analysis and wave studies. Finally, some techniques have been developed to deal with the whole system, which has some similarities

with fluid physics, but with the magnetic field playing a relevant role.

In this Chapter the MHD equations are presented and some important general consequences are also explained. Next the linearization is discussed and the low-β plasma assumption is presented. Then, a comment on boundary conditions is included, specially because it will be very important in some Chapters. Finally, some relevant wave solutions of simple plasma configurations are studied, in particular the ones that have some relation with loop and prominence fibril oscillations.

2.1 The equations of ideal magnetohydrodynamics

MHD can be viewed basically as a combination of the electromagnetic equations (Maxwell equations and Ohm's law) and fluid mechanics equations (the Navier-Stokes equations). In Appendix A these equations are introduced starting from these fundamental equations of Physics applied to a continuous plasma. However, these MHD equations can also be derived by averaging the corresponding kinetic equations. It is beyond the scope of this work to discuss the interesting topic of the properties of a medium called plasma, the ideal MHD that models it (and specially its assumptions and breakouts) and the postulates used for the derivation of the equations; more information can be obtained in standard textbooks, such as Goedbloed (1983), Priest (2000) or Goossens (2003).

Putting together all the relevant equations that are introduced in Appendix A, we obtain the set of *ideal MHD equations*,

$$\frac{\partial \rho}{\partial t} + \nabla \cdot (\rho \mathbf{v}) = 0, \tag{2.1}$$

$$\rho \frac{D\mathbf{v}}{Dt} = -\nabla p + \frac{1}{\mu}(\nabla \times \mathbf{B}) \times \mathbf{B}, \tag{2.2}$$

$$\frac{Dp}{Dt} + \gamma p \nabla \cdot \mathbf{v} = 0, \tag{2.3}$$

$$\frac{\partial \mathbf{B}}{\partial t} = \nabla \times (\mathbf{v} \times \mathbf{B}), \tag{2.4}$$

$$\nabla \cdot \mathbf{B} = 0, \tag{2.5}$$

namely the continuity equation (Eq. 2.1), the equation of motion (Eq. 2.2), the energy equation (Eq. 2.3), the induction equation (Eq. 2.4) and the solenoidal condition (Eq. 2.5). These equations constitute a set of nine non-linear partial differential equations for eight variables, $\rho(\mathbf{r}, t)$, $\mathbf{v}(\mathbf{r}, t)$, $p(\mathbf{r}, t)$, $\mathbf{B}(\mathbf{r}, t)$, from which other quantities like $\mathbf{j}(\mathbf{r}, t)$ or $\mathbf{E}(\mathbf{r}, t)$ can be obtained with the relations introduced in Appendix A. This system can also be expressed in a conservative form (see Appendix B).

There are two forces in Eq. (2.2). It is worthwhile to have a more detailed look into the second term of this equation, the so-called Lorentz force ($\mathbf{j} \times \mathbf{B}$). This term may be rearranged

by means of Eq. (A.6) and a vector identity, leading to

$$\mathbf{j} \times \mathbf{B} = (\mathbf{B} \cdot \nabla)\frac{\mathbf{B}}{\mu} - \nabla\left(\frac{B^2}{2\mu}\right). \tag{2.6}$$

The first term in this equation represents the effect of a tension parallel to the magnetic field and the second the gradient of a scalar magnetic pressure. The Lorentz force has therefore two effects on the plasma: to compress it through the magnetic pressure term and also to shorten magnetic field lines through the tension force, τ, which represents the effect of a tension parallel to $\mathbf{B}$ which appears whenever magnetic field lines are curved. It is often convenient to rearrange Eq. (2.2) taking into account this decomposition,

$$\rho\frac{D\mathbf{v}}{Dt} = -\nabla p_{\mathrm{T}} + (\mathbf{B} \cdot \nabla)\frac{\mathbf{B}}{\mu}, \tag{2.7}$$

where the quantity

$$p_{\mathrm{T}} = p + \frac{B^2}{2\mu} \tag{2.8}$$

is called the total pressure and sometimes substitutes the pressure as a dependent variable, specially in wave analysis.

Furthermore, a non-ideal energy equation can also be included to find stationary equilibrium configurations. For example, in the solar corona the coronal heating is often included in the equilibrium considerations and in this work is considered in some models instead of using "pure" Magnetohydrodynamics (see the Appendix A).

2.1.1 Linearized magnetohydrodynamic equations and oscillatory modes

For many purposes it is desirable to have a deeper insight into the dynamics of the plasma than is obtained from a study of the non-linear Eqs. (2.1)–(2.5), specially because of the extreme limitations posed by present-day mathematical knowledge about analytical solutions of non-linear partial differential equations. Once the system has been linearized many techniques become available and, consequently, a much better grasp of the problem is obtained. Obviously, not all the situations are suited to this kind of description, but since our main interest is to study small-amplitude oscillations, it is possible to describe the *equilibrium state* of a realistic configuration, simple enough to be solved. Next the problems of linear stability and waves can be studied as small deviations from the equilibrium state by solving the linearized MHD equations.

Consider a static equilibrium configuration ($\partial/\partial t = 0, \mathbf{v} = 0$) that satisfies the MHD equations. The equilibrium variables, which are hereafter labelled with the subscript "0", are assumed to suffer small displacements from their equilibrium values,

$$\mathbf{B}(\mathbf{r}, t) \;=\; \mathbf{B}_0(\mathbf{r}) + \mathbf{B}_1(\mathbf{r}, t), \tag{2.9}$$

$$\mathbf{v}(\mathbf{r},t) = 0 + \mathbf{v}_1(\mathbf{r},t), \tag{2.10}$$
$$\rho(\mathbf{r},t) = \rho_0(\mathbf{r}) + \rho_1(\mathbf{r},t), \tag{2.11}$$
$$p(\mathbf{r},t) = p_0(\mathbf{r}) + p_1(\mathbf{r},t). \tag{2.12}$$

Notice that the equilibrium velocity has been set to zero, although it is not strictly necessary, but in the models of coronal structures studied here equilibrium flows are not included. Now Eqs. (2.1)–(2.5) are linearized and squares and products of the small quantities are neglected, giving as a result

$$\frac{\partial \rho}{\partial t} + (\mathbf{v}\cdot\nabla)\,\rho_0 + \rho_0\,(\nabla\cdot\mathbf{v}) = 0, \tag{2.13}$$
$$\rho_0\frac{\partial \mathbf{v}}{\partial t} = -\nabla p + \frac{1}{\mu}(\nabla\times\mathbf{B})\times\mathbf{B}_0 + \frac{1}{\mu}(\nabla\times\mathbf{B}_0)\times\mathbf{B}, \tag{2.14}$$
$$\frac{\partial p}{\partial t} + (\mathbf{v}\cdot\nabla)\,p_0 - c_{\rm s}^2\left(\frac{\partial \rho}{\partial t} + (\mathbf{v}\cdot\nabla)\,\rho_0\right) = 0, \tag{2.15}$$
$$\frac{\partial \mathbf{B}}{\partial t} = \nabla\times(\mathbf{v}\times\mathbf{B}_0), \tag{2.16}$$
$$\nabla\cdot\mathbf{B} = 0, \tag{2.17}$$

where the subscript "1" in the perturbed quantities has been dropped and the adiabatic sound speed $c_{\rm s}^2 = \gamma p_0/\rho_0$ has been introduced. The linearized magnetic tension in Eq. (2.7) has two terms, namely

$$\tau = (\mathbf{B}_0\cdot\nabla)\frac{\mathbf{B}}{\mu} + (\mathbf{B}\cdot\nabla)\frac{\mathbf{B}_0}{\mu}, \tag{2.18}$$

while the perturbed total pressure is obtained from the linearization of Eq. (2.8),

$$p_{\rm T} = p + \frac{\mathbf{B}_0\cdot\mathbf{B}}{\mu}. \tag{2.19}$$

Notice that the system of Eqs. (2.13)–(2.17) is linear for the perturbation variables and some solutions are known for special geometries. Since we are looking for oscillatory perturbations, the time coordinate is Fourier analysed

$$a(\mathbf{r},t) = \hat{a}(\mathbf{r})\; e^{-i\omega t}, \tag{2.20}$$

a being any perturbed magnitude in Eqs. (2.13)–(2.17); for the sake of simplicity the hats will also be dropped in the following.

In order to gain insight into the properties of the linearized equations, we first consider an unbounded homogeneous medium. In this case, all the equilibrium parameters in Eqs. (2.13)–(2.17) are constant, so these equations are considerably simplified and the space coordinates can be Fourier analysed by considering plane-wave solutions for the perturbed magnitudes. Two parameters arise then, the sound speed and the *Alfvén speed*, defined by $c_{\rm A}^2 = B_0^2/(\mu\rho_0)$, which

are characteristic of the medium. Finally, the condition for having non-trivial solutions gives the dispersion relation for *magnetoacoustic waves*. In an unlimited homogeneous plasma permeated by a uniform magnetic field there are three modes of oscillation, whose main properties are summarised here:

- *Alfvén mode.* Driven by tension forces with no pressure or density variations (incompressible). Plasma motion is transverse to both the applied magnetic field and the direction of propagation. Highly anisotropic mode, unable to propagate across the field, with energy flowing along field lines at the Alfvén speed.
- *Slow mode.* Driven by tension and pressure forces, with pressure and density variations. Anisotropic, unable to propagate across the field lines, the energy flow is confined to the vicinity of certain magnetic field lines.
- *Fast mode.* Driven by tension and pressure forces, with pressure and density variations too. Roughly isotropic, although propagating faster across the field.

It should be pointed out that under other conditions, the above distinction is not clear (if not impossible), because the modes become coupled. Anyway, in some situations it is still possible to identify the characteristics of a wave and to classify it by comparing with the most suitable mode in an infinite homogeneous medium.

2.2 Low-beta plasma

In many applications, specially in the solar atmosphere, there is an important simplification that can be done in the MHD equations. In the equation of motion Eq. (2.2) (or the linearized version Eq. 2.14) there are only two forces: the pressure gradient and the magnetic force. The relative importance of the two terms can be estimated by the plasma β parameter, defined as

$$\beta = \frac{\text{gas pressure}}{\text{magnetic pressure}} = \frac{p}{B^2/2\mu}, \tag{2.21}$$

where the magnetic pressure is one of the terms obtained when the Lorentz force is rearranged (Eq. 2.7). A general expression can be used to evaluate this parameter (Priest 2000),

$$\beta = 3.5 \times 10^{-21}\, nTB^{-2}. \tag{2.22}$$

In the solar interior β is usually large, so the pressure gradient dominates the plasma behaviour, but for typical coronal values of particle density $n = 10^{14}\,\mathrm{m}^{-3}$, temperature $T = 10^6\,\mathrm{K}$ and magnetic field strength $B = 10\,\mathrm{G}$ we obtain a value $\beta_{\text{corona}} = 3.5 \times 10^{-3}$, while for typical values of a prominence (Table 1.1) the result is $\beta_{\text{prominence}} = 0.025$. Therefore, it can be assumed that $\beta \approx 0$ in coronal and prominence applications of the MHD equations. This is called the low-β plasma assumption and under these conditions the plasma is completely dominated by the magnetic field. Then the problem is to find a magnetic field configuration that satisfies the

solenoidal condition and $(\nabla \times \mathbf{B}) \times \mathbf{B} = 0$, but even this relative simple problem has lots of interesting solutions still under research.

Taking into account this approximation in the linearization of the MHD equations, the perturbation Eqs. (2.13)–(2.17) can be written as

$$\rho_0 \frac{\partial \mathbf{v}}{\partial t} = \frac{1}{\mu}(\nabla \times \mathbf{B}) \times \mathbf{B}_0 + \frac{1}{\mu}(\nabla \times \mathbf{B}_0) \times \mathbf{B}, \tag{2.23}$$

$$\frac{\partial \mathbf{B}}{\partial t} = \nabla \times (\mathbf{v} \times \mathbf{B}_0), \tag{2.24}$$

$$\nabla \cdot \mathbf{B} = 0, \tag{2.25}$$

where the pressure term has been dropped in the equation of motion. Notice that the energy and continuity equations are no longer necessary except for calculating the pressure and density perturbations, since these magnitudes are no longer relevant for solving the system and can be regarded as derived quantities.

The wave modes of Sect. 2.1.1 are also modified by this *low-beta plasma approximation* (often called cold plasma approximation). The sound speed is then $c_s = 0$ (in fact c_s/c_A is related to the plasma beta). Typical numerical values for the corona are $c_s^2 = 150$ km/s, $c_A^2 = 2800$ km/s (Priest 2000), so the Alfvén speed is much larger that the sound speed in coronal conditions. Using typical values for a prominence (Table 1.1) the characteristic speeds are $c_s^2 = 10$ km/s and $c_A^2 = 90$ km/s, so the Alfvén speed is still higher that the sound speed in a prominence plasma.

There are two modes left under these conditions, a fast mode and an Alfvén mode, while the slow mode has disappeared. It is important to remark that Alfvén modes are not driven by pressure gradient forces; only the tension force in Eq. (2.18) is acting for Alfvén waves, while both the tension force and total pressure gradient are driving fast waves (as was stated in Sect. 2.1.1 in more general conditions).

2.3 Boundary conditions

The model of ideal MHD includes the equations of ideal MHD but also the *boundary conditions* on a prescribed boundary and optionally *initial data* on and inside that boundary. The equations can describe many physical phenomena, specially magnetohydrostatic equilibria or wave modes and their properties. Anyway, more complex geometries lead to more tedious analysis, but also to new physics, which cannot be analysed in homogeneous media. In solar physics the more common boundaries are interfaces between plasmas of different properties (inhomogeneities, shocks, ...), but it is also interesting to study interfaces with other media, like vacuum or a wall (more common in laboratory plasma physics).

There is also another kind of boundary conditions. First of all, we are not interested in expressions having divergences, a condition which usually limits the functional form of the required solution. Boundaries at "infinite" are also relevant, where additional conditions are imposed, such as avoiding a diverging function or no energy income into our system from the

exterior. These conditions are imposed in general physical problems, but in this section we are interested in "jump" conditions, that is, boundary conditions relating the physical parameters of the plasma of two different media with a common contact surface. The whole deduction is included in Appendix B, but here we will only discuss the consequences.

There are two types of contact discontinuities, depending on whether the magnetic field is normal to the boundary or not (Fig. 2.1). We shall use in the following the convention $[a] = a_2 - a_1$ for the jump of the quantity a across the boundary between two regions having different plasma properties and labelled "1" and "2". Now, after putting the MHD equations (2.1)–(2.5) in a conservative form and using the Gauss's theorem we obtain a set of conditions. Two different situations arise, depending whether the magnetic field is perpendicular to the contact surface or not:

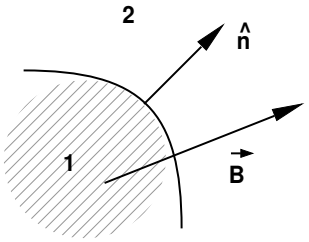

Figure 2.1: Schematic drawing showing the boundary, the normal vector and the magnetic field.

- $\boxed{\hat{\mathbf{n}} \cdot \mathbf{B} = 0.}$ In this case the resulting boundary conditions are

$$\hat{\mathbf{n}} \cdot [\mathbf{v}] = \hat{\mathbf{n}} \cdot [\mathbf{B}] = 0, \quad [p + B^2/(2\mu)] = 0, \tag{2.26}$$

  whereas the other components of the magnetic field and velocity may have discontinuities. This is quite a common situation in solar physics, since conduction and motions across magnetic field lines are strongly impeded, so these inhomogeneities can be sustained for long times.

- $\boxed{\hat{\mathbf{n}} \cdot \mathbf{B} \neq 0.}$ The only possibility if the magnetic field is normal to the surface is

$$[\mathbf{v}] = [\mathbf{B}] = 0, \quad [p] = 0, \tag{2.27}$$

  that is, the only allowed jump is $[\rho] \neq 0$. This kind of discontinuity tends to be smoothed by motions or conduction along magnetic field lines, but it still can be regarded as a limit or an approximation. Notice that these conditions are more restrictive than the ones of Eq. (2.26).

In the previous discussion, the boundary conditions have been derived for ideal MHD. The next step is to linearize also Eqs. (2.26) and (2.27). Here one should be extremely careful when the quantities involved in these equations are calculated, because the boundary is also moving. In the remaining of this section the equilibrium quantities will be labelled again with subscript "0" and the perturbations with "1".

First of all, it is necessary to find an expression for the perturbed normal unitary vector $\hat{\mathbf{n}}_1$. We shall follow the discussion in Goedbloed (1983), who uses the displacement of a fluid particle

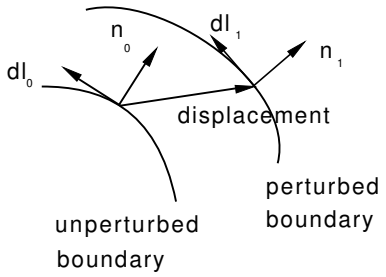

Figure 2.2: Sketch of the vectors used to linearize the "jump" conditions. ξ is the displacement vector.

ξ. Since we are Fourier analysing all the quantities (Eq. 2.20) there is a simple linear relation between ξ and $\mathbf{v}$ to first order:

$$\mathbf{v} = \frac{d\xi}{dt} \approx \frac{\partial \xi}{\partial t} = -i\omega\xi. \tag{2.28}$$

A sketch of the perturbed boundary is shown in Fig. 2.2. The change of a line element moving along the fluid comes from dynamic considerations,

$$d\mathbf{l} \approx d\mathbf{l}_0 \cdot (\vec{I} + \nabla\xi) \tag{2.29}$$

to first order. The total normal unitary vector $\hat{\mathbf{n}} = \hat{\mathbf{n}}_0 + \hat{\mathbf{n}}_1$ must satisfy

$$0 = \hat{\mathbf{n}} \cdot d\mathbf{l} \approx d\mathbf{l}_0 \cdot (\nabla\xi \cdot \hat{\mathbf{n}}_0 + \hat{\mathbf{n}}_1). \tag{2.30}$$

Hence,

$$\hat{\mathbf{n}}_1 = -(\nabla\xi) \cdot \hat{\mathbf{n}}_0 + \zeta\hat{\mathbf{n}}_0, \tag{2.31}$$

where ζ is a proportionality constant whose value can be obtained using the unitary condition $|\hat{\mathbf{n}}| = 1$, so $\hat{\mathbf{n}}_0 \cdot \hat{\mathbf{n}}_1 = 0$ and

$$\hat{\mathbf{n}}_1 = -(\nabla\xi) \cdot \hat{\mathbf{n}}_0 + \hat{\mathbf{n}}_0 \ [\hat{\mathbf{n}}_0 \cdot (\nabla\xi) \cdot \hat{\mathbf{n}}_0]. \tag{2.32}$$

Now this expression can be inserted in Eqs. (2.26) or (2.27) and taking into account that the quantities should be evaluated on the boundary

$$\mathbf{B} \approx \mathbf{B}_0 + \mathbf{B}_1 + (\xi \cdot \nabla)\, \mathbf{B}_0. \tag{2.33}$$

For example, the linearized version of $[\hat{\mathbf{n}} \cdot \mathbf{B}]$ is

$$0 = [\hat{\mathbf{n}} \cdot \mathbf{B}] \approx [\hat{\mathbf{n}}_0 \cdot \mathbf{B}_0 \ (1 + \nabla \cdot \xi + \hat{\mathbf{n}}_0 \ (\hat{\mathbf{n}}_0 \cdot (\nabla\xi) \cdot \hat{\mathbf{n}}_0)] + [\hat{\mathbf{n}}_0 \cdot (\mathbf{B}_1 - \nabla \times (\xi \times \mathbf{B}_0))]. \tag{2.34}$$

In the models that we consider in the next Chapter, the magnetic field points in the z-direction and the vector normal to the boundary in a perpendicular direction, so all the terms other than $\hat{\mathbf{n}}_0 \cdot \mathbf{B}_1$ in Eq. (2.34) vanish. Then, we should apply the set

$$\hat{\mathbf{n}}_0 \cdot [\mathbf{v_1}] = \hat{\mathbf{n}}_0 \cdot [\mathbf{B}_1] = \mathbf{0}, \quad [p_1 + \mathbf{B}_1 \cdot \mathbf{B}_0/(2\mu)] = [p_{\mathrm{T}1}] = 0. \tag{2.35}$$

instead of Eqs. (2.26).

As a conclusion, the boundary conditions on a interface of two different media are very similar to their non-linear counterparts (Eqs. 2.26 and 2.27). Notice however that in other problems there might be additional terms, for example the ones coming from Eq. (2.34). It is also remarkable that we have clearly distinguished between the two types of interfaces, depending on whether the equilibrium magnetic field is perpendicular to the surface or not, since Goedbloed (1983) did not mention this possibility and deduced expressions only for the case of magnetic field parallel to the contact discontinuity.

2.4 Magnetohydrodynamic waves in non-homogeneous plasmas

After having discussed in detail the boundary conditions, there are many plasma configurations that can be studied. These models are in general very simple compared with observed solar structures, but they provide with a valuable tool to understand the physics involved. Since we are interested in describing prominence and loop oscillations using the equilibrium models explained in next Chapter, only some classical results related to these topics will be presented. First of all, a brief introduction about the effect of inhomogeneities across the field and its implications (continuum spectrum, resonant absorption) is given. Then, a contact surface (Roberts 1981), a plasma slab (Edwin & Roberts 1982) and a flux tube (Edwin & Roberts 1983) are described. Finally, some of the recent developments in the field are mentioned.

The results of Sect. 2.1.1 are only a reference for more complicated plasma configurations with dependence of the plasma parameters or the magnetic field on the spatial coordinates. As a first step, we describe some results about inhomogeneities across the field, leading to the well-known appearance of the Alfvén continuum (and also slow continuum in non zero-beta plasmas). Consider an equilibrium state in the form

$$\mathbf{B}_0 = B_0(x)\hat{\mathbf{z}}, \quad p_0 = p_0(x), \quad \rho_0 = \rho_0(x), \quad T_0 = T_0(x), \tag{2.36}$$

where all the equilibrium quantities only depend on the x-coordinate, which marks the direction perpendicular to the magnetic field. The momentum equation demands

$$\frac{d}{dx}\left[p_0(x) + B_0^2(x)/(2\mu)\right] = 0. \tag{2.37}$$

The next step is to Fourier analyse the y- and z-directions (since there is no structure in these directions), so the perturbed quantities take the form

$$a_1(x,y,z) = \hat{a}_1(x) e^{i(k_y y + k_z z)}, \tag{2.38}$$

where the hats and subscripts are dropped again in the following relations. Taking into account the equilibrium state of Eq. (2.36), the wave equation takes the form

$$\frac{d}{dx}\left\{ \frac{\rho_0(x)(k_z^2 c_{\rm A}^2(x) - \omega^2)}{m^2(x) + k_y^2} \frac{dv_x}{dx} \right\} = \rho_0(x)(k_z^2 c_{\rm A}^2(x) - \omega^2)\, v_x, \tag{2.39}$$

where the following definition has been used

$$m^2 = \frac{(k_z^2 c_{\rm s}^2 - \omega^2)(k_z^2 c_{\rm A}^2 - \omega^2)}{(c_{\rm s}^2 + c_{\rm A}^2)(k_z^2 c_{\rm T}^2 - \omega^2)}, \tag{2.40}$$

where the *cusp speed*, $c_{\rm T}^2 = c_{\rm A}^2 c_{\rm s}^2/(c_{\rm A}^2 + c_{\rm s}^2)$, has been introduced. Notice that the quantity defined in Eq. (2.40) may be real or imaginary. From this equation it is also easy to recover the results of Sect. 2.1.1 assuming that the equilibrium quantities are uniform.

2.4.1 Contact surface

The first configuration to be studied consists of a contact surface between two unlimited plasmas of different properties. Suppose that the density, pressure and magnetic field strength change discontinuously across the surface $x = 0$ (Fig. 2.3),

$$B_0(x) = \begin{cases} B_{\rm e}, & x > 0, \\ B_0, & x < 0, \end{cases} \qquad \rho_0(x) = \begin{cases} \rho_{\rm e}, & x > 0, \\ \rho_0, & x < 0, \end{cases} \tag{2.41}$$

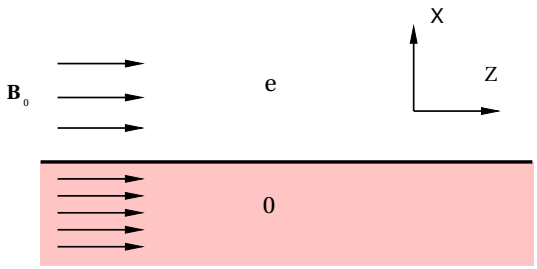

Figure 2.3: Sketch of the equilibrium configuration for a contact surface. The regions are labelled "0" and "e".

but otherwise are uniform in each region. This simple model is a first step to more realistic configurations, but it shows some of the features which are also present in more complicated models.

Now the boundary conditions of Eq. (2.27) give us the relation

$$p_0 + \frac{B_0^2}{2\mu} = p_{\rm e} + \frac{B_{\rm e}^2}{2\mu}. \tag{2.42}$$

We will restrict for simplicity to the case of parallel propagation ($\partial/\partial y = 0$) and two-dimensional perturbation $\mathbf{v} = (v_x, 0, v_z)$. Now equation Eq. (2.39) takes a really simple form,

$$\frac{d_2 v_x}{dx^2} + m^2 v_x = 0, \tag{2.43}$$

with m equal to m_0 in the region $x < 0$ and m_e in $x > 0$. The general solution such that the oscillation energy ($\rho_0 v^2$) vanishes as $|x| \to \infty$, corresponding to modes confined to the interface, is

$$v_x(x) = \begin{cases} A_\mathrm{e} e^{-m_\mathrm{e} x}, & x > 0, \\ A_0 e^{m_0 x}, & x < 0. \end{cases} \tag{2.44}$$

Now the boundary conditions Eqs. (2.35) are applied, that is, the continuity of the normal component of the perturbed velocity v_x and the total pressure p_T are imposed. After some mathematical manipulations, the dispersion relation is obtained,

$$\rho_0(k_z^2 c_{\mathrm{A}0}^2 - \omega^2) m_\mathrm{e} + \rho_e(k_z^2 c_{\mathrm{A}\mathrm{e}}^2 - \omega^2) m_0 = 0. \tag{2.45}$$

This is a transcendental algebraic equation for the frequencies of the magnetoacoustic surface modes at a single interface. After having found its solutions, other relevant features (such as the velocity perturbations) can be computed, a procedure that will be applied in the more complicated problems tackled in this Thesis. For a further discussion about the conditions for the existence of solutions of the contact surface and their description see Roberts (1981).

2.4.2 Slab in Cartesian geometry

The next interesting configuration is the *slab* in Cartesian geometry (Edwin & Roberts 1982; 1983). Now our equilibrium magnitudes are (Fig. 2.4)

$$B_0(x), \rho_0(x), p_0(x) = \begin{cases} B_\mathrm{e}, \rho_\mathrm{e}, p_\mathrm{e}, & |x| > b, \\ B_0, \rho_0, p_0, & |x| < b, \end{cases} \tag{2.46}$$

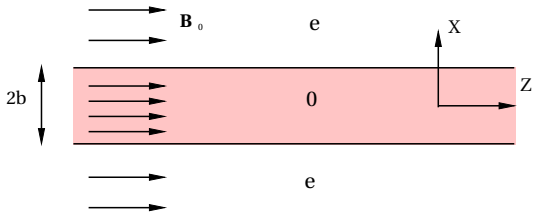

Figure 2.4: Sketch of the equilibrium configuration for a slab of width $2b$. The regions are labelled again "o" (internal) and "e" (external).

and Eq. (2.42) is still satisfied. Again, Eq. (2.43) is valid in each region (with the same m_e and m_0 defined before), since all its coefficients are constant. The solution for the perturbed velocity is

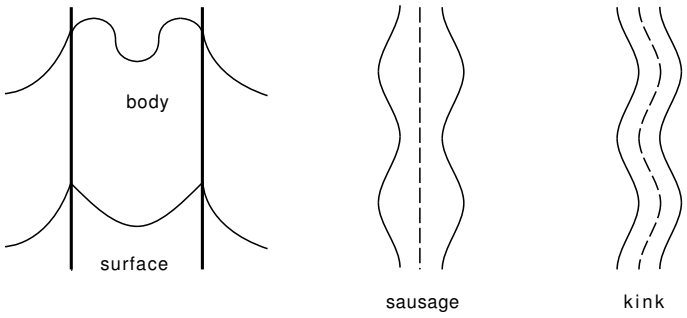

Figure 2.5: Sketch of the different types of modes supported by a plasma a slab.

$$v_x(x) = \begin{cases} A_{\rm e1}\, e^{-m_{\rm e}(x-b)}, & x > b, \\ A_{01}\cosh m_0 x + A_{02}\sinh m_0 x, & |x| < b, \\ A_{\rm e2}\, e^{m_{\rm e}(x+b)}, & x < -b. \end{cases} \tag{2.47}$$

Again, the boundary conditions of Eqs. (2.35) are applied on the boundaries $x = b$ and $x = -b$ and the requirement to have a non-trivial solution gives rise to our dispersion relations

$$\rho_e(k_z^2 c_{\rm Ae}^2 - \omega^2) m_0 \tanh m_0 b + \rho_0(k_z^2 c_{\rm A0}^2 - \omega^2) m_{\rm e} = 0, \tag{2.48}$$

$$\rho_e(k_z^2 c_{\rm Ae}^2 - \omega^2) m_0 \coth m_0 b + \rho_0(k_z^2 c_{\rm A0}^2 - \omega^2) m_{\rm e} = 0. \tag{2.49}$$

Depending on the symmetry with respect to the origin, there are *sausage modes* (Eq. 2.48 and $A_{01} = 0$ in Eq. 2.47), with the axis of symmetry remaining undisturbed, and *kink modes* (Eq. 2.49 and $A_{02} = 0$ in Eq. 2.47), with the slab axis moving back and forth during the wave motion. There are also two other kind of modes because the quantity m_0^2 in Eq. (2.40) can be either positive or negative, so solutions with $m_0^2 > 0$ are referred to as *surface modes* and those with $m_0^2 < 0$ as *body modes*. Notice that $m_e^2 > 0$ is required to have evanescent solutions outside the slab, a condition that leads to the existence of a *cut-off frequency*, over which the modes become leaky. These different types of evanescent modes are sketched in Fig. 2.5.

In Fig. 2.6 the dispersion relations Eqs. (2.48) and (2.49) are plotted against the free parameter k_z for a coronal slab. There are only body modes present under these conditions ($m_0^2 < 0$). It is also remarkable that slow modes are confined in a small frequency band. This band is very narrow and close to zero when typical prominence and coronal values are used (as the ones in Sect. 2.1.1). If the low-β plasma assumption is used then the slow modes disappear, while fast modes are hardly modified.

As a final comment, this model can be applied to some solar structures, such as prominences, which are roughly slabs in which their length and height are much larger than their width. In Joarder & Roberts (1992a, 1992b, 1993) and Oliver et al. (1992) a prominence is described as an infinite sheet of plasma with finite width $2a$ in the x-direction (slab of Fig. 1.8), while the y- and z-directions are Fourier-analysed and the resulting eigenfrequencies are discussed and the output is compared with observational data. This idea has been pushed forward including more realistic prominence models (Oliver et al. 1993) and a smooth transition region (Oliver &

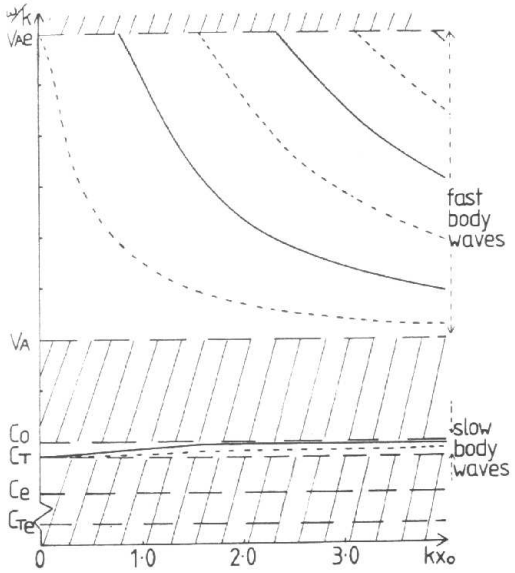

Figure 2.6: Dispersion relation for a coronal slab with an external Alfvén speed $c_{\rm Ae} = 5c_0$, external sound speed $c_{\rm e} = 0.5c_0$ and internal Alfvén speed $c_{\rm A0} = 2c_0$, with c_0 the internal sound speed. Solid lines represent sausage modes and dashed lines kink modes. The product $k_z b$ is named kx_0 in this plot (after Edwin & Roberts 1982, 1983).

Ballester 1996). There is also an interesting extension for an array of periodic slabs (Berton & Heyvaerts 1987).

2.4.3 The cylindrical flux tube

Obviously, the cylindrical geometry provides with a more realistic model than the previous Cartesian one for coronal flux tubes and thin prominence fibrils. The dispersion relations have similar properties to the ones obtained for the Cartesian slab described before (Edwin & Roberts 1983; Edwin, Roberts & Benz 1984). In this case, it is easier to work with the perturbed total pressure, $p_{\rm T} = p + \mathbf{B}_0 \cdot \mathbf{B}/\mu$. Since there is no dependence of the equilibrium parameters on the φ- and z-coordinates, the dependence of the magnitudes on these variables can be Fourier analysed in the form $\hat{a}(r,\varphi,z,t) = a(r)e^{i(k_z z - n\varphi - \omega t)}$. An expression similar to Eq. (2.39), sometimes called the Hain-Lüst equation (Hain & Lüst 1958, Roberts 1991), can then be derived,

$$\rho_0 \frac{1}{r}\frac{d}{dr}\left\{\frac{1}{\rho_0(r)(k_z^2 v_{\rm A}^2(r) - \omega^2)} r \frac{dp_{\rm T}}{dr}\right\} = \left(m^2 + \frac{n^2}{r^2}\right)\, p_{\rm T}, \tag{2.50}$$

where the parameter m is defined in Eq. (2.40). For a uniform medium this equation is just a form of Bessel's equation, namely

$$\frac{d^2 p_{\rm T}}{dr^2} + \frac{1}{r}\frac{dp_{\rm T}}{dr} - \left(m^2 + \frac{n^2}{r^2}\right)\, p_{\rm T} = 0. \tag{2.51}$$

This equation is now solved in an isolated flux tube (Fig 2.7), in which the equilibrium can be expressed in the form

$$B_0(r), \rho_0(r), p_0(r) = \begin{cases} B_\mathrm{e}, \rho_\mathrm{e}, p_\mathrm{e}, & r > b, \\ B_0, \rho_0, p_0, & r < b. \end{cases} \tag{2.52}$$

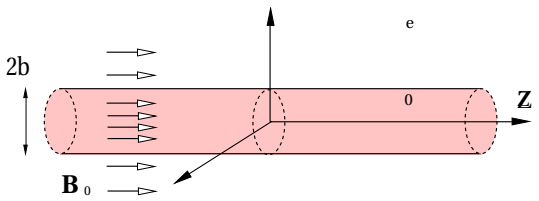

Figure 2.7: Sketch of the equilibrium configuration for a cylinder of diameter $2b$. The regions are labelled again "0" (internal) and "e" (external). The tube is unlimited in the z-direction.

The solutions to Eq. (2.51) can be expressed in terms of Bessel functions,

$$p_\mathrm{T}(r) = \begin{cases} A_\mathrm{e} K_n(m_\mathrm{e} r), & r > b, \\ A_0 I_n(m_0 r), & r < b, \end{cases} \tag{2.53}$$

where boundary conditions have already been taken into account: the solution is bounded as $r \to 0$ and there is no propagation of energy away from or towards the cylinder. Applying also the jump conditions of Eq. (2.35) a relation dispersion is deduced,

$$\rho_0 (k_z^2 c_{\mathrm{A}0}^2 - \omega^2) m_\mathrm{e} \frac{K_n'(m_\mathrm{e} b)}{K_n(m_\mathrm{e} b)} = \rho_\mathrm{e} (k_z^2 c_{\mathrm{Ae}}^2 - \omega^2) m_0 \frac{I_n'(m_0 b)}{I_n(m_0 b)}, \tag{2.54}$$

the dash denoting the derivative of a Bessel function.

These relations have similar properties to the ones obtained for the Cartesian slab. There are *surface modes* (described by Eqs. (2.53) and (2.54)) but also *body modes*, with $m_0^2 < 0$ and the Bessel function J_n instead of the modified Bessel function I_n in these two equations. The $n = 0$ mode corresponds to a *sausage mode*, the $n = 1$ to a *kink mode* and the $n \geq 2$ are commonly referred as *fluting modes*. The plots of their dispersion relations (Fig. 2.8) are also not very different from the ones in the slab (Fig. 2.6), although the mathematics involved are far more complicated. Despite not being too representative of flux tubes, many other models have been developed using Cartesian geometry to represent these flux tubes because of this similarity. Probably, the most important difference shown in Fig. 2.8 is that the fundamental kink mode tends to a value c_k different from the cut-off frequency of the slab.

These results have been widely used in the two decades elapsed from their publication. We just point out here the applications to oscillations of coronal loops (e.g. Nakariakov et al. 1999, Nakariakov & Ofman 2001) or as the starting point for studies of other effects (e.g. Ruderman & Roberts 2002 and Goossens, Andries & Aschwanden 2002 to study damping of waves due to resonant absorption or Karami, Nasiri & Sobouti 2002 for dissipation of waves due to other mechanisms). There are many other effects that can affect the oscillatory modes of non-uniform plasmas, although they are usually studied under simplifying assumptions or with numerical methods, for example: curvature (Smith, Roberts & Oliver 1997), twist in the equilibrium magnetic field (Bennett, Roberts & Narain 1999, Sakai et al. 2000), stratification in a slender flux tube (Hollweg & Roberts 1981), flows in an infinite flux tube (Nakariakov & Roberts 1995, Erdélyi & Goossens 1996, Somasundaram, Venkatraman & Sengottuvel 1999,

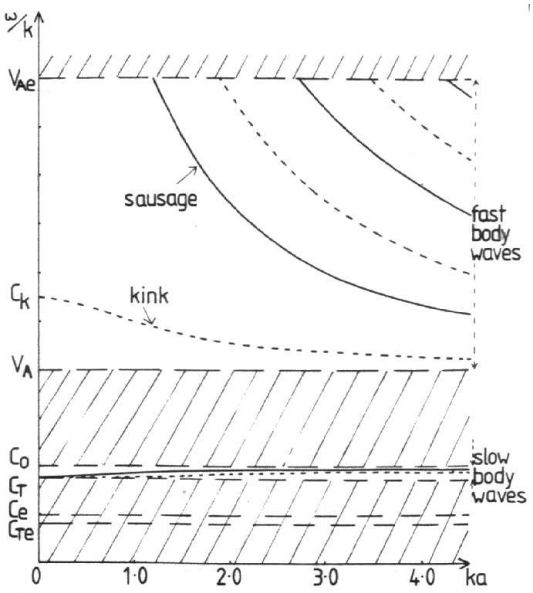

Figure 2.8: Dispersion relation for a cylindrical flux tube with an external Alfvén speed $c_{\mathrm{Ae}} = 5c_0$, external sound speed $c_{\mathrm{e}} = 0.5c_0$ and internal Alfvén speed $c_{\mathrm{A0}} = 2c_0$, with c_0 the internal sound speed. Solid lines represent sausage modes and dashed lines kink modes. The product $k_z b$ is named ka in this plot (after Edwin & Roberts 1983).

Homem, Erdélyi & Ballai 2003), collective effects (Bogdan & Zweibel 1985, 1987, Zweibel & Bogdan 1986, Bogdan 1987a, 1987b), smooth profiles instead of jump discontinuities (Edwin & Roberts 1988, Nakariakov & Roberts 1995), non-ideal MHD effects such as resonant absorption or phase mixing (e.g., Heyvaerts & Priest 1983; Ruderman & Roberts 2002), non-stationary response to prescribed perturbations (Goedbloed 1983; Poedts & Goossens 1991, Heyvaerts & Priest 1983 for example). Finally, we also recommend the reviews Roberts (2002) and Oliver & Ballester (2002) for an overview of current theoretical developments about oscillations in the solar corona and solar prominences.

However, it should be remarked that this is a very active research field, since there is no theory including all the relevant facts. Therefore, we will go forward and study new effects in the rich spectrum presented in this section, since there are many observational aspects that are not described properly with the models in this Chapter.

Chapter 3

Equilibrium models

It is a capital mistake to theorize before one has data. Insensibly one begins to twist facts to suit theories instead of theories to suit facts.

Sherlock Holmes (Sir Arthur Conan Doyle).

The scientific method is regarded as the main procedure to deal with new problems or questions in the modern vision of Science. This procedure involves the following steps:

- Describe the problem which is being studied.
- Build a suitable model, trying to keep only the relevant facts and sweeping away the effects that only introduce minor differences, but complicate the understanding of the physics involved.
- Check the model predictions with experiments or observations.
- Positive results act as a backup of the model, while negative ones lead to modifications (or rejections) of the models.
- In a feedback process, more suitable models are developed, so our knowledge is improved and more predictions can be achieved.

Modelling is a key process in this scheme. Normally, raw observation do not lead to knowledge, since it can be affected by our perceptions and previous thoughts. It is more convenient to direct observations by developing theories and then testing them with specifically designed experiments or related observations. Then, new theories can be introduced to explain the contradictory observed effects. This process can lead to new concepts and explanations of reality, but it must be highlighted that models can be just a step towards a better understanding, not a dogmatic closed explanation of the phenomena.

Therefore, if we want to apply this procedure in our study of coronal oscillations, we must build suitable models of the structures that are the subject of this work. After having explained

the fundamental equations of the MHD theory, in this Chapter we briefly present the concept and aims of coronal seismology, and then the models for loop and prominence oscillations used in our work. Such as was pointed out in Chapter 1, the solar corona displays lots of plasma configurations in which one of the dimensions is much larger than the others. The scope of the study is restricted to coronal regions with closed magnetic field (that is, field lines with both endpoints on the solar surface) and the most common example are coronal loops, which are thought to be magnetic flux tubes filled with plasma. However, there are other kind of structures, as prominences or coronal arcades, which can be modelled roughly with slabs or flux tubes. In this Thesis we focus on the oscillatory modes of loops and prominence fibrils, mainly for two reasons: not only they are more easily adapted to this kind of models, but their oscillations are also an active investigation field nowadays, from both the theoretical and observational point of view.

3.1 Coronal seismology

The idea underlying coronal seismology is to take advantage of the observational fact that many structures can support oscillations, and that the properties of these oscillations (which can be observed and measured) are related with the physical properties of the supporting structures. As a consequence, we can obtain information about the physical conditions of an object from the way it "dances to the music". This procedure has been applied in many other fields of Physics, such as Earth seismology (probing the internal structure of the Earth by measuring propagating waves, i.e., earthquakes) or helioseismology (determining the properties of the solar interior from the standing global modes of the Sun). Other not so straightforward examples are the radar or sonar, the analysis techniques involving Fourier decomposition, the determination of the dimension of a resonant cavity from the harmonics it supports, and so on.

The purpose of coronal seismology is to extract information of the equilibrium by using the data from oscillations and thus, to help to understand of the equilibrium properties of these structures. However, this is quite a complicated task, which can be performed in the following way: an equilibrium model based on the known properties of the object is built, trying to simplify all the supposed minor effects. Then, the oscillatory properties of this model can be computed and as an output, some magnitudes of the waves are obtained. These predictions are now compared with current observations, such as periods, damping times or spatial distribution. From this comparison one can deduce whether the model can explain the facts and, if the agreement is significative, calculate some equilibrium parameters from the observed wave data; or, if there is no agreement, to point out that the starting equilibrium model is not compatible with the observed data, so a more advanced equilibrium model is required as a starting point. It is important to realize that following this process we are indirectly measuring equilibrium quantities (such as the plasma pressure or the equilibrium magnetic field) that are very difficult to determine directly from observations. However, the values (or ranges) depend highly on the model, so the limitations of the models that have been used to calculate this values should never be forgotten, and one must be extremely careful with the assumptions that lead to these results. Obviously, as a feedback, new models can be put forward, so the wave analysis becomes closer to the rich spectrum displayed by real structures in an iterative process. We can summarise these concepts in the diagram of Fig. 3.1.

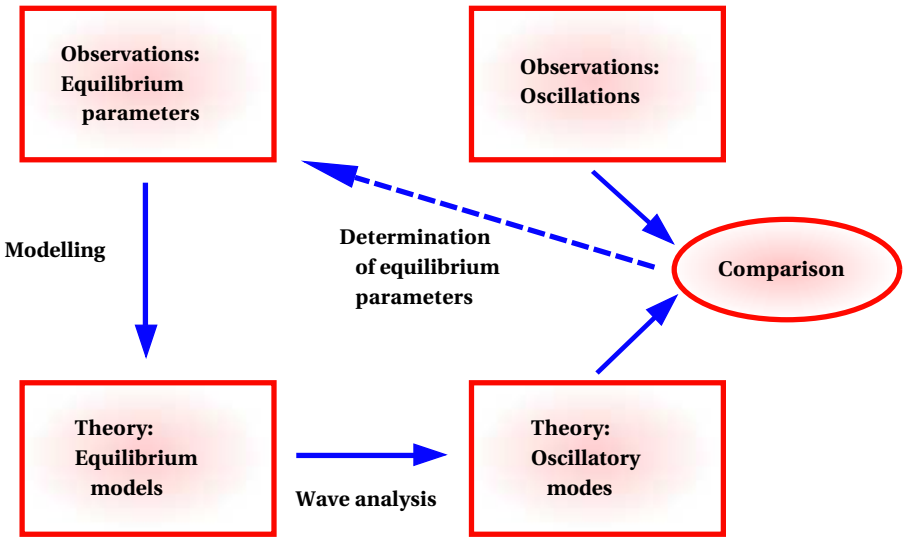

Figure 3.1: Diagram for coronal seismology.

This procedure looks fine, but in practise one should be very careful when it is applied. It has been very successful in areas such as helioseismology, but in the corona it is still in the beginnings, mainly because in the coronal region there is a high variety of features that can support oscillations, so we are not restricted to a unique object of well known properties (or even geometric structure). Another difference between helioseismology and coronal seismology is that a single coronal structure (displaying its own peculiarities) can only be observed for short periods of time (of the order of days at most), whereas the Sun as whole can support oscillations for much longer periods of time, making much easier to measure and characterize properties of its global oscillatory modes. However, considerable progress has been achieved in the previous decades, so we are encouraged to push this field one step further. Since observations of oscillating coronal loops and prominences (among other coronal structures) are being reported, it would be possible to do coronal seismology. Moreover, the situation has improved a lot with the new generation of space telescopes, since for many years the description of oscillatory properties of coronal objects had been a pure theoretical field, with very little input from observations due to poor temporal or spatial resolution. In fact, better data are expected from the following projected space missions, so more complicated theories will be necessary in a short time in order to explain these observations.

It is also important to remark that each coronal structure supports a high variety of oscillatory modes with their peculiar periods, but these periods depend on several equilibrium parameters which are not directly measured, such as temperature or plasma pressure, magnetic field strength and orientation, density ratio with respect to the coronal environment, etc. As a result, it is always possible to "tune" a few of these parameters to reproduce the observed periods. The subject can thus look despairing, but there is a number of paths along which future investigations can improve our present knowledge of coronal oscillations. For instance, constraints on the free variables of theoretical models must be imposed by determining, if possible, the physical properties of the objects at the time they are observed for oscillations. Thus, information of the geometry of the structure under analysis and plasma properties can be introduced in the

theoretical models to determine which ones better reproduce the observed oscillatory features.

Finally, it is also worthwhile mentioning that the wave analysis is not only important for doing seismology, but can also give interesting results for other studies, such as instabilities or heating in the corona. Determining the oscillatory properties and modes of a given structure is a problem interesting on its own, even if it is not used to do coronal seismology.

3.2 Coronal loop models

It is clear from *X-ray* observations that the solar corona is structured in regions with open magnetic fields or coronal holes, and regions with closed magnetic fields (with both endpoints of magnetic field lines anchored in the photosphere), with small-scale energetic features (*X-ray bright points*) scattered over all the Sun's surface. Closed regions are in fact composed of myriads of coronal loops, with a wide range of densities and temperatures, which evolve and interact with their neighbours continuously.

As we have stated before, coronal loops are mainly modelled as magnetic flux tubes for studying their equilibria. These models tend to be quite simple, with the aim of studying the most relevant and generic features first and then adding other effects. The most simple model is a cylindrical flux tube in isothermal equilibrium and without gravity, curvature and radiation or extra terms of heating. This leads to a profile with constant pressure along the tube and, if the heating is not taken into account, also with constant temperature and density. However, we just want to study the oscillatory properties of these structures, so we start with equilibrium models which are easy to compute. We first consider the effect of adding a photospheric line-tying boundary condition: the photospheric plasma is so dense that perturbations generated in the corona must vanish on the boundary. Our analysis is an extension of the basic case of an infinite homogeneous flux tube (Edwin & Roberts 1983, resumed in Sect. 2.4.3). It is of interest to investigate this simple model because the oscillatory modes of an infinite flux tube have already proved useful in explaining some observations (e.g. Roberts, Edwin & Benz 1984; Nakariakov et al. 1999; Nakariakov & Ofman 2001) or have been taken as the starting point for the inclusion of other effects (e.g. Ruderman & Roberts 2002; Goossens et al. 2002), so every advance will lead to a better understanding of the physics involved. Therefore, it is convenient to study in some depth the new features arising from the introduction of the photosphere. And, last but not least, this will provide a solid basis for further analysis of other effects.

In this work we also consider another deviation from the uniform flux tube: a loop in hydrostatic and thermal equilibrium in a non self-consistent way, that is, with a prescribed heating function from which the equilibrium plasma parameters are deduced (and thereafter the oscillatory modes). The reason for introducing this modification is that coronal loops do not seem to be uniform. There are many studies of the conditions of the loops in the solar atmosphere and different equilibrium profiles have been proposed, for example Rosner, Tucker & Vaiana (1978); Hood & Priest (1979); Serio et al. (1981) among others; and more recently Priest et al. (2000); Aschwanden, Schrijver & Alexander (2001); Aschwanden & Schrijver (2002); Chae, Poland & Aschwanden (2002), depending on what effects are considered relevant or not (for example gravity or stratification). In this Thesis we use some of the models described in Priest et al. (2000).

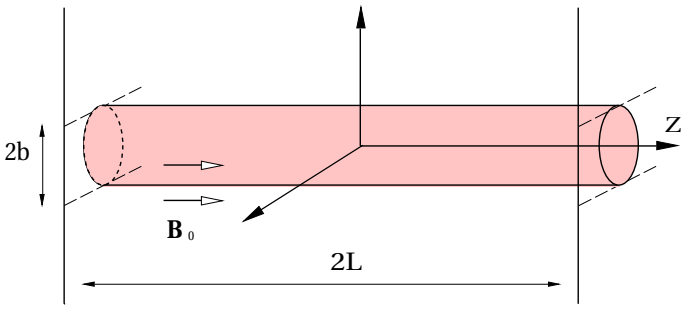

Figure 3.2: Sketch of the equilibrium configuration of a straightened flux tube of length $2L$ and radius b. The density inside the loop (colored in the figure) is *rhol* and the density in the coronal environment is *rhoc*. The magnetic field is uniform and parallel to the z-axis.

Putting all together, we use two types of equilibrium models for coronal loops. First of all, a uniform flux tube with photospheric boundaries is considered and then a loop with other equilibrium profiles is presented. We proceed to discuss these models right now.

3.2.1 Basic features of the model and governing equilibrium equations

We are interested in studying an isolated coronal loop embedded in the solar corona, which for the sake of simplicity is considered a uniform plasma. The radius of the flux tube is b and its length is $2L$, with photospheric plasma in both limits. The magnetic field (the same inside and outside the tube) is uniform and parallel to the loop axis. Following previous studies, the flux tube is straightened (i.e. curvature effects are discarded), so the loop is transformed in the one of Fig. 3.2. The loop is symmetric with respect to the coordinate z and has no dependence across the fibril axis, although all the equilibrium plasma parameters can depend upon the z-coordinate along the loop.

Now we consider parameter values appropriate for coronal loops. In Nakariakov et al. (1999) a tube with length $2L = 130$ Mm, diameter $2b = 1$ Mm was considered and a density ratio $\rho_{\rm l}/\rho_{\rm c} \approx 10$ was assumed (supposed constant all along the loop). This gives the value $b/L = 0.015$; using the coronal particle number $n_{\rm p} = 5 \times 10^{14}$ m^{-3} and a magnetic field strength $B_0 = 10$ G, we derive the coronal Alfvén speed $c_{\rm Ac} = 2.8 \times 10^{12} B_0 n_{\rm p}^{-1/2} = 1252$ km s^{-1}. We consider this set of values as typical for coronal loops, although there is a wide variety of observed loops with different physical parameters (see for example, Aschwanden et al. 2001, Nagata et al. 2003)

To describe the equilibrium profile of a loop we follow Priest et al. (2000), with the difference of having straightened the loop, so their s-coordinate (the distance along the loop) is replaced by the cylindrical z-coordinate. We assume a loop in hydrostatic and thermal equilibrium between conduction and the prescribed heating $H(z)$, while neglecting radiation in front of them. Notice that no assumptions or assertions about the heating source or mechanism are made, a subject interesting on its own that is currently under investigation. We just consider a prescribed static heating mechanism (that is, $\partial_t H(z) = 0$) and using the assumption of thermal equilibrium, the energy equation, Eq. (A.27), can be written in the form

$$\frac{1}{A}\frac{d}{dz}\left(\kappa_0 A T^{5/2}\frac{dT}{dz}\right) + H(z) = 0, \tag{3.1}$$

where A is the area of the section across the loop and $\kappa_0 = 9.24 \times 10^{-12}$ Jm^{-1}s^{-1} is a coefficient that appears in the component of the thermal conduction tensor along the field, which in typical coronal conditions is much larger than the perpendicular component (see Appendix A). We also assume that the cross section A is the same all along the loop, so $dA/dz = 0$, so this quantity is eliminated from Eq. (3.1), which reduces to

$$\frac{d}{dz}\left(\kappa_0 T^{5/2}\frac{dT}{dz}\right) = -H(z). \tag{3.2}$$

This equation must be solved with the following boundary conditions: the temperature at the footpoints is fixed, so that $T(\pm L) = T_0$, and the temperature distribution is symmetric about the summit, so

$$\left.\frac{dT}{dz}\right|_{z=0} = 0,$$

which means that there is no heat flux between the two halves of the loop. Using these conditions, Eq. (3.2) can be integrated,

$$T(z) = T_0\left[1 + \frac{7}{2\kappa_0 T_0^{7/2}}\int_{z'}^{L} dz' \int_0^{z''} H(z'')dz''\right]^{2/7}. \tag{3.3}$$

Eq. (3.3) gives the temperature profile along the loop for a given heating function $H(z)$.

Therefore, for a given heating function, $H(z)$, a temperature profile can be derived from Eq. (3.3), and then the pressure and density profiles can be computed. Here we will apply our next assumption: the loop is isobaric (the pressure is constant along the loop, $p = p_0 = $ const.), so the density is directly related with the temperature profile by means of Eq. (A.20),

$$\rho(s) = \mu m_p n_e(s) = \frac{\mu m_p p_0}{2k_B}\frac{1}{T(s)} = \rho_0\frac{T_0}{T(s)}, \tag{3.4}$$

with $\rho_0 = (\mu m_p p_0)/(2k_B T_0)$.

Now many profiles can be studied. We are interested in a homogeneous loop (such as stated before), and a loop with uniform heating or heating near the footpoints (with some dependence, for example slab-like or exponential), although many other profiles can be studied (such as a model with heating in the apex). It is left for further work to study other more complicated equilibria, or even observational profiles.

3.2.2 Uniform profile (no heating)

As a first application, we deal with the simplest case: the homogeneous flux tube. It is obtained directly from the previous formulae by assuming that there is no heating in the tube, so the

temperature profile is simply a constant along the tube, and therein also the density and the Alfvén speed are constant. We label these quantities as T_l, ρ_l and c_Al.

$$c_\mathrm{A}(z) = c_\mathrm{Al} = \text{const.} \tag{3.5}$$

The oscillatory properties of this model have been studied in many previous works, although we will go a step further and consider the modifications induced by the addition of a line-tying boundary condition to model the effects of the solar photosphere.

3.2.3 Profiles with uniform heating

As the next application of the formulae derived in Sect. 3.2.1, we consider the case of uniform heating all along the loop,

$$H(z) = H_0 = \text{const.} \tag{3.6}$$

Now it is possible to write an explicit expression for the equilibrium temperature, $T(z)$, from Eq. (3.3) and subsequently from Eq. (3.4) an expression for the equilibrium density, $\rho(z)$, (Priest et al. 2000)

$$T(z) = T_0 \left\{ 1 + \frac{7}{2\kappa_0 T_0^{7/2}} H_0 (L^2 - z^2) \right\}^{2/7} = T_0 \left\{ 1 + \frac{\bar{H}}{2} \left[1 - \left(\frac{z}{L} \right)^2 \right] \right\}^{2/7}, \tag{3.7}$$

$$\rho(z) = \rho_\mathrm{l} \left\{ 1 + \frac{\bar{H}}{2} \left[1 - \left(\frac{z}{L} \right)^2 \right] \right\}^{-2/7}. \tag{3.8}$$

Here a new parameter has been introduced,

$$\bar{H} = \frac{7 H_0 L^2}{2\kappa_0 T_0^{7/2}}, \tag{3.9}$$

which is a measure of the ratio of heating to conduction; if $\bar{H}$ is increased, the consequences are that the temperature in the summit is also increased and the density is lowered. Notice that for $H_0 = 0$ ($\bar{H} = 0$) the isothermal line-tied loop of the previous section is recovered. A typical density profile for this kind of models is plotted in Fig. 3.3, among other profiles that are explained later.

The Alfvén speed profile in this solution is then

$$c_\mathrm{A}^2(z) = c_\mathrm{A}^2(L) \left\{ 1 + \frac{\bar{H}}{2} \left[1 - \left(\frac{z}{L} \right)^2 \right] \right\}^{2/7}. \tag{3.10}$$

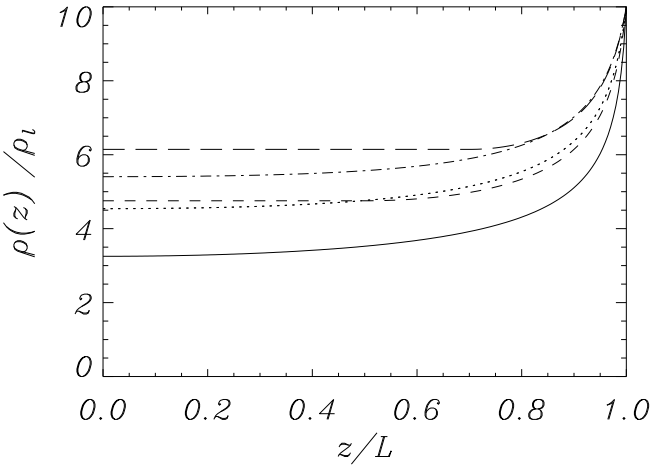

Figure 3.3: Plot of some equilibrium density profiles against the normalized coordinate along the loop, z/L, with $2L$ the loop length. The ratio of loop footpoints to coronal (ambient) density is $\rho_{\rm l}/\rho_{\rm c} = 10$ and the heating magnitude is $\bar{H} = 100$. The constant heating profile is plotted with a solid line, while the dashed and long-dashed lines are for heating in a layer with $L_{\rm H} = 0.5L$ and $L_{\rm H} = 0.3L$, respectively, and the dotted and dash-dotted lines for exponential heating with $L_{\rm e} = 0.5L$ and $L_{\rm e} = 0.3L$, respectively.

3.2.4 Profiles with uniform heating only in a layer

Although nowadays there is some controversy about the heating of coronal loops, there are some works which point that the heating might be only acting near the loop footpoints. Following this suggestion, it is also interesting to study a different family of models: the ones with constant heating in a layer of height $L_{\rm H}$ at both ends of the tube and with no heating near the loop apex,

$$H(z) = \begin{cases} 0, & z \leq L - L_{\rm H}, \\ H_0, & L - L_{\rm H} \leq z \leq L. \end{cases} \tag{3.11}$$

Again, using Eqs. (3.3) and (3.4) we derive the temperature and density profiles,

$$T(z) = \begin{cases} T_0 \left[1 + \frac{\bar{H}}{2}\left(1 - \frac{z}{L}\right)^2 - 2\left(1 - \frac{z}{L}\right)\left(1 - \frac{L_{\rm H}}{L}\right)\right]^{2/7}, & z \leq L - L_{\rm H}, \\ T_0 \left[1 + \frac{\bar{H}}{2}\frac{L_{\rm H}^2}{L^2}\right]^{2/7}, & L - L_{\rm H} \leq z \leq L, \end{cases} \tag{3.12}$$

$$\rho(z) = \begin{cases} \rho_{\rm l} \left[1 + \frac{\bar{H}}{2}\left(1 - \frac{z}{L}\right)^2 - 2\left(1 - \frac{z}{L}\right)\left(1 - \frac{L_{\rm H}}{L}\right)\right]^{-2/7}, & z \leq L - L_{\rm H}, \\ \rho_{\rm l} \left[1 + \frac{\bar{H}}{2}\frac{L_{\rm H}^2}{L^2}\right]^{-2/7}, & L - L_{\rm H} \leq z \leq L. \end{cases} \tag{3.13}$$

Finally, the Alfvén speed profile is

$$c_{\rm A}^2(z) = \begin{cases} c_{\rm A}^2(L)\left[1+\frac{\bar{H}}{2}\left(1-\frac{z}{L}\right)^2 - 2\left(1-\frac{z}{L}\right)\left(1-\frac{L_{\rm H}}{L}\right)\right]^{2/7}, & z \le L - L_{\rm H}, \\ c_{\rm A}^2(L)\left[1+\frac{\bar{H}}{2}\frac{L_{\rm H}^2}{L^2}\right]^{2/7}, & L - L_{\rm H} \le z \le L. \end{cases} \tag{3.14}$$

Probably, the most remarkable fact is that in the limit $L_{\rm H} \to L$ the uniform heating profile of Eq. (3.10) is recovered, while in the limit $L_{\rm H} \to 0$ the uniform flux tube is obtained. For the intermediate cases ($0 < L_{\rm H} < H$) the profile in the layer region is similar to the uniform heating model, but in the non-heated region the temperature remains constant (since there is no conduction). In Fig. 3.3 two of these models are represented, so the effect of the new parameter $L_{\rm H}$ can be appreciated compared with the model with constant heating all along the loop.

3.2.5 Profiles with exponential heating

Another possibility is that the heating decreases exponentially with height all along the loop,

$$H(z) = H_0 e^{-(L-z)/L_{\rm e}}, \;\; z \ge 0, \tag{3.15}$$

where $L_{\rm e}$ is the scale height. After performing the integrals in Eq. (3.3) we obtain

$$T(z) = T_0\left\{1+\bar{H}\frac{L_{\rm e}^2}{L^2}\left[1-e^{-(L-z)/L_{\rm e}} - e^{-L/L_{\rm e}}\left(\frac{L}{L_{\rm e}}-\frac{z}{L_{\rm e}}\right)\right]\right\}^{2/7}, \tag{3.16}$$

and hence

$$\rho(z) = \rho_{\rm l}\left\{1+\bar{H}\frac{L_{\rm e}^2}{L^2}\left[1-e^{-(L-z)/L_{\rm e}} - e^{-L/L_{\rm e}}\left(\frac{L}{L_{\rm e}}-\frac{z}{L_{\rm e}}\right)\right]\right\}^{-2/7}, \tag{3.17}$$

and for the Alfvén speed profile

$$c_{\rm A}^2(z) = c_{\rm A}^2(L)\left\{1+\bar{H}\frac{L_{\rm e}^2}{L^2}\left[1-e^{-(L-z)/L_{\rm e}} - e^{-L/L_{\rm e}}\left(\frac{L}{L_{\rm e}}-\frac{z}{L_{\rm e}}\right)\right]\right\}^{2/7}. \tag{3.18}$$

Finally, density profiles for different values of the parameter $L_{\rm e}$ are plotted in Fig. 3.3 for a comparison. An interesting point is that these modes are slightly denser near the footpoints than the model with heating in a layer with $L_{\rm H} = L_{\rm e}$, but the density still decreases slowly for $z < L - L_{\rm e}$, while for the models of Sect. 3.2.4 remains constant, so a lower value of density is reached in the summit. Also notice that for large values of $L_{\rm e}$ the uniform heating profile can be recovered. A more detailed description and discussion of these and akin equilibria can be found in Priest et al. (2000).

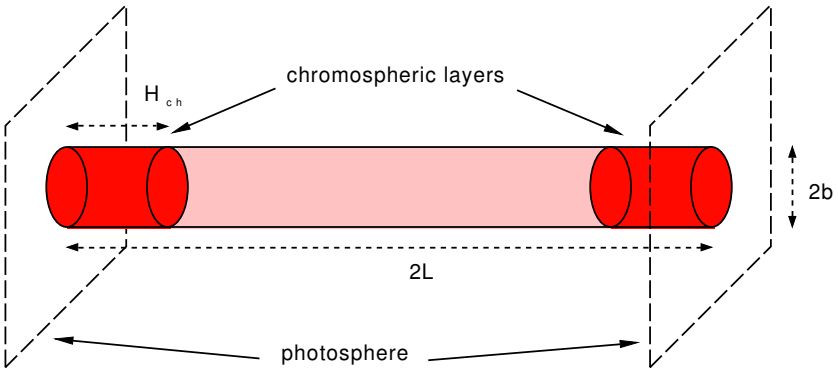

Figure 3.4: Sketch of the equilibrium configuration representing a coronal flux tube of length $2L$ and radius b with chromospheric material at its footpoints (grey in the figure) extending up to a height $H_{\rm ch}$. The density inside the loop is $\rho_{\rm l}$, $\rho_{\rm ch}$ is the density in the chromospheric part and $\rho_{\rm c}$ in the coronal environment. In the straight flux tube model of this loop, the magnetic field is uniform and parallel to the z-axis.

3.2.6 Coronal loops with a chromospheric layer

The equilibrium structure and properties of coronal loops are still being investigated, but it is clear that there is at least some inhomogeneity along the loop: the chromospheric layer near the photosphere (Fig. 3.4). The photosphere-corona transition is not as abrupt as it has been modelled here (via the line-tying boundary condition), so it is worthwhile studying the modifications that a thin dense layer modelling the chromosphere induces in the models described in this work.

Here we consider a chromospheric layer of uniform density $\rho_{\rm ch}$ and height $H_{\rm ch}$ (Fig. 3.4). For these parameters we use as numerical values $\rho_{\rm ch}/\rho_{\rm c} = 200$ and $H_{\rm ch}/L = 0.08$, since a typical height of $H_{\rm ch} = 5.2$ Mm is quite adequate for the chromospheric layer and $L = 65$ Mm, as was measured for the loop observation described in Nakariakov et al. (1999). In the remaining part of the tube another profile can be selected, such as a uniform one or one with constant heating.

Therefore, our model of a loop with chromospheric material at the footpoints consists of two layers of height $H_{\rm ch}$ at the footpoints and the rest of coronal plasma between them, with constant plasma parameters at first, and then with some other profile, like the ones described previously for a loop without chromospheric layers.

3.3 Prominence fibril models

The other kind of structures studied in this Thesis are prominence fibrils. In Chapter 1 prominences were presented as cool, dense clouds of plasma suspended in the coronal medium. Focusing on the study of the oscillatory properties of prominences and their fine structure, first of all it is necessary to model a prominence taking into account this fine structure, clearly shown in Figs. 1.9 and 1.10 among many other observations. It will be assumed that a prominence is made by piling up small scale flux tubes (fibrils) in both the vertical and horizontal directions, forming a sheet appearance in a sheared magnetic arcade with a dip at the top (Fig. 1.8). A

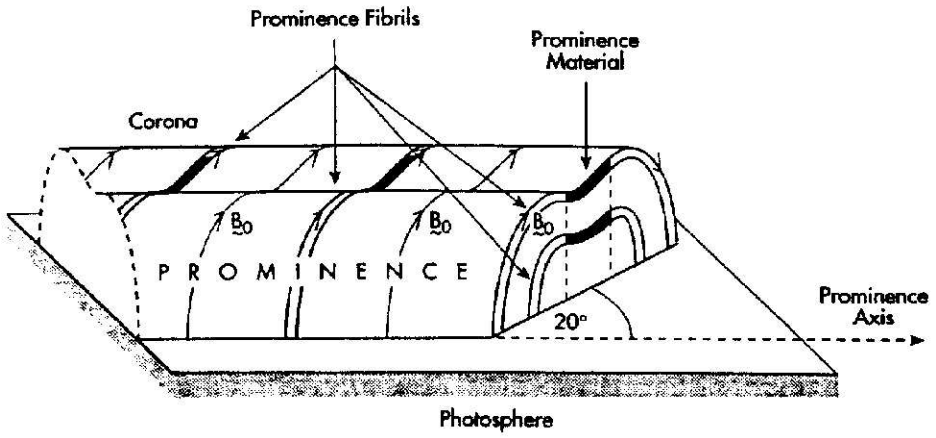

Figure 3.5: Schematic diagram of a prominence with its fibrils, which are flux tubes only partially filled with dense prominence material. These fibrils are stacked up one above another to give rise to the sheet like appearance of a prominence, such as that in Fig. 1.8. (After Joarder et al. 1997).

sketch of this model is shown in Fig. 3.3. These fibrils are most likely field-aligned plasma tubes, taking into account that the magnetic field in a prominence forms an angle of 20° with the prominence long axis. It must be emphasized that the underlying magnetic structure is not visible, so the only part that can be observed is the one having prominence material.

Following Joarder, Nakariakov & Roberts (1997), we consider a single prominence fibril surrounded by the coronal medium (Fig. 3.6). In essence, the equilibrium is similar to that in Joarder & Roberts (1993) (prominence modeled as an infinitely high and long plasma sheet) with the difference that the plasma slab has a limited height, so the configuration is reminiscent of a thin thread with finite width and length. Nevertheless, the fibril is infinitely deep since the equilibrium configuration is invariant in the y-direction. The configuration that we use consists of a straight flux tube of total length $2L$ made of a cold and dense part (the prominence fibril itself) with length $2W$ and density $\rho_{\rm p}$ and a hotter, coronal gas with density $\rho_{\rm e}$ occupying the reminder of the thin loop. This structure, whose thickness is $2b$, is embedded in the coronal environment, with density $\rho_{\rm c}$. The loop is anchored at the photosphere, so its footpoints are subject to line-tying conditions. Finally, the plasma is permeated by a uniform magnetic field directed along the prominence fibril $\mathbf{B}_0 = B_0\hat{\mathbf{z}}$, the same for the loop and the corona. The reason for setting the magnetic field equal inside and outside is that the fibrils appear to be due to local density and temperature inhomogeneities, rather than an inhomogeneity in the magnetic field (see Leroy 1989; Mein 1994). Because gravity is neglected, all other physical variables (ρ, T and p) are also uniform in each of the three regions.

The parameter values used in the model, which are similar to those considered by Joarder et al. (1997), are taken from Wijk, Schmieder & Noëns (1994), Engvold et al. (1989), Engvold et al. (1990a), Jensen & Wijk (1990), Tandberg-Hanssen (1995). The thickness of prominence fibrils is $2b \simeq 200$–400 km and their length is $2W \simeq 20,000$ km. The total length of magnetic field lines can be estimated as $2L \simeq 60,000$–$200,000$ km, so that $b/L \simeq 0.001$–0.007 and $W/L \simeq 0.1$–0.3. In addition, we use $\rho_{\rm e}/\rho_{\rm c} = 0.6$ and $\rho_{\rm p}/\rho_{\rm c} = 200$, so that the prominence material is 200 times

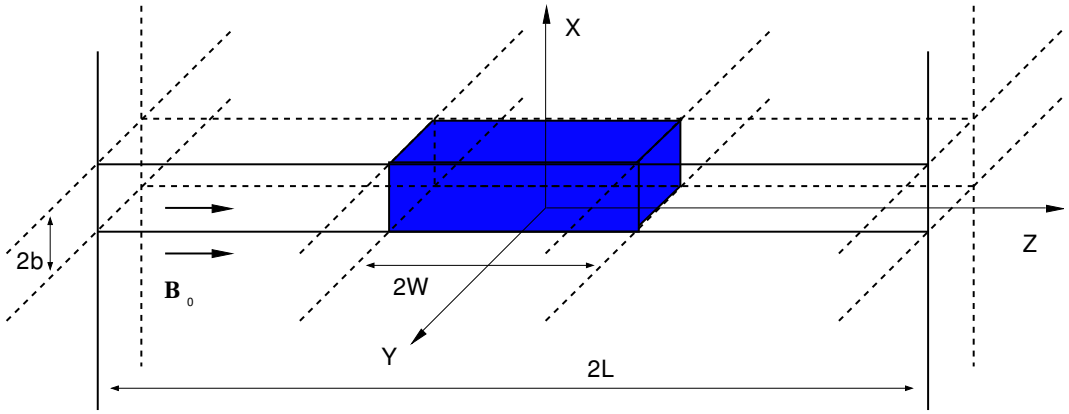

Figure 3.6: Sketch of the equilibrium configuration of a Cartesian fibril. The grey zone represents the cold part of the loop, modeling the prominence fibril. The density in the fibril, $\rho_{\rm p}$, in the evacuated (coronal) part of the loop, $\rho_{\rm e}$, and in the coronal environment, $\rho_{\rm c}$, are all uniform. Moreover, the magnetic field is uniform and parallel to the z-axis and the whole configuration is invariant in the y-direction (after Joarder et al. 1997).

denser than the coronal one and the hot gas in the evacuated part of the loop is about half as dense as the coronal plasma. In our calculations we have also taken $\rho_{\rm c} \simeq \rho_{\rm e}$ (the evacuated part having the same properties as the coronal medium) and $\rho_{\rm p} \simeq 1000\rho_{\rm c}$, which corresponds to a still denser prominence compared to its surroundings (cf. Hvar Reference Atmosphere of Quiescent Prominences; Engvold et al. 1989), since no consensus has been reached yet about typical values of these parameters and solar prominences exhibit a wide range of physical properties.

Putting all together, a single prominence fibril is modeled as a straight magnetic tube with a density slab-like inhomogeneity (Fig. 3.6). It is straightforward to show that this simple equilibrium model is consistent with the MHD equations and boundary conditions of Chapter 2. The parameters of this model are then:

- $2W$, length of the fibril (thickness of the prominence),
- $2L$, length of the magnetic supporting arcade,
- $2b$, thickness of the fibril,
- $\rho_{\rm c}$, coronal density ($|x| > b$),
- $\rho_{\rm e}$, density of the evacuated part ($|x| < b$ & $W > |z| > L$),
- $\rho_{\rm p}$, prominence density ($|x| > b$),
- B_0, magnetic field strength of the supporting arcade.

It is worthwhile remembering that a real prominence is composed of many fibrils pilled up, so one must consider multifibril systems, like that in Fig. 3.7, in which two fibrils (each with its own equilibrium parameters) have been put together.

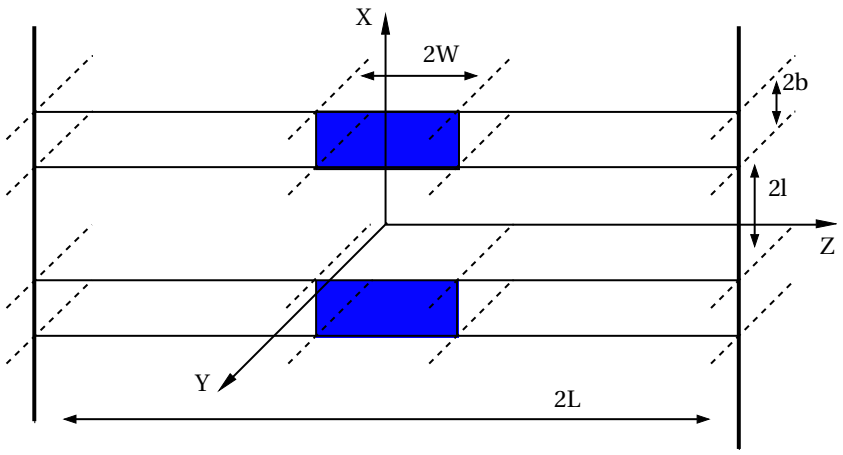

Figure 3.7: Sketch of the equilibrium configuration used in this study for a system of two fibrils. The grey zone represents the cold part of the loops, i. e. the prominence. The density in the prominence region is $\rho_{\rm p}$, in the evacuated (coronal) part of the loop, $\rho_{\rm e}$, and in the coronal environment, $\rho_{\rm c}$. The magnetic field is uniform and parallel to the z-axis, and the whole configuration is invariant in the y-direction.

Finally, A more suitable model can be built using cylindrical geometry. Then, our equilibrium model consists of a cylindrically symmetric prominence fibril surrounded by the coronal medium (Fig. 3.8). The configuration consists of a straight flux tube of total length $2L$ made of a cold and dense part (the prominence fibril itself) with length $2W$ and density $\rho_{\rm p}$ and a hotter coronal gas with density $\rho_{\rm e}$ occupying the remainder of the thin loop. The radius of the flux tube is b and this structure is embedded in the coronal environment, with density $\rho_{\rm c}$. The loop is anchored in the photosphere, so its footpoints are subject to line-tying conditions. As for the Cartesian fibril, the plasma is permeated by a uniform magnetic field directed along the prominence fibril and, since gravity has been neglected, all other physical variables (ρ, T and p) are also uniform in each of the three regions. Notice that the parameters are very similar to the ones of the Cartesian geometry and the only difference is that the tube radius replaces here the fibril thickness.

3.4 Summary of shared features of the equilibrium models

In this Chapter we have explained the equilibrium models that are studied in this work, divided in two kinds: those for coronal loops and those for prominence fibrils. However, all these models share some features:

- In these structures the length along the magnetic field is much larger than the other characteristic lengths (specially the cross section).
- The structure has been straightened (so curvature effects are not taken into account). As a consequence, the photosphere lies at both ends and consists of two parallel planes where line-tying boundary conditions are imposed.
- The magnetic field is uniform in all the region (no differences between the inner and outer parts).

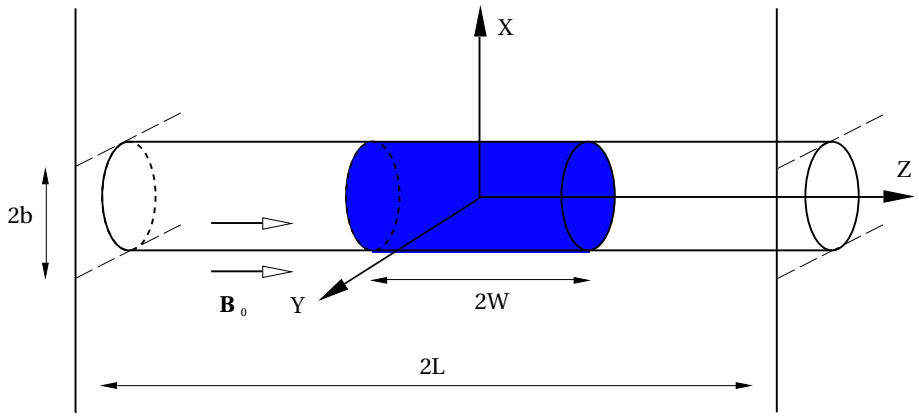

Figure 3.8: Sketch of the equilibrium configuration used for a cylindrical prominence fibril. The grey zone represents the cold part of the loop, i. e. the prominence. The density in the prominence region is $\rho_{\rm p}$, in the evacuated (coronal) part of the loop, $\rho_{\rm e}$, and in the coronal environment, $\rho_{\rm c}$. The magnetic field is uniform and parallel to the z-axis, and the whole configuration is invariant in the φ-direction.

- There is no structure across the tube or slab other than the sharp discontinuity in density marking the limit of the structure.
- The coronal environment is modelled as a region with uniform plasma parameters. Obviously, this is not very realistic, but since we just want to study the modes of the structure, it will simplify the analysis substantially.
- It is possible to have some sort of dependence of the plasma parameters on the coordinate along the structure, but not across it (except the abrupt transition to the coronal region). The z-axis has been placed in this preferred direction, along which the magnetic field points.

Following these general remarks, in the next Chapter we develop a theory to study the oscillations of these kind of structures. The results and specific models for each case are studied in later Chapters.

Chapter 4

Magnetohydrodynamic waves in line-tied structures: Analytical development*

We are all amateurs. Life is too short for us to be anything else.

Charles Chaplin.

Nowadays there is a considerable gap between solar physics observations and theory, apart from certain areas such as helioseismology. In general, solar processes are too complicated to be dealt with directly, with the exception of numerical developments, but that does not mean that no theoretical work can be applied. The key is modelling: a less complicated structure that has just the most relevant features is defined, so its properties can be discussed. In a feed-back process, the results can be compared with observational data and the differences can give rise to new more complicated models in better accordance with observations and so on. However, many of the observational data and images, as the ones of Chapter 1, are often described as "the nightmare of a theoretician", but it must be always kept in mind that the final goal is to understand the complicated processes shown in that kind of figures (although studying them in detail often involves computational calculations than analytical studies).

On the other hand, it is also very useful to develop analytical solutions. A numerical program to solve the MHD equations may give us a numerical solution for a particular parameter set, but it is very difficult to extrapolate or distinguish the effects of the underlying physics. An analytical solution may be less straightforward, but general properties can be deduced, the effects of different parameters can be better studied and it can be more easily applied to different problems. Obviously, the price one may pay is that more complicated mathematics are involved. In fact, an analytical solution is often used as a check of the results given by numerical solutions (in the appropriate limit) before dealing with less idealized problems. For example, the analytical

*This Chapter is based on: Díaz, A. J., Oliver, R., Erdélyi, R., & Ballester, J. L. 2001, "Fast MHD Oscillations in Prominence Fine Structures", A&A, 379, 1083 and Díaz, A. J., Oliver, R. and Ballester, J. L. 2002, "Fast Magnetohydrodynamic Oscillations in Cylindrical Prominence Fibrils", ApJ, 580, 550.

solutions proposed in this work were also used to test numerical codes based on a finite-difference discretization of first and second order derivatives of the linearized MHD equations, which in turn helped to solve other kind of problems (Arregui 2003). Both types of approach (analytical and numerical) are tools to solve a problem, but can work even better if each is related to the other and both are used together to complement our knowledge about a particular problem.

Here the mathematics involved to solve analytically the wave equations are developed. First of all, starting with the general linearized MHD equations for a low-beta plasma of Chapter 2 and using the properties and assumptions from the equilibrium models of Chapter 3, such as uniform magnetic field, a group of partial differential equations is derived for the fast MHD oscillatory mode. The next step is to describe the appropriate boundary conditions for these models and thus, to complete the description of the problem. Then we turn our attention to the two remaining types of MHD waves in the low-beta plasma limit: Alfvén modes and the fast modes, since the slow mode is absent in that limit. Finally, a general analytical procedure based in separation of variables is presented and its consequences are studied. The details are worked out for the Cartesian and cylindrical geometries, but the procedure can be extended to other types of configurations. Then, we discuss the spatial dependence along the structure for some configurations. We also remark that some equations of the present Chapter (specially the partial differential equations) are the starting point for the numerical solution.

4.1 Wave equations

4.1.1 General equations

We start by deriving a general wave equation for the linear MHD waves in the low-beta limit. First of all, the general set of partial MHD wave equations of Sect. 2.1.1 can be adapted to suit better our problem. Following Roberts (1991), the first step is to rewrite the equation of motion in Eq. (2.17) using the vector identity

$$\nabla \cdot (\mathbf{B} \cdot \mathbf{B_0}) = (\mathbf{B_0} \cdot \nabla)\mathbf{B} + (\mathbf{B} \cdot \nabla)\mathbf{B_0} + \mathbf{B_0} \times (\nabla \times \mathbf{B}) + \mathbf{B} \times (\nabla \times \mathbf{B_0}), \tag{4.1}$$

so we have

$$\rho_0 \frac{\partial \mathbf{v}}{\partial t} = -\nabla \left[p + \frac{\mathbf{B_0} \cdot \mathbf{B}}{\mu} \right] + \frac{1}{\mu}(\mathbf{B_0} \cdot \nabla)\mathbf{B} + \frac{\mathbf{1}}{\mu}(\mathbf{B} \cdot \nabla)\mathbf{B_0}, \tag{4.2}$$

which using the total pressure, p_{T} (Eq. 2.19), and taking another time derivative reduces to

$$\rho_0 \frac{\partial^2 \mathbf{v}}{\partial t^2} = -\nabla \left[\frac{\partial p_{\mathrm{T}}}{\partial t} \right] + \frac{1}{\mu}(\mathbf{B_0} \cdot \nabla)\frac{\partial \mathbf{B}}{\partial \mathbf{t}} + \frac{\mathbf{1}}{\mu}\left(\frac{\partial \mathbf{B}}{\partial \mathbf{t}} \cdot \nabla \right) \mathbf{B_0}. \tag{4.3}$$

Before going on, we use some properties of the equilibrium configurations we deal with. First of all, the equilibrium magnetic field is uniform, constant and points along the z-direction, so $\mathbf{B} = B_0 \hat{\mathbf{z}}$; also it is assumed that all other equilibrium quantities (such as the density, ρ_0, or the

Alfvén speed, $c_{\rm A} = B_0/\sqrt{\mu\rho_0}$) only depend on the z-coordinate. Notice that the last term in Eq. (4.3) vanishes, since the equilibrium magnetic field is uniform.

The induction equation, Eq. (2.16), is invoked now to calculate the time derivative of the perturbed magnetic field. Using some vector identities this equation becomes

$$\begin{aligned}\frac{\partial \mathbf{B}}{\partial t} &= \nabla \times (\mathbf{v} \times \mathbf{B_0}) = (\mathbf{B_0} \cdot \nabla)\mathbf{v} - \mathbf{B_0}(\nabla \cdot \mathbf{v}) - (\mathbf{v} \cdot \nabla)\mathbf{B_0} + \mathbf{v}(\nabla \cdot \mathbf{B_0}) = \\ &= B_0 \frac{\partial \mathbf{v}}{\partial z} - B_0 \hat{\mathbf{z}}(\nabla \cdot \mathbf{v}), \end{aligned} \tag{4.4}$$

in which the conditions of divergence-free and uniform magnetic field have been used to eliminate some of the terms.

Since the magnetic field introduces a preferred direction, it is convenient to separate the equation of motion, Eq. (4.3), in its parallel and perpendicular components. In the following development, the symbol $\perp$ stands for the components of the perturbed quantities and gradients perpendicular to $\mathbf{B_0}$. Using Eq. (4.4), the perpendicular component of Eq. (4.3) can be rewritten as

$$\rho_0 \left[\frac{\partial^2}{\partial t^2} - c_{\rm A}^2(z) \frac{\partial^2}{\partial z^2} \right] \mathbf{v}_\perp + \nabla_\perp \frac{\partial p_{\rm T}}{\partial t} = 0. \tag{4.5}$$

Before dealing with the parallel component another expression for the perturbed total pressure is required. From Eq. (2.15) we have

$$\frac{\partial p}{\partial t} = -(\mathbf{v} \cdot \nabla) p_0(z) - \rho_0(z) c_{\rm s}^2(z)\, \nabla \cdot \mathbf{v}. \tag{4.6}$$

Using the definition of the magnetic pressure and Eq. (4.4) we also obtain

$$\frac{\partial p_{\rm m}}{\partial t} = \frac{B_0}{\mu} \frac{\partial B_z}{\partial t} = -\rho_0 c_{\rm A}^2(z)\, \nabla_\perp \cdot \mathbf{v}_\perp, \tag{4.7}$$

and using Eqs. (4.6) and (4.7) together an expression for the perturbed total pressure is derived, namely

$$\begin{aligned}\frac{\partial p_{\rm T}}{\partial t} &= \frac{\partial p}{\partial t} + \frac{\partial p_{\rm m}}{\partial t} = -v_z \frac{\partial p_0}{\partial z} - \rho_0(z) c_{\rm s}^2(z) \frac{\partial v_z}{\partial z} - \rho_0 c_{\rm f}^2(z) \nabla_\perp \cdot \mathbf{v}_\perp = \\ &= \rho_0(z) c_{\rm A}^2(z) \frac{\partial v_z}{\partial z} - \rho_0 c_{\rm f}^2(z) \nabla \cdot \mathbf{v}, \end{aligned} \tag{4.8}$$

where $c_{\rm s}(z) = \sqrt{\gamma p_0/\rho_0(z)}$ is the sound speed (see Chapter 2) and the other characteristic speeds are defined as $c_{\rm f}^2 = c_{\rm s}^2 + c_{\rm A}^2$ and $c_{\rm T}^{-2} = c_{\rm s}^{-2} + c_{\rm A}^{-2}$. In the last equality of Eq (4.8) it has also been used that p_0 is constant, so its derivative along the field vanishes.

Finally, the component of Eq (4.3) along the field is

$$\rho_0(z) \quad \frac{\partial^2 v_z}{\partial t^2} + \frac{\partial}{\partial z}\frac{\partial p_{\rm T}}{\partial t} = -\frac{B_0^2}{\mu}\frac{\partial}{\partial z}(\nabla \cdot \mathbf{v}) =$$
$$= \quad -\rho(z)c_{\rm A}^2(z)\frac{\partial}{\partial z}\left[-\frac{c_{\rm s}^2(z)}{c_{\rm f}^2(z)}\frac{\partial v_z}{\partial t} - \frac{1}{\rho(z)c_{\rm f}^2(z)}\frac{\partial p_{\rm T}}{\partial z}\right]. \tag{4.9}$$

Now it must be remarked that the characteristic speeds only depend on z via the equilibrium density, but the equilibrium magnetic field strength is constant. Therefore, for our equilibrium model the product

$$\rho(z)c_{\rm A}^2(z) = \frac{B_0^2}{\mu}, \tag{4.10}$$

is constant (and this is also true for the other characteristic speeds), so the derivative in Eq. (4.9) only affects v_z and $p_{\rm T}$.

Putting all the derived equations together we have

$$\frac{\partial p_{\rm T}}{\partial t} = \rho_0 c_{\rm A}^2(z)\frac{\partial v_z}{\partial z} - \rho_0 c_{\rm f}^2(z)\nabla \cdot \mathbf{v}, \tag{4.11}$$

$$\rho_0\left[\frac{\partial^2}{\partial t^2} - c_{\rm A}^2(z)\frac{\partial^2}{\partial z^2}\right]\mathbf{v}_\perp + \nabla_\perp \frac{\partial p_{\rm T}}{\partial t} = 0, \tag{4.12}$$

$$\rho_0\left[\frac{\partial^2}{\partial t^2} - c_{\rm T}^2(z)\frac{\partial^2}{\partial z^2}\right]v_z + \frac{c_{\rm s}^2(z)}{c_{\rm f}^2(z)}\frac{\partial}{\partial z}\left(\frac{\partial p_{\rm T}}{\partial t}\right) = 0, \tag{4.13}$$

which are formally the same as in Roberts (1991), although in that paper the details of the derivation are slightly different: they were deduced with the assumption of Cartesian coordinates and $B_0(x)$ and $\rho_0(x)$ instead of $\rho_0(z)$.

4.1.2 Wave equations in the low-beta limit

Since the plasma β is much less than 1 in the solar corona (Sect. 2.2), we can restrict ourselves to studying the oscillatory modes in the low-beta limit. This assumption implies $c_{\rm s} \to 0$, $c_{\rm T} \to 0$ and $c_{\rm f} \to c_{\rm A}$. Now, selecting the velocity components as our dependent variables leads to a pair of coupled partial differential equations, although by choosing the total pressure perturbation, $p_{\rm T}$, as our dependent variable a single partial differential equation is obtained.

First of all, from Eq. (4.9) in the low-beta limit we have

$$\frac{\partial^2 v_z}{\partial t^2} = 0. \tag{4.14}$$

In fact, the second derivative was introduced when we obtained Eq. (4.3) from Eq. (4.2). The equation that governs the z-component of the perturbed velocity in this limit is

$$\frac{\partial v_z}{\partial t} = 0, \tag{4.15}$$

which can be obtained from the z-component of Eq. (4.2) neglecting the pressure term. Eq. (4.15) has $v_z = const$ as solution, but here constant flows are not taken into account (they could be considered in the equilibrium configuration), so we just take it as zero. Thus, we have for the z-component of the perturbed velocity

$$v_z = 0. \tag{4.16}$$

Then, we take the gradient in the perpendicular plane of Eq. (4.5) and use $\nabla_\perp \rho_0(z) = 0$ and $\nabla_\perp(\rho_0(z)c_{\rm A}^2(z)) = 0$,

$$\rho_0(z)\left[\frac{\partial^2}{\partial t^2} - c_{\rm A}^2(z)\frac{\partial^2}{\partial z^2}\right]\nabla_\perp \cdot \mathbf{v}_\perp - \nabla_\perp \cdot \left(\nabla_\perp \frac{\partial \mathbf{p}_{\rm T}}{\partial \mathbf{t}}\right) = \mathbf{0}. \tag{4.17}$$

Next, we write Eq. (4.8) in the low-beta limit,

$$\frac{\partial p_{\rm T}}{\partial t} = -\rho_0 c_{\rm A}^2(z)\nabla_\perp \cdot \mathbf{v}_\perp, \tag{4.18}$$

to eliminate the velocity components in Eq. (4.17), which can be cast as

$$\left[\frac{\partial^2}{\partial t^2} - c_{\rm A}^2(z)\frac{\partial^2}{\partial z^2}\right]\frac{\partial p_{\rm T}}{\partial t} - c_{\rm A}^2(z)\nabla_\perp \cdot \left(\nabla_\perp \frac{\partial p_{\rm T}}{\partial t}\right) = 0. \tag{4.19}$$

Thus, we have only one partial differential equation to solve. In any orthonormal coordinate system (such as the cylindrical and Cartesian ones) in which one of the basis vectors points in the z-direction, the operator $\nabla_\perp \cdot \nabla_\perp$ is equal to $\nabla_\perp^2$ and so we end up with

$$\left[\frac{\partial^2}{\partial t^2} - c_{\rm A}^2(z)\frac{\partial^2}{\partial z^2}\right]p_{\rm T} - c_{\rm A}^2(z)\nabla_\perp^2 p_{\rm T} = 0, \tag{4.20}$$

or

$$\boxed{\left[\frac{\partial^2}{\partial t^2} - c_{\rm A}^2(z)\nabla^2\right]p_{\rm T} = 0.} \tag{4.21}$$

Putting together the derived partial differential equations for the total pressure perturbation and the perpendicular components of the perturbed velocity (which is present in some of the jump conditions), we have

$$\rho_0 \left[\frac{\partial^2}{\partial t^2} - c_{\rm A}^2(z) \frac{\partial^2}{\partial z^2} \right] \mathbf{v}_\perp + \nabla_\perp \frac{\partial p_{\rm T}}{\partial t} = 0, \tag{4.22}$$

$$\left[\frac{\partial^2}{\partial t^2} - c_{\rm A}^2(z) \nabla^2 \right] p_{\rm T} = 0. \tag{4.23}$$

Notice that $p_{\rm T} = 0$ is a solution to Eq (4.23), and dropping the second term of Eq. (4.22) it is straightforward to check that this solution corresponds to an Alfvén mode, which from Eq. (4.18) is incompressible. On the other hand, if $p_{\rm T} \neq 0$ this physical variable can be determined from Eq. (4.23) and then $\mathbf{v}_\perp$ from Eq. (4.22); these are the fast modes and, since the Alfvén ones have been widely studied in previous works for models similar to the ones we are dealing with, we concentrate on studying these fast modes.

Next, we consider magnetic field perturbations. Notice that the total pressure perturbation in the zero-β limit becomes

$$p_{\rm T} = \frac{B_0 B_z}{\mu}, \tag{4.24}$$

and the magnetic field perturbation becomes

$$\frac{\partial \mathbf{B}}{\partial t} = B_0 \frac{\partial \mathbf{v}_\perp}{\partial z} + B_0 \hat{\mathbf{z}} \frac{1}{\rho_0 c_{\rm A}^2} \frac{\partial p_{\rm T}}{\partial t}. \tag{4.25}$$

The parallel component of this expression is equivalent to the time derivative of Eq. (4.24) whereas the perpendicular component is

$$\frac{\partial \mathbf{B}_\perp}{\partial t} = B_0 \frac{\partial \mathbf{v}_\perp}{\partial z}. \tag{4.26}$$

Finally, the density perturbation can also be computed from Eq. (2.13), which using the result in Eq. (4.16) can be written as

$$\frac{\partial \rho}{\partial t} = -\rho_0 \nabla_\perp \cdot \mathbf{v}_\perp, \tag{4.27}$$

where it has been taken into account that the density only depends on the z-coordinate. Thus, with the help of Eq. (4.18) we obtain

$$\rho = \frac{1}{c_{\rm A}^2} p_{\rm T}. \tag{4.28}$$

Therefore, the perturbed magnetic field and perturbed density can be obtained easily once the total pressure and velocity perturbations have been computed.

4.1.3 Partial differential equations for the perturbed velocity (low-beta limit)

In the previous development we have derived a partial differential equation for a single variable ($p_{\rm T}$), although this expression alone is not enough because some of the boundary conditions involve the perturbed velocity components. It is convenient to study that equation if we look for analytical solutions, but for numerical applications it is much more convenient to work with the perturbed velocity components and find coupled partial differential equations for them. This is easily accomplished by substituting the expression for the total pressure of Eq. (4.18) in Eq. (4.22), so we have

$$\left(\frac{\partial^2}{\partial t^2} - c_{\rm A}^2 \frac{\partial^2}{\partial z^2}\right) \mathbf{v}_\perp - c_{\rm A}^2 \nabla_\perp \left(\nabla_\perp \cdot \mathbf{v}_\perp\right) = \mathbf{0}. \tag{4.29}$$

Notice that a more general set of equations can be obtained with a similar procedure from Eqs. (4.11) and (4.12), i.e. not specific of the low-beta limit. In fact, the system of equations in Eq. (4.29) is a particular application of the general wave equations derived in Arregui, Oliver & Ballester (2001).

In Cartesian geometry, the x- and y-components of Eq. (4.29) are

$$\frac{1}{c_{\rm A}^2}\frac{\partial^2 v_x}{\partial t^2} = \frac{\partial^2 v_x}{\partial x^2} + \frac{\partial^2 v_y}{\partial x \partial y} + \frac{\partial^2 v_x}{\partial z^2}, \tag{4.30}$$

$$\frac{1}{c_{\rm A}^2}\frac{\partial^2 v_y}{\partial t^2} = \frac{\partial^2 v_y}{\partial y^2} + \frac{\partial^2 v_x}{\partial x \partial y} + \frac{\partial^2 v_y}{\partial z^2}, \tag{4.31}$$

while in cylindrical geometry the r- and φ-components are

$$\frac{1}{c_{\rm A}^2}\frac{\partial^2 v_r}{\partial t^2} = \frac{\partial}{\partial r}\left[\frac{1}{r}\left(\frac{\partial}{\partial r}(r\, v_r) + \frac{\partial v_\varphi}{\partial \varphi}\right)\right] + \frac{\partial^2 v_r}{\partial z^2}, \tag{4.32}$$

$$\frac{1}{c_{\rm A}^2}\frac{\partial^2 v_\varphi}{\partial t^2} = \frac{1}{r^2}\left[\frac{\partial^2}{\partial r \partial \varphi}(r\, v_r) + \frac{\partial^2 v_\varphi}{\partial \varphi^2}\right] + \frac{\partial^2 v_\varphi}{\partial z^2}. \tag{4.33}$$

It should be noticed that there is a special limit in which these systems of equations are greatly simplified. If we assume invariance in one of these perpendicular directions, namely the y-direction in Cartesian geometry (that is, $\partial/\partial y = 0$) and the azimuthal direction in cylindrical geometry ($\partial/\partial \varphi = 0$), then the equations can be written in the form

$$\frac{1}{c_{\rm A}^2}\frac{\partial^2 v_x}{\partial t^2} = \frac{\partial^2 v_x}{\partial x^2} + \frac{\partial^2 v_x}{\partial z^2}, \tag{4.34}$$

$$\frac{1}{c_{\rm A}^2}\frac{\partial^2 v_y}{\partial t^2} = \frac{\partial^2 v_y}{\partial z^2}, \tag{4.35}$$

and

$$\frac{1}{c_{\rm A}^2}\frac{\partial^2 v_r}{\partial t^2} = \frac{\partial}{\partial r}\left[\frac{1}{r}\frac{\partial}{\partial r}(r\,v_r)\right] + \frac{\partial^2 v_r}{\partial z^2}, \tag{4.36}$$

$$\frac{1}{c_{\rm A}^2}\frac{\partial^2 v_\varphi}{\partial t^2} = \frac{\partial^2 v_\varphi}{\partial z^2}, \tag{4.37}$$

which are decoupled systems for these variables. However, this is quite a special situation, so in general we are going to look for solutions to Eqs. (4.22) and (4.23) and keep the total pressure as the main dependent variable.

In this Thesis we have also applied numerical methods to check the analytical solutions. To achieve this, we used a numerical code based in a discretization of the partial differential equations for the perturbed velocity derived in this section (see Appendix C and Arregui et al. 2001, 2003 for more information about the code).

4.2 Boundary conditions

Next we study the boundary conditions that must be applied to the solutions of Eq. (4.23) (and also Eq. 4.22). It is well known that a problem involving partial differential equations can be ill-posed depending on the specific boundary conditions. In general, stability and unicity of the solution are demanded, and the same partial differential equation can satisfy these requirements with some set of boundary conditions but not with others (see Arfken 1985 for a more detailed discussion on this interesting topic).

We first demand that modes are *stationary*. The standard method to impose this is to examine the external flux $F = pv_\perp$ and to require the average flux to be zero, $\langle F\rangle = 0$ (Bray & Loughhead 1974, Cally 1986), although in Cartesian coordinates it is enough to impose the kinetic energy $\rho v_\perp^2$ to vanish far away from the loop or fibril. This results in the conditions

$$\mathbf{v} \to 0, \qquad p_{\rm T} \to 0, \tag{4.38}$$

far away from the structure (that is, when $|x| \to \infty$ in Cartesian geometry). However, in cylindrical geometry the condition in Eq. (4.38) imposed when $r \to \infty$ is not sufficient, so the condition of null average flux is necessary. We will comment on this point later when presenting the solution in cylindrical geometry.

The second condition is the so-called *line-tying* at the photosphere (that in our system of coordinates is situated on the surfaces $z = \pm L$). This condition is intended to model the fact that the magnetic structure is anchored in the lower layer of the solar atmosphere, which is much denser than the corona (Fig. 1.2). It is easy to realize that the dense photospheric plasma acts as a reflecting and stabilising layer, mainly because there is not enough energy in the perturbations carried by the coronal material to drive important motions in the photosphere. Using this condition is also very convenient, since it eliminates the coupling between the coronal and photospheric material (so the dynamics of the photospheric plasma is not taken into consideration) and assumptions about the physical condition and configuration of the inner layers of the

structure. Therefore, it is assumed that no motions of coronal material perpendicular to the field lines take place on the photospheric surface. There are two sets of ideal MHD boundary conditions suitable and commonly used (see for example Hood (1986), Van der Linden, Hood & Goedbloed (1994) and references therein for a deeper discussion on this topic):

- the *rigid wall* (or "perfectly reflective") condition, wherein the velocity (and displacement) components along the magnetic field are also zero (so the perturbed velocity vanishes on the photospheric surface). In our notation this condition is expressed as $\mathbf{v}(|z| = L) = 0$. This condition is quite restrictive and decouples totally the coronal dynamics from the photospheric one.

- the *flow-through* condition, that states that the parallel velocity does not need to be zero (although there are conditions over it, such as the requirement of Eqs. (2.26)). Notice that a stationary flow across the boundary is allowed under these conditions, which might be in accordance with some observations of coronal structures that point out the existence of flows. This condition requires some knowledge or assumptions about the photospheric plasma, which is coupled to the coronal dynamics via Eqs. (2.26). Using the notation of this work the flow-through condition is written as $\mathbf{v}_\perp(|z| = L) = 0$.

There is however some controversy about this type of boundary conditions and some authors use the rigid wall while others apply the flow-through conditions. Clearly, a more accurate description would be achieved by using a model with a proper solar atmospheric stratification (where it would be necessary to include gravity, since the gravitational scale is quite short in the photospheric region), although that scheme would complicate quite a lot the wave analysis (and even the equilibrium configuration). Anyway, for the purposes of this work, it is not important whether description is more suitable, since we are going to use the low-beta plasma approximation in the corona. From Eq. (4.16) we have then that the component parallel to the magnetic field lines is identically zero in all the region, and as a consequence on the photospheric boundary. That is why we are going to use simply the name of line-tying boundary conditions, without making any other assumption about the two possibilities stated before. As a conclusion, our line-tying boundary condition is simply

$$\mathbf{v}_\perp(|z| = L) = 0. \tag{4.39}$$

On the other hand, we must also apply the boundary conditions of Sect. 2.3 on the *interfaces of plasmas* with different physical properties. There are two distinct types of boundaries in the models that we use: inhomogeneities across the magnetic field and along it. All the models presented in Chapter 3 have a contact discontinuity in the loop or fibril surface, on which $\hat{\mathbf{n}}_0 \cdot \mathbf{B}_0 = \hat{\mathbf{n}}_\perp \cdot (B_0 \hat{\mathbf{z}}) = 0$ is satisfied, so the "jump conditions" of Eqs. (2.26) should be used. In other words, our boundary conditions on those surfaces are

$$\mathbf{n} \cdot [\mathbf{v}] = 0, \quad \mathbf{n} \cdot [\mathbf{B}] = 0, \quad [p_{\mathrm{T}}] = 0, \tag{4.40}$$

where brackets represent $[A] \equiv A_2 - A_1$, the subscripts 1 and 2 indicating the values of the variable A on either side of the boundary. Notice that all the extra terms discussed in Chapter

2 are zero in this problem. The last condition of Eq. (4.40) directly implies the continuity of the total pressure. The first condition implies the continuity of the component of the perturbed velocity perpendicular to the boundary and, since the magnetic field is along that boundary, that component is the one perpendicular to the magnetic field. The second condition of Eq. (4.40) is equivalent to the first one, since $\mathbf{B}_\perp \sim \partial \mathbf{v}_\perp / \partial \mathbf{z}$ from Eq. (4.26) and the continuity of $v_\perp$ on this boundary (on which z remains constant) also implies the continuity of $\partial \mathbf{v}_\perp / \partial \mathbf{z}$ along it. Also notice that for inhomogeneities along the field (for example a chromospheric layer in Fig. 3.4) $\hat{\mathbf{n}}_0 \cdot \mathbf{B}_0 = \hat{\mathbf{z}} \cdot (B_0 \hat{\mathbf{z}}) \neq 0$ is satisfied, so the set of Eqs. (2.27) must be used then.

All these boundary conditions are enough to solve the problem, but it is convenient to use the fact that there are symmetries in our problem. The structure is symmetric at least about the surface $z = 0$, so we can restrict ourselves to solve the equations in the region $0 \leq z \leq L$. An important consequence of this symmetry is that there will be even and odd modes in the z-direction, the even modes having

$$\left. \frac{\partial p_{\mathrm{T}}}{\partial z} \right|_{z=0} = 0, \tag{4.41}$$

and the odd modes having

$$p_{\mathrm{T}}(z = 0) = 0. \tag{4.42}$$

Moreover, in most of the problems there is also symmetry with respect to perpendicular coordinate. For example, in Cartesian geometry there is a similar symmetry about the surface $x = 0$ (so our physical domain can be restricted to $x \geq 0$) and in the cylindrical geometry there is the well-know symmetry in the azimuthal coordinate (so $0 \leq \varphi \leq 2\pi$) together with considerations about the radial coordinate, such as imposing the solution to be regular in all the region (specially as $r \to 0$).

In a nutshell, the boundary conditions of this eigenvalue problem are

- evanescence far away from the loop (trapped waves), $\mathbf{v} \to 0$ far away from the structure,
- photospheric line-tying, $\mathbf{v}_\perp(z = \pm L) = 0$,
- jump conditions on $\mathbf{v}$ and $\mathbf{B}$ on the interface surfaces, Eqs. (4.40),
- symmetry about $z = 0$ (and possibly also about other surfaces).

4.3 Analytical solution in Cartesian geometry

Here we deal with the problem in the Cartesian geometry, which is easier to solve and interpret than more realistic geometries and represents reasonably accurately some solar structures, like the prominence as a whole. All the models discussed in Chapter 3 share a common feature: the structure was situated along the magnetic field and surrounded by the corona. Therefore, we distinguish between two different zones: the flux tube (hereafter labelled "l") and the coronal environment (labelled "c"), with two different Alfvén speeds

$$c_{\rm A} = \begin{cases} c_{\rm Ac}, & x > b, \\ c_{\rm Al}(z), & x < b. \end{cases} \tag{4.43}$$

The standard method to solve partial differential equations like Eq. (4.23) is to use separation of variables in the form

$$p_{\rm T}(x,y,z) = u(x)g(y)h(z), \tag{4.44}$$

which leads to the ordinary differential equations

$$\frac{d^2}{dx^2}u(x) = \lambda^2\, u(x), \tag{4.45}$$

$$\frac{d^2}{dy^2}g(y) = -k_y^2\, g(y), \tag{4.46}$$

$$\left[\frac{d^2}{dz^2} + \frac{\omega^2}{c_{\rm A}^2(z)}\right] h(z) = -(\lambda^2 - k_y^2)\, h(z), \tag{4.47}$$

where two separation constants, λ and k_y, have been introduced. Here it must be remarked that the equilibrium models do not have any dependence on the y-coordinate. Generally there are many solutions to Eqs. (4.45)–(4.47), which we label with a subscript n.

On the boundary between the structure and the surrounding corona the normal component of the perturbed velocity and the magnetic field and the total magnetic pressure have to be continuous. In general a solution in the form of Eq. (4.44) with only one of the functions of Eq. (4.47) cannot satisfy these requirements on the boundary. Therefore, a linear combination of all the solutions is required, so the total pressure perturbation can be written as

$$p_{\rm T}(x,y,z) = \sum_{n=1}^{\infty} u_n(x)\, g(y)\, h_n(z). \tag{4.48}$$

As a consequence, we must solve an infinite number of ordinary differential equations like Eqs. (4.45)–(4.47), namely,

$$\frac{d^2}{dx^2}u_n(x) = \lambda_n^2\, u_n(x), \tag{4.49}$$

$$\frac{d^2}{dy^2}g(y) = -k_y^2\, g(y), \tag{4.50}$$

$$\left[\frac{d^2}{dz^2} + \frac{\omega^2}{c_{\rm A}^2(z)}\right] h_n(z) = -(\lambda_n^2 - k_y^2)\, h_n(z), \tag{4.51}$$

The perturbed velocity, which is also involved in the boundary conditions of Eqs. (4.40), can be calculated from Eq. (4.22) and turns out to be

$$\mathbf{v}_\perp(x,y,z) = \frac{i\omega}{\rho_0 c_{\rm A}^2}\sum_{n=1}^{\infty}\frac{1}{\lambda_n^2 - k_y^2}\nabla_\perp\left\{u_n(x)g(y)h_n(z)\right\}, \tag{4.52}$$

or in terms of its x- and y-components,

$$v_x(x,y,z) = \frac{i\omega}{\rho_0 c_{\rm A}^2}\sum_{n=1}^{\infty}\frac{1}{\lambda_n^2 - k_y^2}u_n'(x)\,g(y)\,h_n(z) \tag{4.53}$$

and

$$v_y(x,y,z) = \frac{\omega k_y}{\rho_0 c_{\rm A}^2}\sum_{n=1}^{\infty}\frac{1}{\lambda_n^2 - k_y^2}u_n(x)\,g(y)\,h_n(z). \tag{4.54}$$

4.3.1 Spatial structure along the magnetic field

Our first task is to solve the ordinary differential equation

$$\left[\frac{d^2}{dz^2} + \frac{\omega^2}{c_{\rm A}^2(z)}\right] h_n(z) = -\lambda_n^2\, h_n(z), \tag{4.55}$$

which is Eq. (4.47) with $k_y = 0$, since the case $k_y \neq 0$ can be easily recovered from it (and will be discussed later). In this section we develop a general method for dealing with this kind of equation, taking into account the boundary condition requirements that have been mentioned before.

Consider an ordinary differential operator, $\mathcal{L}$, determined in the interval $[-L, L]$ by the differential expression

$$\frac{d^2}{dz^2} + \frac{\omega^2}{c_{\rm Aj}^2(z)}, \tag{4.56}$$

where j = c, l, and the boundary conditions

$$p_{\rm T} = 0 \ \text{ at } \ z = \pm L. \tag{4.57}$$

By virtue of Eq. (4.48) the perturbed total pressure has contributions from all the basis functions $h_n(z)$, so the only possibility to fulfill this condition is that all the relevant solutions of Eq. (4.55) satisfy

$$h_n(\pm L) = 0, \quad n = 1, 2, \ldots \tag{4.58}$$

It is straightforward to see that the operator in Eq. (4.56) is selfadjoint. According to the theory of selfadjoint ordinary regular differential operators, the eigenvalues of this operator

constitute a monotonically decreasing countable set tending to $-\infty$. We write the n-th eigenvalue in the region j as $-(\lambda_n^{(\mathrm{j})})^2$, where either $\lambda_n^{(\mathrm{j})}$ is real and positive ($\lambda_n^{(\mathrm{j})} > 0$), or it is a purely imaginary number with positive imaginary part ($\lambda_n^{(\mathrm{j})} = i\lambda_n^{*(\mathrm{j})}$, $\lambda_n^{*(\mathrm{j})} > 0$), and $\lambda_n^{(\mathrm{j})} \to \infty$ as $n \to \infty$. The corresponding eigenfunction, $h_n^{(\mathrm{j})}(z)$, satisfies the equation

$$\frac{d^2 h_n^{(\mathrm{j})}}{dz^2} + \frac{\omega^2}{c_{\mathrm{Aj}}^2(z)}\, h_n^{(\mathrm{j})} = -{\lambda_n^{(\mathrm{j})}}^2 h_n^{(\mathrm{j})}. \tag{4.59}$$

The set of eigenfunctions $\{h_n^{(\mathrm{j})}(z)\}$ constitutes a complete system of functions (a basis) in $[-L, L]$, so that any well-behaved function $f(z)$ can be expanded into a generalized Fourier series,

$$f(z) = \sum_{n=1}^{\infty} f_n^{(\mathrm{j})} h_n^{(\mathrm{j})}(z), \tag{4.60}$$

$$f_n^{(\mathrm{j})} = \langle f, h_n^{(\mathrm{j})} \rangle \equiv \int_{-L}^{L} f(z) h_n^{(\mathrm{j})}(z)\, dz, \tag{4.61}$$

where $\langle f, g \rangle$ indicates the scalar product of the functions f and g and it has been assumed that the basis $\{h_n^{(\mathrm{j})}(z)\}$ is orthonormal, i.e.

$$\|h_n^{(\mathrm{j})}\|^2 \equiv \langle h_n^{(\mathrm{j})}, h_n^{(\mathrm{j})} \rangle = 1. \tag{4.62}$$

Note that, by virtue of Eq. (4.59), the eigenvalues and eigenfunctions depend on ω and can be found for any given Alfvén speed profile. Hence, following Eq. (4.61), the functions $h_n^{(\mathrm{l})}(z)$ can be expanded into a "generalized Fourier series" in terms of the functions $h_n^{(\mathrm{c})}(z)$,

$$h_n^{(\mathrm{l})}(z) = \sum_{m=1}^{\infty} H_{nm} h_m^{(\mathrm{c})}(z). \tag{4.63}$$

The coefficients H_{nm} play an important role in the following discussion. Using the completeness of our basis of eigenfunctions, the following expression for H_{nm} is obtained,

$$H_{nm} = \int_{-L}^{L} h_n^{(\mathrm{l})}(z)\, h_m^{(\mathrm{c})}(z), \tag{4.64}$$

so it is possible to match the inner an outer solutions for whatever dependence on the z-coordinate is obtained from Eq. (4.59).

Since the coronal medium is uniform in all our models, the basis functions coming from solving Eq. (4.59) in the coronal region are

$$h_{2n-1}^{(\mathrm{c})}(z) = \frac{1}{L^{1/2}} \cos \frac{(2n-1)\pi z}{2L} = \frac{1}{L^{1/2}} \cos \kappa_{2n-1} z, \tag{4.65}$$

$$\left(\lambda_{2n-1}^{(\mathrm{c})}\right)^2 = \kappa_{2n-1}^2 - \frac{\omega^2}{c_{\mathrm{Ac}}^2} = \frac{\pi^2(2n-1)^2}{4L^2} - \frac{\omega^2}{c_{\mathrm{Ac}}^2}, \tag{4.66}$$

for even modes and

$$h_{2n}^{(\mathrm{c})}(z) = \frac{1}{L^{1/2}} \sin\frac{n\pi z}{L} = \frac{1}{L^{1/2}} \sin\kappa_{2n} z, \tag{4.67}$$

$$\left(\lambda_{2n}^{(\mathrm{c})}\right)^2 = \kappa_{2n}^2 - \frac{\omega^2}{c_{\mathrm{Ac}}^2} = \frac{\pi^2 n^2}{L^2} - \frac{\omega^2}{c_{\mathrm{Ac}}^2}, \tag{4.68}$$

for odd modes, that is, simple trigonometric functions with the appropriate constants to fulfil the conditions in Eq. (4.62). The constant $\kappa_n^{(\mathrm{c})}$ is defined as

$$\kappa_n^{(\mathrm{c})} = \frac{\omega^2}{c_{\mathrm{Ac}}^2} + {\lambda_n^{(\mathrm{c})}}^2. \tag{4.69}$$

Notice that rearranging this equation it is obtained that our separation constant λ is equivalent to the m wavelength in Eq. (2.40) in the low-beta limit, but it must be remarked that in our solution λ is not a wavelength of the eigenmodes, since these modes have contributions of many eigenfunctions. Finally, the photospheric line-tying condition (Eq. 4.58), once imposed on $h_n^{(\mathrm{c})}(z)$ gives

$$\kappa_n^{(\mathrm{c})} = \frac{2n-1}{2L}\pi, \ n = 1, 2, \ldots, \tag{4.70}$$

for even modes and

$$\kappa_n^{(\mathrm{c})} = \frac{n}{L}\pi, \ n = 1, 2, \ldots, \tag{4.71}$$

for odd modes. Inside the structure the dependence is more complicated. Some examples are presented in later in Sect. 4.5

Finally, if $k_y \neq 0$ is considered the equation satisfied by the eigenfunction $h_n^{(\mathrm{j})}$ is

$$\frac{d^2 h_n^{(\mathrm{j})}}{dz^2} + \left[\frac{\omega^2}{c_{\mathrm{Aj}}^2(z)} - k_y^2\right] h_n^{(\mathrm{j})} = -{\lambda_n^{(\mathrm{j})}}^2 h_n^{(\mathrm{j})}, \tag{4.72}$$

instead of Eq. (4.59), so the operator in Eq. (4.56) has a new term $-k_y^2$. However, the sets of eigenfunctions $\{h_n^{(\mathrm{j})}(z)\}$ still constitute a complete system of functions and the rest of properties are still satisfied. This new term has also to be included in Eqs. (4.66), (4.68) and (4.69).

4.3.2 Spatial structure across the magnetic field

After having studied the solution along the z-coordinate now it is time to investigate the solution for the other spatial coordinates. Separation of variables in Eq. (4.23) in the form of Eq. (4.48) leads to the ordinary differential equations in Eqs. (4.49)–(4.51), where two separation constants were introduced, namely λ and k_y. Here we concentrate on Eqs. (4.49) and (4.50), which will lead to the spatial structure across the magnetic field.

The solution of Eq. (4.46) is a suitable combination of exponential functions

$$g(y) = G_1 e^{-ik_y y} + G_2 e^{ik_y y}. \tag{4.73}$$

Here we assume a dependence with no loss of generality $G_2 = 0$ and $G_1 = 1$, so

$$g(y) = e^{-ik_y y}, \tag{4.74}$$

since we only expect a free propagating wave in the y-direction, in which the equilibrium models are invariant. Notice that this solution suggests that a Fourier analysis of this coordinate is possible, but contrary to other studies, we are not imposing this Fourier decomposition in the wave equations, but obtaining it as a solution of them.

Now the dependence on the x-coordinate is studied. The most general solution of Eq. (4.49) is in the form

$$u_n(x) = C_1 e^{\lambda_n x} + C_2 e^{-\lambda_n x} = C_3 \cosh \lambda_n x + C_4 \sinh \lambda_n x, \tag{4.75}$$

where it has been assumed that $\lambda_n^2 > 0$. On the other hand, when $\lambda_n^2 < 0$ the solution can be written as

$$u(x) = C_5 \cos \lambda_n^* x + C_6 \sin \lambda_n^* x, \tag{4.76}$$

with $\lambda_n^* = i\lambda_n$ a real constant.

Now the boundary conditions are applied to this solution. Only trapped modes are of interest, so we demand that in the coronal region ($|x| > b$) the solutions must satisfy the condition $u^{(\mathrm{c})} \to 0$ as $|x| \to \infty$ (Eq. 4.38). Then,

$$u_n^{(\mathrm{c})} = \begin{cases} A_n^{(-)} e^{\lambda_n^{(\mathrm{c})}(x+b)}, & x < -b, \\ A_n^{(+)} e^{-\lambda_n^{(\mathrm{c})}(x-b)}, & x > b, \end{cases} \tag{4.77}$$

where the arbitrary constants have been renamed to make easier the application of the remaining boundary conditions at the fibril surface. It is crucial that ${\lambda^{(\mathrm{c})}}^2 > 0$ to have non-leaky solutions, a condition that leads to the existence of cut-off frequencies, since from Eq. (4.69)

$$\omega < c_{\mathrm{Ac}} \kappa_n^{(\mathrm{c})}. \tag{4.78}$$

The solution inside the tube ($|x| < b$) is given by

$$u_n^{(\mathrm{l})}(x) = B_n^{\cos}\cosh(\lambda_n^{(\mathrm{l})}x) + B_n^{\sin}\sinh(\lambda_n^{(\mathrm{l})}x), \quad |x| < b, \tag{4.79}$$

where again the constants have been renamed. Here we could have written the solution as two sets of functions, either even or odd in the x-coordinate, but this symmetry arises naturally in the development.

4.3.3 Dispersion relations

Now we apply the remaining boundary condition at the boundaries $|x| = b$. Since the unperturbed magnetic field is parallel to the boundary we have the conditions of Eq (4.40). We first note that the total pressure continuity requires the z-dependent part to be continuous in the whole range $0 \le z \le L$, a requirement that cannot be fulfilled if only one basis function is taken, since the "wavelengths" κ inside and outside are different. This means that a solution to Eq. (4.23) cannot have such a simple z-dependence and it must consist instead of a sum of all the possible basis functions $h_n(z)$. Taking into account that both $u_n(x)$ and $h_n(z)$ are mutually linked by a given separation constant λ_n, such a sum has to include all the possible $u_n(x)$ in each region. Thus,

$$p_{\mathrm{T}}(x,z) = \begin{cases} \displaystyle\sum_{n=1}^{\infty} u_n^{(l)}(x)\, e^{-ik_y y}\, h_n^{(l)}(z), & |x| \le b, \\ \displaystyle\sum_{n=1}^{\infty} u_n^{(c)}(x)\, e^{-ik_y y}\, h_n^{(c)}(z), & |x| \ge b. \end{cases} \tag{4.80}$$

The boundary conditions that involve the perturbed velocity (Eqs. 4.52–4.54) can be translated into requirements on $u_n(x)$ and $h_n(z)$. It is also evident that kink modes, for which $u_n(x)$ is an odd function, are characterized by p_{T} and v_y symmetric in the x-direction (the opposite applies for sausage modes).

Moreover, to match the solutions at $x = b$ one should use the Sturm-Liouville theorem, as in the previous section. Using Eqs. (4.63), (4.77) and (4.79) and imposing the boundary conditions Eq. (4.40) leads to

$$A_n^{(-)} = \sum_{m=1}^{\infty} H_{mn}\,[B_m^{\cos}\cosh(\lambda_m^{(\mathrm{l})}b) - B_m^{\sin}\sinh(\lambda_m^{(\mathrm{l})}b)], \tag{4.81}$$

$$\frac{\lambda_n^{(\mathrm{c})}}{{\lambda_n^{(\mathrm{c})}}^2 - k_y^2} A_n^{(-)} = -\sum_{m=1}^{\infty} H_{mn}\frac{\lambda_m^{(\mathrm{l})}}{{\lambda_m^{(\mathrm{l})}}^2 - k_y^2}[B_m^{\cos}\sinh(\lambda_m^{(\mathrm{l})}b) - B_m^{\sin}\cosh(\lambda_m^{(\mathrm{l})}b)], \tag{4.82}$$

$$A_n^{(+)} = \sum_{m=1}^{\infty} H_{mn}[B_m^{\cos}\cosh(\lambda_m^{(\mathrm{l})}b) + B_m^{\sin}\sinh(\lambda_m^{(\mathrm{l})}b)], \tag{4.83}$$

$$\frac{\lambda_n^{(\mathrm{c})}}{{\lambda_n^{(\mathrm{c})}}^2 - k_y^2} A_n^{(+)} = -\sum_{m=1}^{\infty} H_{mn}\frac{\lambda_m^{(\mathrm{l})}}{{\lambda_m^{(\mathrm{l})}}^2 - k_y^2}[B_m^{\cos}\sinh(\lambda_m^{(\mathrm{l})}b) + B_m^{\sin}\cosh(\lambda_m^{(\mathrm{l})}b)]. \tag{4.84}$$

Now, eliminating $A_n^{(-)}$ and $A_n^{(+)}$ from these equations, we obtain

$$\sum_{m=1}^{\infty} H_{mn} \left\{ B_m^{\cos} \left[\frac{\lambda_n^{(c)}}{{\lambda_n^{(c)}}^2 - k_y^2} \cosh(\lambda_m^{(l)} b) + \frac{\lambda_m^{(l)}}{{\lambda_m^{(l)}}^2 - k_y^2} \sinh(\lambda_m^{(l)} b) \right] \right. \tag{4.85}$$
$$\left. - B_m^{\sin} \left[\frac{\lambda_n^{(c)}}{{\lambda_n^{(c)}}^2 - k_y^2} \sinh(\lambda_m^{(l)} b) + \frac{\lambda_m^{(l)}}{{\lambda_m^{(l)}}^2 - k_y^2} \cosh(\lambda_m^{(l)} b) \right] \right\} = 0,$$

$$\sum_{m=1}^{\infty} H_{mn} \left\{ B_m^{\cos} \left[\frac{\lambda_n^{(c)}}{{\lambda_n^{(c)}}^2 - k_y^2} \cosh(\lambda_m^{(l)} b) + \frac{\lambda_m^{(l)}}{{\lambda_m^{(l)}}^2 - k_y^2} \sinh(\lambda_m^{(l)} b) \right] \right. \tag{4.86}$$
$$\left. + B_m^{\sin} \left[\frac{\lambda_n^{(c)}}{{\lambda_n^{(c)}}^2 - k_y^2} \sinh(\lambda_m^{(l)} b) + \frac{\lambda_m^{(l)}}{{\lambda_m^{(l)}}^2 - k_y^2} \cosh(\lambda_m^{(l)} b) \right] \right\} = 0.$$

Subtracting or adding Eqs. (4.85) and (4.86) we can eliminate the terms having $B_m^{\cos}$ and $B_m^{\sin}$, respectively, so we obtain the so called sausage (odd modes about $x = 0$) and kink (even modes about $x = 0$) oscillations. Notice that this could have been done in Eq. (4.79) by separating the two symmetries in the x-direction (that is, setting $B_m^{\cos} = 0$ or $B_m^{\sin} = 0$, depending on whether sausage or kink modes are studied).

Hence, the following expressions are obtained,

$$\sum_{m=1}^{\infty} H_{mn} B_m^{\sin} \left[\frac{\lambda_m^{(l)}}{{\lambda_m^{(l)}}^2 - k_y^2} \sinh(\lambda_m^{(l)} b) + \frac{\lambda_n^{(c)}}{{\lambda_n^{(c)}}^2 - k_y^2} \cosh(\lambda_m^{(l)} b) \right] = 0, \tag{4.87}$$

for sausage modes and

$$\sum_{m=1}^{\infty} H_{mn} B_m^{\cos} \left[\frac{\lambda_m^{(l)}}{{\lambda_m^{(l)}}^2 - k_y^2} \cosh(\lambda_m^{(l)} b) + \frac{\lambda_n^{(c)}}{{\lambda_n^{(c)}}^2 - k_y^2} \sinh(\lambda_m^{(l)} b) \right] = 0, \tag{4.88}$$

for kink modes. By using this notation we are assuming the common terminology by which kink modes stand for even solutions in the direction across the fibril and sausage modes for the odd ones (Fig. 2.5). These two kinds of modes become separated because of the symmetry of the problem.

Eqs. (4.87) and (4.88) constitute two infinite systems of homogeneous algebraic equations for $B_m^{\sin}$ and $B_m^{\cos}$, respectively, with coefficients that depend on ω. For these systems to have non-trivial solutions only particular values of ω are acceptable: the eigenfrequencies of the problem under consideration. Hence, the determinant of Eqs. (4.87) or (4.88) must be zero, which provides us with the dispersion relation from which ω can be computed. Since it is not possible to solve these infinite determinants, they are truncated by taking $B_m^{\sin} = 0$ or $B_m^{\cos} = 0$ for $m > N$, with N a sufficiently large integer number. Then, we obtain a generalized eigenvalue problem with a finite matrix and the eigenfrequencies can be determined from the condition that the determinant of the $N \times N$ matrix is zero, which results in a transcendental equation for ω.

By neglecting B_n for large values of n we are simply assuming that solutions are well represented by the first N basis functions, which is certainly true as long as such solutions do not possess strong spatial variations, i.e. as long as we restrict ourselves to the fundamental modes and their first harmonics (which anyway are the modes of interest in the present problem).

After solving the dispersion relation to calculate the eigenfrequency ω, all the other quantities can be easily calculated, except for the coefficients $B_n^{\cos}$ or $B_n^{\sin}$. These must be obtained from the systems of equations in Eqs. (4.87) and (4.88), using the fact that for the eigenfrequencies the equations in these systems are not linearly independent, so all the coefficients $B_n^{\cos}$ can be expressed in terms of $B_1^{\cos}$ (and the $B_n^{\sin}$ in terms of $B_1^{\sin}$), which can be set to 1 as an arbitrary normalization choice. Finally, the total pressure can be obtained from Eqs. (4.77) and (4.79). The process of computing p_{T}, v_x and v_y is therefore quite cumbersome.

Finally, some of the lower eigenvalues may satisfy $\lambda_1^{(\mathrm{l})2} < 0$. If we assume that the first c parameters are purely imaginary and define

$$\lambda_n^{*(\mathrm{l})} = i\,\lambda_n^{(\mathrm{l})}, \quad n = 1, 2, \ldots, c, \tag{4.89}$$

the dispersion relations are also modified (see Appendix D),

$$\begin{aligned}
&\sum_{m=1}^{c} H_{mn}^{*} B_m^{\cos *} \left[\frac{-\lambda_m^{(\mathrm{l})*}}{{\lambda_m^{(\mathrm{l})*}}^2 + k_y^2} \cos(\lambda_m^{(\mathrm{l})*} b) + \frac{\lambda_n^{(\mathrm{c})}}{{\lambda_n^{(\mathrm{c})}}^2 - k_y^2} \sin(\lambda_m^{(\mathrm{l})*} b) \right] = 0 + \\
&\sum_{m=c+1}^{\infty} H_{mn} B_m^{\cos} \left[\frac{\lambda_m^{(\mathrm{l})}}{{\lambda_m^{(\mathrm{l})}}^2 - k_y^2} \cosh(\lambda_m^{(\mathrm{l})} b) + \frac{\lambda_n^{(\mathrm{c})}}{{\lambda_n^{(\mathrm{c})}}^2 - k_y^2} \sinh(\lambda_m^{(\mathrm{l})} b) \right] = 0,
\end{aligned} \tag{4.90}$$

$$\begin{aligned}
&\sum_{m=1}^{c} H_{mn}^{*} B_m^{\sin *} \left[\frac{\lambda_m^{(\mathrm{l})*}}{{\lambda_m^{(\mathrm{l})*}}^2 + k_y^2} \sin(\lambda_m^{(\mathrm{l})*} b) + \frac{\lambda_n^{(\mathrm{c})}}{{\lambda_n^{(\mathrm{c})}}^2 - k_y^2} \cos(\lambda_m^{(\mathrm{l})*} b) \right] = 0 + \\
&\sum_{m=c+1}^{\infty} H_{mn} B_m^{\sin} \left[\frac{\lambda_m^{(\mathrm{l})}}{{\lambda_m^{(\mathrm{l})}}^2 - k_y^2} \sinh(\lambda_m^{(\mathrm{l})} b) + \frac{\lambda_n^{(\mathrm{c})}}{{\lambda_n^{(\mathrm{c})}}^2 - k_y^2} \cosh(\lambda_m^{(\mathrm{l})} b) \right] = 0,
\end{aligned} \tag{4.91}$$

It is also remarkable that in the two-dimensional problem ($k_y = 0$) the solution can also be obtained starting from the wave equations for the perturbed velocity, namely Eqs. (4.34) and (4.35) (Díaz et al. 2001a), but this is not straightforward to do in the three-dimensional problem. In fact, we first used this approach of using the perturbed velocity as the main dependent variable, but we next used p_{T} as the main independent variable because it leads to a more tractable mathematical problem.

4.4 Cylindrical geometry

The coronal loop models and some of prominence fibrils ones in Chapter 3 have cylindrical geometry, so we now extend to cylindrical geometry the procedure used in the previous section for deducing the dispersion relations for a Cartesian slab. Again, we assume $p_{\rm T}$ is separable in r, φ and z and write it in the form

$$p_{\rm T}(r,\varphi,z) = \sum_{n=1}^{\infty} u_n(r)\,\Phi(\varphi)\,h_n(z), \tag{4.92}$$

The resulting equations for the functions $u(r)$, $\Phi(\varphi)$ and $h(z)$ are

$$\frac{1}{r}\frac{d}{dr}\left(r\frac{du_n(r)}{dr}\right) - \left(\lambda_n^2 + \frac{m^2}{r^2}\right) u_n(r) = 0, \tag{4.93}$$

$$\frac{d^2\Phi_m(\varphi)}{d\varphi^2} = -m^2\Phi_m(\varphi), \tag{4.94}$$

$$\left(\frac{d^2}{dz^2} + \frac{\omega^2}{c_{\rm A}^2}\right) h_n(z) = -\lambda_n^2 h_n(z), \tag{4.95}$$

with λ_n and m the two separation constants. The subscript n has been introduced because there are many solutions to Eqs. (4.93)–(4.95) and it is necessary to distinguish between them. Notice that in Eq. (4.92) a linear combination of all the solutions has been taken into account, since a solution with only one of the functions of Eq. (4.95) cannot the requirements on the boundary.

Now the velocity components v_r and v_φ can be derived from the r- and φ-components of Eq. (4.22), which, with the help of Eq. (4.92) and taking into account the assumed time dependence, can be written as

$$\rho_0\left[\omega^2 + c_{\rm A}^2(z)\frac{\partial^2}{\partial z^2}\right] v_r + \sum_{n=1}^{\infty} i\omega\frac{du_n(r)}{dr}h_n(z)\Phi_m(\varphi) = 0 \tag{4.96}$$

and

$$\rho_0\left[\omega^2 + c_{\rm A}^2(z)\frac{\partial^2}{\partial z^2}\right] v_\varphi - \sum_{n=1}^{\infty} m\omega\frac{u_n(r)}{r}h_n(z)\Phi_m(\varphi) = 0. \tag{4.97}$$

Thus, considering that the velocity components are also separable functions in r, φ and z, v_r and v_φ are

$$v_r(r,\varphi,z) = \frac{i\omega}{\rho_0(z)c_{\rm A}^2(z)}\sum_{n=1}^{\infty}\frac{1}{\lambda_n^2}\frac{du_n(r)}{dr}h_n(z)\Phi_m(\varphi) \tag{4.98}$$

and

$$v_\varphi(r,\varphi,z) = \frac{-m\omega}{\rho_0(z)c_{\rm A}^2(z)} \sum_{n=1}^{\infty} \frac{1}{\lambda_n^2} \frac{u_n(r)}{r} h_n(z)\Phi_m(\varphi). \tag{4.99}$$

4.4.1 Spatial structure along the magnetic field

First of all, notice that Eqs. (4.95) and (4.55) are identical, so the solutions described in Sect. 4.3.1 can also be applied to this problem. Therefore, the z-eigenfunctions satisfy Eq. (4.59), namely

$$\frac{d^2 h_n^{(\rm j)}}{dz^2} + \frac{\omega^2}{c_{\rm Aj}^2(z)} h_n^{(\rm j)} = -(\lambda_n^{(\rm j)})^2 h_n^{(\rm j)}. \tag{4.100}$$

Eq. (4.100) can be solved using analytical or numerical techniques, depending on the Alfvén speed profile of the equilibrium model. Here we only remark that due to the line-tying boundary condition (Eq. 4.57) the set of z-eigenfunctions forms a complete basis, so we can express the inner ones in terms of the outer ones in the form of Eq. (4.63), namely

$$h_n^{(\rm l)}(z) = \sum_{m=1}^{\infty} H_{nm} h_m^{(\rm c)}(z), \tag{4.101}$$

and that the basis functions are the same described in Sect. 4.3.1.

So far, Eqs. (4.92), (4.98) and (4.99) provide us with the functional form of the total pressure and velocity components in each of the regions present in our equilibrium. Next, appropriate boundary conditions must be considered. This includes the evanescent wave condition (since only trapped waves are of interest in this section) and the line-tying condition at the surface $z = L$. As in the previous section, the basis functions in the coronal region are described in Eqs. (4.65)–(4.68) and the constant $\kappa_n^{(\rm c)}$ is defined again as

$$\kappa_n^{(\rm c)} = \frac{\omega^2}{c_{\rm Ac}^2} + {\lambda_n^{(\rm c)}}^2 \tag{4.102}$$

and the photospheric line-tying condition, once imposed on $h_n^{(\rm c)}(z)$ gives

$$\kappa_n^{(\rm c)} = \frac{2n-1}{2L}\pi, \ n = 1, 2, \ldots, \tag{4.103}$$

for even modes and

$$\kappa_n^{(\rm c)} = \frac{n}{L}\pi, \ n = 1, 2, \ldots, \tag{4.104}$$

for odd modes. Also, the existence of cut-off frequencies is found in cylindrical geometry.

4.4.2 Spatial structure across the magnetic field

Since Eq. (4.95) has been already solved, the remaining task is to solve Eqs. (4.93) and (4.94). We see that the φ-dependent function is simply

$$\Phi_m(\varphi) = e^{im\varphi},\ m = 0, 1, 2, \ldots, \tag{4.105}$$

and so Φ_m comes in the form of a Fourier decomposition that arises from the original equation after applying the separation of variables technique. It is remarkable that this kind of solution has not been imposed, but it comes naturally from the wave equations.

Regarding the radial dependence, when $\lambda_n^2 > 0$ the equation for the r-dependent part is a modified Bessel's equation of order m whose solution is

$$u_n(r) = B_{In} I_m(\lambda_n r) + B_{Kn} K_m(\lambda_n r). \tag{4.106}$$

On the other hand, when $\lambda_n^2 < 0$, Eq. (4.93) becomes Bessel's equation of order m and its solution can be written as

$$u_n(r) = B_{Jn} J_m(\lambda_n^* r) + B_{Yn} Y_m(\lambda_n^* r), \tag{4.107}$$

with $\lambda_n^* = i\lambda_n$ a real constant.

The azimuthal wavenumber, m, classifies the modes depending on their azimuthal dependence in Eq. (4.105) and also the order of the Bessel functions in Eqs. (4.106) and (4.107). These modes are commonly referred as sausage ($m = 0$), kink ($m = 1$) and fluting ($m \geq 2$) modes.

4.4.3 Dispersion relations

On the boundary $r = b$ the conditions are those of Eq. (4.40) and we use the identities

$$\rho_0 c_{\rm A}^2 \equiv \rho_{\rm c} c_{\rm Ac}^2 = \rho_{\rm l}(z) c_{\rm Al}(z)^2 \tag{4.108}$$

for relating the velocity components inside and outside the tube. We first note that the equalities in Eq. (4.40) must be satisfied for all φ, so the azimuthal "wavenumber", m, must be the same inside and outside the loop. In addition, the total pressure continuity at $r = b$ requires $h_n(z)$ to be continuous in the whole range $-L \leq z \leq L$, a requirement that cannot be fulfilled if the z-dependent part of $p_{\rm T}$ is given by just one basis function, since the "wavelengths" inside and outside the loop are different. This means that a solution to Eq. (4.23) cannot have such a simple z-dependence and that it must consist instead of a sum of all the basis functions $h_n(z)$, such as it was stated in Eq. (4.92). Taking into account that both $u_n(r)$ and $h_n(z)$ are mutually linked by a given separation constant, λ_n, such a sum has to necessarily include all the possible $u_n(r)$. Thus,

$$p_{\mathrm{T}}(r,\varphi,z) = \Phi_m(\varphi) \times \begin{cases} \displaystyle\sum_{n=1}^{\infty} u_n^{(\mathrm{l})}(r) h_n^{(\mathrm{l})}(z), & r \le -b, \\ \displaystyle\sum_{n=1}^{\infty} u_n^{(\mathrm{c})}(r) h_n^{(\mathrm{c})}(z), & r \ge b. \end{cases} \tag{4.109}$$

Next, a series expansion of the inner basis functions, $h_n^{(\mathrm{l})}(z)$, in terms of the outer ones, $h_n^{(\mathrm{c})}(z)$, is performed (Eq. 4.101). From Eq. (4.109), the expression $[p_{\mathrm{T}}] = 0$ at $r = b$ leads to

$$\sum_{n=1}^{\infty} u_n^{(\mathrm{c})}(b) h_n^{(\mathrm{c})}(z) = \sum_{s=1}^{\infty} u_s^{(\mathrm{l})}(b) \left[\sum_{n=1}^{\infty} H_{sn} h_n^{(\mathrm{c})}(z) \right]. \tag{4.110}$$

After gathering together the coefficients of the functions $h_n^{(\mathrm{c})}(z)$ we obtain

$$u_n^{(\mathrm{c})}(b) = \sum_{s=1}^{\infty} H_{sn} u_s^{(\mathrm{l})}(b), \tag{4.111}$$

for $n = 1, 2, \ldots$

Next, before imposing the condition $[v_r] = 0$, Eq. (4.98) must be written in a form similar to Eq. (4.109) To derive the perturbed velocity components we obtain with the help of Eq. (4.109)

$$v_r(r,\varphi,z) = -\frac{i\omega}{\rho_0 c_{\mathrm{Ac}}} \Phi_m(\varphi) \times \begin{cases} \displaystyle\sum_{n=1}^{\infty} \frac{1}{\lambda_n^{(\mathrm{l})2}} \frac{du_n^{(\mathrm{l})}(r)}{dr} h_n^{(\mathrm{l})}(z), & r \le b, \\ \displaystyle\sum_{n=1}^{\infty} \frac{1}{\lambda_n^{(\mathrm{c})2}} \frac{du_n^{(\mathrm{c})}(r)}{dr} h_n^{(\mathrm{c})}(z), & r \ge b, \end{cases} \tag{4.112}$$

$$v_\varphi(r,\varphi,z) = -\frac{m\omega}{\rho_0 c_{\mathrm{Ac}}} \Phi_m(\varphi) \times \begin{cases} \displaystyle\sum_{n=1}^{\infty} \frac{1}{\lambda_n^{(\mathrm{l})2}} \frac{u_n^{(\mathrm{l})}(r)}{r} h_n^{(\mathrm{l})}(z), & r \le b, \\ \displaystyle\sum_{n=1}^{\infty} \frac{1}{\lambda_n^{(\mathrm{c})2}} \frac{u_n^{(\mathrm{c})}(r)}{r} h_n^{(\mathrm{c})}(z), & r \ge b. \end{cases} \tag{4.113}$$

In addition, the factor i in Eq. (4.112) implies that v_r is not in phase with respect to p_{T} and v_φ, but advanced a quarter of a period. The presence of the factor m in Eq. (4.113) indicates that the sausage mode does not have an azimuthal velocity component, while all other modes have both components of the perturbed velocity. This can be also appreciated from Eqs. (4.36) and (4.37), which for $m \neq 0$ constitute a system of coupled partial differential equations for v_r and v_φ, while for $m = 0$ the system is uncoupled and gives place to fast and Alfvén modes with only r- and φ-components of the velocity, respectively (see Appendix E for further discussion on this topic).

Then, the continuity of v_r at this boundary implies

$$\frac{i\omega}{\rho_{\rm c}c_{\rm Ac}^2}\sum_{n=1}^{\infty}\frac{1}{\lambda_n^{({\rm c})2}}\frac{du_n^{({\rm c})}(b)}{dr}h_n^{({\rm c})}(z)=\frac{i\omega}{\rho_p c_{\rm Ap}^2}\sum_{s=1}^{\infty}\frac{1}{\lambda_s^{({\rm l})2}}\frac{du_s^{({\rm l})}(b)}{dr}\sum_{n=1}^{\infty}H_{sn}h_n^{({\rm c})}(z), \tag{4.114}$$

which upon using Eq. (4.108) reduces to

$$\frac{1}{\lambda_n^{({\rm c})2}}\frac{du_n^{({\rm c})}(b)}{dr}=\sum_{s=1}^{\infty}\frac{1}{\lambda_s^{({\rm l})2}}H_{sn}\frac{du_s^{({\rm l})}(b)}{dr}, \tag{4.115}$$

for $n=1,2,\ldots$ Probably, the most remarkable point about this equation is that it does not only involve the derivatives of the r-dependent functions, but also the "wavenumbers" $\lambda_n^{({\rm j})}$ in the loop and in the coronal environment. The two infinite sets of algebraic Eqs. (4.111) and (4.115) will next be used to obtain the dispersion relation.

We finally request that solutions do not diverge at $r=0$ and that are evanescent as $r\to\infty$. As a consequence, the coefficient B_K in Eq. (4.106) must vanish inside the loop while the coefficient B_I in the same formula must be zero in the coronal environment. Therefore, the r-dependent part of the solution can be written in the form

$$\begin{aligned} u_n^{({\rm l})}(r) &= B_n I_m(\lambda_n^{({\rm l})}r), \\ u_n^{({\rm c})}(r) &= C_n K_m(\lambda_n^{({\rm c})}r). \end{aligned} \tag{4.116}$$

In writing these expressions we have assumed that $\lambda_n^{({\rm l})2}$ and $\lambda_n^{({\rm c})2}$ are both positive, although $\lambda_n^{({\rm l})2}$ can be negative for some n (this issue is discussed below). The allowed range of frequencies for oscillatory modes can be derived by inserting the condition $\lambda_1^{({\rm c})2}>0$ into Eq. (4.102). We then get $\omega<\kappa_1^{({\rm c})}c_{\rm Ac}$ and, with the help of Eqs. (4.103) and (4.104), we obtain $\omega L/c_{\rm Ac}<\pi/2$ for even modes and $\omega L/c_{\rm Ac}<\pi$ for odd modes. Therefore, oscillatory modes are characterized by normalised frequencies below a cut-off value, namely $\pi/2$ and π for even and odd modes, respectively, while modes with frequency above these cut-offs are leaky.

To obtain the dispersion relation one just needs to insert the expressions for $u_n^{({\rm l})}(r)$ and $u_n^{({\rm c})}(r)$ from Eq. (4.116) into equations (4.111) and (4.115). Then it is possible to eliminate the constants C_n in favour of the constants B_n, so the following expression is derived

$$\sum_{s=1}^{\infty}H_{sn}\left\{\frac{1}{\lambda_n^{({\rm c})}}I_m(\lambda_s^{({\rm l})}b)K_m'(\lambda_n^{({\rm c})}b)-\frac{1}{\lambda_s^{({\rm l})}}K_m(\lambda_n^{({\rm c})}b)I_m'(\lambda_s^{({\rm l})}b)\right\}B_s=0, \tag{4.117}$$

where $n=1,2,\ldots$ and I_m' and K_m' represent the derivatives of the functions I_m and K_m. Just like in Cartesian geometry, we have obtained an infinite system of homogeneous algebraic equations for the quantities B_s, with coefficients that depend on ω through $\lambda_n^{({\rm c})}$, $\lambda_n^{({\rm l})}$ and the weights H_{sn}. The condition to have a non-trivial solution is that the determinant of this system vanishes, giving the dispersion relation which allows us to calculate the eigenvalues (ω) of the problem. Obviously, an infinite determinant is extremely difficult to handle, so we reduce it to

a finite one by taking $B_n = 0$ for $n > N$ so that we finally have to deal again with a $N \times N$ determinant.

Once the eigenfrequency has been obtained from Eq. (4.117), all the other quantities (i.e. $\lambda_n^{(c)}$, $\lambda_n^{(l)}$, $\kappa_n^{(p)}$ and $\kappa_n^{(e)}$, with $n = 1, 2, \ldots$) and basis functions (i.e. $u_n^{(c)}(r)$, $u_n^{(l)}(r)$, $h_n^{(c)}(z)$ and $h_n^{(l)}(z)$, with $n = 1, 2, \ldots$) can be computed. Notice that this procedure is very close to the one used in the Cartesian problem, the main difference being the presence of Bessel functions because of the considered cylindrical geometry.

The above procedure does not completely work in practice since at least the first inner eigenvalue satisfies $\lambda_1^{(l)2} < 0$. Therefore, we now assume that the first c parameters $\lambda_n^{(l)}$ are purely imaginary and define their corresponding $\lambda_n^{*(l)}$ as follows,

$$\lambda_n^{*(l)} = i\,\lambda_n^{(l)}, \quad n = 1, 2, \ldots, c. \tag{4.118}$$

Next, the manipulations that lead to Eq. (4.117) must be repeated by taking into account that $u_n^{(l)}(r)$ is given by Eq. (4.116) for $n > c$ and by

$$u_n^{(l)}(r) = B_n^* J_m(\lambda_n^{*(l)} r), \tag{4.119}$$

for $n = 1, 2, \ldots, c$. The Y_m contribution in the above formula has been eliminated so that solutions do not diverge at $r = 0$. An important consequence of this sum of ordinary and modified Bessel functions is that in the present configuration there are no longer pure "body" and "surface" modes, as in Edwin & Roberts (1983), but a mixture of them.

Finally, Eq. (4.117) becomes

$$\begin{aligned} &\sum_{s=1}^{c} H_{sn} \left\{ \frac{1}{\lambda_n^{(c)}} J_m(\lambda_s^{*(l)} b) K_m'(\lambda_n^{(c)} b) + \frac{1}{\lambda_s^{*(l)}} K_m(\lambda_n^{(c)} b) J_m'(\lambda_s^{*(l)} b) \right\} B_s^* \\ &+ \sum_{s=c+1}^{\infty} H_{sn} \left\{ \frac{1}{\lambda_n^{(c)}} I_m(\lambda_s^{(l)} b) K_m'(\lambda_n^{(c)} b) - \frac{1}{\lambda_s^{(l)}} K_m(\lambda_n^{(c)} b) I_m'(\lambda_s^{(l)} b) \right\} B_s = 0. \end{aligned} \tag{4.120}$$

The number of imaginary "wavelengths" in the radial direction depends on the values of the parameters of the equilibrium model (usually $c = 1$ is obtained).

4.5 Examples of spatial dependence along the magnetic field

As an example, the functional dependence along the magnetic field (Eq. 4.59) can be studied in some equilibrium configurations described in Chapter 3 that will be applied later in this work to model structures in the solar corona.

4.5.1 The homogeneous structure

The analytical method can be checked in a well-known situation: the *homogeneous flux tube* (Fig. 3.2). Here we consider a structure filled with material denser than the surrounding coronal plasma. In this configuration there is no inhomogeneity in the z-direction other than the photosphere (all the lengths could be re-scaled against the magnetic supporting structure length L), so the model is similar to the magnetic slab described in Chapter 2 (with the low-β plasma assumption).

Now the Alfvén profile in Eq. (4.43) is just $c_{\rm Al}$ inside the tube and $c_{\rm Ac}$ outside it, with no dependence on the z-coordinate. The basis functions coming from solving Eq. (4.59) in the coronal region are described in Eqs. (4.65)–(4.68) Inside the structure, solutions are the same except for the separation constant $\lambda^{(\rm I)}$, in which $c^2_{\rm Ac}$ is substituted by $c^2_{\rm Al}$, that is

$$h^{(\rm I)}_{2n-1} = \frac{1}{L^{1/2}} \cos \frac{(2n-1)\pi z}{2L} = \frac{1}{L^{1/2}} \cos \kappa_{2n-1} z, \tag{4.121}$$

$$\left(\lambda^{(\rm I)}_{2n-1}\right)^2 = \kappa^2_{2n-1} - \frac{\omega^2}{c^2_{\rm Al}} = \frac{\pi^2 (2n-1)^2}{4L^2} - \frac{\omega^2}{c^2_{\rm Al}}, \tag{4.122}$$

for even modes and

$$h^{(\rm I)}_{2n} = \frac{1}{L^{1/2}} \sin \frac{n\pi z}{L} = \frac{1}{L^{1/2}} \sin \kappa_{2n} z, \tag{4.123}$$

$$\left(\lambda^{(\rm I)}_{2n}\right)^2 = \kappa^2_{2n} - \frac{\omega^2}{c^2_{\rm Al}} = \frac{\pi^2 n^2}{L^2} - \frac{\omega^2}{c^2_{\rm Al}}, \tag{4.124}$$

for odd modes. In Eqs.(4.121)–(4.124) the line-tying boundary condition has been imposed to find the values of the constants κ_n, which are equal inside and outside the structure,

$$\kappa_n = \frac{\pi (n+1)}{2L}, \tag{4.125}$$

and the requirement of orthonormal basis functions of Eq. (4.62) has been used to find the constants that multiply the sine and cosine functions.

The next step is to write the inner basis functions in terms of the outer ones. In this problem this is accomplished easily because $h^{(\rm I)}_n(z) = h^{(\rm c)}_n(z)$ so the coefficients in Eq. (4.63), calculated with the help of Eq. (4.64) and using the fact that the two sets are orthonormal basis, are just

$$H_{nm} = \delta_{nm} = \begin{cases} 1, & n = m, \\ 0, & n \neq m. \end{cases} \tag{4.126}$$

One might expect this result, since it only states that in this simple problem it is not necessary to use the sum of Eq. (4.48), but it is enough to use only the same eigenfunction inside and outside because the ordinary differential equation for $h_n(z)$ is exactly the same in both regions. Finally,

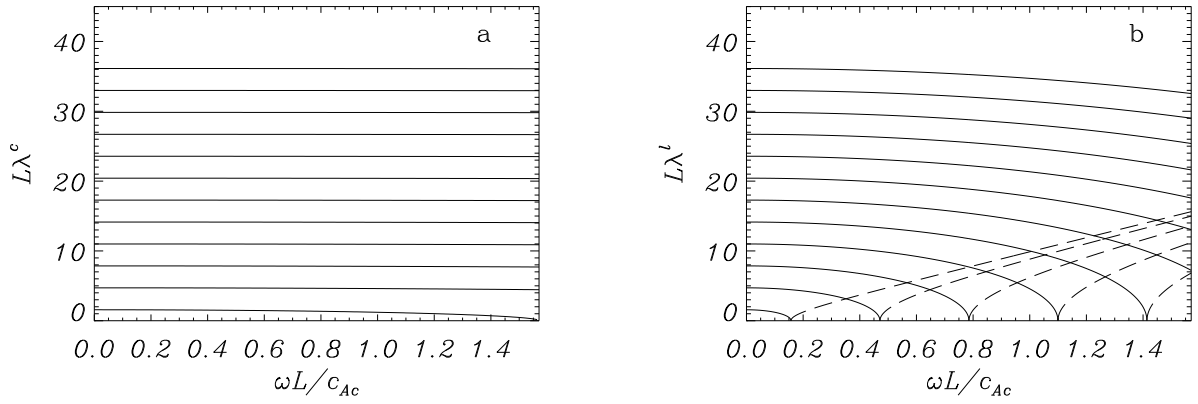

Figure 4.1: Homogeneous structure: plot of the the lowest 12 even eigenvalues **a)** $\lambda^{(c)}L$ (outer region) and **b)** $\lambda^{(1)}L$ (inner region) against frequency for a structure 10 times denser than its surroundings. Solid lines are for real $\lambda^{(j)}L$, while dashed lines represent a eigenvalue when it becomes complex, so then $\lambda^{(1)*}L = i\lambda^{(1)}L$ is plotted instead. Notice that $\lambda_1^{(1)}L$ goes to zero when $\omega L/c_{\rm Ac} \to 0$, a result which will be very important in the discussion of the dispersion relations of the models.

the eigenvalues are represented in Fig. 4.1. It is not necessary to plot the spatial dependence of the basis functions, since the they are simply Fourier basis functions: sine and cosine functions with the appropriate wavelength to satisfy the line-tying boundary conditions.

4.5.2 Structure with density enhancement

We next turn our attention to the fibril model described in Sect. 3.3 and shown in Figs. 3.6 and 3.8. First of all, the Alfvén speed is $c_{\rm Ac}$ outside the fibril, whereas inside it is defined as

$$c_{\rm Al}(z) = \begin{cases} c_{\rm Ap}, & |z| < W, \\ c_{\rm Ae}, & W < |z| < L, \end{cases} \tag{4.127}$$

where the subindex "e" marks quantities in the evacuated part of the slab and "p" marks quantities in the prominence (dense) part. In this section $c_{\rm Ac}$, $c_{\rm Ap}$ and $c_{\rm Ae}$ are constant and $c_{\rm Ap} < c_{\rm Ae}$. The solution in the coronal region is again described in Eqs. (4.65) and (4.68). The following quantities are also defined in the coronal region,

$$\kappa_{\rm c}^{\rm od} = \frac{\pi(2n-1)}{2L}, \qquad \kappa_{\rm c}^{\rm ev} = \frac{\pi n}{L}. \tag{4.128}$$

Now we concentrate in solving Eq. (4.59) in the fibril region, so we start looking for the most suitable form of our boundary conditions. First of all, the line-tying boundary condition Eq. (4.57) is applied. Since the perturbed velocity has contributions from all the basis functions $h_n^{(j)}(z)$ (Eq. 4.48), this condition requires that $h_n^{(1)}(\pm L) = 0$, so the basis function can be written as

$$h_n^{(1)}(z) = \begin{cases} C_- \sin[\kappa_{\rm e}(z+L)], & -L < z < -W, \\ D_{\cos}\cos(\kappa_{\rm p} z) + D_{\sin}\sin(\kappa_{\rm p} z), & -W < z < W, \\ C_+ \sin[\kappa_{\rm e}(z-L)], & W < z < L, \end{cases} \tag{4.129}$$

where

$$\kappa_{\rm p}^2 = {\lambda^{(1)}}^2 + \frac{\omega^2}{c_{\rm Ap}^2}, \quad \kappa_{\rm e}^2 = {\lambda^{(1)}}^2 + \frac{\omega^2}{c_{\rm Ae}^2}. \tag{4.130}$$

In these equations and in the following, the subscript n has been dropped in the quantities $\kappa_{\rm p}, \kappa_{\rm e}, \kappa_{\rm c}, C_-, C_+, D_{\cos}, D_{\sin}$ and $\Lambda_{\rm ev}, \Lambda_{\rm od}$ (see below) to simplify the notation.

In Eq. (4.129) we have assumed that the infinite values of $\kappa_{\rm p}$ and $\kappa_{\rm e}$ satisfy $\kappa_{\rm p}^2 > 0$ and $\kappa_{\rm e}^2 > 0$, but these requirements are not necessarily fulfilled. In the parameter range of interest, $\kappa_{\rm p}^2 > 0$ holds ($c_{\rm Ap}^{-2} \sim \rho_{\rm p}$, so the term with ω in Eq. 4.130 is positive and large), while the sign of $\kappa_{\rm e}^2$ can be arbitrary, so $\kappa_{\rm e}$ is either real and positive or purely imaginary with positive imaginary part. Nevertheless, in our model at least the fundamental basis function has $\kappa_{\rm e}^2 < 0$ (and depending on the choice of parameters, this can be true for other harmonics too), so Eq. (4.129) should be written in terms of hyperbolic functions for this basis function. The general expression that takes into account this possibility is derived the Appendix D, but here we continue with the assumption $\kappa_{\rm e}^2 > 0$.

On the other hand, on the boundaries $z = \pm W$ the dot product of the equilibrium magnetic field and the normal is not zero, so the boundary conditions that must be applied are Eqs. (2.27), which are more restrictive than Eqs. (4.40) (see Appendix B), namely,

$$[\mathbf{v}] = \mathbf{0}, \quad [\mathbf{B}] = \mathbf{0}, \quad [p] = 0. \tag{4.131}$$

Using Eqs. (4.48) and (4.52) these conditions imply the continuity of each of the functions $h_n^{(1)}$ and their derivatives at this boundary. Since one of the coefficients in Eq. (4.55) for $h_n^{(1)}(z)$ is discontinuous, the second derivative of $h_n^{(1)}(z)$ is also discontinuous, while its first derivative and the function itself are continuous. The continuity conditions at $z = \pm W$ lead to

$$\begin{aligned} C_- \sin[\kappa_{\rm e}(L-W)] &= D_{\cos}\cos(\kappa_{\rm p} W) - D_{\sin}\sin(\kappa_{\rm p} W), & (4.132)\\ \kappa_{\rm e} C_- \cos[\kappa_{\rm e}(L-W)] &= \kappa_{\rm p}[D_{\cos}\sin(\kappa_{\rm p} W) + D_{\sin}\cos(\kappa_{\rm p} W)], & (4.133)\\ -C_+ \sin[\kappa_{\rm e}(L-W)] &= D_{\cos}\cos(\kappa_{\rm p} W) + D_{\sin}\sin(\kappa_{\rm p} W), & (4.134)\\ \kappa_{\rm e} C_+ \cos[\kappa_{\rm e}(L-W)] &= \kappa_{\rm p}[-D_{\cos}\sin(\kappa_{\rm p} W) + D_{\sin}\cos(\kappa_{\rm p} W)]. & (4.135) \end{aligned}$$

These expressions constitute a system of linear homogeneous equations with respect to C_-, C_+, $D_{\cos}$ and $D_{\sin}$, and has a non-trivial solution only if its determinant is zero, which gives

$$\begin{aligned} \kappa_{\rm p}^2 \sin^2[\kappa_{\rm e}(L-W)]\sin(2\kappa_{\rm p} W) & -\kappa_{\rm p}\kappa_{\rm e}\sin[2\kappa_{\rm e}(L-W)]\cos(2\kappa_{\rm p} W)] \\ & -\kappa_{\rm e}^2\cos^2[\kappa_{\rm e}(L-W)]\sin(2\kappa_{\rm p} W) = 0. \end{aligned} \tag{4.136}$$

There are two ways the previous equality can be satisfied,

$$\kappa_{\rm p}\tan(\kappa_{\rm p}W) = \kappa_{\rm e}\cot[\kappa_{\rm e}(L-W)] \tag{4.137}$$

or

$$\kappa_{\rm p}\cot(\kappa_{\rm p}W) = -\kappa_{\rm e}\cot[\kappa_{\rm e}(L-W)], \tag{4.138}$$

which are just Eqs. (22) and (23) in Joarder et al. (1997). It is straightforward to show that Eq. (4.138) corresponds to solutions to the system of Eqs. (4.132)–(4.135) with $D_{\rm sin} = 0$ and $C_+ = -C_-$, i.e. to even solutions with respect to the z-coordinate, while Eq. (4.137) corresponds to solutions with $D_{\rm cos} = 0$ and $C_+ = C_-$, i.e. to odd solutions. According to the general theory of Sturm-Liouville problems, Eq. (4.137), considered as an equation for $(\lambda^{(\rm l)})^2$, has an infinite set of solutions $\{(\lambda^{(\rm l)}_{2n-1})^2\}$ such that $(\lambda^{(\rm l)}_{2n-1})^2 \to \infty$ as $n \to \infty$. Eq. (4.138), considered as an equation for $(\lambda^{(\rm l)})^2$, also has an infinite set of solutions $\{(\lambda^{(\rm l)}_{2n})^2\}$ such that $(\lambda^{(\rm l)}_{2n})^2 \to \infty$ as $n \to \infty$. In addition, $(\lambda^{(\rm l)}_{2n-1})^2 < (\lambda^{(\rm l)}_{2n})^2 < (\lambda^{(\rm l)}_{2n+1})^2$ for $n = 1, 2, \ldots$ Notice that in both cases the eigenvalues $\lambda^{(\rm l)}_n$ depend on ω.

The even eigenfunctions are given by

$$h^{(\rm l)}_{2n-1}(z) = \Lambda_{\rm ev}\begin{cases}\cos(\kappa_{\rm p}W)\sin[\kappa_{\rm e}(L+z)], & -L < z < -W,\\ \sin[\kappa_{\rm e}(L-W)]\cos(\kappa_{\rm p}z), & -W < z < W,\\ \cos(\kappa_{\rm p}W)\sin[\kappa_{\rm e}(L-z)], & W < z < L,\end{cases} \tag{4.139}$$

and the odd ones by

$$h^{(\rm l)}_{2n}(z) = \Lambda_{\rm od}\begin{cases}-\sin(\kappa_{\rm p}W)\sin[\kappa_{\rm e}(L+z)], & -L < z < -W,\\ \sin[\kappa_{\rm e}(L-W)]\sin(\kappa_{\rm p}z), & -W < z < W,\\ \sin(\kappa_{\rm p}W)\sin[\kappa_{\rm e}(L-z)], & W < z < L.\end{cases} \tag{4.140}$$

The coefficients $\Lambda_{\rm ev}$ and $\Lambda_{\rm od}$ are determined by the normalization condition $\|h^{(\rm l)}_{2n-1}\| = \|h^{(\rm l)}_{2n}\| = 1$ in Eq. (4.62), i.e.

$$\int_{-L}^{L}[h^{(\rm l)}_{2n-1}(z)]^2\,dz = \int_{-L}^{L}[h^{(\rm l)}_{2n}(z)]^2\,dz = 1. \tag{4.141}$$

We can evaluate these coefficients by using Eqs. (4.139) and (4.140) to obtain the expressions

$$\begin{aligned}\Lambda_{\rm ev}^{-2} = (L-W)\cos^2(\kappa_{\rm p}W) &+ W\sin^2[\kappa_{\rm e}(L-W)] - \frac{1}{2\kappa_{\rm e}}\cos^2(\kappa_{\rm p}W)\sin[2\kappa_{\rm e}(L-W)]\\ &+ \frac{1}{2\kappa_{\rm p}}\sin^2[\kappa_{\rm e}(L-W)]\sin(2\kappa_{\rm p}W),\end{aligned} \tag{4.142}$$

$$\Lambda_{\rm od}^{-2} = (L-W)\sin^2(\kappa_{\rm p}W) \quad + \quad W\sin^2[\kappa_{\rm e}(L-W)] - \frac{1}{2\kappa_{\rm e}}\sin^2[\kappa_{\rm p}W]\sin[2\kappa_{\rm e}(L-W)]$$
$$- \quad \frac{1}{2\kappa_{\rm p}}\sin^2[\kappa_{\rm e}(L-W)]\sin(2\kappa_{\rm p}W). \tag{4.143}$$

The next step is to express the inner basis of functions in terms of the outer one. To achieve this we need to calculate the "Fourier coefficient" from Eq. (4.64). It is straightforward to check that even and odd parities are never mixed, i.e.

$$H_{2n,2m-1} = 0, \;\; m,n \in \mathcal{N}. \tag{4.144}$$

The other coefficients are given by

$$H_{2n,2m} = \Lambda_{\rm od}L^{-\frac{1}{2}}\left\{\sin[\kappa_{\rm e}(L-W)]\left(\frac{\sin[(\kappa_{\rm p}-\kappa_{\rm c}^{\rm od})W]}{\kappa_{\rm p}-\kappa_{\rm c}^{\rm od}} - \frac{\sin[(\kappa_{\rm p}+\kappa_{\rm c}^{\rm od})W]}{\kappa_{\rm p}+\kappa_{\rm c}^{\rm od}}\right)\right.$$
$$\left. + \sin[\kappa_{\rm p}W]\left(\frac{\sin[\kappa_{\rm e}(L-W)-\kappa_{\rm c}^{\rm od}W]}{\kappa_{\rm e}+\kappa_{\rm c}^{\rm od}} - \frac{\sin[\kappa_{\rm e}(L-W)+\kappa_{\rm c}^{\rm od}W]}{\kappa_{\rm e}-\kappa_{\rm c}^{\rm od}}\right)\right\}, \tag{4.145}$$

$$H_{2n-1,2m-1} = \Lambda_{\rm ev}L^{-\frac{1}{2}}\left\{\sin[\kappa_{\rm e}(L-W)]\left(\frac{\sin[(\kappa_{\rm p}-\kappa_{\rm c}^{\rm ev})W]}{\kappa_{\rm p}-\kappa_{\rm c}^{\rm ev}} + \frac{\sin[(\kappa_{\rm p}+\kappa_{\rm c}^{\rm ev})W]}{\kappa_{\rm p}+\kappa_{\rm c}^{\rm ev}}\right)\right.$$
$$\left. + \cos[\kappa_{\rm p}W]\left(-\frac{\cos[\kappa_{\rm e}(L-W)-\kappa_{\rm c}^{\rm ev}W]}{\kappa_{\rm e}+\kappa_{\rm c}^{\rm ev}} - \frac{\cos[\kappa_{\rm e}(L-W)+\kappa_{\rm c}W]}{\kappa_{\rm e}-\kappa_{\rm c}^{\rm ev}}\right)\right\}, \tag{4.146}$$

where $\kappa_{\rm c}$, $\kappa_{\rm e}$ and $\kappa_{\rm p}$ are defined in Eqs. (4.128) and (4.130), with the appropriate values of $\lambda_n^{(\rm j)}$. Expressions for these quantities when at least one of the $\kappa_{\rm e}$ is imaginary are given in Appendix D.

The coronal basis functions are a simple Fourier basis (sines and cosines), so we concentrate on the inner ones. The inner basis depend on the frequency of the mode, so for a given set of parameters there is a different basis for each frequency. First we need to solve Eq. (4.137) for odd modes or (4.138) for even modes. We shall concentrate here on the even ones, but the description of the odd ones is very similar. The values of $\lambda^{(\rm l)}$ are plotted in Fig. 4.2 for two set of the parameters and it can be appreciated that as $\rho_{\rm p}/\rho_{\rm c}$ is raised more basis functions have imaginary $\lambda^{(\rm l)}$. A similar effect is observed when increasing W/L.

Now, if for a selected frequency all the coefficients can be calculated. As an example, in Fig. 4.3 the basis functions for the two sets of parameters used in Fig. 4.2 and two arbitrarily chosen frequencies are plotted. It is interesting to remark that with this particular basis the dispersion relations may not be satisfied, since the frequency may be the wrong one. In Fig. 4.3a there is only one basis function that satisfies $\kappa_{\rm e}^2 < 0$, the typical situation for the realistic range of parameters. In Fig. 4.3b a different situation is plotted, with two basis functions satisfying $\kappa_{\rm e}^2 < 0$ and hence with different spatial dependence, while the other basis functions have a very small amplitude in the inner region.

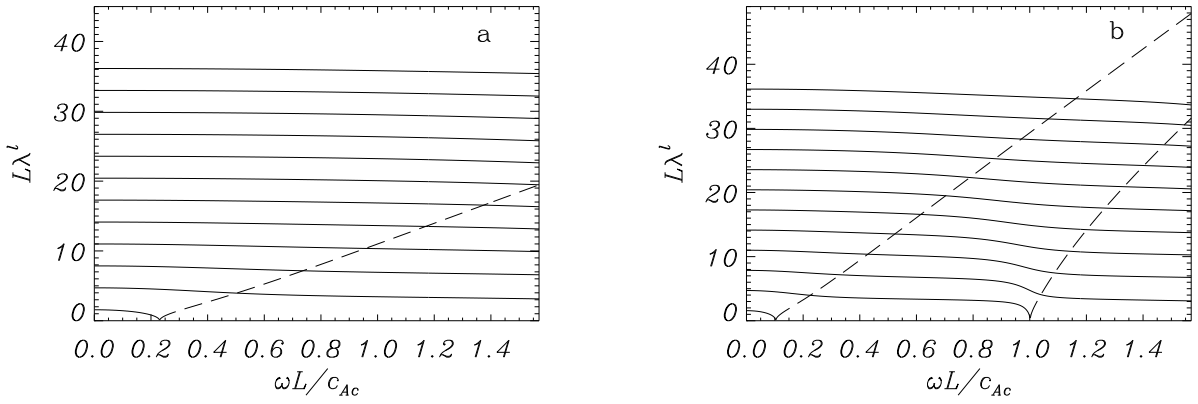

Figure 4.2: Structure with density enhancement: plot of the the lowest 12 eigenvalues $\lambda^{(l)}L$ against frequency for the parameters **a)** $\rho_p/\rho_c = 200$, $\rho_e/\rho_c = 0.6$, $W/L = 0.1$ and **b)** $\rho_p/\rho_c = 1000$, $\rho_e/\rho_c = 1$, $W/L = 0.1$. Solid lines are for real $\lambda^{(l)}L$, while dashed lines represent an eigenvalue when $\kappa_e^2 < 0$ in Eq. (4.130), so then $\lambda^{(l)*}L = i\lambda^{(l)}L$ is plotted instead.

4.5.3 Models with other dependences

The above analytical procedure can be applied to other types of configurations, like the ones presented in Sect. 3.2, in which the Alfvén speed depends on the coordinate z. Therefore, Eq. (4.59) has to be solved for a given Alfvén speed profile $c_A(z)$.

First of all, there are other profiles that lead to analytical expressions to this eigenvalue problem, like the ones developed in Edwin & Roberts (1988) and Nakariakov & Roberts (1995) (although in the direction across the magnetic field and without line-tying) which could be adapted to our models. However, we find quite more interesting to use other kind of profiles, the ones derived from the equilibrium configurations described in Sect. 3.2.3. For that kind of profiles is quite more convenient to solve numerically the $1D$ eigenvalue problem rather than to solve directly the resulting partial differential equations. This procedure gives an approximation to the sets $\{h_n^{(c)}(z)\}$ and $\{\lambda_n^{(c)}\}$ and then use a numerical integration algorithm to calculate the coefficients H_{nm} of Eq. (4.64). The code is based in the NAG routines, in particular, the routine D02KEF for solving the eigenvalue problem, D01GAF for performing the necessary numerical integrations, C05ADF for solving algebraic equations and other routines to calculate the values of Bessel functions and to evaluate the determinants. This code results to be quite robust, allowing for discontinuities along the loop in the Alfvén speed profile or singularities in the boundaries.

As an example, we can work out the eigenvalues of the constant heating problem of Sect. 3.2.3. We just need the Alfvén speed profile as a function of the coordinate along the loop. The results are plotted in Fig. 4.4, while the corresponding eigenfunctions for a given frequency value are represented in Fig. 4.5. Regarding this plot, the similarity with the standard Fourier basis is quite remarkable.

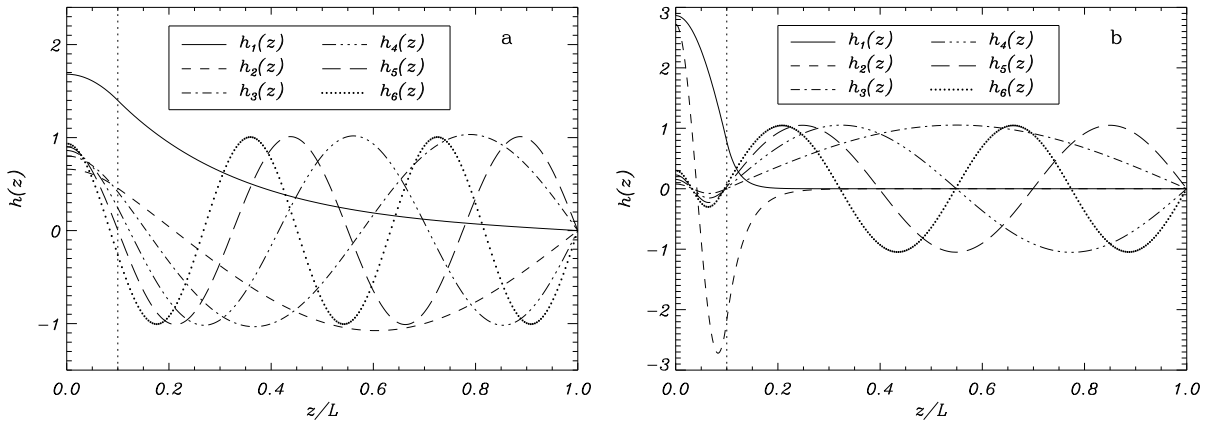

Figure 4.3: Plot of the 6 basis functions $h_n^{(1)}(z)$ with the lowest eigenvalues in Fig. 4.2. The parameters are **a)** $\rho_{\rm p}/\rho_{\rm c} = 200$, $\rho_{\rm e}/\rho_{\rm c} = 0.6$, $W/L = 0.1$ and $\omega L/v_{\rm Ac} = 0.5$ and **b)** $\rho_{\rm p}/\rho_{\rm c} = 1000$, $\rho_{\rm e}/\rho_{\rm c} = 1$, $W/L = 0.1$ and $\omega L/v_{\rm Ac} = 1.5$ ($\rho_{\rm p}/\rho_{\rm c}$ and $\omega L/v_{\rm Ac}$ have been selected to have high values to show a different case). In **a)** only the first basis function, $h_1(z)$, is behaving as in Appendix D, while in **b)** the first two $h_1(z)$ and $h_2(z)$ are like this, all the others being described by the expressions in this section. The boundary of the dense part ($z = W$) is marked with a vertical dotted line. Notice that the order of each basis function can be easily identified by the number of extrema it displays.

4.6 Conclusions

Putting all together, a procedure has been explained to find the dispersion relations for the stationary oscillatory modes of plasma structures in Cartesian and cylindrical geometry. The most relevant features of the analytical solution developed in this Chapter are:

- A single partial differential equation for the total pressure (Eq. 4.23) has been derived for the fast MHD modes.
- Separation of variables is performed, leading to an eigenvalue problem.
- Boundary conditions (involving also perturbed velocity components) make necessary to use a sum of all the eigenfunctions to represent the perturbed variables. Therefore, the whole solution is no longer separable.
- A system of algebraic equations is obtained for the amplitude coefficients of the eigenfunctions. The condition the for existence of a non-trivial solution is that the determinant of the system vanishes. This condition is then the dispersion relation of the modes.
- Once an equilibrium profile in the direction along the field is prescribed, the frequencies and spatial distributions can be computed.

The following Chapters are devoted to the application of these results, taking into account suitable equilibrium models for different solar structures.

It is also very remarkable that the dependent variables are not in phase. In fact, the perturbed pressure is in opposition of phase with respect to one of the perpendicular components of

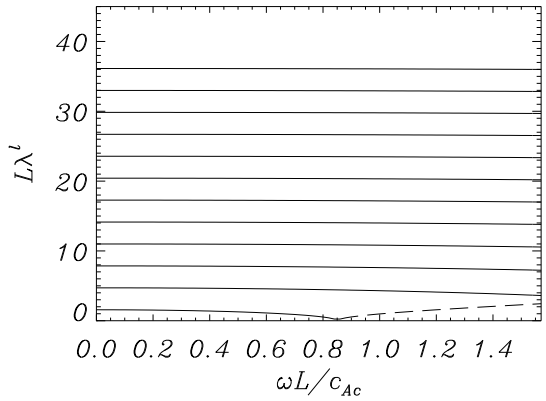

Figure 4.4: Structure with other spatial dependence: plot of the the lowest 12 even eigenvalues $\lambda^{(1)}L$ (inner region) against frequency for a structure 10 times denser than its surroundings and a heating parameter of $\hat{H} = 100$. Solid lines are for real $\lambda^{(j)}L$, while dashed lines represent the eigenvalue when it becomes complex, so $\lambda^{(1)*}L = i\lambda^{(1)}L$ is plotted then.

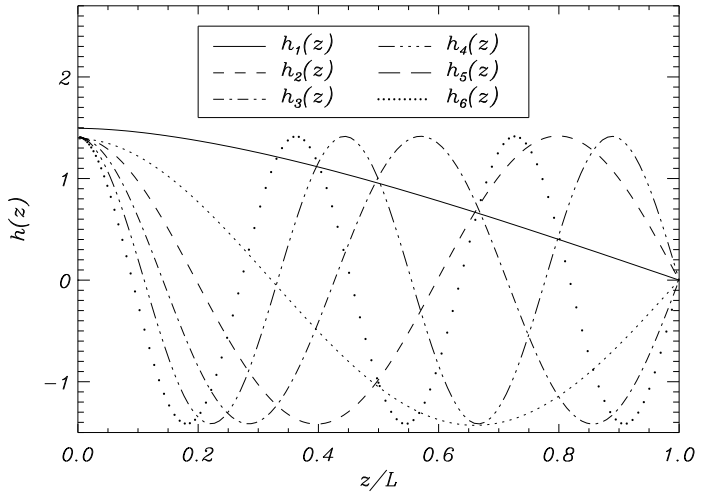

Figure 4.5: Plot of the 6 basis functions $h_n^{(1)}(z)$ with the lowest eigenvalues in Fig. 4.4. The parameters are $\rho_l/\rho_c = 10$, $\bar{H} = 100$ and $\omega L/v_{Ac} = 1$. Only the first basis function $h_1^{(1)}(z)$ is behaving as in Appendix D , all the others being described by the expressions in this section. Notice that the order of the basis function can be easily identified by the number of extrema it displays.

the perturbed velocity due the minus sign in Eqs. (4.54) or (4.113), and displaced a quarter of a period with respect to the other component due the imaginary factor in Eqs. (4.53) or (4.112). This is an important result, since the total pressure is related to the density perturbation by Eq.(4.28), which is related in turn with the intensity emitted by the loops, while the perpendicular component of the perturbed velocity is measured using the Doppler effect. Thus, signatures of stationary waves could be detected due to this phase shift (which can be measured, see for example Molowny-Horas et al. (1997)). This conclusion has also been found in other problems Sakurai et al. (2002), Ofman & Wang (2002) and has been pointed out in observational works (like Wang et al. (2003a)).

Chapter 5

Fast Magnetohydrodynamic waves in line-tied coronal loops *

If you love what you do, it will never be a job.

Confucius

Our first application of the procedure that has been explained in the last Chapter is to find the oscillatory modes of a coronal flux tube. The reason is that this model is an starting point for other applications and, moreover, it is a first step to compare with observational and previous works. At first, we are going to apply it to homogeneous coronal tubes, that is, the structure has cylindrical geometry and has no dependence of the equilibrium parameters along the loop. In this simple model the leaky modes can also be studied, even being restricted to practical applications by the fact that we are still studying only stationary modes, whereas the fully temporal dependence should be taken into account. However, further insight is achieved for other situations in which these modes are quite more difficult to determine, and specially, to compute. For these reasons, in one of the sections of this Chapter we drop the restriction of demanding real eigenfrequencies in the temporal dependence of the magnitudes of Eq. (2.20).

After that, we extend the oscillatory analysis to more complicated equilibrium loop models. Here we will concentrate on the effects in the modes introduced by non-uniform equilibrium profiles (along the loop axis) due to heating. The heating function is assumed to be time independent, but may depend on the spatial coordinate along the loop.

*This Chapter is based on: Díaz, A. J., Oliver, R., Ballester, J. L., & Roberts, B. 2004, "Fast MHD Oscillations in line-tied homogeneous coronal loops", A&A, submitted and Díaz, A. J., Oliver, R., & Ballester, J. L. 2004, "Fast MHD Oscillations in coronal loops with heating profiles", in preparation.

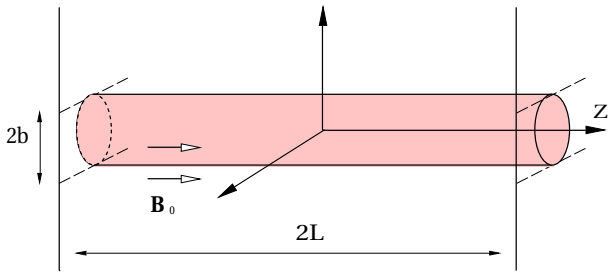

Figure 5.1: Sketch of the equilibrium configuration of a straightened flux tube, in which the grey zone represents the hot and dense plasma of the loop. The density inside the loop is $\rho_{\rm l}$ and in the coronal environment $\rho_{\rm c}$, while the tube footpoints are located in the photosphere (and subject to line-tying) at the positions $z = \pm L$, so its length is $2L$. The magnetic field is uniform and parallel to the z-axis, and the whole configuration is invariant in the φ-direction.

5.1 Homogeneous line-tied coronal loops

5.1.1 Equilibrium model and dispersion relations

The equilibrium configuration consists of a single homogeneous straight flux tube of length $2L$ embedded in a magnetic environment (Fig. 5.1). The magnetic field is uniform and parallel to the z-axis ($\mathbf{B}_0 = B_0\hat{\mathbf{z}}$) and the plasma density inside the loop is $\rho_{\rm l}$, while in the surrounding coronal medium is $\rho_{\rm c}$. Finally, the radius of the tube is b. Notice that in this simple model the temperature and pressure of the loop are not relevant, it is just necessary to assume they are constant (for a more detailed discussion about the equilibrium profile of coronal loops see Priest et al. (2000), Aschwanden & Schrijver (2002) and Testa, Peres & Reale (2002)).

The starting point are the linearized MHD equations for adiabatic perturbations in a uniform, static plasma with unperturbed density ρ_0 and equilibrium magnetic field B_0 pointing along the tube axis. In this configuration, the magnetic field and pressure perturbations, $\mathbf{B}$ and p, are eliminated in favor of the velocity and total pressure perturbations, $\mathbf{v}$ and $p_{\rm T}$ (see Chapter 4). In the solar corona (and also in coronal loops) the plasma β is much less than 1 (of the order of 10^{-3}), so we can restrict ourselves to perturbations in a low-beta plasma. In the present configuration, selecting the velocity components as our dependent variables leads to a pair of coupled partial differential equations, although it is possible to write our expressions in terms of the total pressure perturbation, $p_{\rm T}$, and have only one partial differential equation with one dependent variable to solve; for this reason, $p_{\rm T}$ will be our main dependent variable in the following. Also notice that the slow mode is absent in this low-β plasma limit and we have $v_z = 0$ (see Chapter 4). Now, the following partial differential equations are derived for the total pressure perturbation and the velocity components perpendicular to $\mathbf{B}_0$ (the later are necessary, since some of the jump conditions involve these quantities),

$$\left(\frac{\partial^2}{\partial t^2} - c_{\rm A}^2\nabla^2\right) p_{\rm T} = 0, \tag{5.1}$$

$$\rho_0\left(\frac{\partial^2}{\partial t^2} - c_{\rm A}^2\frac{\partial^2}{\partial z^2}\right)\mathbf{v}_\perp + \nabla_\perp\frac{\partial p_{\rm T}}{\partial t} = 0. \tag{5.2}$$

$p_{\rm T}$ has to be determined from Eq. (5.1) in order to calculate the spatial velocity distribution from Eq. (5.2); these solutions are the *fast modes* and it is remarkable that some of the observational reports of oscillations in coronal loops seem to be signatures of fast waves, so we are going to concentrate on studying them in the present Chapter.

Since we are looking for stationary states, the time component is Fourier-analysed in the form $e^{-i\omega t}$ (Eq. 2.20), and therefore our aim is to calculate the set of allowed frequencies for the model. The standard method for solving this kind of equations in a region with boundaries is separation of variables, which leads to

$$p_{\rm T}(r,\varphi,z) = \Phi_m(\varphi) \times \begin{cases} \displaystyle\sum_{n=1}^{\infty} u_n^{(\rm l)}(r) h_n^{(\rm l)}(z), & r \le -b, \\ \displaystyle\sum_{n=1}^{\infty} u_n^{(\rm c)}(r) h_n^{(\rm c)}(z), & r \ge b. \end{cases} \tag{5.3}$$

This expression, introduced into Eq. (5.1), results in the following differential equations,

$$\frac{1}{r}\frac{d}{dr}\left(r\frac{du_n(r)}{dr}\right) - \left(\lambda_n^2 + \frac{m^2}{r^2}\right) u_n(r) = 0, \tag{5.4}$$

$$\frac{d^2\Phi_m(\varphi)}{d\varphi^2} = -m^2\Phi_m(\varphi) \Rightarrow \Phi(\varphi) = e^{im\varphi},\ m = 0,1,2,\ldots, \tag{5.5}$$

$$\left(\frac{d^2}{dz^2} + \frac{\omega^2}{c_{\rm A}^2}\right) h_n(z) = -\lambda_n^2 h_n(z), \tag{5.6}$$

Now, if there is no inhomogeneity in the z-direction (along the magnetic field), from Eq. (5.6) it immediately follows that the z-dependent part of $p_{\rm T}$ is in the form of trigonometric functions, as it was stated in Section 4.4.1, namely

$$h_n(z) = \frac{1}{\sqrt{L}} \cos \kappa_n z, \tag{5.7}$$

$$h_n(z) = \frac{1}{\sqrt{L}} \sin \kappa_n z, \tag{5.8}$$

for even and odd modes about $z = 0$, respectively, where the wavenumber κ is defined as

$$\kappa_n^2 = \lambda_n^2 + \frac{\omega^2}{c_{\rm A}^2}. \tag{5.9}$$

The photospheric line-tying boundary condition on the surfaces $z = \pm L$ ($p_{\rm T}(\pm L) = 0$, Eq. 4.58) leads to the quantization of κ in the form

$$\kappa_n = \frac{(n+1)\pi}{2L}, \quad n = 0,1,2,\ldots, \tag{5.10}$$

for even or odd modes about $z = 0$ when the number n is even or odd, respectively. Notice that the κ and λ in Eq. (5.9) are be labelled with the number $n = 0, 1, 2, \ldots$, but hereafter we drop it for the sake of simplicity.

It is important to remark that Eq. (5.6) together with the line-tying condition leads to a Stürm-Liouville problem, so the solutions found are a complete basis, and therefore any arbitrary solution of Eq. (5.1) can be expressed as a sum of these functions, which were studied in Sect. 4.5 in some detail. It is also necessary to use "jump" conditions to connect the solution in the interior (hereafter labelled (l)) and the exterior (c) regions. On the boundary $r = b$ (on which $\mathbf{n} \cdot \mathbf{B} = 0$ is satisfied, where $\mathbf{n}$ is the vector normal to the boundary) these conditions are Eq. (4.40). Eq. (5.4) is the modified Bessel's differential equation, so its general solution can be written as a combination of Bessel functions. Imposing the boundary conditions on the surface $r = b$ leads to the dispersion relation

$$\frac{1}{\lambda^{(\mathrm{c})*}} \frac{\mathrm{H}_m^{(1)\prime}(\lambda^{(\mathrm{c})*} b)}{\mathrm{H}_m^{(1)}(\lambda^{(\mathrm{c})*} b)} - \frac{1}{\lambda^{(\mathrm{l})*}} \frac{\mathrm{J}_m{}'(\lambda^{(\mathrm{l})*} b)}{\mathrm{J}_m(\lambda^{(\mathrm{l})*} b)} = 0, \tag{5.11}$$

which is again a particular form of other well-known dispersion relations (Edwin & Roberts (1983), Cally (1986) and more recently Karami et al. (2002)).

If fact, this dispersion relations of Eq. (5.11) are a particular case of Eq. (4.120). To show that, it is necessary to take into account that the z-dependent functions are the same in the loop and coronal region, so we can invoke Eq. (4.126), which separates the contribution of each basis function in Eq. (4.117). Therefore, there is no determinant and the dispersion relations become a set of algebraic equations, one for each number n, a label that has been dropped in Eq. (5.11) for the sake of simplicity. However, here we have used the Hankel function instead of the modified Bessel function K_m for the coronal part, since the leaky modes are also studied. In the dispersion relation Eq. (5.11) the external wavenumber $\lambda^{(\mathrm{c})}$ can be real or imaginary, thus we are not restricted to trapped modes. Also notice that a so called surface mode is obtained if $\lambda^{(\mathrm{l})} \in \mathcal{R}$, and a body mode if $\lambda^{(\mathrm{l})*} = i\lambda^{(\mathrm{l})} \in \mathcal{R}$ (replacing the Bessel function J_m by its corresponding modified Bessel function I_m to take this into account). In the following discussion, magnitudes will be non-dimensionalized against L, the half-length of the magnetic flux tube and c_{Ac}, the Alfvén speed in the coronal environment.

Trapped modes in the $b/L \to 0$ limit

This special case is interesting mainly because in the solar atmosphere structures tend to be thin in comparison with the length of the supporting magnetic field lines. It is similar to the limit $\kappa a \to 0$ in Edwin & Roberts (1983), taking into account that $L \sim 1/\kappa$.

For trapped modes it is necessary that λ^* be a pure imaginary number, so the external solution can be expressed in terms of the modified Bessel function K_m, and under this condition the dispersion relation Eq. (5.11) can be rewritten as (Edwin & Roberts 1983)

$$\frac{1}{\lambda^{(\mathrm{c})}} \frac{\mathrm{K}_m{}'(\lambda^{(\mathrm{c})} b)}{\mathrm{K}_m(\lambda^{(\mathrm{c})} b)} - \frac{1}{\lambda^{(\mathrm{l})}} \frac{\mathrm{I}_m{}'(\lambda^{(\mathrm{l})} b)}{\mathrm{I}_m(\lambda^{(\mathrm{l})} b)} = 0. \tag{5.12}$$

Notice that, since $\lambda^{(c)}$ and $\lambda^{(l)}$ remain finite in the limit $b/L \to 0$, the arguments of the Bessel functions in this expression also tend to zero in this limit.

Now it is necessary to invoke series expansions for the Bessel functions and their derivatives for $z \ll 1$ (Abramowitz & Stegun 1967),

$$\begin{aligned}
&\mathrm{I}_m(z) \sim \frac{(z/2)^m}{\Gamma(m+1)},\\
&\mathrm{K}_0(z) \sim -\ln(z),\\
&\mathrm{K}_m(z) \sim \frac{1}{2}\Gamma(m)(z/2)^{-m},\ m \neq 0,\\
&\mathrm{I}_0{}'(z) \sim 0 + O(z^2),\\
&\mathrm{I}_m{}'(z) \sim \frac{(z/2)^{m-1}}{2\Gamma(m)},\ m \neq 0,\\
&\mathrm{K}_0{}'(z) \sim -1/z,\\
&\mathrm{K}_m{}'(z) \sim \frac{-(z/2)^{-m-1}}{4}\Gamma(m+1),\ m \neq 0.
\end{aligned} \tag{5.13}$$

There are two possibilities, $m = 0$ and $m \neq 0$. If $m = 0$, then $K_0(\lambda^{(c)}b) \sim \log\lambda^{(c)}b$ and there is no possibility of balancing the two terms in Eq. (5.12), so no sausage ($m = 0$) solution exists in the thin tube limit. If $m \neq 0$, then Eq. (5.12) can be written (after some algebra) as

$$\lambda^{(c)^2} + \lambda^{(l)^2} = 0, \tag{5.14}$$

which leads to

$$\frac{\omega}{c_{\mathrm{Ac}}}L = \frac{c_{\mathrm{k}}}{c_{\mathrm{Ac}}}\kappa L = \sqrt{\frac{2}{1+\rho_{\mathrm{l}}/\rho_{\mathrm{c}}}}\,\frac{(n+1)\pi}{2}. \tag{5.15}$$

Here c_{k} denotes the kink speed, an intermediate speed between the lower Alfvén speed of the tube and the higher one of the surrounding coronal medium,

$$c_{\mathrm{k}} = \sqrt{\frac{\rho_{\mathrm{l}}c_{\mathrm{Al}}^2 + \rho_{\mathrm{c}}c_{\mathrm{Ac}}^2}{\rho_{\mathrm{l}}+\rho_{\mathrm{c}}}} = \sqrt{\frac{2c_{\mathrm{Al}}^2c_{\mathrm{Ac}}^2}{c_{\mathrm{Al}}^2+c_{\mathrm{Ac}}^2}} = c_{\mathrm{Ac}}\sqrt{\frac{2}{1+\rho_{\mathrm{l}}/\rho_{\mathrm{c}}}}. \tag{5.16}$$

The equalities in this expression come from our assumption of equal magnetic field inside and outside the tube. The kink ($m = 1$) and all the fluting ($m \geq 2$) modes tend to the same value of the frequency in the limit $b/L \to 0$.

From this development another difference between the slab and the tube becomes evident: for a thin slab $\lambda^{(c)} \to 0$ as $b/L \to 0$ (from Eq. (F.7) in Appendix F), but in a tube Eqs. (5.9) and (5.15) in this limit give

$$\lambda^{(c)} = \kappa^2\left(1 - \frac{c_{\mathrm{k}}^2}{c_{\mathrm{Ac}}^2}\right), \tag{5.17}$$

so that $\lambda^{(c)}$ is different from 0. The immediate consequence of this different behaviour is that in a slab the perturbation reaches long distances from the fibril axis (see the later sections), while in a cylinder it remains confined for arbitrarily small values of the radius. Nevertheless, this is only for thin structures, since for thick ones the results of cylindrical and Cartesian loops are in a good agreement (Díaz, Oliver & Ballester (2002), expanded in Chapter 8), with only minor shifts in frequency but similar spatial structure along and across the magnetic field.

5.1.2 Trapped modes of line-tied coronal tubes

The next step is to study the solutions of Eq. (5.11), focusing on the set of frequencies of trapped modes. It is important to remark that $\lambda^{(c)}$ has to be real to have trapped modes, requiring from Eq. (5.9) that

$$\lambda^{(c)} \in \mathcal{R} \Rightarrow \lambda^{(c)^2} \geq 0 \Rightarrow \frac{\omega}{c_{\rm Ac}} \leq \kappa. \tag{5.18}$$

Therefore, there is a cut-off frequency, $\omega_{\rm cut}$, for each value of κ,

$$\frac{\omega_{\rm cut}}{c_{\rm Ac}} L = \frac{(n+1)\pi}{2}, \tag{5.19}$$

In Fig. 5.2 the variation of the mode frequencies with the tube radius is plotted for a high density flux tube, while in Fig. 5.3 a density ratio typical of coronal loops has been selected. In the less dense tube there are fewer trapped modes, but otherwise the structure of the dispersion diagrams is quite similar. Each mode can be labelled by three numbers: n for the z-wavenumber in Eq. (5.10), related to the number of extrema in the z-direction; m for the azimuthal wavenumber in Eq. (5.5) and in the Bessel functions, representing the sausage ($m = 0$), kink ($m = 1$) and fluting ($m \geq 2$) modes; and another one (say l) for the number of extrema in the r-direction. Each family of modes having the same value of n have a cut-off frequency given by Eq. (5.19), which modes belonging to other families can cross. Notice that the denser the loop the better the modes are confined (and also the smaller their frequency).

In fact, Figs. 5.2 and 5.3 are just the low-β limit ($c_{\rm s} \to 0$) of Fig. 4 in Edwin & Roberts (1983), reproduced in this work as Fig. 2.8, although in that figure the fluting modes are not represented. However, it should be taken into account that their plot is drawn using the dependent variable ω/κ, while in Figs. 5.2 and 5.3 $\omega L/c_{\rm Ac}$ is used, so each family of modes has a different vertical (and also horizontal) scale. Notice that the value of $\rho_{\rm l}/\rho_{\rm c} = 200$ used in Fig. 5.2 is too big for a solar coronal loop, but nevertheless has been included to show the general behaviour of the solutions.

Finally, in the thin tube limit, it is easy to check that Eq. (5.15) (valid for $b/L \to 0$) is satisfied, so for each family of modes with the same n the sausage mode ($m = 0$) is no longer trapped, while the kink and all fluting modes tend to a frequency of value

$$\omega \frac{L}{c_{\rm Ac}} = (n+1)\frac{\pi}{2}\frac{c_{\rm k}}{c_{\rm Ac}} = 0.157\,(n+1), \tag{5.20}$$

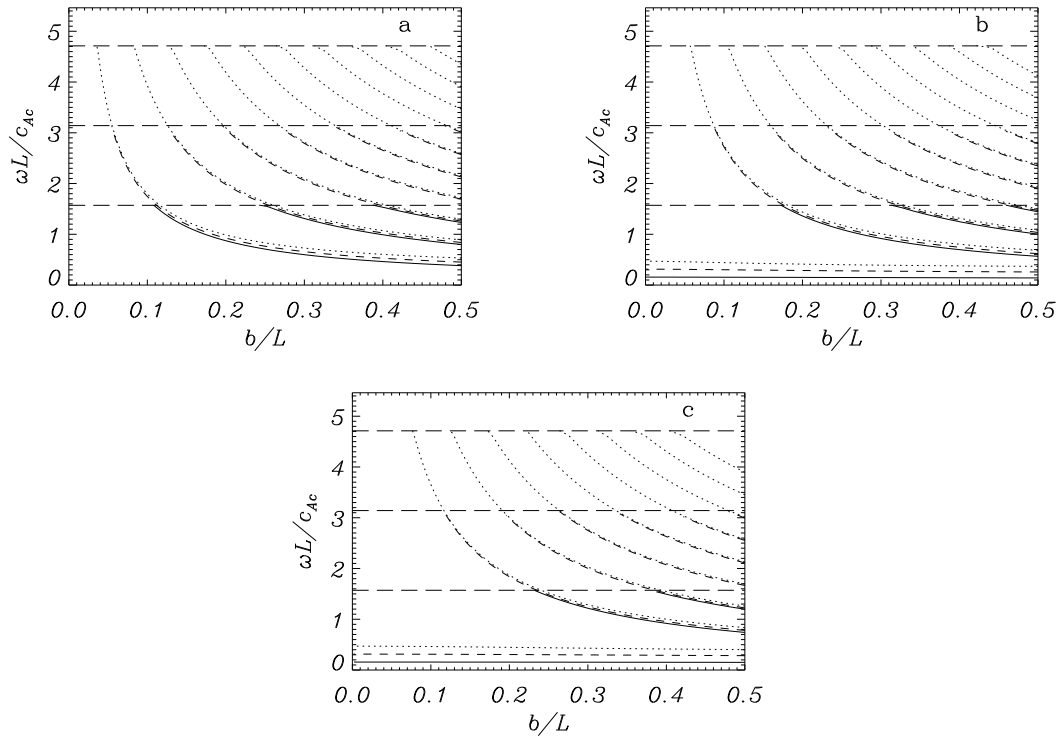

Figure 5.2: High density flux tubes: variation of the dimensionless frequency, $\omega L/c_{\rm Ac}$, with b/L, the tube radius as a fraction of loop half-length, for modes $n = 0$ (even, solid lines), $n = 1$ (odd, dashed lines) and $n = 2$ (even, dotted lines) of a tube with density ratio $\rho_{\rm l}/\rho_{\rm c} = 200$. The modes represented are **a)** sausage modes ($m = 0$), **b)** kink modes ($m = 1$) and **c)** first fluting modes ($m = 2$). The cut-off frequencies are marked with horizontal long dashed lines.

in the case of $\rho_{\rm l}/\rho_{\rm c} = 200$ and

$$\omega \frac{L}{c_{\rm Ac}} = (n+1)\frac{\pi}{2}\frac{c_{\rm k}}{c_{\rm Ac}} = 0.670\,(n+1), \tag{5.21}$$

for $\rho_{\rm l}/\rho_{\rm c} = 10$, in agreement with Figs. 5.2 and 5.3, respectively. Notice that the fine scale structure of coronal loops suggested by observations do not affect the results for these frequencies, since for low b/L these frequencies do not depend on the loop radius.

5.1.3 Leaky modes of line-tied coronal tubes

Following our study of the solutions of trapped modes, we can deal with the more general case of the leaky modes allowing the frequency, ω, to become complex. In this section we use the notation $Re\{\omega\} = \omega_r$, $Im\{\omega\} = \omega_i$, $Re\{\lambda^{({\rm c})*}\} = \lambda_r^{({\rm c})}$ and $Im\{\lambda^{({\rm c})*}\} = \lambda_i^{({\rm c})}$ to denote the real and imaginary parts of ω and $\lambda^{({\rm c})}$. Notice that the spatial dependence on the r-coordinate can be rewritten in terms of the Hankel functions instead of the ordinary Bessel functions in Sect. 4.4.2, namely,

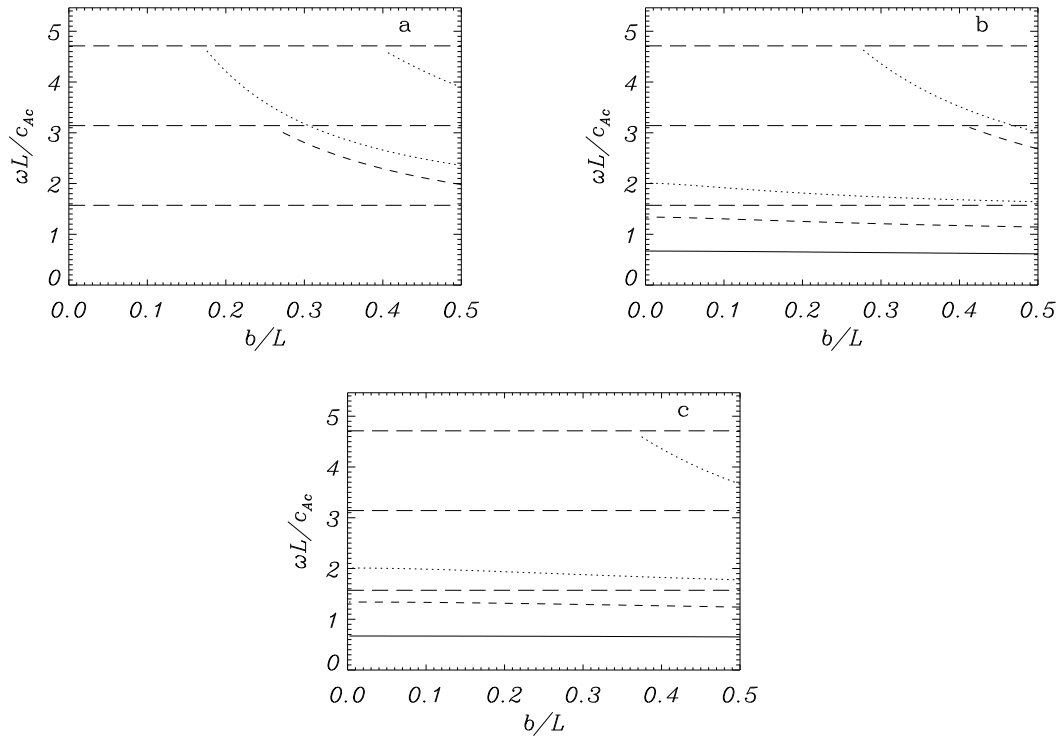

Figure 5.3: Coronal loops: variation of the dimensionless frequency with the tube radius for modes $n = 0$ (even, solid lines), $n = 1$ (odd, dashed lines) and $n = 2$ (even, dotted lines) of a tube with density ratio $\rho_1/\rho_c = 10$. The modes represented are **a)** sausage modes ($m = 0$), **b)** kink modes ($m = 1$) and **c)** first fluting modes ($m = 2$). The cut-off frequencies are marked with horizontal long dashed lines. Notice that in panel **a)** the sausage modes with $n = 1$ (solid lines) are absent because all of them are leaky.

$$u_n(r) = B_{H1n}\mathrm{H}_m^{(1)}(\lambda_n^* r) + B_{H2n}\mathrm{H}_m^{(2)}(\lambda_n^* r). \tag{5.22}$$

Therefore, the r-dependent part of the perturbed pressure is

$$u(r) = \begin{cases} A\,\mathrm{J}_m(\lambda^{(1)^*} r), & 0 \le r \le b, \\ B\,\mathrm{H}_m^{(1)}(\lambda^{(c)^*} r), & r > b. \end{cases} \tag{5.23}$$

The starting point is that all solutions of the dispersion relation Eq. (5.11) satisfy either

$$\lambda_r^{(c)} \ge 0, \;\; \lambda_i^{(c)} \le 0, \;\; \omega_r \ge 0, \;\; \omega_i \le 0, \tag{5.24}$$

or

$$\lambda_r^{(c)} \ge 0, \;\; \lambda_i^{(c)} \le 0, \;\; \omega_r \le 0, \;\; \omega_i \ge 0. \tag{5.25}$$

Therefore, we proceed to study the properties of these two types of solutions. The temporal dependence can be written in the following way

$$e^{-i\omega t} = e^{-i\omega_r t}\, e^{\omega_i t} = e^{-i\omega_r t}\, e^{-t/\tau}, \tag{5.26}$$

with a damping time, τ, defined as

$$\tau = -1/\omega_i. \tag{5.27}$$

The next step is to take into account the spatial dependence for large values of r. It is convenient to use the expansion of the Hankel function for large arguments, namely $\mathrm{H}_m^{(1)}(z) \sim e^{-iz}$, $z \gg 1$ (Abramowitz & Stegun 1967). Thus,

$$p_{\mathrm{T}} \sim e^{i\omega t}\mathrm{H}_m^{(1)}(\lambda^{(\mathrm{c})} r) \sim e^{-t/\tau}\, e^{\lambda_i^{(\mathrm{c})} r}\, e^{-(\lambda_r^{(\mathrm{c})} r + i\omega_r t)}, \tag{5.28}$$

when $r \to \infty$.

Now it is evident that solutions satisfying Eq. (5.24) correspond to waves propagating away from the density enhancement and exponentially decaying with time, but growing exponentially for large r. On the other hand, the solutions satisfying Eq. (5.25) correspond to waves decaying exponentially for large r, but propagating inwards and, even worse, exponentially increasing with time.

There have been some arbitrary selections that can be justified now. If we choose a time dependence of the form $e^{i\omega t}$ instead of the one of Eq. (5.26), the behaviour of the solutions satisfying Eq. (5.24) and Eq. (5.25) is exchanged, but the physics is the same. A different possibility is to choose the other sign for $\lambda^{(\mathrm{c})}$ in Eq. (5.9), but then there are no solutions of the dispersion relation Eq. (5.11). However, there is also another possibility for choosing the spatial dependence outside the tube: to take the Hankel function of second order $\mathrm{H}_m^{(2)}(z)$ instead of the first order one used through this Section, $\mathrm{H}_m^{(1)}(z)$. In this case the dispersion relation Eq. (5.11) becomes

$$\frac{1}{\lambda^{(\mathrm{c})*}} \frac{\mathrm{H}_m^{(2)\prime}(\lambda^{(\mathrm{c})*} b)}{\mathrm{H}_m^{(2)}(\lambda^{(\mathrm{c})*} b)} - \frac{1}{\lambda^{(\mathrm{l})*}} \frac{\mathrm{J}_m{}'(\lambda^{(\mathrm{l})*} b)}{\mathrm{J}_m(\lambda^{(\mathrm{l})*} b)} = 0, \tag{5.29}$$

and now the solutions satisfy either

$$\lambda_r^{(\mathrm{c})} \leq 0, \;\; \lambda_i^{(\mathrm{c})} \geq 0, \;\; \omega_r \leq 0, \;\; \omega_i \geq 0, \tag{5.30}$$

or

$$\lambda_r^{(\mathrm{c})} \leq 0, \;\; \lambda_i^{(\mathrm{c})} \geq 0, \;\; \omega_r \geq 0, \;\; \omega_i \leq 0. \tag{5.31}$$

Nevertheless, taking into account the asymptotic expansion of the Hankel function of second order for large arguments, namely $\mathrm{H}_m^{(2)}(z) \sim e^{iz}$, $|z| \gg 1$ (Abramowitz & Stegun 1967) the same two types of solutions are recovered, so no different behaviour is achieved with the choice of $\mathrm{H}_m^{(2)}(z)$.

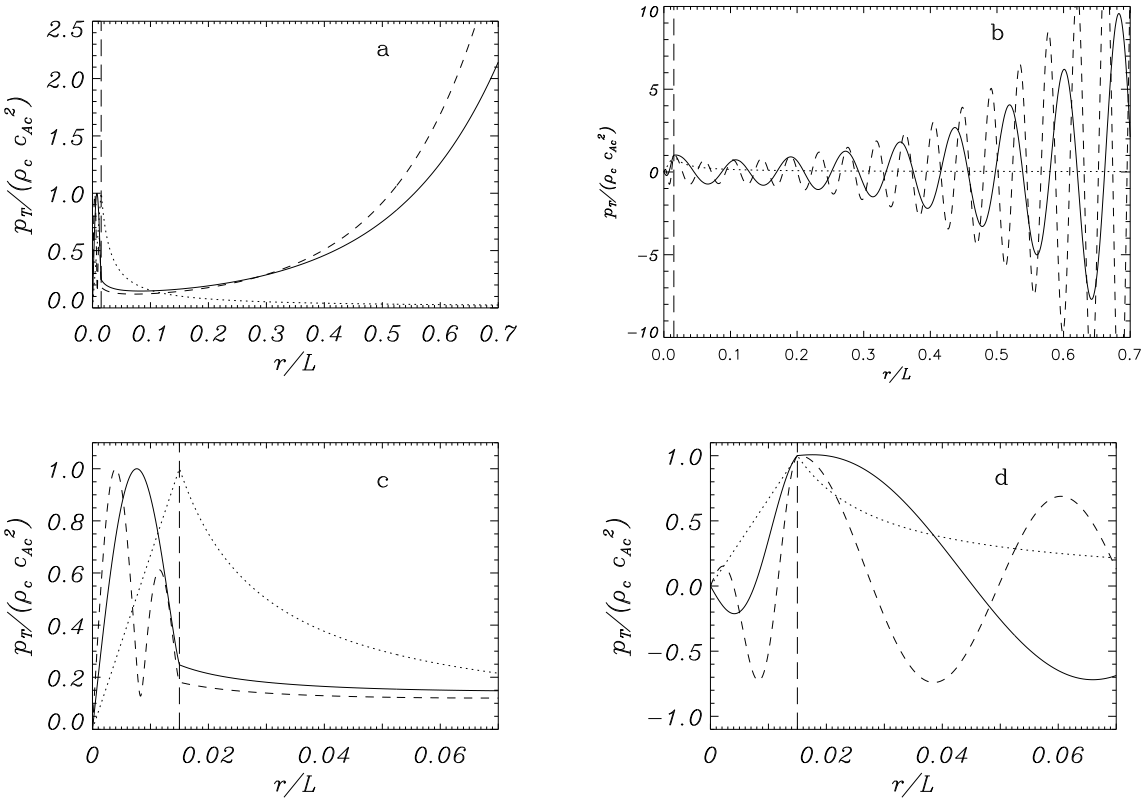

Figure 5.4: Cuts in the direction $z = 0$ of **a)** the modulus and **b)** the imaginary part of $p_{\rm T}$ for the kink even modes ($n = 0$, $m = 1$). The fundamental mode ($l = 1$), which is trapped, is plotted as dotted line, while the first and second harmonics ($l = 2, 3$), which are leaky modes, are plotted as solid and dashed lines, respectively. The parameters used are $\rho_{\rm l}/\rho_{\rm c} = 10$ and $b/L = 0.015$. Panels **c)** and **d)** are zooms of panels **a)** and **b)** respectively to better show the behaviour in the loop region. In each panel the loop limit is marked with a long-dashed vertical line.

The appearance of a solution which grows exponentially away from the cylinder was already noticed in Cally (1986, 2003) and Stenuit, Keppens & Goossens (1998). The interpretation of this fact is that the larger the distance from the tube, the earlier the perturbation departed from the tube and, because of the exponential growth of Eq. (5.28) for reversed time, the bigger the amplitude was at that moment in the density enhancement. This is an unphysical solution, since it is unbounded and not square integrable, but we are looking for stationary states, and a leaky wave can only be stationary with this behaviour; hence for more appropriate modeling to this problem the full temporal dependence should be used instead of a Fourier decomposition. However, it remains worthwhile studying these unbounded solutions because we still can learn from these modes some properties of the system. Spatial plots of $p_{\rm T}(r)$ are shown in Fig. 5.4 for a parameter set typical of coronal loops; it is clear that functions grow exponentially far away from the tube. It is interesting to remark that near the tube there is a region where the amplitude decreases with distance.

Now the leaky modes of a cylindrical flux tube, which were discussed admirably by Cally (1986)

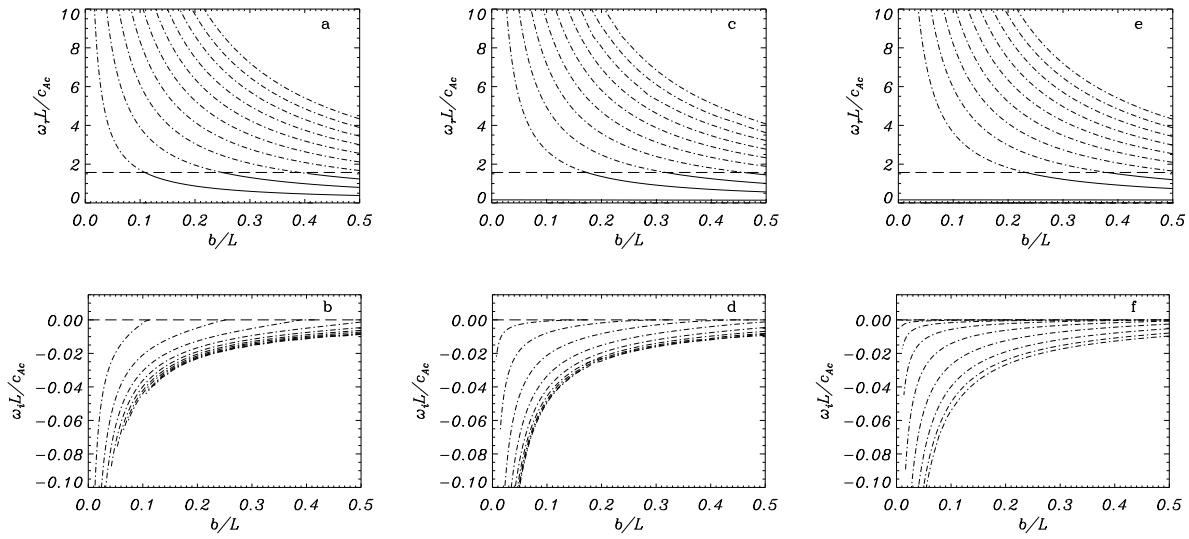

Figure 5.5: Variation of **a), c)** and **e)** the real part and **b), d)** and **f)** the imaginary part of the dimensionless frequency with the fibril half-thickness for the $n = 0$ even modes of a flux tube with density ratio $\rho_l/\rho_c = 200$. The cut-off frequency is marked with a horizontal long dashed line. Panels **a)** and **b)** correspond to the sausage modes, panels **c)** and **d)** to the kink ones and panels **e)** and **f)** to the first fluting ones ($m = 2$). In the plots of the real part a solid line denotes a trapped mode (see Fig. 5.2), while in the plots of the imaginary part only the values different from zero are plotted. Notice that when a mode becomes leaky (i.e. when its ω_r surpasses the cut-off frequency) the imaginary part of its frequency is shown in the corresponding panel to the right.

without line-tying boundary conditions, can be studied from the dispersion relations of Eq. (5.11). The resulting plots of the remaining fast modes are shown in Fig. 5.6 for the $n = 0$ sausage, kink and first fluting modes; note that the trapped modes with $n = 0$ of Fig. 5.3 (solid lines there) are shown alongside their respective leaky modes. It is clear that when the frequency of a trapped mode surpasses the corresponding cut-off, the mode becomes leaky, but otherwise its properties are not changed (for example, the number of extrema of p_T in the tube). Notice also that for leaky modes the behaviour for thin tubes is quite different from the case of a slab (see Appendix E): the complex part of the frequencies of the harmonics tend very slowly to the same value, contrary to what is found in a thin slab (Fig. F.3b), so the spectrum is much richer because many values of frequency and damping time are possible for a given set of parameters.

Now we consider parameter values appropriate for coronal loops. In Nakariakov et al. (1999) a tube with length $2L = 130$ Mm, diameter $2b = 1$ Mm was observed, a density ratio $\rho_l/\rho_c \approx 10$ was assumed and the resulting observed period was $T = 4.27$ min with an exponential decay with a damping time of $\tau = 14.5$ min. This gives the value $b/L = 0.015$ and, using the coronal particle number $n_p = 5 \times 10^{14}$ m^{-3} and a magnetic field strength $B_0 = 10$ G, we derive the coronal Alfvén speed $c_{Ac} = 2.8 \times 10^{12} B_0 n_p^{-1/2} = 1252$ km s^{-1}. The resulting frequencies, periods and damping times of leaky modes are presented in Table 5.1. The higher leaky modes have a damping time of the same order, but a much higher frequency (a lower period). Notice that these modes have periods that are too low to be detected from *TRACE* (although they may have been reported in eclipse measurements by Katsiyannis et al. (2003)) and are also rapidly

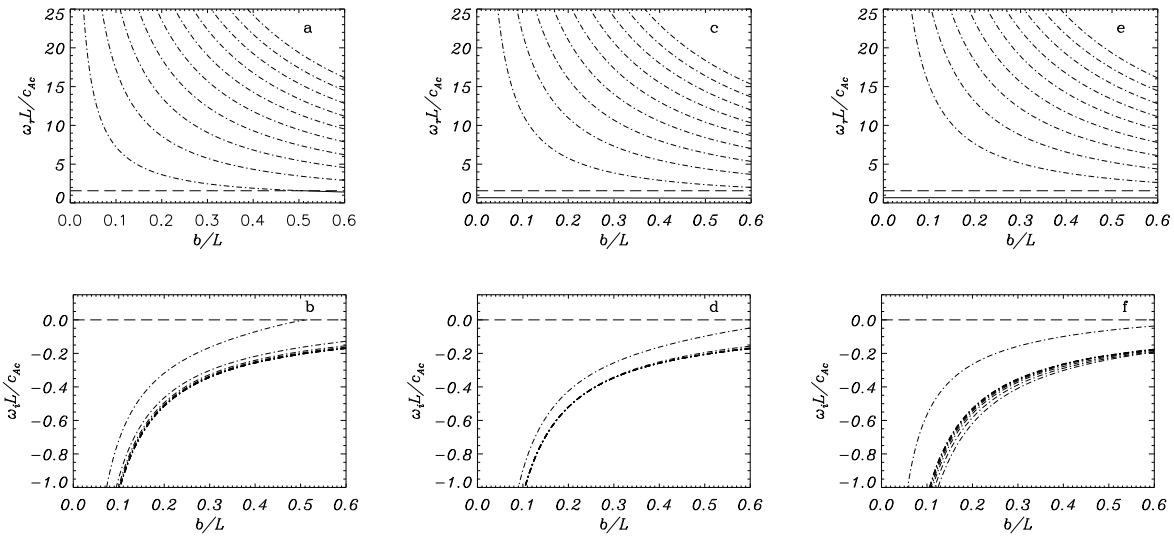

Figure 5.6: Variation of **a), c)** and **e)** the real part and **b), d)** and **f)** the imaginary part of the dimensionless frequency with the fibril half-thickness for the $n = 0$ even modes of a flux tube with density ratio $\rho_l/\rho_c = 10$. The cut-off frequency is marked with a horizontal long dashed line. Panels **a)** and **b)** correspond to the sausage modes, panels **c)** and **d)** to the kink ones and panels **e)** and **f)** to the first fluting ones ($m = 2$). In the plots of the real part a solid line denotes a trapped mode (see Fig. 5.3), while in the plots of the imaginary part only the values different from zero are plotted. Notice that when a mode becomes leaky (i.e. when its ω_r surpasses the cut-off frequency) the imaginary part of its frequency is shown in the corresponding panel to the right.

attenuated by leakage. For trapped modes with higher order n, the periods and damping times are given in Table 5.1, but divided by $(n+1)$ (see Eq. (5.15)), so they have even lower periods. However, the real and imaginary parts of the frequency of leaky modes for $n \geq 1$ take very similar values for given m and l. This is apparent in Fig. 5.3, in which the frequencies of modes with different values of n almost overlap, a trend found also for the real part of the frequencies of the leaky modes (Fig. 5.6).

It is important to remark that for the numerical values introduced in the previous paragraph the fundamental modes with $m \geq 1$ are trapped, and have a frequency $\omega_r L/c_{\rm Ac} \approx (c_{\rm k}/c_{\rm Ac})\pi(n+1)$ and a period $T_{\rm stand} \approx 8.12/(n+1)$ min; they are not damped in this model. The first mode was used in Nakariakov & Ofman (2001) to deduce the magnetic field strength $B_0 = 13 \pm 9$ G, compared to the value that we use here, $B_0 = 10$ G. However, the many effects not taken into account in our work and in previous ones make a small variation in the parameters irrelevant for the interpretation of the results. On the other hand, We note that Nakariakov & Ofman (2001) make no comments about the lack of detection of trapped modes with $n > 1$, that could in principle have been excited together with the $n = 1$ mode.

5.1.4 Effects of a chromospheric layer on the trapped modes

In previous sections it has been made clear that for the homogeneous flux tube of Fig. 5.1 the wavenumber in the z-direction, κ, is quantized (see Eq. (5.10)) and that for each family of

Table 5.1: Frequency, period and damping time for the first even modes with $\kappa = \pi/(2L)$ ($n = 0$). The equilibrium parameters are $b/L = 0.015$, $\rho_{\rm l}/\rho_{\rm c} = 10$, $L = 65$ Mm, $n_{\rm p} = 5 \times 10^{14}$ m^{-3} and $B_0 = 10$ G, giving an Alfvén speed of $c_{\rm Ac} = 1252$ km s^{-1}.

m	l	$\omega_r L/c_{\rm Ac}$	$\omega_i L/c_{\rm Ac}$	T (min)	τ (min)
1 (kink)	0	0.670	0	8.12	∞
2 (fluting)	0	0.670	0	8.12	∞
3 (fluting)	0	0.670	0	8.12	∞
0 (sausage)	0	48.04	-4.98	0.113	0.17
1 (kink)	1	76.62	-6.07	0.071	0.14
2 (fluting)	1	101.27	-3.85	0.054	0.23
3 (fluting)	1	128.0	-1.28	0.042	0.68

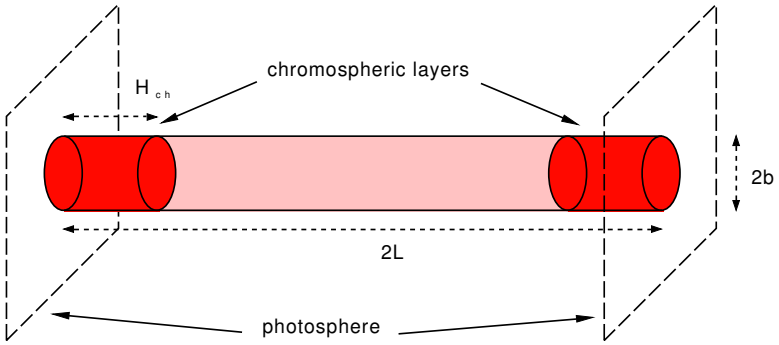

Figure 5.7: Sketch of the equilibrium configuration representing a coronal flux tube of length $2L$ and radius b with chromospheric material at its footpoints (deep red in the figure) extending up to a height $H_{\rm ch}$. The density inside the loop is $\rho_{\rm l}$, $\rho_{\rm ch}$ is the density in the chromospheric part and $\rho_{\rm c}$ in the coronal environment. The magnetic field is uniform and parallel to the z-axis.

solutions sharing the same n, a different cut-off frequency is found. However, Díaz et al. (2002) pointed out that the addition of structure along the magnetic field changes this result, since the modes with the same symmetry become mixed and the cut-off is just the lowest one ($\omega_{\rm cut} L/c_{\rm Ac} = \pi/2$ for even modes and $\omega_{\rm cut} L/c_{\rm Ac} = \pi$ for the odd ones).

It is quite clear that there is at least some inhomogeneity along the loop: the chromospheric layer near the photosphere (Fig. 5.7). Therefore, we next study how the modes described in Sect. 5.1.2 are modified when this structure is taken into account. The coronal parameters used in the previous section are also used here ($2L = 130$ Mm, $2b = 1$ Mm and $\rho_{\rm l}/\rho_{\rm c} = 10$) and for the chromospheric layer a typical height $H_{\rm ch} = 5$ Mm and density ratio $\rho_{\rm ch}/\rho_{\rm c} = 200$ are used (although the height and density of this layer are far from uniform and quite difficult to estimate). To solve analytically this problem we use the formulae in Sect. 4.5.2 for a structure with a density depression (instead of an enhancement, but otherwise the expressions are the same) and the dispersion relation for cylindrical geometry of Sect. 4.4.

The resulting dispersion relations versus the loop radius for the trapped modes are plotted in Fig. 5.8. For a typical value $b/L = 0.015$, sausage modes are leaky (this is true even for much larger values of b/L). In addition, there are only two trapped kink and two trapped fluting ($m = 2$, but also $m > 2$, not shown here) modes, which correspond to the waves of the

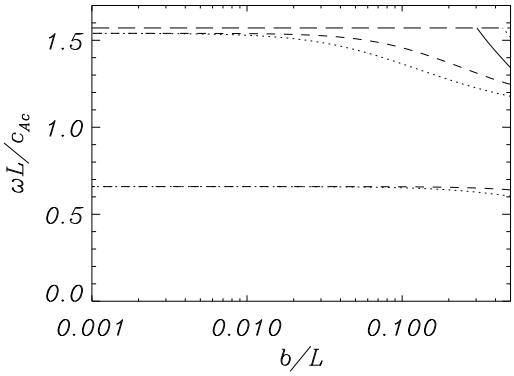

Figure 5.8: Variation of the dimensionless frequency with the loop radius for even modes of a tube with density ratio $\rho_l/\rho_c = 10$ and chromospheric density ratio $\rho_{ch}/\rho_c = 200$. The solid line corresponds to the trapped sausage mode ($m = 0$), the dotted line to the kink modes ($m = 1$) and the dashed line to the first fluting modes ($m = 2$). The cut-off frequency, marked with a horizontal long dashed line, is $\omega_{cut}L/c_{Ac} = \pi/2$.

Table 5.2: Dimensionless frequency ($\omega L/c_{Ac}$) and period T (in minutes) for the trapped kink even modes in a coronal flux tube with chromospheric footpoints. The parameters are $\rho_l/\rho_c = 10$, $n_p = 5 \times 10^{14}$ m^{-3} and $B_0 = 10$ G, giving an Alfvén speed of $c_{Ac} = 1252$ km s^{-1}. The last column gives the period of the corresponding mode for the homogeneous tube. Short period modes with $n \geq 2$ are leaky in the chromospheric model (but not in the absence of chromosphere).

n	$\omega L/c_{Ac}$	T (min)	T_{homog} (min)
0	0.659	8.25	8.12
1	1.519	3.58	2.71
2	–	–	1.62
3	–	–	1.16

homogeneous tube ($n = 0$ and $n = 1$ and frequencies $\omega_r L/c_{Ac} \approx (c_k/c_{Ac})(n+1)\pi/2$, Eq. 5.21). The other $m = 1$ and $m = 2$ modes with $n \geq 2$ are above the new common cut-off frequency, $\omega_r L/c_{Ac} = \pi/2$, so they all become leaky. However, due to the chromospheric structure the two remaining trapped modes do not correspond to a single n but have contributions from the basis functions for all values of n. The frequencies and periods for the kink modes are summarized in Table 5.2 for the same coronal density and magnetic field strength considered in the previous Section. The periods of the $n = 0$ and $n = 1$ kink modes are only slightly modified by the presence of the chromospheric layers, so the most important result is that the higher order modes become leaky (though we have not determined their frequencies and damping times). As noted in before, these damping times can be quite small, perhaps preventing these modes from being detected, whereas for the homogeneous tube they are non-leaky and thus detectable in principle.

5.1.5 Conclusions

The oscillations of coronal flux tubes with line-tying boundary conditions at the photospheric footpoints have been studied for a low-beta plasma. A rich array of modes, trapped and leaky, have been classified, focusing on their frequency and spatial structure. We have compared our results with current observational data.

The line-tying boundary conditions introduce some important differences from the classical

results for unlimited flux tubes (Edwin & Roberts 1983, summarised in Sect. 2.4.3):

1. The introduction of the line-tying adds a new characteristic length and a quantization (n) in the direction along the flux tube. The plots of the dispersion relation display these features a well as the quantizations in the azimuthal (m) and radial (l) directions.

2. In a straight and uniform magnetic cylinder, for values of length, thickness and density of the flux tube in accordance with observations, the sausage modes ($m = 0$) are leaky since their frequency lies above the cut-off frequency. If a sausage mode is excited in the loop, its energy is quickly transferred to the coronal environment and the oscillation dies out. For all other modes ($m > 0$) at least the fundamental mode lies below the cut-off frequency. Hence, if any of these modes is excited the oscillatory energy in the loop plasma does not decay. Moreover, as the density ratio between the loop and the coronal medium ($\rho_{\rm l}/\rho_{\rm c}$) is increased, the frequency of other harmonics may move below the cut-off and so a dense loop may support a higher number of oscillatory modes.

3. Leaky modes have very short periods and short damping times. If these modes were excited, their energy would be quickly pumped out to the corona, making them difficult to detect (a high cadence would be necessary). Their strong attenuation would also lower their amplitude below the noise level in just a few oscillations.

4. The modes of a homogeneous flux tube with higher values of n, i.e. shorter wavelength along the loop, have periods $T_n = T_0/(n+1)$, where T_0 is the period of the kink or fluting mode with the same numbers l and m, but with $n = 0$. These modes could be detected, since their period is still in the range of the fundamental one and current spatial resolution is high enough. Observational data should contain signatures of these higher harmonics.

5. Currently available observational data does not usually show such short period modes. The suggested explanation is that if some structure is added to the model (for example, the chromospheric layers), the modes having the same m and l are combined to satisfy the MHD boundary conditions on the loop-corona interface. Under such conditions, all the higher order modes become leaky and therefore are undetectable in current observations.

Finally, since typical calculated periods are in the range of the observational data, so we are encouraged to develop more complicated models. The results can be applied to calculate various equilibrium parameters from observations of the oscillatory properties, but the model needs to be refined first. The obvious next step would be to use a more accurate equilibrium profile than that with a simple chromospheric layer. This work is a first step towards such studies.

5.2 Line-tied coronal loops with heating profiles

After having studied the simple model of homogeneous coronal loops, our main aim now is to extend the oscillatory analysis to more complicated equilibrium models. Here we concentrate on the effects in the modes introduced by non-uniform equilibrium models (along the loop axis) due to heating. The heating function is assumed to be time independent, but may depend on the spatial coordinate along the loop.

5.2.1 Equilibrium model, oscillatory model and dispersion relations

First of all, the equilibrium model explained in Sect. 3.2 is reviewed. We are interested in studying an isolated coronal loop embedded in the solar corona, which for the sake of simplicity is considered as a uniform, hot and rarefied plasma. The radius of the flux tube is b and its length is $2L$, with photospheric plasma in both limits. The magnetic field (the same inside and outside the tube) is uniform and parallel to the loop axis ($\mathbf{B}_0 = B_0\hat{\mathbf{z}}$, where z is the direction along the loop axis). The loop is symmetric with respect to the coordinate z, and has no dependence across the fibril axis, although all the equilibrium plasma parameters depend upon the coordinate z along the loop. Following the approach of previous studies, the flux tube is going to be straightened (no curvature effects), so the loop is transformed in the one in Fig. 5.1 for wave analysis purposes.

Next step is to describe an equilibrium profile for these loops. The profiles are different inside and outside the flux tube because the Alfvén speed is also different,

$$c_{\rm A} = \begin{cases} c_{\rm A}^{(\rm c)}(z) \doteq c_{\rm Ac}, & r > b, \\ c_{\rm A}^{(\rm l)}(z), & r \leq b, \end{cases} \tag{5.32}$$

For a given heating function $H(z)$, a temperature profile can be derived from Eq. (3.3), and then the pressure and density profiles can be computed. Now we can consider different types of heating functions, which lead to the following alfvén speed profiles:

- Loop equilibria with uniform heating.

$$H(z) = H_0 = \text{const.} \tag{5.33}$$

$$c_{\rm A}^2(z) = \frac{B_0^2}{\mu_m \rho(z)} = c_{\rm A}^2(L)\left\{1 + \frac{\bar{H}}{2}\left[1 - \left(\frac{z}{L}\right)^2\right]\right\}^{2/7}. \tag{5.34}$$

- Loop equilibria with uniform heating only in a layer near the footpoints.

$$H(z) = \begin{cases} 0, & z \leq L - L_{\rm H}, \\ H_0, & L - L_{\rm H} \leq z \leq L. \end{cases} \tag{5.35}$$

$$c_{\rm A}^2(z) = \begin{cases} c_{\rm A}^2(L)\left[1 + \frac{\bar{H}}{2}(1 - \frac{z}{L})^2 \right. \\ \qquad \left. -2(1 - \frac{z}{L})(1 - \frac{L_{\rm H}}{L})\right]^{2/7}, & L - L_{\rm H} \leq z \leq L, \\ c_{\rm A}^2(L)\left(1 + \frac{\bar{H}}{2}\frac{L_{\rm H}^2}{L^2}\right)^{2/7}, & z \leq L - L_{\rm H}. \end{cases} \tag{5.36}$$

- Loop equilibria with exponential heating

$$H(z) = H_0 e^{-(L-z)/L_{\rm e}}, \quad z \geq 0, \tag{5.37}$$

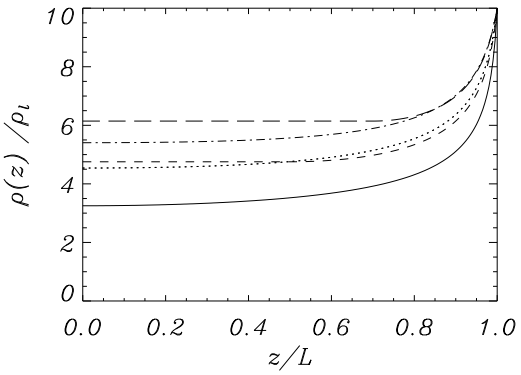

Figure 5.9: Plot of some equilibrium density profiles against the coordinate along the loop z, with footpoints density $\rho_\mathrm{l}/\rho_\mathrm{c} = 10$ and heating magnitude $\bar{H} = 100$. The constant heating profile is plotted with a solid line, while the dashed and long-dashed lines are for heating in a layer of $L_\mathrm{H} = 0.5$ and $L_\mathrm{H} = 0.3$ respectively, and the dotted and dash-dotted lines for exponential heating with $L_\mathrm{e} = 0.5$ and $L_\mathrm{e} = 0.3$ respectively.

$$c_\mathrm{A}^2(z) = c_\mathrm{A}^2(L)\left\{1 + \bar{H}\frac{L_\mathrm{e}^2}{L^2}\left[1 - e^{-(L-z)/L_\mathrm{e}} - e^{-L/L_\mathrm{e}}\left(\frac{L}{L_\mathrm{e}} - \frac{z}{L_\mathrm{e}}\right)\right]\right\}^{2/7}. \tag{5.38}$$

Density profiles for different values of the equilibrium parameters are plotted in Fig. 5.9 for a comparison. A more detailed description and discussion of these and akin equilibria can be found in Priest et al. (2000).

After having described some equilibrium models, its oscillatory properties are studied now. The starting point are the linearized MHD equations for adiabatic perturbations in a uniform, static plasma with unperturbed density ρ_0 and equilibrium magnetic field B_0 pointing along the tube axis. The following partial differential equations are derived for the total pressure perturbation and the velocity components perpendicular to $\mathbf{B}_0$ (the later are necessary, since some of the jump conditions involve these quantities),

$$\left(\frac{\partial^2}{\partial t^2} - c_\mathrm{A}^2\nabla^2\right)p_\mathrm{T} = 0, \tag{5.39}$$

$$\rho_0\left(\frac{\partial^2}{\partial t^2} - c_\mathrm{A}^2\frac{\partial^2}{\partial z^2}\right)\mathbf{v}_\perp + \nabla_\perp\frac{\partial p_\mathrm{T}}{\partial t} = 0. \tag{5.40}$$

p_T has to be determined from Eq. (5.39) in order to calculate the spatial velocity distribution from Eq. (5.40). Since we are looking for stationary states, the time component is Fourier-analysed in the form $e^{-i\omega t}$ (Eq. 2.20), and therefore our aim is to calculate the set of allowed frequencies for the model. The standard method for solving this kind of equations in a region with boundaries is separation of variables, which leads to

$$p_\mathrm{T}(r,\varphi,z) = e^{im\varphi} \times \begin{cases} \displaystyle\sum_{n=1}^{\infty} u_n^{(\mathrm{l})}(r)h_n^{(\mathrm{l})}(z), & r \le -b, \\ \displaystyle\sum_{n=1}^{\infty} u_n^{(\mathrm{c})}(r)h_n^{(\mathrm{c})}(z), & r \ge b. \end{cases} \tag{5.41}$$

Now the procedure developed in Chapter 4 is used to obtain a dispersion relation,

$$\sum_{s=1}^{c} H_{sn} \left\{ \frac{1}{\lambda_n^{(c)}} J_m(\lambda_s^{*(l)} b) K'_m(\lambda_n^{(c)} b) + \frac{1}{\lambda_s^{*(l)}} K_m(\lambda_n^{(c)} b) J'_m(\lambda_s^{*(l)} b) \right\} B_s^* + \sum_{s=c+1}^{\infty} H_{sn} \left\{ \frac{1}{\lambda_n^{(c)}} I_m(\lambda_s^{(l)} b) K'_m(\lambda_n^{(c)} b) - \frac{1}{\lambda_s^{(l)}} K_m(\lambda_n^{(c)} b) I'_m(\lambda_s^{(l)} b) \right\} B_s = 0, \qquad (5.42)$$

which is solved with the techniques described in Sect. 4.4. Here we remark that in this particular problem the solution involves numerical computation of the inner basis function set, $\{h_n^{(c)}(z)\}$. For that kind of profiles is quite more convenient to solve numerically the $1D$ eigenvalue problem, and then use a numerical integration algorithm to calculate the coefficients H_{nm} of Eq. (5.42). We performed that task with a code based in the NAG routines.

5.2.2 Dispersion relations for uniform heating

Now it is time to solve Eq. (4.120) and find the eigenfrequencies of the problem with constant heating along the loop, while in previous sections the other aspects of the solution are studied. The first important parameter is the loop radius, b, which can be expected to have a relevant impact only for $b/L \approx 1$, far from the typical values, that are $b/L \approx 10^{-2}$ (see for example Aschwanden et al. (2002), who present an extensive compilation of observed oscillating coronal loops and their physical parameters). In Fig. 5.10 the dispersion relations have been plotted against b/L keeping all the other parameters fixed; the main conclusion from these panels is that the frequencies do not drastically depend on this parameter. Notice that for the values of radius and density used in the plot there is only one trapped oscillatory mode in each symmetry (the modes with $m \neq 0$ have a very similar frequency in the realistic range of radius of the loop), all the higher harmonics are leaky under these conditions, which are typical of coronal flux tubes.

The next effect to take into account is the amount of heating, assumed constant all along the loop in this section. The behaviour of the frequency of the kink even mode when the heating magnitude ($\bar{H}$) is changed is plotted in Fig. 5.11a. Contrary to what happened with the loop radius b/L, the frequency is shifted significantly when the parameter $\bar{H}$ is modified. To understand the obtained curve it is very convenient to have a look on the modifications that this parameter induces in the equilibrium: the main effect of the addition of heating in the equilibrium configuration is to raise the temperature in the apex of the loop, and therefore by Eq. (3.4), to lower the density in the summit, which value is plotted in Fig. 5.11b. Moreover, the equilibrium density profile is almost flat at the top of the loop ($z = 0$) and increases very fast near the loop footpoints ($z = L$) to reach the value $\rho_{\rm l}$ (see Fig. 5.9). A decrease of the loop density induces a rising in the frequencies in a homogeneous loop (Díaz, Oliver & Ballester 2003), so this can explain the main effect in Fig. 5.11a: the higher the heating parameter the higher the frequency. Also notice that for large values of $\bar{H}$ an increase in the heating produces very little change on the summit density and, as a consequence, in the frequency of the resulting fast modes.

Finally, the effect of modifying both the footpoint density and the heating constant can be seen in the surface plots of Fig. 5.12. The first remarkable fact is that the frequency (and

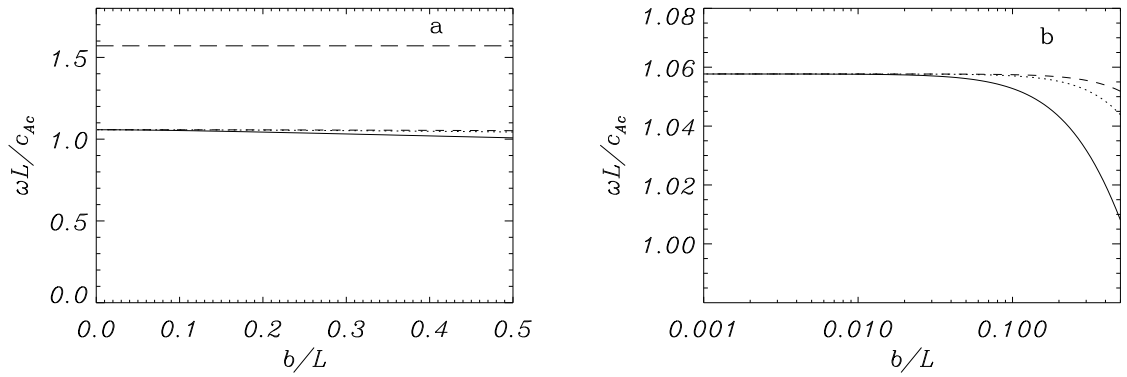

Figure 5.10: Constant heating along the loop: **a)** Plot of the dispersion relation against the loop radius, b/L, for the fundamental kink even mode ($m = 1$, solid line), the first fluting mode ($m = 2$, dotted line) and the second fluting mode ($m = 3$, dashed line). The values for the equilibrium profile have been chosen as $\rho_l/\rho_c = 10$ and $\bar{H} = 100$. Notice that the sausage mode $m = 0$ is leaky for all the values of b/L. **b)** Zoom of panel **a)** in semilogarithmic scale.

therefore the period) of the modes depend heavily on these parameters, so the frequencies are significantly shifted when these parameters are modified. However, there are no trapped modes for loops with a very small density enhancement from the coronal density, i.e. all the oscillatory fast modes are leaky and are shown in the panels of Fig. 5.12 as a horizontal plane with $\omega = \omega_{\rm cut}$. The change of a mode from trapped to leaky can be due to a low footpoint density, but also due to a very efficient heating mechanism that lowers the summit density too much (even if the footpoint density is high enough): for example, if a footpoint density of $\rho_l/\rho_c = 4$ the fundamental mode is trapped until the heating constant reaches the value $\bar{H} \approx 3\,500$ and then for higher values of $\bar{H}$ the summit density has become too low to sustain the mode. On the other hand, for very dense tubes ($\rho_l > 15\rho_c$) the first harmonic is also trapped for low values of the heating parameter (Fig. 5.12b).

5.2.3 Dispersion relations for non-uniform heating profiles

After having studied the solutions of the dispersion relations Eqs. (4.120) for the constant heating problem, we next describe the eigenmodes for coronal loops with the equilibrium profiles of Sect. 3.2.4 and 3.2.5, namely, heat only in a layer of length $L_{\rm H}$ and heating with an exponential decrease $L_{\rm e}$, respectively.

The main difference of the the resulting equilibrium profiles is that the density in the upper parts of the loop is increased respect to the value of the constant heating corresponding model (Fig. 5.9), and the consequence of that fact is that the frequencies of the modes tend to be lowered (Díaz et al. 2002). This prediction is easily checked in Fig. 5.13, in which it is clear that the higher the layer, the higher the frequency. It is also clear that when the layer height tends to zero, the results for the homogeneous tube are recovered (in this figure the frequency of the homogeneous tube would be a horizontal line with $\omega L/c_{\rm Ac} = 0.670$, since it would not matter the numeric value of the heating under those conditions of uniform density).

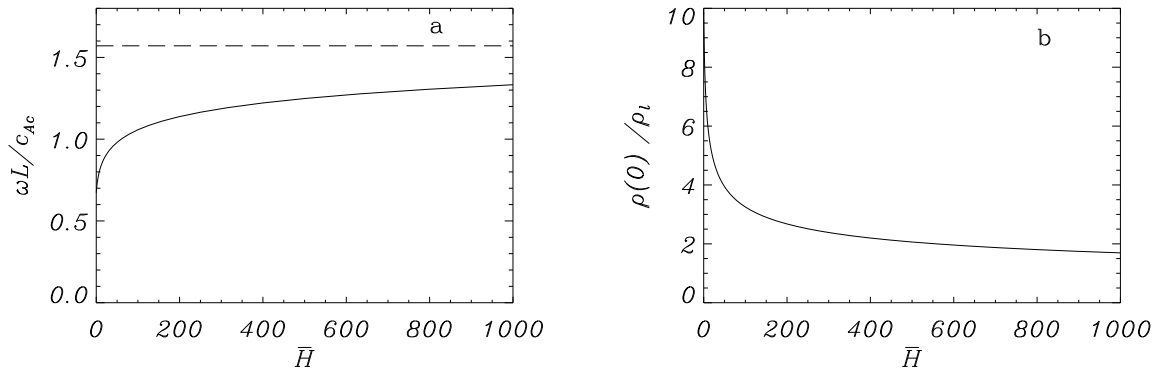

Figure 5.11: Constant heating along the loop: **a)** frequency of the fundamental kink even mode vs. the heating magnitude, $\bar{H}$, for the set of parameters $b/L = 0.015$ and $\rho_l/\rho_c = 10$. **b)** Summit density ($\rho(0)/\rho_l$) vs. the heating magnitude for the same parameters.

Regarding the exponentially decreasing heating model, the resulting solutions are plotted in Fig. 5.14. The results are quite similar to the ones of heating in a layer, although it is easy to check that the frequencies tend slowly to the uniform heating when L_e is increased. Anyway, there are only minor differences between these two models under this point of view.

From the previous figures it is straightforward to infer that this modification of the equilibrium profiles is a first order effect on the frequencies of the oscillatory modes, and there are certainly important deviations from the results for a homogeneous loop (Edwin & Roberts 1983, Díaz et al. 2003). The main point is that the density near the apex is modified, so it can be calculated how the periods change from the results from the homogeneous tube with the footpoints density and the summit density (Table 5.3). The results clearly show that it is quite more relevant to calculate the frequencies and the periods using a homogeneous flux tube with the summit density rather than the footpoint density or the density of the plasma that is near the photosphere (which is quite easier to measure from current observations), and also that under these conditions, there is not a high quantitative difference in using the homogeneous flux tube model, although the existence of other non-leaky modes and other features described in Díaz et al. (2003) should be taken into account if that simplification is carried out.

Another important fact from Table 5.3 is that the differences between the different types of models are mainly due to the different changes in the summit density. One may wonder if this kind of models could be used to make some loop seismology: let us assume that the summit and footpoints equilibrium density ($\rho(0)$ and ρ_l) are known. Therefore, from equilibrium considerations we can deduce the values of the heating constant (not currently measured), or a relation of it and L_H or L_e, and finally calculate the resulting oscillatory periods. However, it is even more interesting the following situation: let us assume that the summit and footpoint density have been measured, and that we also know the period (frequency) of the kink fundamental mode of oscillation (the magnetic field and loop length are also necessary). For a numerical example, for a coronal loop of radius $b/L = 0.015$ with $\rho_l/\rho_c = 10$ and $\rho(0)/\rho_c = 6$ the uniform heating constant must be $\bar{H} = 9.95$, and therefore the fundamental mode has a frequency $\omega L/c_{Ac} = 0.826$, but if we assume that the heating is in a layer, then the same summit density and frequency is obtained if $\bar{H} = 10.46$ and $L_H/L = 0.97$ (that is, a bit higher heating in almost all the loop),

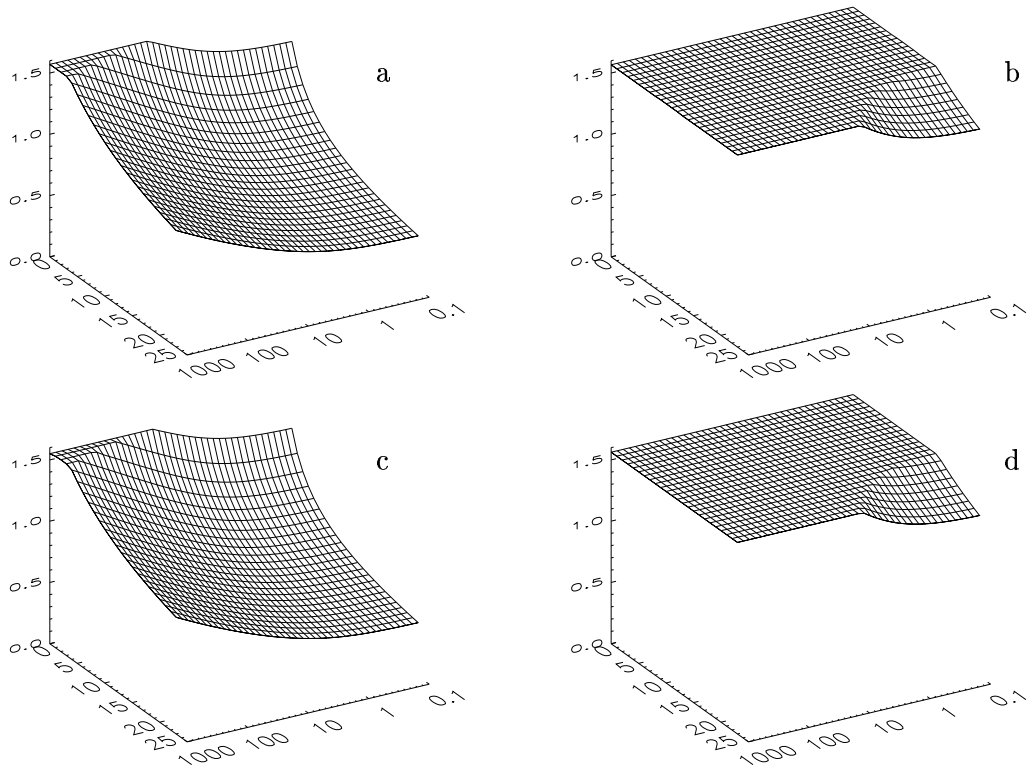

Figure 5.12: Constant heating equilibrium profile: frequency of the **a)** fundamental kink even mode, **b)** the first kink harmonic, **c)** fundamental fluting ($m = 2$) even mode and **d)** the first fluting ($m = 2$) harmonic vs. the heating magnitude ($\bar{H}$) and the footpoints density ($\rho_{\rm l}$) for a loop radius of $b/L = 0.015$. The flat surfaces stand for the regions where the mode has gone through a cut-off (there should not be any point there at all).

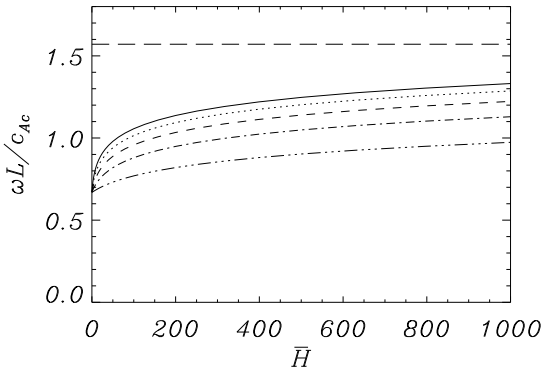

Figure 5.13: Frequency of the fundamental kink even mode for the set of parameters $b/L = 0.015$, $\rho_{\rm l} = 10$ and $L_{\rm H}/L = 1$ (solid line, which is exactly the uniform heating model whose result is plotted in Fig. 5.11a), $L_{\rm H}/L = 0.8$ (dotted line), $L_{\rm H}/L = 0.6$ (dashed line), $L_{\rm H}/L = 0.4$ (dot-dashed line) and $L_{\rm H}/L = 0.2$ (dot-dot-dashed line). Notice that for $\bar{H} \to 0$ the result of the homogeneous tube ($\omega L/c_{\rm Ac} = 0.670$) is recovered for all the models.

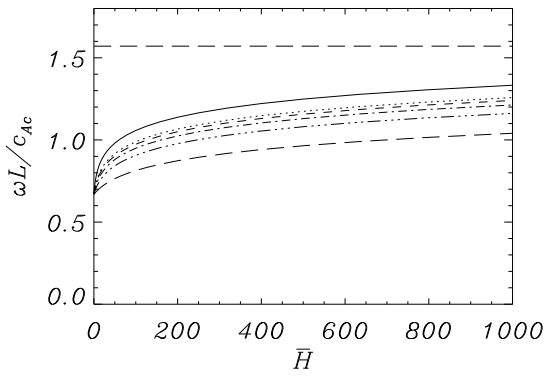

Figure 5.14: Frequency of the fundamental kink even mode for the set of parameters $b/L = 0.015$, $\rho_1 = 10$ and $L_e/L = 1$ (dotted line), $L_e/L = 0.8$ (dashed line), $L_e/L = 0.6$ (dot-dashed line), $L_e/L = 0.4$ (dot-dot-dashed line) and $L_e/L = 0.2$ (long dashed line). The result for the corresponding uniform heating model (Fig. 5.11a) has also been plotted in solid line. Again, for $\bar{H} \to 0$ the result of the homogeneous tube is recovered for all the models.

Table 5.3: Period of kink fundamental modes for a loop with $b/L = 0.015$ and physical parameters $\rho_c = 8.37 \times 10^{-13}$ kg/m^3, $L = 65 \times 10^6$ km and $B_0 = 10$ G, so the Alfvén speed is $c_A = 1252$ km/s. The type of equilibrium model can be "const" (constant heating), "layer" (heating in a layer from the footpoints) and "expon" (exponentially decreasing heating from the footpoints), ρ_1 and $\rho(0)$ are the equilibrium densities in the footpoints and the summit respectively and finally, T is the period of the corresponding model, while T_{hl} and T_{h0} are the resulting periods for a homogeneous loop with the footpoints density value and the summit value respectively.

Type	$\bar{H}$	L_H/L	L_e/L	ρ_l/ρ_c	$\rho(0)/\rho_c$	T_{hl} (min)	T_{h0} (min)	T (min)	$\Delta T/T_{0h}$ %
const	10			10	5.99	8.12	6.47	6.58	1.7
const	100			10	3.25	8.12	5.05	5.14	1.8
const	500			10	2.06	8.12	4.28	4.35	1.6
layer	100	0.25		10	6.67	8.12	6.78	6.79	0.1
layer	100	0.50		10	4.75	8.12	5.87	5.89	0.3
layer	500	0.25		10	4.47	8.12	5.73	5.74	0.2
expon	100		0.25	10	5.81	8.12	6.39	6.44	0.8
expon	100		0.50	10	4.54	8.12	5.76	5.84	1.4
expon	500		0.25	10	3.81	8.12	5.34	5.41	1.3

since we have two constraints for the only remaining parameters. In fact, these calculations demonstrate that the relevant parameter for this kind of models is the summit density, as it can be easily checked in Table. 5.3.

On the other hand, it is interesting to investigate the effect in the frequency of changing the heating profile maintaining the apex density, which is plotted in Fig. 5.15a. The correction in frequency is quite small (of the order of 1%, as shown in Table 5.3), although the footpoint density is certainly modified (Fig. 5.15b). Therefore, our assertion that the most important parameter is the apex density for this kind of models is directly checked.

5.2.4 Spatial structure

It must be taken into account that a solution in the form of Eq. (4.80) is not a separable function in r and z, so the spatial structure is better represented in a surface plot. However, it is also very convenient to have a look at the numerical solution for the inner basis functions, $h_n^{(1)}(z)$, obtained

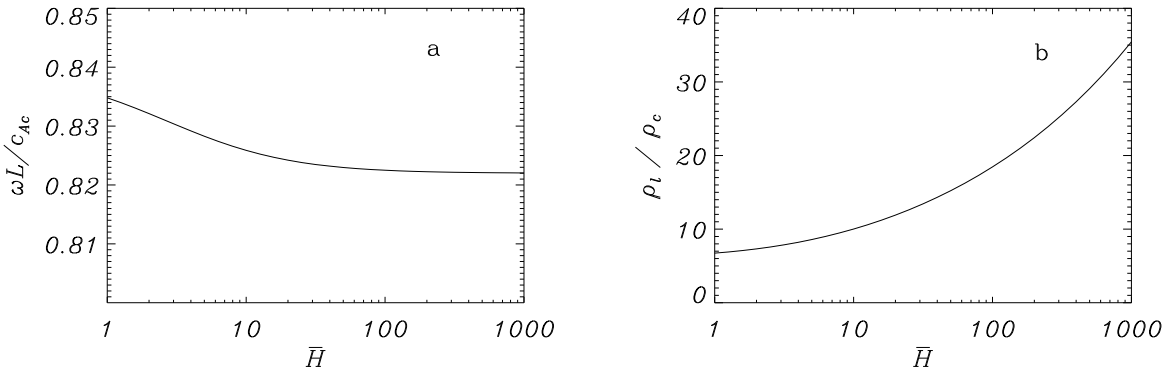

Figure 5.15: **a)** Frequency of the fundamental kink even mode vs. the heating magnitude $\bar{H}$, for the set of parameters $b/L = 0.015$ and $\rho(0)/\rho_c = 6$. **a)** Footpoint density (ρ_l/ρ_c) vs. the heating magnitude for the same parameters. Notice that this footpoint density is really changed while the frequency remains quite similar to the one without heating pointing out that this density is not a relevant parameter.

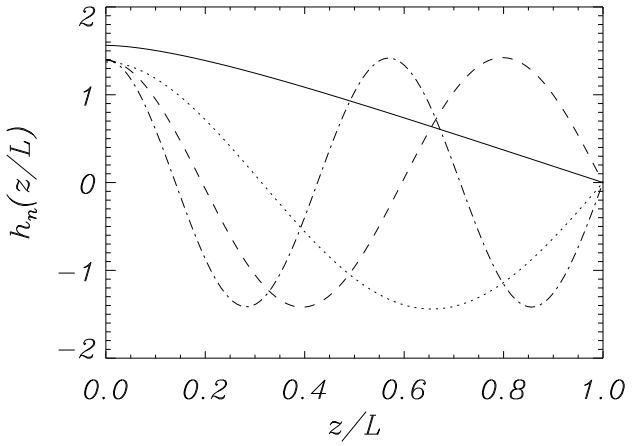

Figure 5.16: Plots of the 4 inner basis functions $h_n^{(1)}(z)$ with the lowest eigenvalues for the set of parameters $\rho_l = 25$ and $\bar{H} = 500$, with an arbitrary fixed frequency $\omega L/c_{Ac}$=1. The corresponding eigenvalues are $\lambda_1^{(1)} = 2.212i$ (purely imaginary), $\lambda_2^{(1)} = 3.942$, $\lambda_3^{(1)} = 7.424$ and $\lambda_4^{(1)} = 10.695$.

from Eq. (4.95), some of which are represented in Fig. 5.2.4. Typically, there is only one basis function with a complex eigenvalue (only $\lambda_1^{(1)}$ is purely imaginary). It is also remarkable that the order of the basis function is the same that the number of extrema displayed in Fig. 5.2.4. However, it must be pointed out that these basis functions are not quite different from the simple Fourier basis functions of the coronal region, described by Eqs (5.7)–(5.8).

The typical spatial structure of these modes in shown in Fig. 5.17. Notice that in this symmetry, the normalized perturbed velocity is higher than the total pressure perturbation, unlike in the Cartesian geometry, in which the three quantities are of similar magnitude (see Chapter 6). Since all the trapped modes are kink or fluting, both polarities are present for each mode, and are roughly of the same magnitude; therefore the polarisation of a mode cannot be used to distinguish its type (fast, slow or Alfvén) in these coronal loops. Also the r-component has no derivative on the tube boundary and the φ-component is not continuous on this surface; this behaviour is in accordance with the boundary conditions Eq. (4.40).

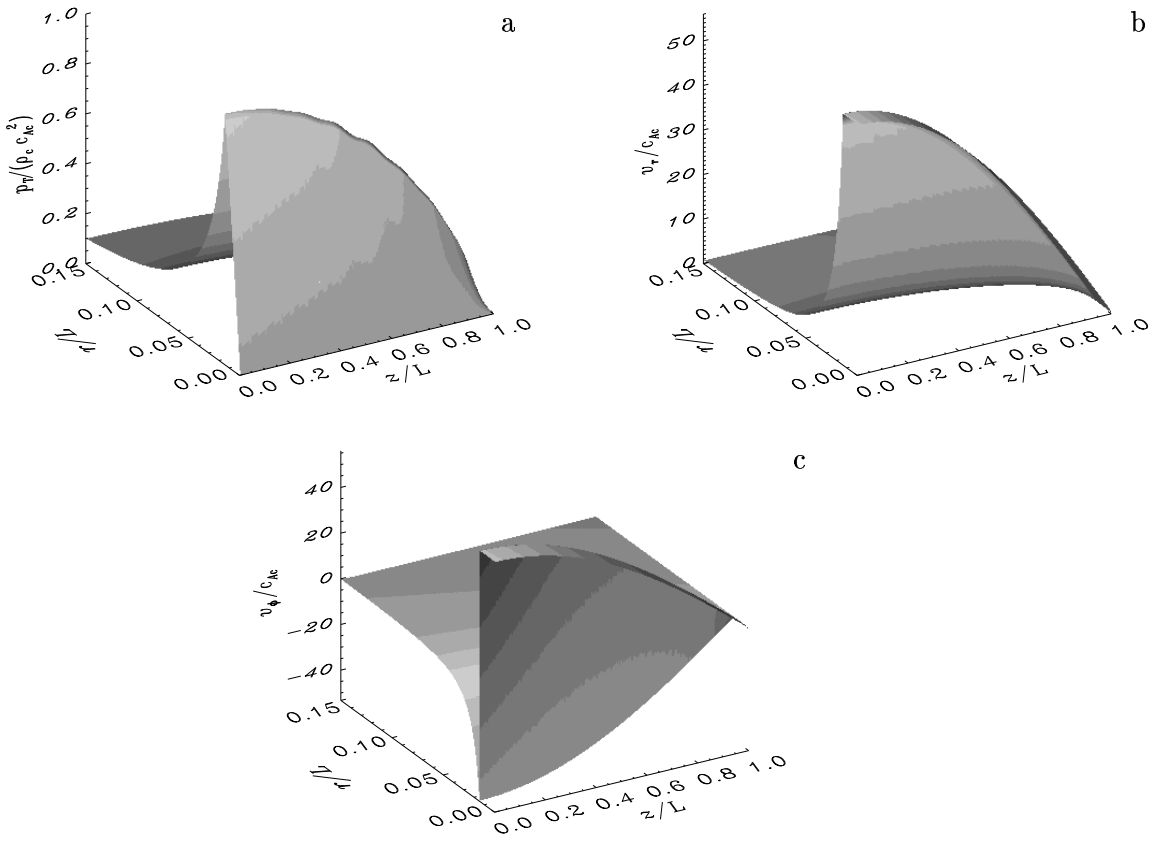

Figure 5.17: Surface plots of perturbed magnitudes of the fundamental kink even mode for the set of parameters $b/L = 0.015$, $\rho_1 = 10$ and $\bar{H} = 100$ ($\omega L/c_{\rm Ac} = 1.058$). Panel **a)** corresponds to the total pressure perturbation $p_{\rm T}/(\rho_{\rm c} c_{\rm Ac}^2)$, panel **b)** to $v_r/c_{\rm Ac}$ and panel **c)** to $v_\varphi/c_{\rm Ac}$.

It is also important to remark that the mode amplitude decreases smoothly along the loop (the line-tying boundary conditions Eq. (4.57) demand that in the footpoints the perturbations must vanish), even having a density enhancement near the footpoints. Since the locations in the loop with higher density tend to oscillate also with higher amplitude, the footpoints should have higher amplitude than the loop summit, but the line-tying boundary conditions demand that the amplitude must vanish at the photospheric surface, so the amplitude decreases when we move further from the loop summit and no bumps are observed near the footpoints.

The spatial structure of the resulting modes for the other equilibrium profiles described in Section 3.2 is quite similar to the one of the constant heating problem (Fig 5.17): the fundamental mode has only one extremum in the center of the loop, and outside the loop boundary the perturbation vanishes in a short distance (usually two or three times the loop radius). Obviously the structure along the magnetic field is changed slightly, but it is not a relevant modification and observations could not distinguish between these spatial profiles and the ones of constant heating of Fig 5.17.

5.2.5 Effects of the addition of a chromospheric layer

The photosphere-corona transition is not as abrupt as it has been modelled here (via the line-tying boundary condition), so it is worthwhile studying the modifications that a thin dense layer modelling the chromosphere induces in the modes described in this work. In this section we consider a chromospheric layer of uniform density $\rho_{\rm ch}$ and height $H_{\rm ch}$. For these parameters we use as numerical values $\rho_{\rm ch}/\rho_{\rm c} = 200$ and $H_{\rm ch}/L = 0.08$, since a typical height of $H_{\rm ch} = 5.2$ Mm is quite adequate for the chromospheric layer and $L = 65$ Mm, as was measured for the loop observation described in Nakariakov et al. (1999). However, it should be noticed that the height and density of this layer are far from uniform, and more accurate models of the chromospheric region should drop the assumption of constant density $\rho_{\rm ch}$ used here.

First of all, it can be computed the frequency shift induced by this addition in the previous models. For example, for a uniformly heated loop with $\bar{H} = 100$ and $\rho_{\rm l} = \rho_0(L - H_{\rm ch}) = 10$ (so $\rho_0(0)/\rho_{\rm c} = 3.25$), we had $\omega L/c_{\rm Ac} = 1.058$, while the addition of the previously described chromospheric layer shifts the resulting frequency to $\omega L/c_{\rm Ac} = 1.034$ (lower because we have increased the density in some places). Under this conditions, the change in the resulting periods would be $\Delta T/T_{0\rm h} = 2.3\%$, so the correction is of the order of the ones introduced by the consideration of different heating mechanisms.

However, it is also interesting to consider that on the chromosphere layer boundary the density is continuous. Therefore, to reach the same summit density of $\rho_0(0)/\rho_{\rm c} = 3.25$, it must be imposed that $\bar{H} = 4.32 \times 10^6$ (extremely high compared with the values used through this Thesis) and the resulting shifted frequency is $\omega L/c_{\rm Ac} = 1.051$, which is only shifted in period $\Delta T/T_{0\rm h} = 0.6\%$. Clearly, to reach such a requirement in the equilibrium density, the heating must be extremely high, and as a consequence, the profile is almost flat with a high derivative near the chromospheric layer boundary.

In conclusion, the addition of a dense chromospheric layer in the footpoints does not change very much the overall picture, and this result is in coherence with the one described in Díaz et al. (2003). However, more realistic chromospheric models should be used to check this conclusion, although it is not expected from the results presented here that more accurate models would induce any substantial changes.

5.2.6 Conclusions

We have developed a semi-analytical model for MHD oscillations (low-β limit) of straightened coronal loops with structure along the magnetic field because of density variations. We found more convenient to solve numerically only one eigenvalue ordinary differential equation than the whole coupled partial differential equation, mainly because the properties of the solution of a second order ordinary differential equation are well-known. We have applied this model to investigate the oscillatory properties of coronal loops with different heating profiles assuming constant cross-section, neglecting radiative terms in the energy equation and gravity in the balance equation. The main conclusions of these models are summarized now:

1. Few modes are trapped under coronal loop conditions. Only the fundamental kink and fluting modes can be sustained, except for very dense coronal loops, in which some higher

harmonics might also be trapped.

2. The radius of the loop has a very little effect on the oscillatory properties, provided is small compared with the loop length. Therefore, the oscillatory frequencies would not be modified substantially if the coronal loop was made of filaments with smaller radius (unless collective effects change a lot the description).

3. The frequency of the modes is very sensitive to variations on the heating magnitude and the footpoint density, and the results are far from the ones of a homogeneous tube.

4. However, the frequency is very similar to the one of a homogeneous tube with density equal to the apex density. The reason of this result is that the equilibrium model has a significant density enhancement only near the footpoints, but the MHD oscillatory modes are constrained by the line-tying condition near them, so the amplitude is still small in that region. It must be emphasized that if the homogeneous density flux tube results are applied, the density must be measured near the apex, not in the footpoints, despite being more difficult to estimate.

5. The other studied heating profiles do not introduce too many modifications. It seems quite difficult to estimate the heating profile from the observational periods, although some information might be obtained about the magnitude of the heating term.

6. The addition of a very dense layer in the footpoints simulating the chromosphere only introduces slight corrections (because of the restriction of the amplitude near the footpoints due the line-tying condition).

The plots in Fig. 5.12 could also be used for loop seismology purposes: given the loop radius (not really relevant, just need to be small compared with the loop length) and the footpoints density and magnetic field, one could infer the heating constant from the shift in frequency from the homogeneous flux tube results. However, it must be remembered that there are many effects that have not been taken into account in this Thesis, like their dynamical or static equilibrium or the existence of plasma flows. In fact, it is still under discussion if these loops are in hydrodynamic equilibrium (Winebarger et al. 2003).

Chapter 6

Fast Magnetohydrodynamic waves in prominence fibrils: Cartesian geometry *

Nature laughs at the difficulties of integration.
Pierre-Simon de Laplace

After having applied the analytical solution to coronal loop oscillations, here we consider the oscillations of another type of solar coronal structure: prominence fibrils. In this Chapter we model a single prominence fibril (a model which is explained in more detail in Sect. 3.3 and which is reviewed in Fig. 6.1) as a Cartesian slab with a density enhancement in a region of width $2W$ centered in the apex and low density plasma in the rest of the slab. The linearized MHD equations governing the oscillatory modes were introduced in Sect. 4.1, basically Eqs. (4.22) and (4.23), then by virtue of separation of variables dispersion relations were found. Now we look for the results of these dispersion relations and to study the properties of their solutions for prominence fibrils.

To perform numerical calculations, the parameter values given in Sect. 3.3 are used. Following Joarder et al. (1997) and references therein, we set $W/L = 0.1$ for a fibril whose length is one tenth the total length of the thin loop (including both the cool and the evacuated parts). In addition, the following density ratios are considered, $\rho_{\rm e}/\rho_{\rm c} = 0.6$ and $\rho_{\rm p}/\rho_{\rm c} = 200$. These variables are useful because the equilibrium magnetic field is uniform and so the Alfvén speed in the hot and cool parts of the loop can be cast as $c_{\rm Ae}^2 = \frac{\rho_{\rm c}}{\rho_{\rm e}} c_{\rm Ac}^2$ and $c_{\rm Ap}^2 = \frac{\rho_{\rm c}}{\rho_{\rm p}} c_{\rm Ac}^2$. All quantities can be non-dimensionalized against L and $c_{\rm Ac}$, and Eq. (4.23) can be solved by analytical or numerical means. There is still a free parameter, namely b/L, whose value must be specified before these equations can be solved to find the eigenfrequencies and spatial properties of the modes. Putting all together, the parameters of our model for solving mathematically Eq. (4.23) and its boundary conditions are $\rho_{\rm p}/\rho_{\rm c}$, $\rho_{\rm e}/\rho_{\rm c}$, W/L and b/L.

*This Chapter is based on: Díaz, A. J., Oliver, R., Erdélyi, R., & Ballester, J.L. "Fast MHD Oscillations in Prominence Fine Structures", 2001a, A&A, 379, 1083 and Díaz, A. J., Oliver, R. and Ballester, J. L. 2003, "Fast MHD Oscillations on a 3-dimensional Prominence Fibril", A&A, 402, 781.

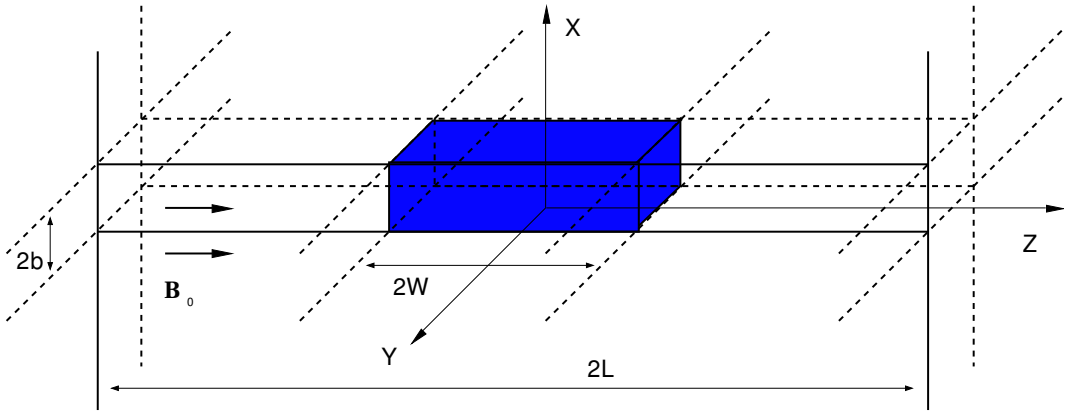

Figure 6.1: Sketch of the equilibrium configuration used in this study. The grey zone represents the cold part of the loop, modeling the prominence fibril. The density in the fibril, $\rho_{\rm p}$, in the evacuated (coronal) part of the loop, $\rho_{\rm e}$ and in the coronal environment, $\rho_{\rm c}$, are all uniform. Moreover, the magnetic field is uniform and parallel to the z-axis and the whole configuration is invariant in the y-direction (after Joarder et al. 1997).

On the other hand, apart from the analytical method, a numerical approach has also been used to solve the partial differential wave equations (Appendix C). There are a few reasons for using numerical techniques: first, if the cold plasma assumption is removed (such as must be done to better describe the real conditions in quiescent prominences), the mathematical problem changes to two coupled partial differential equations which are hard to solve analytically; second, the analytical solution involves large computational efforts when realistic (i.e. small) values of the fibril half-thickness, b, are considered. The advantage of having an analytical formalism to obtain fast mode frequencies is that the goodness of numerical values can be checked.

In this Chapter, first of all the solutions of the dispersion relations are discussed starting with the dependence of the eigenfrequencies on the various parameters of the model. Then, the spatial structure of the perturbed velocity is studied and finally, the theoretical predictions for the oscillatory periods are shown. However, there are two different problems that can be considered: independence on the third spatial coordinate y (Sect. 6.1) and dependence on that direction (Sect. 6.2).

6.1 Solution with no longitudinal propagation ($k_y = 0$)

6.1.1 Dispersion relations

In this section we consider $k_y = 0$, so independence on the y-coordinate is assumed. We do this in order to achieve some insight in the complicated properties of the solutions of this problem, and once we have completed this study, we will cover the solutions with $k_y \neq 0$ in the next Section.

Separation of variables for the perturbed total pressure leads to

$$p_{\rm T}(x,z) = \begin{cases} \displaystyle\sum_{n=1}^{\infty} u_n^{(l)}(x) h_n^{(l)}(z), & |x| \le b, \\ \displaystyle\sum_{n=1}^{\infty} u_n^{(c)}(x) h_n^{(c)}(z), & |x| \ge b. \end{cases} \tag{6.1}$$

Following the procedure explained in Chapter 4, the z-dependent basis functions $h_n(z)$ are described in Sect. 4.5.2 and also the coefficients H_{mn} (with the special cases of Appendix D), while the dispersion relation is deduced in Sect. 4.3.3. However, in that section it was not assumed that $k_y = 0$, so the formulae deduced there are more general and will be used later in this Chapter. If we consider the limit $k_y \to 0$ in Eqs. (4.87) and (4.88), the following expressions are obtained,

$$\sum_{m=1}^{\infty} H_{mn} B_m^{\rm sin} \left[\frac{1}{\lambda_m^{(\rm l)}} \sinh(\lambda_m^{(\rm l)} b) + \frac{1}{\lambda_n^{(\rm c)}} \cosh(\lambda_m^{(\rm l)} b) \right] = 0, \tag{6.2}$$

for sausage modes and

$$\sum_{m=1}^{\infty} H_{mn} B_m^{\rm cos} \left[\frac{1}{\lambda_m^{(\rm l)}} \cosh(\lambda_m^{(\rm l)} b) + \frac{1}{\lambda_n^{(\rm c)}} \sinh(\lambda_m^{(\rm l)} b) \right] = 0, \tag{6.3}$$

for kink modes. By using this notation we are assuming the common terminology by which kink modes stand for even solutions in the direction across the fibril and sausage modes for the odd ones (Fig. 2.5). These two kind of modes become separated because of the symmetry of the problem.

Eqs. (6.2) and (6.3) constitute two infinite systems of homogeneous algebraic equations for $B_m^{\rm sin}$ and $B_m^{\rm cos}$, respectively, which are truncated by taking $B_n^{\rm r} = 0$ ($\rm r = sin, cos$) for $n > N$. It is worth commenting on the number of basis functions, N, to be used when Eqs. (6.2) or (6.3) are truncated. Tests have been done by using 12 and 24 basis functions and the difference in the frequency is of the order of 0.01%. Consequently, frequencies have been computed using 12 basis functions (that is, only values up to $m = 12$ have been retained in Eqs. (6.2) and (6.3)). Regarding the eigenfunctions, $p_{\rm T}$ and v_x are not well reproduced with such a small number of basis functions for realistic values of the fibril thickness ($b/L \simeq 0.001$–0.005) and many more basis functions ($N \sim 100$) are necessary in order to capture well the spatial structure of the modes.

One important result from Sect. 4.1.3 is that under the condition of independence on the y-coordinate the perturtubed velocity component v_y is decoupled from the component v_x, so we obtain $v_y = 0$ for the fast modes and we just have the component v_x left. Then, the dispersion relations can also be obtained starting from the wave equations for the perturbed velocity (Eq. (4.34)), although some properties of the determinants have to be invoked to find the same expressions than Eqs. (4.87) and (4.88) (see Appendix E). Moreover, in the low-beta limit we obtain

$$\frac{\partial p_{\rm T}}{\partial t} = -\rho_0 c_{\rm A} \nabla_\perp \cdot \mathbf{v}_\perp = -\rho_0 c_{\rm A} \frac{\partial v_x}{\partial x} \tag{6.4}$$

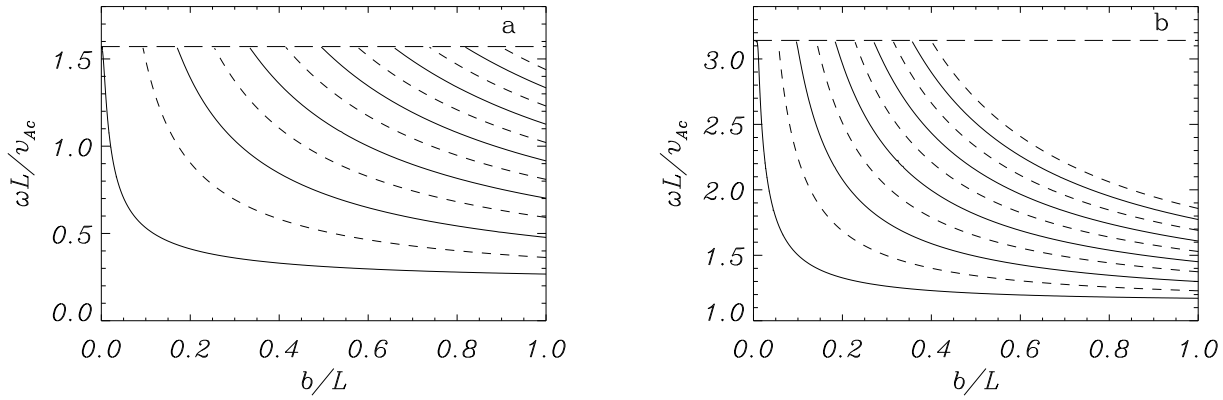

Figure 6.2: Dimensionless frequency, $\omega L/c_{\rm Ac}$, versus half-thickness of the prominence fibril, b/L, for **a)** even modes and **b)** odd modes (only the 5 lower frequency odd modes for each symmetry are shown). These results correspond to $W/L = 0.1$, $\rho_{\rm e}/\rho_{\rm c} = 0.6$ and $\rho_{\rm p}/\rho_{\rm c} = 200$. The solid lines represent kink modes whether the dashed ones are sausage modes. This graphs are similar to the ones in the slab (Fig. 2.8) for this values of the parameters.

so the total pressure is directly related to the x-derivative of the only surviving component of the perturbed velocity. When the boundary conditions in Eq. (4.40) are applied, the perturbed velocity must be continuous on the boundary $x = b$, and from Eq. (6.4) its derivative must be continuous too. However, even in this situation of $k_y = 0$, the perturbed pressure has no derivative at the fibril boundary, a fact that was present in the coronal loop problem of previous Chapters and will appear also here.

6.1.2 Dependence of the fast mode on the fibril thickness

We first study the dependence of the mode frequency on the half-thickness of the fibril, b. The analytical results of the dispersion relations Eqs. (4.87) and (4.88) for even and odd modes are plotted separately in Figs. 6.2a and b, which clearly show the presence of frequency cut-offs at $\omega_{\rm cut} = \frac{\pi}{2}\frac{c_{\rm Ac}}{L}$ and at $\omega_{\rm cut} = \pi\frac{c_{\rm Ac}}{L}$, respectively. These upper cut-offs were already discussed by Joarder et al. (1997) and they are important since, for $\omega > \omega_{\rm cut}$, modes become leaky and decay in time by driving waves in the coronal medium. The occurrence of cut-offs is similar to that found for coronal slabs and loops (e.g. Edwin & Roberts 1982, 1983 and Roberts et al. 1984).

It must be emphasized that the difference between the analytical treatment in Joarder et al. (1997) and ours is that those authors just used one basis function for each mode, so their solution does not match properly at the boundary $b = L$ and can be considered a sort of first approximation to the correct solution. From the comparison between Fig. 3 of Joarder et al. (1997) and our Fig. 6.2, it may seem that the proper treatment of this "jump" condition does not give rise to drastic modifications in the frequency of modes, but it will now be shown that this is only the case for unrealistic values of the fibril thickness and that for $2b \leq 500$ km, such as suggested by observations, the ω and spatial properties of fast modes are the wrong ones if conditions (4.40) at $|x| = b$ are not considered. We have replotted Fig. 6.2 using a

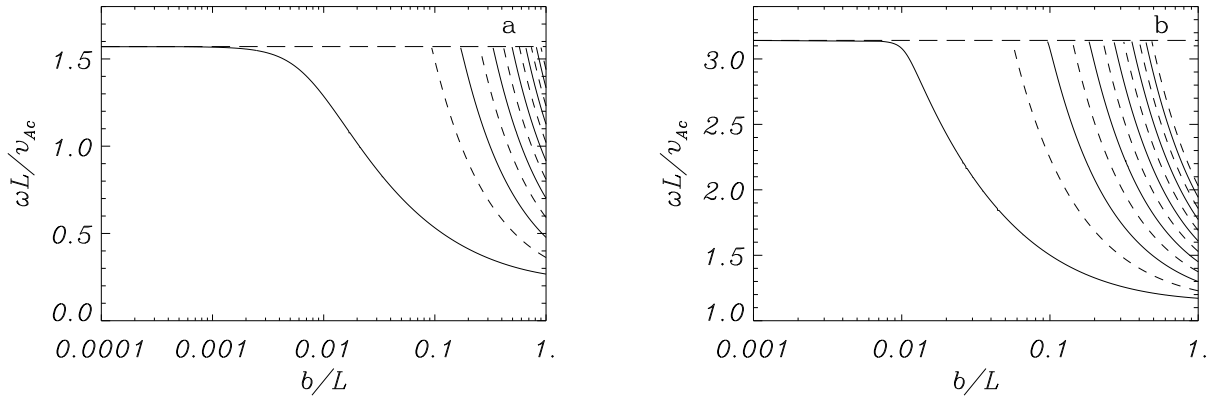

Figure 6.3: Plot of the data in Fig. 6.2 using a logarithmic axis for b/L. Notice that fundamental even and odd modes do not have a frequency cut-off, but exist for very small values of the fibril thickness.

logarithmic axis for the fibril half-thickness (see Fig. 6.3) and it is obvious that the even and odd fundamental modes do not show a frequency cut-off and that, instead, they display a maximum at their respective $\omega_{\rm cut}$, which they approach asymptotically as $b \to 0$. This result is in contradiction with that obtained by Joarder et al. (1997), since their fundamental even and odd modes reach their corresponding cut-off frequency for $b_{\rm cut}/L = 0.08$ and 0.04, and become evanescent for $b < b_{\rm cut}$.

It has been said before that there is no evanescent solution for $\omega L/c_{\rm Ac} > \pi/2$ (even modes). In this situation the fundamental basis function becomes leaky and, because the sum in Eq. (4.77) always includes this first basis function, no solution satisfies the requirement $|u| \to 0$ exponentially as $|x| \to \infty$. That is the reason why all harmonics in Fig. 6.2 have the same cut-off frequency. Odd modes display a similar behaviour, but taking into account that the cut-off frequency is $\omega L/c_{\rm Ac} = \pi$. Notice that this behaviour is different from the homogeneous slab in Appendix F, where each eigenfunction has its own cut-off frequency.

6.1.3 Exploring the parameter space

We next investigate the effect of modifying the other parameters, $\rho_{\rm p}/\rho_{\rm c}$, $\rho_{\rm e}/\rho_{\rm c}$ and W/L, with respect to the values considered so far. Some simulations have been performed with other possible combinations of these parameters since, in real prominences, different fibrils are probably characterized by different density and/or length. Our approach is to concentrate on the frequency of modes and to compare the resulting $\omega L/c_{\rm Ac}$ vs. b/L diagrams with Fig. 6.2.

Varying the quantity $\rho_{\rm e}/\rho_{\rm c}$ does not give rise to important changes in ω, specially because one does not expect the density in the coronal environment and in the evacuated part of the fibril to be much different from one another. Calculations have also been carried out with $\rho_{\rm e}/\rho_{\rm c} = 0.3$ and $\rho_{\rm e}/\rho_{\rm c} = 1$, but the differences are very small (sometimes under our working precision), so we can concentrate on studying the dependence on the remaining parameters.

The effects of modifying the other two parameters are more important and, for example,

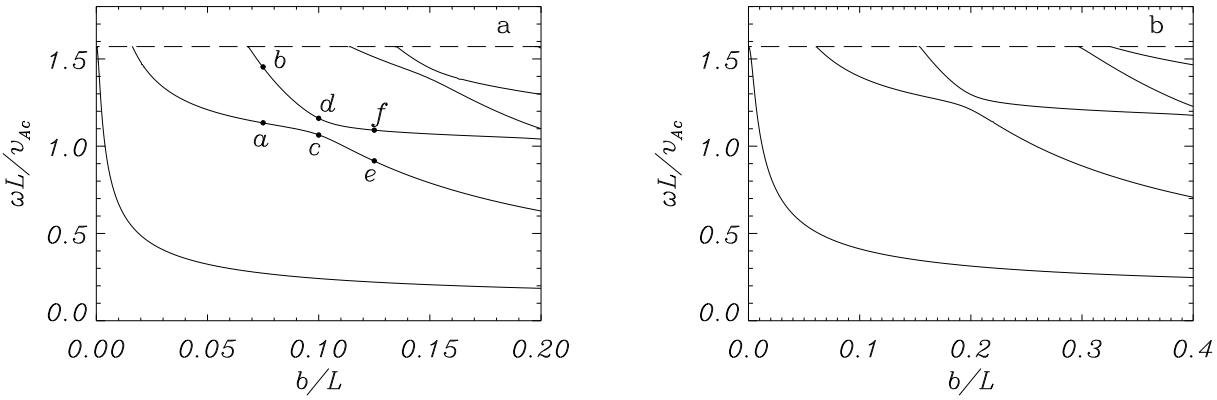

Figure 6.4: **a)** Variation of frequency with the fibril half-thickness for kink even modes ($W/L = 0.1$, $\rho_e/\rho_c = 1$ and $\rho_p/\rho_c = 1000$). Dots are used to mark solutions for which the spatial profile of v_x is plotted in Fig. 6.5. **b)** Same plot for the set $W/L = 0.2$, $\rho_e/\rho_c = 0.6$ and $\rho_p/\rho_c = 200$. In these plots, a range of b/L smaller than that used in Figs. 6.2 and 6.3 has been selected to better show the behaviour for realistic values of this parameter.

by increasing the ratio of prominence to coronal density from 200 to 1000, Fig. 6.2 changes to Fig. 6.4a. It can be appreciated that, for a fixed fibril thickness, the number of normal modes supported by the fibril increases when ρ_p/ρ_c is increased (something similar happens with the parameter W/L, cf. Fig. 6.4b). Therefore, for realistic values of $b/L \leq 0.01$, higher harmonics could also be excited in a prominence fibril.

Another noticeable effect in Fig. 6.4 is *mode coupling* between fast modes, which arises from their different spatial structure. Let us concentrate on the first and second kink even harmonics for $b/L = 0.075$ (points a and b in Fig. 6.4). Their corresponding eigenfunctions, shown in Figs. 6.5a and b, have two extrema in the x-direction and two extrema in the z-direction, respectively. During the coupling (points c and d in Fig. 6.4, $b/L = 0.1$) the two modes start to interchange their spatial structure (cf. Figs. 6.5c and d) and the extrema do not lie parallel to either the x- or z-axis. Finally, after the coupling (points e and f in Fig. 6.4, $b/L = 0.125$) the first harmonic displays two extrema in the x-direction, whereas the second harmonic has two extrema in the z-direction (Figs. 6.5e and f) and the structure interchange is finished. It is clear that this coupling is only possible because of the summation of different basis functions in Eqs. (4.77) and (4.79), which is forced by the fact that solutions must be continuous at the interfaces $|x| = b$. Obviously, the fundamental mode does not couple to higher harmonics because its spatial shape, with only one maximum, does not allow it to interact with other modes. Anyway, this mode coupling is not relevant in prominence fibril oscillations, because for realistic values of the fibril thickness b, all these modes are leaky.

6.1.4 Spatial structure of eigenfunctions

After having studied the frequencies of the eigenmodes, we next concentrate on the shape of eigenfunctions. First of all, because of the sum in Eq. (6.1), the obtained solutions are not

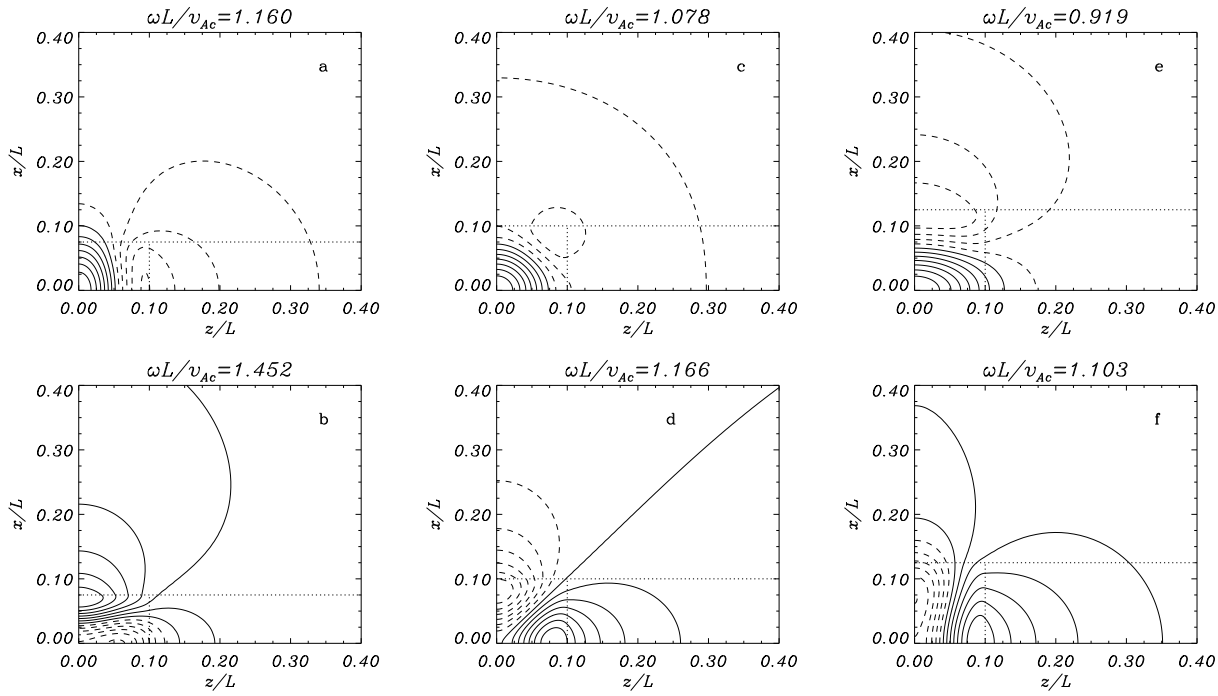

Figure 6.5: Contour plots of v_x at the dots marked in Fig. 6.4a, showing the change in shape of eigenfunctions as the first and second harmonics (kink even symmetry) couple together. These modes correspond to $W/L = 0.1$, $\rho_{\rm p}/\rho_{\rm c} = 1000$ and $\rho_{\rm e}/\rho_{\rm c} = 1$. The dimensionless fibril half-thickness is **a)** and **b)** $b/L = 0.075$, **c)** and **d)** $b/L = 0.1$, and **e)** and **f)** $b/L = 0.125$. Solid and dashed lines represent, respectively, positive and negative contour values, while the thick, solid line corresponds to zero v_x. The boundaries between the dense and evacuated part of the loop and the coronal medium have been plotted using dotted lines.

separable functions in x and z (that is, $v_x(x,z) \neq f_1(x) \cdot f_2(z)$). This point has become clear with the contour plots in Fig. 6.5, specially with panels c and d. First of all, a case in which many modes are not leaky can be studied (Fig. 6.6). Here the four even modes for $b/L = 0.3$ of Fig. 6.2a have been represented in the whole range of the variables (not only in $x \geq 0$ and $z \geq 0$) to better show the properties. It can be seen that the highest the order, the more confined the mode, except for the second sausage mode (Fig. 6.6d), which is near the cut-off frequency and has started to decay slowly (this point will be commented later, specially in Fig. 6.10). Also notice that for this parameter values there are no mode couplings like the ones described in Fig. 6.5, so the order of the mode corresponds to the number of extrema is displays too.

It was mentioned above that the fundamental kink even and odd modes are those suitable for driving oscillations in prominence fibrils, for which b/L is probably smaller than 0.01 (cf. Figs. 6.3 and 6.4), so we will concentrate on describing them. Thus, we start with the first of these modes and represent its spatial structure by means of cuts along the x- and z-directions. Fig. 6.7a, which corresponds to a very thick fibril ($b/L = 0.1$), shows that the velocity amplitude quickly decays across the fibril ($x/L > 0.1$) and that it becomes almost zero at a distance about ten times the fibril half-thickness. Along the loop axis (Fig. 6.7b), v_x also decreases from its maximum value at the fibril centre. However, for a realistic, thin fibril there is a noticeable

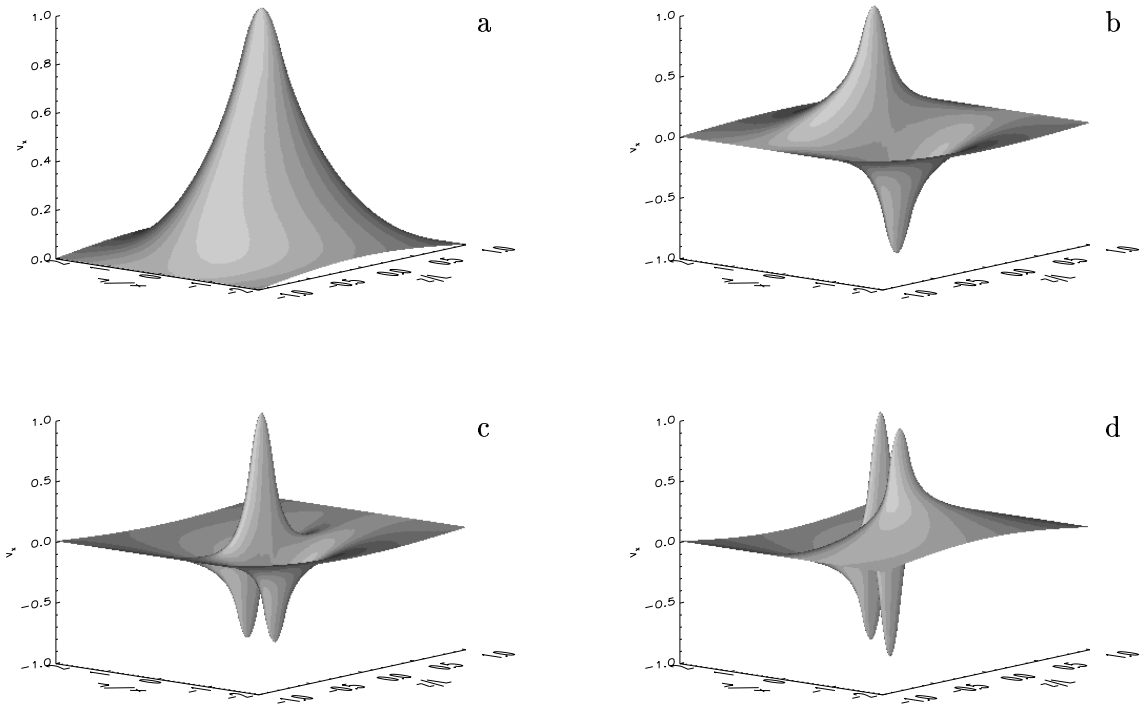

Figure 6.6: Surface plots of the analytical solution for v_x (even modes), in which the set of parameters $\rho_p/\rho_c = 200$, $\rho_e/\rho_c = 0.6$, $W/L = 0.1$ and b/L=0.3 has been selected. **a)** and **c)** are kink modes, while **b)** and **d)** are sausage. In these graphs we have not taken into account the symmetries of the problem, so the whole range of the coordinates has been plotted to better show the structure (although here it is only shown the region $|x| \leq 2L$ to highlight the amplitude of the oscillation near the fibril).

amplitude far away from the dense part (Fig. 6.7c) and it is necessary to move a distance $x \approx 10^3 - 10^4 b$ across the fibril for perturbations to vanish. Therefore, the excitation of this kind of modes in a prominence fibril can also excite perturbations in neighbouring threads and so it is expected that fibrils do not oscillate individually but in groups.

Regarding the kink odd fundamental mode, its spatial structure is such that v_x does not achieve its maximum amplitude at the fibril centre, but somewhere along the thin loop (see Fig. 6.8). In fact, for the values of b/L considered here, the velocity maximum occurs in the evacuated part of the loop rather than inside the cool region and the amplitude in the fibril decreases as the loop thickness is decreased. Thus, because of their small velocity inside fibrils, kink odd modes may be difficult to detect observationally. Also notice that after this transition, the mode resembles the external modes described in Oliver et al. (1993).

Finally, it is worth mentioning what happens when other harmonics approach the cut-off frequency, a situation that can be studied with the numerical code. Just below $\omega_{\rm cut}$ the velocity only vanishes at long distances from the fibril in the x-direction (similarly to the fundamental even kink mode, cf. Fig. 6.7c) and, as $\omega_{\rm cut}$ is exceeded, the mode becomes a free wave and it does not satisfy the boundary conditions $v_x = 0$ as $x \to \pm\infty$. This is shown for the second kink

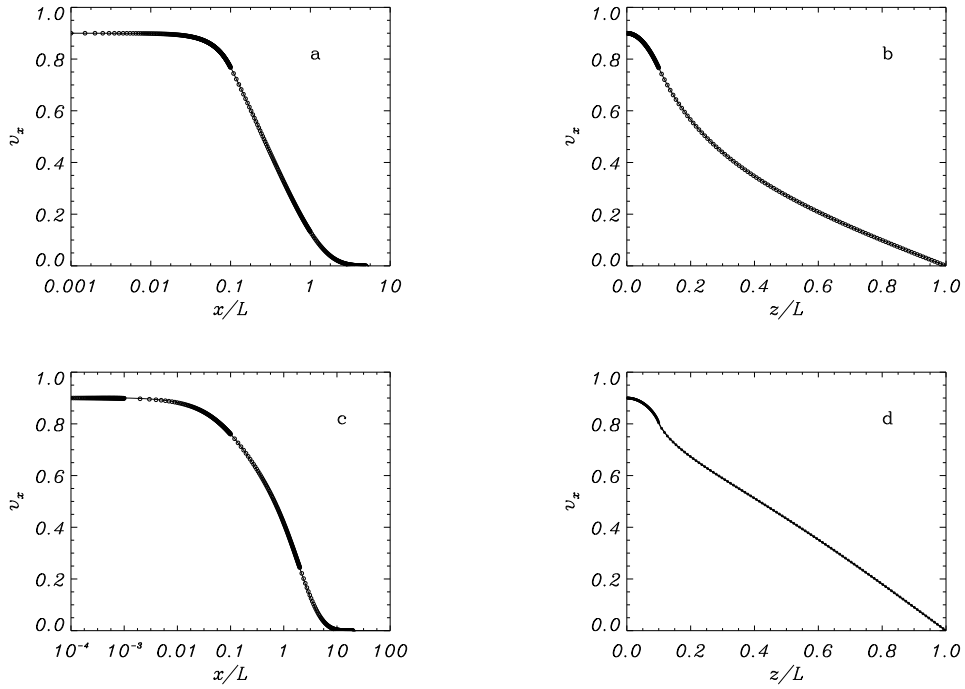

Figure 6.7: The fundamental kink even mode has a single maximum located at $x = z = 0$. The spatial structure of this mode is here displayed for two different values of the fibril thickness through cuts **a)** and **c)** in the direction $z = 0$ (i.e. across the centre of the fibril), and **b)** and **d)** in the direction $x = 0$ (i.e. along the axis of the fibril). **a)** and **b)** v_x for a very thick fibril ($b/L = 0.1$), shown to illustrate the good agreement between the analytical and numerical solutions (solid lines and empty circles, respectively). **c)** and **d)** Analytical and numerical solutions (solid lines and empty circles) for a typical value of fibril thickness, $b/L = 0.001$. The number of basis functions kept to obtain the analytical solution is $N = 70$. Other parameter values used to obtain the two eigensolutions are $W/L = 0.1$, $\rho_{\rm p}/\rho_{\rm c} = 1000$ and $\rho_{\rm e}/\rho_{\rm c} = 1$. The use of various grids of different but uniform mesh sizes to properly capture the spatial structure of these modes is clearly appreciated in the four panels.

even mode of Fig. 6.9 in the panels of Fig. 6.10. In Fig. 6.10a the mode is still far from the cut-off frequency $\omega_{\rm cut}L/c_{\rm Ac} = \pi/2$, so it is confined in the dense part of the fibril. However, in Fig. 6.10b the mode decays very slowly with noticeable amplitude at $x/L = 10$ (more than 1000 times the fibril thickness) and when it is close enough to $\omega_{\rm cut}$ (Fig. 6.10c), it decays too slow to be correctly described with only this region ($H/L = 20$, with $x = H$ the position where the solution is set to zero to represent the evanescent boundary condition in the numerical solution of Eq. C.1). Finally, when the critical value of b/L (the one in which the mode reaches its cut-off frequency) is exceeded the numerical program can only find functions like the one in Fig. 6.10d, clearly telling us that the solution is no longer evanescent but presents oscillations in the x-direction (across the magnetic field). In fact, the frequency given by the numerical code in this figure depends on the position of the border, so it should be regarded as a clue of the behaviour when the cut-off is exceeded because the condition that is being used (Eq. C.1) does not represent a oscillatory mode properly, which could be obtained allowing complex values of the frequency (similar to what we did in Sect. 5.1.3).

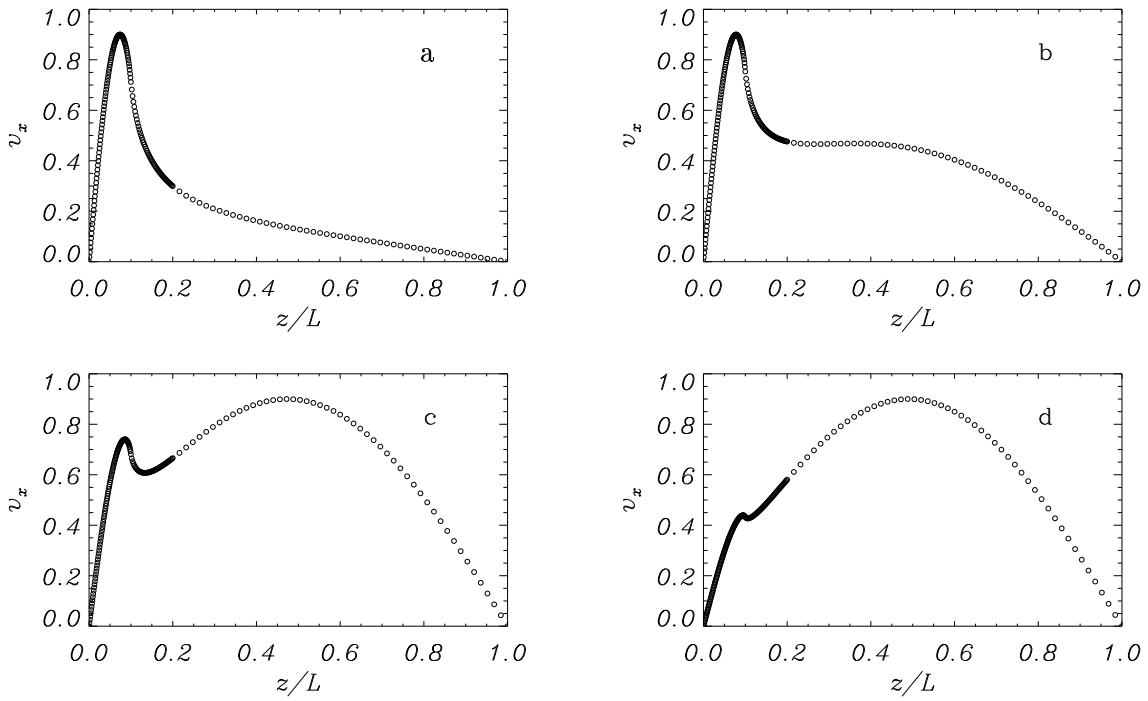

Figure 6.8: Cuts of the velocity of the fundamental kink odd mode along the loop axis, $x = 0$, for $W/L = 0.1$, $\rho_{\rm p}/\rho_{\rm c} = 1000$, $\rho_{\rm e}/\rho_{\rm c} = 1$ and **a)** $b/L = 0.005$ ($\omega L/c_{\rm Ac} = 2.063$), **b)** $b/L = 0.002$ ($\omega L/c_{\rm Ac} = 3.036$), **c)** $b/L = 0.0015$ ($\omega L/c_{\rm Ac} = 3.127$), and **d)** $b/L = 0.001$ ($\omega L/c_{\rm Ac} = 3.140$). The four solutions have been computed numerically using a mesh of non-uniformly spaced points The mode also expands in the x-direction when b/L is raised (not shown in plots).

6.1.5 Oscillatory period

We finally concentrate on the periods of oscillation for various parameter values and compare them with observational data (see Table 6.1). To do such calculations, other parameters not relevant to the mathematical solution due to non-dimensionalization must be set: $\rho_{\rm c}$, L and B_0 (notice that the coronal Alfvén speed is just $c_{\rm Ac} = B_0/(\mu\rho_{\rm c})^{1/2}$). These quantities should also be taken into account when adjusting the results for periods in Table 6.1. Although the equilibrium configuration used lacks some of the properties of a real fibril, like its three-dimensional structure or the pressure gradient force, a comparison can be made. First of all, the parameters in Joarder et al. (1997) have been taken and, by comparing with their Table I, it turns out that periods are in the same range when the MHD boundary conditions at the loop-corona interface are included. The reason for this behaviour is that the modes in Joarder et al. (1997) essentially correspond to the dominant terms in Eqs. (4.77) and (4.79) and so provide a rough approximation to the mode frequency.

Signatures of periods in the 5–15 min range (such as the ones in Table 6.1) have been abundantly reported in the literature, e.g. the 8–9 min and 14–16 min oscillations observed by Yi et al. (1991) and Yi & Engvold (1991) and the range of periods is in agreement with current observations (see Table 1.1). Obviously, this does not mean that waves detected by these authors are actually fast modes and, until better models are considered and better experimental

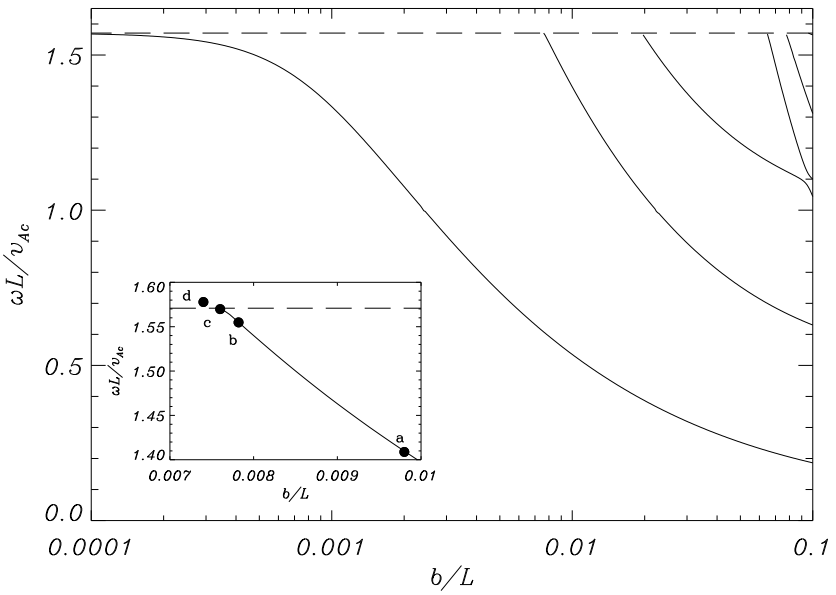

Figure 6.9: Variation of frequency with the fibril half-thickness for kink even modes ($W/L = 0.2$, $\rho_e/\rho_c = 1$ and $\rho_p/\rho_c = 1000$). Dots are used to mark solutions for which the spatial profile of v_x is plotted in Fig. 6.10. Notice that dot marked **d** is not found in the analytical solution used in this plot, but it is included to show where the corresponding eigenfunction given by the numerical program would be (in fact the value of the frequency depends on the position of the border of the region, see the main text).

information becomes available, it will be difficult to make a true comparison between theoretical and observational results. However, the apparent matching between the observed ranges and the theoretical results encourages further work.

6.2 Solution with longitudinal propagation ($k_y \neq 0$)

After having studied the solution with no dependence on the y-coordinate, we now consider $k_y \neq 0$. Using the total pressure as the dependent variable, a 3-dimensional wave equation is obtained and by solving it we construct a model with dependence on the three spatial coordinates for the fast MHD modes of oscillation of the fibril. Here, the simplest example is considered: an equilibrium invariant in the y-direction (that leads to waves propagating with dependence in the form $e^{-ik_y y}$).

6.2.1 Dispersion relations

The procedure for finding the solutions to this problem is the same that was applied in the previous section. The starting wave equations are Eq. (4.22) and Eq. (4.23), and the standard method for solving this kind of partial differential equations in finite region is separation of

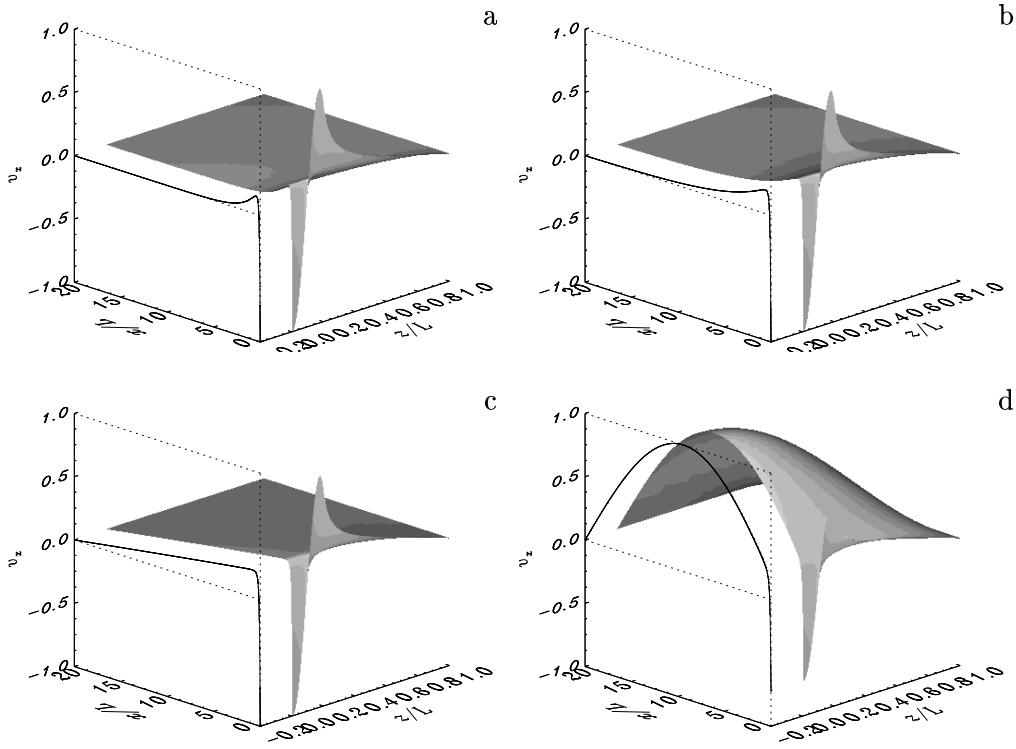

Figure 6.10: Surface plots of the perturbed velocity for the second kink odd mode in Fig. 6.9, for the values $W/L = 0.2$, $\rho_{\rm p}/\rho_{\rm c} = 1000$, $\rho_{\rm e}/\rho_{\rm c} = 1$ and **a)** $b/L = 0.0100$ ($\omega L/c_{\rm Ac} = 1.409$), **b)** $b/L = 0.0080$ ($\omega L/c_{\rm Ac} = 1.555$), **c)** $b/L = 0.0078$ ($\omega L/c_{\rm Ac} = 1.570$) and **d)** $b/L = 0.0076$ ($\omega L/c_{\rm Ac} = 1.578$). These plots has been drawn with the numerical code. A cut in the plane $z = 0$ has been added to show more clearly the behaviour of the solution for large values of x. The limit of the computational box in the x-direction has been set to $H/L = 20$ in Eq. (C.1), although in panel **c)** it is not enough to properly describe the exponential decay of the solution (see the main text for further details). Also notice that **d)** is not an evanescent mode. High values of the parameters $\rho_{\rm p}/\rho_{\rm c}$ and W/L have been chosen to reduce the range of b/L in which this mode is leaky, but the behaviour is the same under different conditions.

variables, which leads to Eq. (4.48) and the ordinary differential equations Eqs. (4.45)–(4.47). Their solutions were introduced in Chapter 4. We note that the solution of Eq. (4.46) is simply a plane wave, provided there is no structure in this direction. Therefore, the following expression can be written,

$$g(y) = e^{-ik_y y}. \tag{6.5}$$

It is very important to remark that this dependence has not been imposed (contrary to what is used in many other papers), but arises naturally from the wave equations. That is a most desirable fact, since all the solutions of the equations can be written as a superposition of these solutions. Also notice that $\kappa^{(\rm c)}$, $\kappa_{\rm p}^{(\rm l)}$ and $\kappa_{\rm e}^{(\rm l)}$ are defined by

Table 6.1: Period of fast modes in a prominence fibril with $\rho_e/\rho_c = 0.6$, $\rho_p/\rho_c = 200$ and $W/L = 0.1$. The magnetic field strength and coronal density have been taken as $B_0 = 5$ G and $\rho_c = 8.37 \times 10^{-13}$ kg/m^3, so the Alfvén speed is $c_{Ac} = 488$ km/s

Fast Mode	Type of solution	$L = 10^5$ km		$L = 3 \times 10^4$ km	
		$b = 100$ km	$b = 200$ km	$b = 100$ km	$b = 200$ km
Fundamental kink even	numerical	13.70 min	13.79 min	4.83 min	5.77 min
	analytical	13.70 min	13.80 min	4.79 min	5.81 min
Fundamental kink odd	numerical	6.84 min	6.84 min	2.47 min	3.15 min
	analytical	6.84 min	6.84 min	2.45 min	3.15 min

$$\kappa^{(j)^2} = \frac{\omega^2}{c_{Aj}^2} + \lambda_n^{(j)^2} - k_y^2 \tag{6.6}$$

and $\kappa^{(c)}$ has the values in Eq. (4.128) to fulfil the line-tying boundary condition.

The perturbed pressure is in the form

$$p_T(x,y,z) = \begin{cases} \displaystyle\sum_{n=1}^{\infty} u_n^{(l)}(x)\, e^{-ik_y y}\, h_n^{(l)}(z), & |x| \leq b, \\ \displaystyle\sum_{n=1}^{\infty} u_n^{(c)}(x)\, e^{-ik_y y}\, h_n^{(c)}(z), & |x| \geq b. \end{cases} \tag{6.7}$$

To match the solutions at $x = b$ one should use the Sturm-Liouville theorem, as in the previous section. Then, a system of equations for the coefficients B_n is obtained, Eq. (4.87) or (4.88), which is reproduced here,

$$\sum_{s=1}^{\infty} H_{sn} \left\{ \frac{\lambda_n^{(c)}}{\lambda_n^{(c)2} - k_y^2} \cosh \lambda_s^{(l)} b + \frac{\lambda_s^{(l)}}{\lambda_s^{(l)2} - k_y^2} \sinh \lambda_s^{(l)} b \right\} B_s = 0, \tag{6.8}$$

for even solutions, and a similar one for odd solutions. For these systems to have non-trivial solutions, the determinant of the coefficients must be zero, which provides us with the dispersion relation. Here it must also be noted that some of the quantities $\lambda_s^{(l)}$ may become complex, similar to what happened in the problem with $k_y = 0$, but now this is favoured by the new term in Eq. (4.130), which is always negative. The consequence is that for $k_y \neq 0$ more $\lambda_s^{(l)}$ become complex when compared with the case $k_y = 0$. In the case of one or more complex $\lambda_s^{(l)}$, some of the previous mathematical expressions have to be modified in order to account for this possibility, but the overall picture remains (see Appendix D for a detailed discussion of this topic).

Therefore, the main differences with the solution with no longitudinal propagation are that perturbations now have y-dependence (see Eqs. (4.48), (4.53) and (4.54)), that both components of the perturbed velocity appear (so there is no polarisation in only one spatial direction for

these fast modes) and that $\kappa^{(c)}$, $\kappa_p^{(l)}$ and $\kappa_e^{(l)}$ in Eq. (4.130) have an extra contribution coming from the wavelength in the y-direction. Consequently, there is also an extra contribution of this new quantity to the dispersion relation, Eq. (6.8). The first noticeable effect is that the cut-off frequency is no longer a fixed value, but depends on k_y. To show this point, one needs to take into account that a mode becomes leaky when $\lambda_n^{(c)2} < 0$ and the first basis function to satisfy this condition is the one with $n = 1$. Hence, the cut-off appears when $\lambda_1^{(c)2} = 0$, so using the first equation in Eq (4.128) the frequencies of even trapped modes must satisfy

$$\frac{\pi}{2L} + k_y^2 - \frac{\omega^2}{c_{\rm Ac}^2} \geq 0, \tag{6.9}$$

and then, the cut-off frequency can be written as

$$\frac{L}{c_{\rm Ac}}\omega_{\rm cut} = \frac{\pi}{2}\sqrt{1 + (k_y L)^2 \frac{4}{\pi^2}}, \tag{6.10}$$

for even modes. For odd modes we have

$$\frac{L}{c_{\rm Ac}}\omega_{\rm cut} = \pi\sqrt{1 + (k_y L)^2 \frac{1}{\pi^2}}. \tag{6.11}$$

These expressions have been written in this form to highlight that lengths are normalized against L and speeds against $c_{\rm Ac}$. Notice that in the limit $k_y \to 0$ the cut-off frequency reduces to $\pi/2$ and π for even and odd modes, respectively, in accordance with the problem with no longitudinal propagation, while for $k_y L \gg \pi/2$ or $k_y \gg \pi$ it grows linearly with k_y in the form $\omega_{\rm cut} L/c_{\rm Ac} = k_y L$ both for even and odd modes.

6.2.2 Dependence of the frequency on the parameters

After having discussed some general properties of the modes, we turn our attention to the solutions of the dispersion relation. First of all, the variation of the frequency of the modes with respect to the longitudinal wavenumber is studied. Fig. 6.11 shows this behaviour for a set of fibril parameters in which the fibril thickness (b/L) is modified.

The first important point to remark is that the cut-off frequency depends on k_y in the form given by Eq. (6.10). Therefore, the larger k_y, the more non-leaky modes can exist. Notice, however, that the frequency of the modes depends on k_y very slightly, except for some modes as they approach the cut-off frequency or for very large k_y ($k_y L \sim 100$, say; Fig. 6.12). As a consequence, the introduction of propagation in the y-direction does not change drastically the frequency of non-leaky modes, but makes it possible to trap other modes that are leaky in the limit $k_y = 0$ for the same set of parameters.

These two effects (slight dependence of the frequency on k_y and apparition of new trapped modes) can be appreciated in Fig. 6.13. The overall picture does not change very much when adding propagation in the y-direction to the model, except that the cut-off frequency is raised. In fact, if a parameter set different from that used in Fig. 6.13 is taken, the result is again that

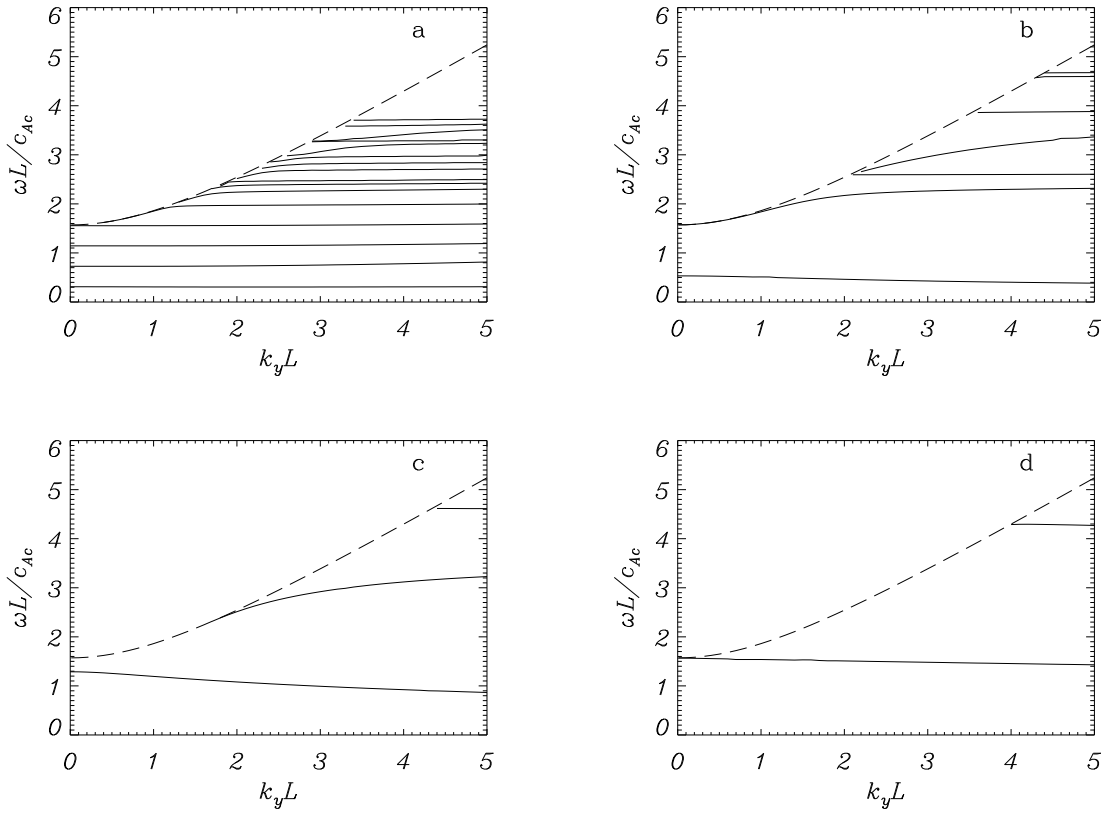

Figure 6.11: Frequency of the kink even modes vs. k_y for the set of parameters $W/L = 0.1$, $\rho_e/\rho_c = 0.6$, $\rho_p/\rho_c = 200$ and **a)** $b/L = 0.5$ (only the 16 lowest frequency modes are shown), **b)** $b/L = 0.1$, **c)** $b/L = 0.01$ and **d)** $b/L = 0.001$. The dashed line is the cut-off frequency, which can be obtained from Eq. (6.10).

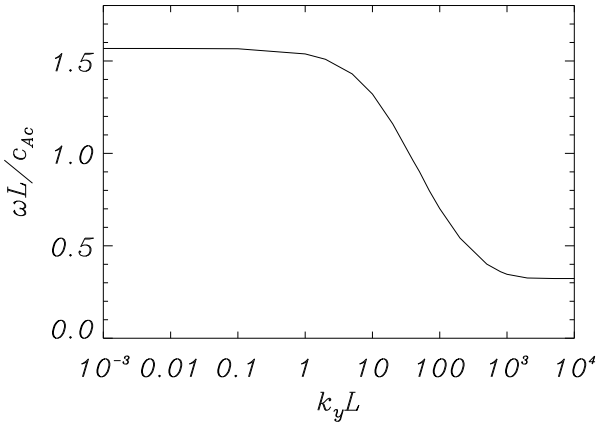

Figure 6.12: Frequency of the fundamental kink even mode vs. $k_y L$, for the set of parameters $W/L = 0.1$, $\rho_e/\rho_c = 0.6$, $\rho_p/\rho_c = 200$ and $b/L = 0.001$.

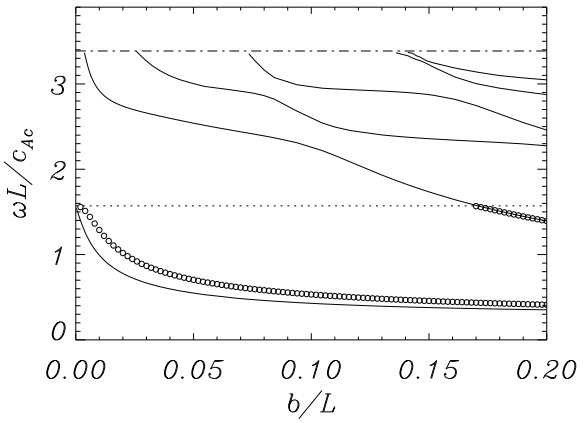

Figure 6.13: Frequency of the kink even modes vs. the fibril thickness, b/L, for the set of parameters $W/L = 0.1$, $\rho_e/\rho_c = 0.6$, $\rho_p/\rho_c = 200$. Circles correspond to $k_y L = 0$ and solid lines to $k_y L = 3$, with the horizontal dotted and dash-dotted lines representing their respective cut-off frequency. Notice that the structure of both sets of modes is very similar, except for the modification in the frequency range caused by the dependence of the cut-off frequency on k_y, which results in more modes being trapped in the loop structure for a given fibril thickness.

the existing mode frequencies for $k_y = 0$ (described in the previous section) are not noticeably affected, while the raising of the cut-off allows more modes to become trapped.

6.2.3 Spatial structure

Following the above discussion about the dispersion relation, the spatial profiles of the different solutions are next studied. Here it should be remarked that for $k_y \neq 0$ all modes have both v_x and v_y non-zero, (see Eqs. (4.53) and (4.54)). The spatial structure of the fundamental kink even mode in an unrealistically thick fibril is displayed in Fig. 6.14. Such as was mentioned before, the symmetries in the solutions allow us to concentrate on the region $0 \leq z \leq L$, $0 \leq x < \infty$, although a finite spatial range across the fibril is used in our plots since solutions decay exponentially in this direction. It can be seen in Figs. 6.14 and 6.15 that the total pressure perturbation, p_T, and the x-component of the velocity, v_x, are not derivable at the boundary $x = b$ and that v_y is not even continuous there. It is also worthwhile to remark that the higher k_y, the more marked the discontinuity in the derivative with respect to x of p_T and v_x at $x = b$. The normalization constant in these figures has been fixed by the condition $Max\{p_T/(\rho_c c_{Ac})\} = 1$.

The number of extrema and the spatial couplings that are found now are quite similar to those in Fig 6.5: when two modes (with different spatial structure and thus with different number of extrema) approach in frequency because of the variation of a parameter, like b/L, there is a coupling and the modes exchange their spatial structure (i.e. the number of extrema in each direction).

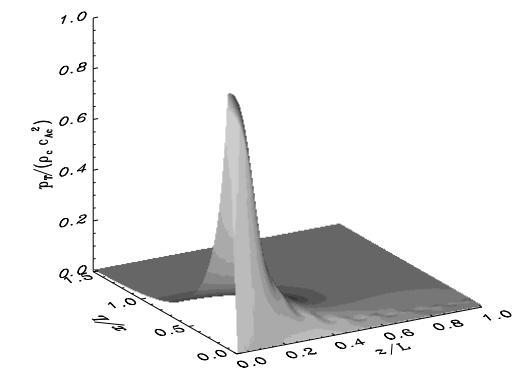

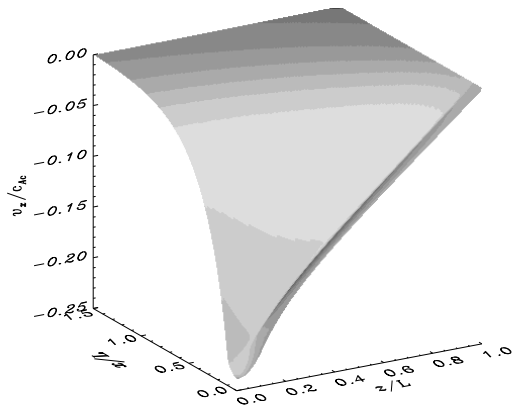

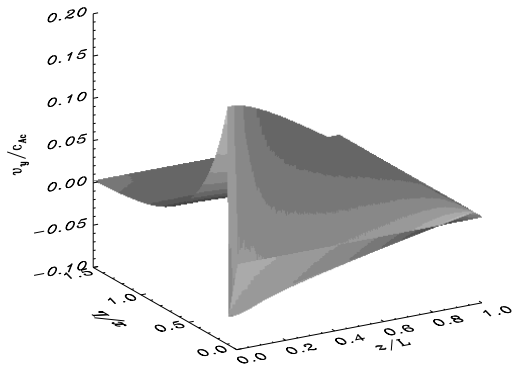

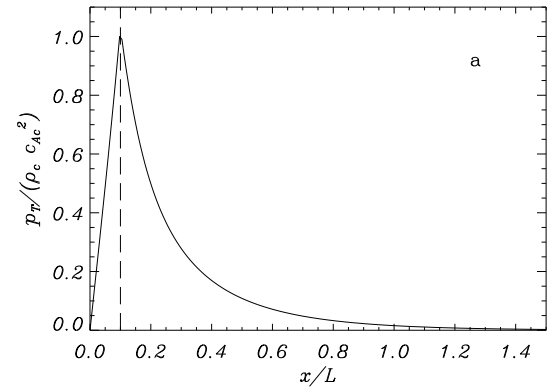

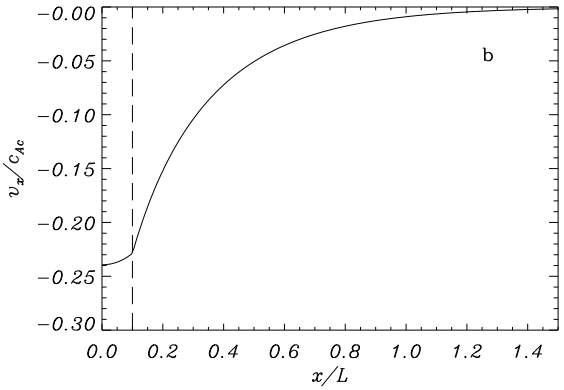

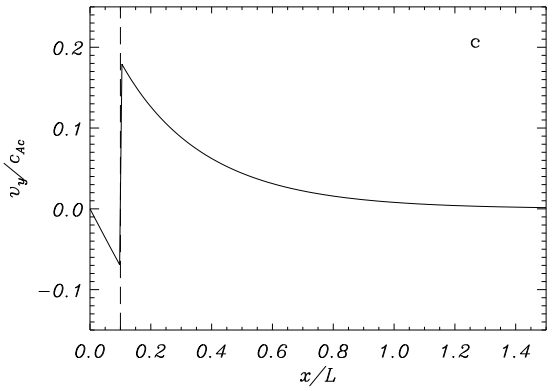

Figure 6.14: Surface plots of the fundamental kink even mode for the set of parameters $b/L = 0.1$, $W/L = 0.1$, $\rho_e/\rho_c = 0.6$, $\rho_p/\rho_c = 200$ and $k_y L = 3$ ($\omega L/c_{Ac} = 0.428$). Panel **a)** corresponds to the total pressure perturbation, **b)** to v_x and **c)** to v_y (which is not continuous at the boundary $x = b = 0.1L$). The structure of these variables across the middle of the fibril is shown in Fig. 6.15.

Figure 6.15: Cut across the centre of the fibril ($z = 0$) of the solutions in Fig. 6.14. Because of the jump conditions imposed at the interface $x = b$, the derivative of both p_T and v_x is not continuous on that surface, whereas v_y is not even continuous there. The fibril limit is marked with a vertical dashed line.

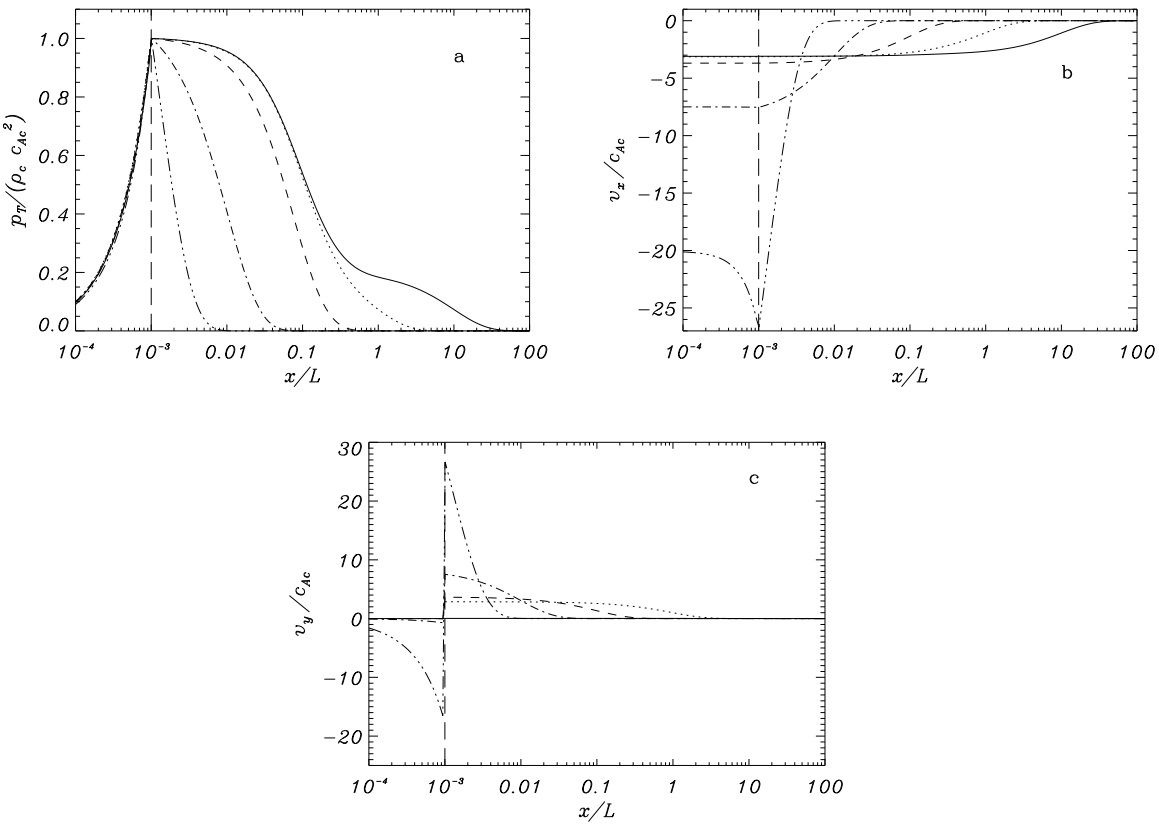

Figure 6.16: Cut across the centre of the fibril ($z = 0$) of **a** $p_{\rm T}/(\rho_{\rm c}c_{\rm Ac}^2)$, **b** $v_x/c_{\rm Ac}$ and **c** $v_y/c_{\rm Ac}$ for the fundamental kink even mode. The values of the parameters used are $b/L = 0.001$, $W/L = 0.1$, $\rho_{\rm e}/\rho_{\rm c} = 0.6$, $\rho_{\rm p}/\rho_{\rm c} = 200$ and $k_yL = 0.001$ ($\omega L/c_{\rm Ac} = 1.567$, solid lines), $k_yL = 1$ ($\omega L/c_{\rm Ac} = 1.538$, dotted lines), $k_yL = 10$ ($\omega L/c_{\rm Ac} = 1.321$, dashed lines), $k_yL = 100$ ($\omega L/c_{\rm Ac} = 0.701$, dash-dotted lines) and $k_yL = 800$ ($\omega L/c_{\rm Ac} = 0.360$, dash-dot-dotted lines). Notice that for $k_yL = 800$ the velocity perturbations are large and the mode looks like a surface wave. The normalization constant has been chosen again from the condition $Max\{p_{\rm T}/(\rho_{\rm c}c_{\rm Ac})\} = 1$.

At this point one may wonder which is the reasonable range of values for k_y. So far we have concentrated in dimensionless values of this parameter of order unity, but larger values of k_y have also been considered. Hence, we study how the relative amplitudes of the three relevant magnitudes ($p_{\rm T}$, v_x, v_y from Eqs. (6.7), (4.53) and (4.54)) change when k_y is modified (Fig. 6.16). First of all, if $k_yc_{\rm Ac} \ll \omega$ then $v_x \sim p_{\rm T}$ and $v_y \sim k_y$ (in dimensionless units), so the velocity component in the x-direction dominates. On the other hand, if $k_yc_{\rm Ac} \gg \omega$ then $v_y \sim k_y$ and $v_x \sim k_y$, since $\lambda^{(\rm l)} \sim \lambda^{(\rm c)} \sim k_y$ from Eq. (6.9) so $\lambda^2 - k_y^2$ is small compared with k_y or λ in Eqs. (4.53) and (4.54), and as a consequence both velocity polarisations are of the same order and quite large in front of the total pressure perturbation. Notice also that for k_y large the modes tend to become a surface wave as those in Roberts (1981), being characterized by having the largest amplitude near the surface and low amplitude inside the fibril. However, for realistic values of b/L this transition is not noticeable unless k_y is rather large (about $k_yL \approx 100$ for $b/L = 0.001$).

The most relevant fact coming from the inclusion of k_y is that the cut-off is raised, so we

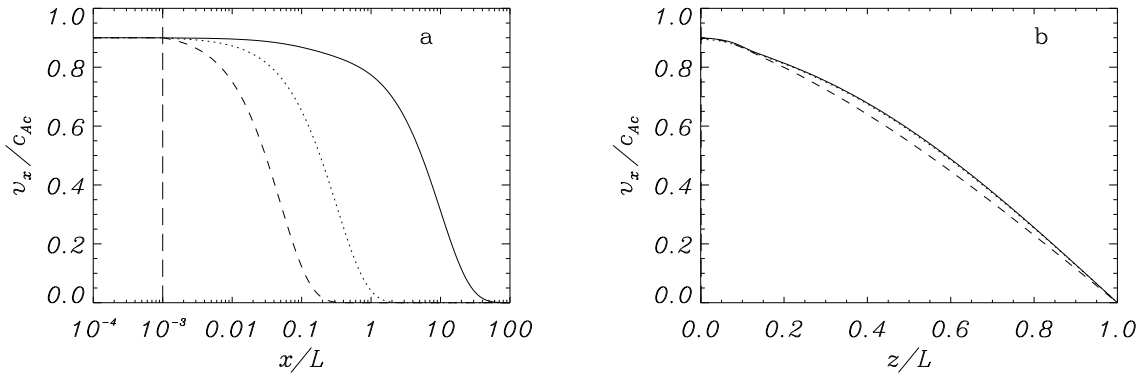

Figure 6.17: Plots of v_x for the fundamental kink even mode, **a)** is a cut across the fibril at $z = 0$ in logarithmic scale and **b)** is a cut along the fibril at $x = 0$. The parameters used are $b/L = 0.001$, $W/L = 0.1$, $\rho_e/\rho_c = 0.6$, $\rho_p/\rho_c = 200$. The solid line corresponds to $k_y L = 0$, the dotted line to $k_y L = 3$ and the dashed line $k_y L = 20$. The fibril boundary is marked by a vertical dashed line. To produce this figure the normalization condition now is $Max\{v_x/c_{Ac}\} = 1$.

next study the variation of the spatial structure of the modes near that frequency for $k_y \neq 0$. In Section 6.1 only one confined mode was present for a realistic range of parameters; this is clearly shown in Fig. 6.13d with $k_y = 0$. Furthermore, for low values of k_y ($k_y L \leq 4$, say) there is still only one non-leaky mode in the system. Fig. 6.17 gives a comparison between v_x with $k_y = 0$, which from Eq. (6.4) is continuous and derivable at the boundary $x = b$, and v_x with $k_y \neq 0$, which is not derivable at $x = L$. The solution becomes more confined as k_y is increased, but it still has a long tail and attains non-negligible values at a distance 100 times the fibril thickness for $k_y L = 3$.

It is also worthwhile studying the new array of confined modes that arise for $k_y \neq 0$. As an example, we concentrate on the first harmonic in Fig. 6.11c and plot cuts of the spatial structure of v_x (Fig. 6.18). This variable has three extrema in the range $-L \leq z \leq L$ (Fig. 6.18b), but when the frequency goes far from the cut-off as a consequence of propagation in the y-direction, some structure develops outside the fibril in the x-direction (Fig. 6.18a), because the second basis function, $u_2(x)$, also has a long decaying length. Again, the larger k_y, the more confined the mode is in the x-direction (although perturbations reach large distances from the fibril axis). On the other hand, in the z-direction the amplitude in the evacuated part is larger than the amplitude in the dense part (similar to what was found for some modes in Sect. 6.1). As k_y is increased, this effect becomes more noticeable, making this kind of modes harder to detect because of their small amplitude in the prominence plasma.

6.3 Conclusions

Analytical and numerical techniques have been used to investigate the features of fast modes propagating in a thin, cool prominence fibril, starting with the case of a solution with no longitudinal propagation. Two are the main conclusions that can be extracted from our results. First,

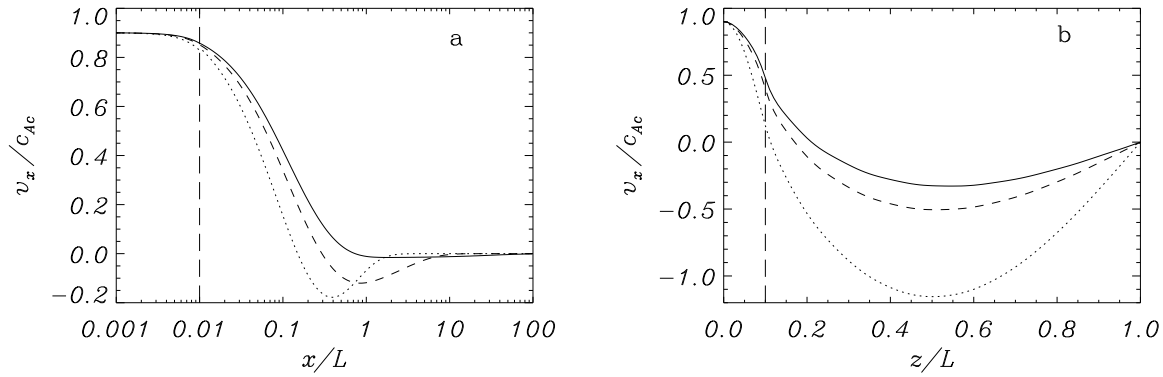

Figure 6.18: Cuts of v_x **a)** in the $z = 0$ direction and **b)** in the $x = 0$ direction of the first kink even harmonic. The equilibrium parameters are $b/L = 0.01$, $W/L = 0.1$, $\rho_e/\rho_c = 0.6$ and $\rho_p/\rho_c = 200$, while $k_y L = 1.7$ (solid line), $k_y L = 2$ (dashed line) and $k_y L = 3.5$ (dotted line). The boundary of the dense part is marked with a vertical dashed line and all the plots have been normalized to the same amplitude at $x = z = 0$.

prominence fibrils can only support a few modes of oscillation, those with smaller frequency, since high harmonics cannot be trapped inside the thin loop. Starting from a thick fibril, fast modes increase their frequency as the fibril thickness is reduced and, as soon as they exceed the cut-off frequency corresponding to kink and sausage modes, they become oscillatory. This is not the case, however, with the fundamental even and odd kink modes, whose ω tends asymptotically to $\omega_{\rm cut}$ but never reaches this value. Second, it has been shown that the spatial structure of the fundamental even and odd kink modes is such that the velocity amplitude outside the fibril takes large values over long distances, the reason being that their frequency is so close to $\omega_{\rm cut}$ that they are little confined to the prominence.

A consequence of the above results is that if fast modes were excited in the kind of fibril considered, most of the energy would be pumped out into the corona. Modes are not very well trapped by the fibril structure and, although the density of the coronal environment is very small compared to that of the dense material, the external region is much larger than the fibril and its total energy content can be comparable to the energy contained in the fibril. Therefore, this physical effect can give rise to damping of perturbations by means of energy leakage between fibrils. In addition, from the current view of prominences as made of a large number of thin fibrils packed together, it seems that fibrils would actually oscillate in groups rather than individually and that if a single fibril is disturbed it will excite perturbations in its neighbours, which may help to explain how prominence oscillations are damped in time. An important corollary is that the study of the collective modes of a multi-fibril prominence model is needed to better understand the oscillatory properties of these objects. Note that the above conclusion about fibrils oscillating in groups rather than individually is not in contradiction with the observations by Yi et al. (1991) and Yi & Engvold (1991) since the spatial resolution in their data is ≥ 1 arcsec.

On the other hand, a solution for the problem with longitudinal propagation has been found and in our discussion of the results we have emphasized the behaviour of the dispersion relations and the spatial structure of the modes. The inclusion of propagation in the y-direction ($k_y \neq 0$)

in the model has two relevant effects with respect to the results with $k_y = 0$:

1. The cut-off frequency now depends on k_y and, as a consequence, more modes become trapped within the fibril for a given set of parameters. However, the frequencies of the modes are only slightly shifted when the value of k_y is increased.

2. The existing modes become more confined, specially the fundamental even and odd ones. Therefore, the effect of the introduction of the third dimension is to weaken the interaction between neighbouring fibrils. Then, when the separation between fibrils is increased, the probability of groups of fibrils oscillating together by mutual interaction diminishes.

The behaviour of the cut-off frequency with k_y and the possibility of more trapped modes for non-zero values of this parameter seems to be an effect of the addition of a free wave (in this work modes are not trapped in the y-direction). It should be emphasized that if the requirement of trapped modes in the x-direction is dropped, then there are leaky modes with higher frequencies than the cut-off, since the cut-off just separates two different kinds of solutions. The present work provides with the first 3-dimensional model of fast MHD oscillations in Cartesian fibrils. Next step could be to consider an orthogonal fibril, leading to trapped modes in the x- and y-directions with a fixed cut-off frequency, such as happens in a truly cylindrical prominence fibril (Chapter 8). Moreover, a comparison of Fig. 6.17a and Fig. 8.12 for cylindrical geometry, which are plotted with the same scales and equilibrium parameters, shows that the inclusion of k_y in the Cartesian model has the effect of a better confinement of modes, with their spatial structure across the fibril tending to that of the cylindrical modes, which will be studied in the mentioned Chapter.

At this point, the spatial dependence of v_x inside and outside the fibril is well characterized and so it is possible to discuss the differences between our solution and that in Joarder et al (1997). Eqs. (4.65) and (4.129) for $h_n^{(\mathrm{c})}(z)$ and $h_n^{(\mathrm{l})}(z)$, tell us that p_{T} is an infinite sum of basis functions with different wavelengths in the z-direction inside and outside the fibril. The situation looks much simpler in Joarder et al (1997), whose Eqs. (16), (19) and (20) provide v_x inside and outside the loop using only one basis function in each region (in the same way that the result in the case of a homogeneous fibril discussed before). The problem with the solution of Joarder et al (1997) is that it cannot satisfy the boundary conditions on the fibril surface since the wavelength outside and inside the loop are different along this boundary. For this reason, their condition (24) makes no sense.

It is also interesting to mention that previous works based on the plasma slab (Edwin & Roberts 1988; Nakariakov and Roberts 1995) show that the simple step profile along the long axis is a good approximation and more complicated shapes of inhomogeneities do not lead to important differences. This is also confirmed in Oliver & Ballester (1996), whose results suggest that a smooth discontinuity profile is only relevant for the modes that have strong variations in that region and since our evanescent modes have much larger scales, the use of a step profile is not expected to be relevant. Therefore, results for the slab are of wider validity and likely to be applicable to solar structures, even though they are an idealisation. Although this is not fully developed in this work, it is also possible with minor modifications of the proposed solution to study that kind of effects (as it has been done for coronal loops).

Chapter 7

Fast Magnetohydrodynamic oscillations in multifibril Cartesian systems *

Any fool can ask more questions
than seven sages can answer.

Motivated by the observations suggesting that groups of fibrils may oscillate together, our main goal now is to study the interactions between oscillating fibrils. Following the same procedure as in Chapter 6, the study will be performed using Cartesian geometry, first dealing with the case of no longitudinal propagation. Then, we study the behaviour of these collective modes when the assumption of independence in the y-direction is removed, as it was done in Chapter 6 for a single fibril. The main results are that more modes were trapped because the cut-off frequency is raised, and the spatial structure shows better confinement when the wavelength in the y-direction is increased. We have only studied here the effects of allowing dependence for two symmetrical fibrils, since the results can be easily extended to the other cases described with only no longitudinal propagation.

The Chapter is organized as follows: First, the equilibrium model and basic assumptions are described; then we present and discuss the results obtained when a couple of fibrils are considered and after that, the numerical solution for the case of several fibrils is considered. Finally, our conclusions are presented.

7.1 Model and analytical solution

First of all, the equilibrium model must be explained. It consists of a collection of fibrils separated a distance $2l$ (which is the relevant parameter and can differ between pairs when more that two fibrils are considered), following our simplifying prominence model of Fig 3.3. Each fibril is then

*This Chapter is based on: Díaz, A. J., Oliver, R., & Ballester, J.L. 2004, "Fast Magnetohydrodynamic oscillations in multifibril Cartesian systems", in preparation.

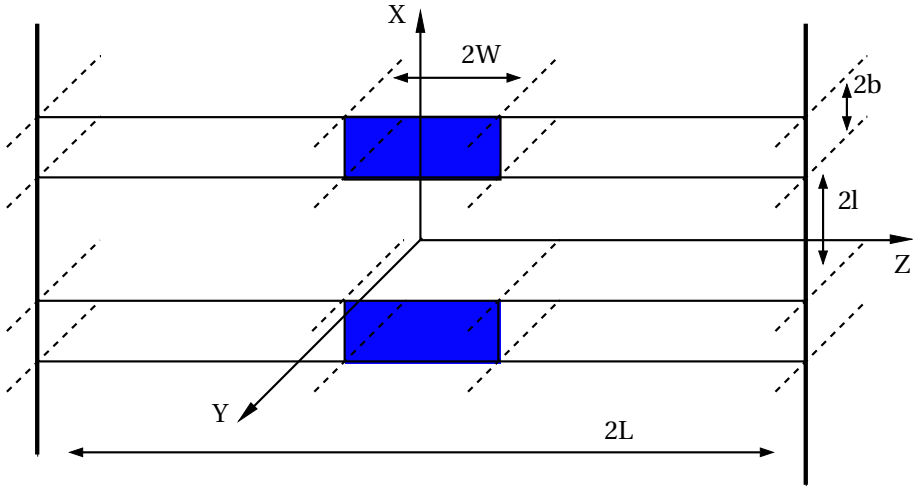

Figure 7.1: Sketch of the equilibrium configuration used in this study of a system of two fibrils. The grey zone represents the cold part of the loops, i. e. the prominence. The density in the prominence region is $\rho_{\rm p}$, in the evacuated (coronal) part of the loop, $\rho_{\rm e}$, and in the coronal environment, $\rho_{\rm c}$. The magnetic field is uniform and parallel to the z-axis, and the whole configuration is invariant in the y-direction.

modeled exactly as in Chapter 6 (Fig. 3.6). The sketch of the model for two fibrils is replotted in Fig. 7.1.

The starting point for the wave analysis are the equations deduced for this kind of models in the low-beta limit, namely Eqs. (4.22) and (4.23). Notice however that we shall use Eqs. (4.30) and (4.31) for the numerical analysis, since it is more convenient to work with these two coupled differential equations for the non-vanishing components of the perturbed velocity. Therefore, the main aim is to solve Eq. (4.23) with the appropriate boundary conditions for the two-fibril system sketched in Fig. 7.1. This type of solution can be extended straightforwardly to other akin multifibril systems. The standard method for solving them in a closed region is separation of variables, which gives us the same three ordinary differential equations that for a single fibril, Eqs. (4.45)–(4.47). If there is no structure in the y-direction, from Eq. (4.46) the dependence on the y-coordinate is simply $g(y) = e^{ik_y y}$ for all the domain. The remaining Eqs. (4.45) and (4.47) must be solved in three regions: the coronal environment ($|x| > 2b + l$), the fibril itself ($l > |x| > 2b + l$) and the material between the fibrils ($|x| < l$), which would be taken identical to the coronal one. Therefore, our solution can be written as

$$p_{\rm T}(x,,y,z) = \begin{cases} \sum_{n=1}^{\infty} u_n^{(1)}(x)\ g(y)\ h_n^{(1)}(z), & |x| \geq 2b + l, \\ \sum_{n=1}^{\infty} u_n^{(2)}(x)\ g(y)\ h_n^{(2)}(z), & l \leq |x| < 2b + l, \\ \sum_{n=1}^{\infty} u_n^{(3)}(x)\ g(y)\ h_n^{(3)}(z), & 0 \leq |x| < l, \end{cases} \tag{7.1}$$

in which the necessity of using all the basis functions to fulfill the boundary conditions on the fibril surfaces has been taken into account. First of all, the z-dependent functions of Eq. (4.47) were calculated in Sect. 4.5.2, taking into account that there is line-tying at $z = \pm L$ and jump conditions at $z = \pm W$ (for the loop region). Notice also that the coronal medium is the same in regions 1 and 3, so $h_n^{(1)}(z) = h_n^{(3)}(z)$.

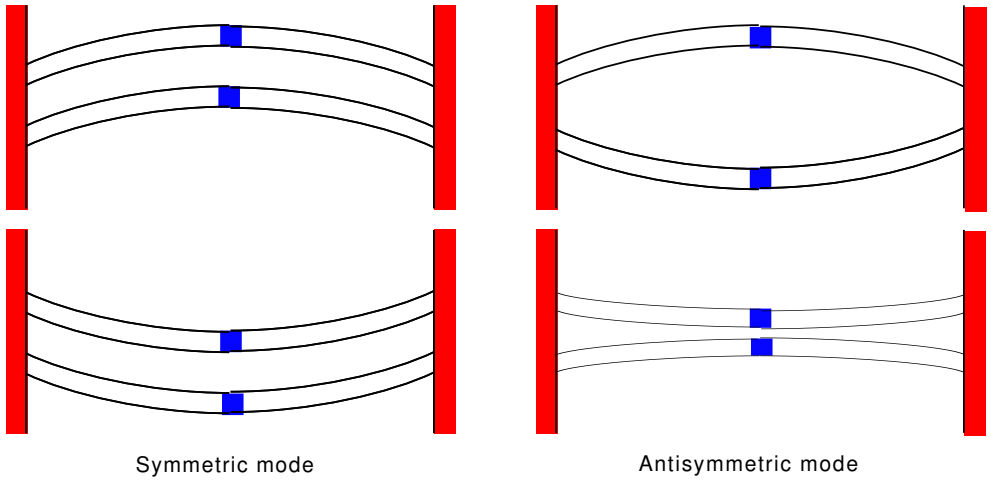

Figure 7.2: Sketch of two fibrils oscillating in phase (symmetric mode) and in opposition of phase (antisymmetric mode).

If a system of two identical fibrils is under consideration, the equations can be solved just in the region $x \geq 0$ and $0 \leq z \leq L$, so there will be even and odd modes in the z-direction and even and odd modes in the x one. The two fibrils are oscillating in phase in the even modes in the x-direction, so hereafter we will call this a symmetric mode, while the odd ones will be called antisymmetric modes (Fig. 7.2). Taking into account these symmetries, the solution of the x-dependent part for a symmetric mode is in the form

$$\begin{array}{ll} u_n^{(1)}(x) = A_n e^{-\lambda_n^{(1)}(x-2b-l)}, & x \geq 2b+l, \\ u_n^{(2)}(x) = B_n^{\sin} \sin \lambda_n^{(2)}(x-l) + B_n^{\cos} \cos \lambda_n^{(2)}(x-l) & l \leq x < 2b+l, \\ u_n^{(3)}(x) = C_n \cosh \lambda_n^{(3)} x & 0 \leq x < l \end{array} \tag{7.2}$$

while the z-dependent part depends on the Alfvén speed profile along the fibril. First of all we could take a cold slab, following the model in Edwin & Roberts (1982), where these functions are just $h_n^{(1)}(z) = h_n^{(2)}(z) = h_n^{(3)}(z) = L^{-1/2} \cos \pi(2n-1)z/(2L)$, and $H_{nm} = \delta_{nm}$, so the modes of two cold Cartesian slabs could be studied, but here we will work directly with our model, and these functions are the same as in Sect 4.5.2 for the corona (numbered 1 and 3) and fibril (numbered 2).

The next step is to apply the boundary conditions at $x = l$ and $x = 2b+l$, that is, continuity of the total pressure and of the x-components of the perturbed velocity and magnetic field, namely Eqs. (4.40). Operating with these expressions the coefficients A_n and C_n in Eq. (7.2) can be eliminated, and we obtain for the symmetric modes

$$\sum_{l=0}^{\infty} \quad H_{ln} \left[B_l^{\cos} \frac{\lambda_n^{(3)}}{{\lambda_n^{(3)}}^2 - k_y^2} \sinh \lambda_n^{(3)} l - B_l^{\sin} \frac{\lambda_n^{(2)}}{{\lambda_n^{(3)}}^2 - k_y^2} \cosh \lambda_n^{(3)} l \right] = 0,$$

$$\sum_{l=0}^{\infty} \quad H_{ln}\left[\frac{\lambda_n^{(1)}}{{\lambda_n^{(1)}}^2-k_y^2}(B_l^{\sin}\sin\lambda_n^{(2)}2b+B_l^{\cos}\cos\lambda_n^{(2)}2b)\right.$$
$$\left.+\frac{\lambda_n^{(2)}}{{\lambda_n^{(2)}}^2-k_y^2}(B_l^{\sin}\cos\lambda_n^{(2)}2b-B_l^{\cos}\sin\lambda_n^{(2)}2b)\right]=0. \tag{7.3}$$

and a similar expression for the antisymmetric ones.

The above equations constitute two infinite system of homogeneous algebraic equations for the coefficients $B_l^{\sin}$ and $B_l^{\cos}$, with coefficients that depend on ω. The condition to have a non-trivial solution is that the determinant of this system vanishes, providing us with the dispersion relation from which the eigenvalues of the problem can be obtained. Again, the determinant is truncated taking $B_s = 0$ for $n > N$. Thus, we are left with a $2N$-order determinant, obtained by using the first N basis functions only (with N large, at least over 20). Once the eigenfrequencies have been obtained, all the other quantities in the problem can be determined.

It is very important to remark that this system only has a non-trivial solution if some of the $\lambda_n^{(2)}$ are allowed to become complex. In this case, the dependence inside the fibril is in form of hyperbolic functions instead of trigonometric ones as in the second equation of Eqs. (7.3).

The solution method developed in this section can also be applied with minor changes to other systems, such as two non-identical fibrils or more than two of them. However, the resulting system of equations is far too more complicated and difficult to handle than Eqs. (7.3), so in that problems we chose to apply numerical methods on Eqs. (4.30) and (4.31) instead of calculating the corresponding analytical solution (see Appendix C).

7.2 Two-fibril system

There is no reason allowing to assume that all the fibrils composing a prominence are identical. In fact, observations of prominences suggest that they are highly non-homogeneous in density and temperature, while the possible inhomogeneity in magnetic field is much more difficult to confirm. However, first of all, we can study the interaction among identical fibrils conforming a homogeneous prominence without dependence on the y-coordinate and, later, the modifications introduced by this dependence will be described. Finally, a similar study will be numerically performed for the case of non-identical fibrils i.e. for an non-homogeneous prominence without y-dependence.

7.2.1 Identical fibrils without longitudinal propagation

As we stated before, the solutions for two identical fibrils without dependence on the y-direction are studied first. First of all, Eqs. (7.3) can be solved with $k_y = 0$, so the resulting system is

$$\sum_{l=0}^{\infty} \quad H_{ln}\left[B_l^{\cos}\lambda_n^{(3)}\sinh\lambda_n^{(3)}l-B_l^{\sin}\lambda_n^{(2)}\cosh\lambda_n^{(3)}l\right]=0,$$
$$\sum_{l=0}^{\infty} \quad H_{ln}\left[\lambda_n^{(1)}(B_l^{\sin}\sin\lambda_n^{(2)}2b+B_l^{\cos}\cos\lambda_n^{(2)}2b)\right.$$

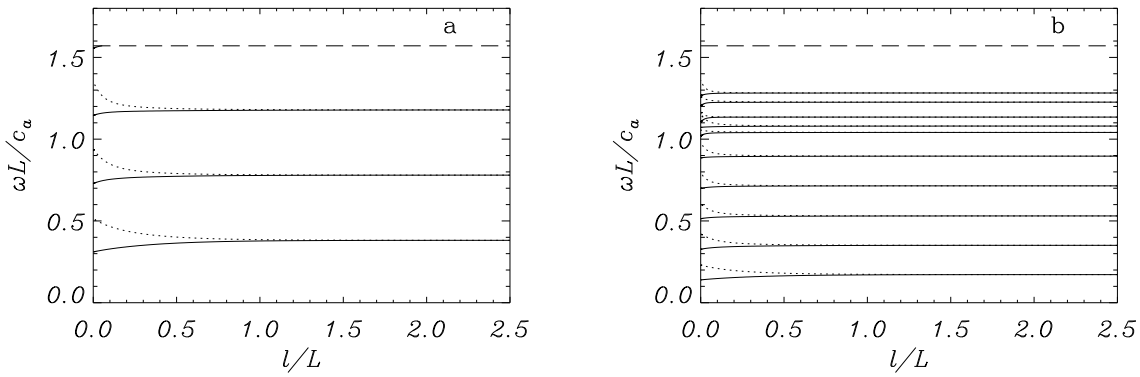

Figure 7.3: Two identical fibrils: variation of frequency with the half-separation for symmetric even modes (solid lines) and antisymmetric even modes (dotted lines) for two different sets of parameters **a)** $W/L = 0.1$, $\rho_e/\rho_c = 0.6$, $\rho_p/\rho_c = 200$ and $b/L = 0.25$; **b)** $W/L = 0.1$, $\rho_e/\rho_c = 1$, $\rho_p/\rho_c = 1000$ and $b/L = 0.25$ (only the 10 first eigenfunctions are shown in each symmetry). Notice that in **a**) the fourth symmetric mode appears from the cut-off (dashed line) when the fibrils get closer.

$$+ \lambda_n^{(2)} (B_l^{\sin} \cos \lambda_n^{(2)} 2b - B_l^{\cos} \sin \lambda_n^{(2)} 2b)\Big] = 0. \tag{7.4}$$

Dependence of the modes on the fibril separation

For this study, the key parameter is l, half the distance between the two fibrils. Notice that in the limit $l \to \infty$, two separate fibrils are recovered (and both the sausage and kink modes from Chapter 6 should be present), while in the limit $l \to 0$ there is only one fibril left having width $4b$ and, as before, the sausage or kink modes corresponding to this situation must be present. Then, it is important to study the behaviour of the modes when l has a value between these two limits.

First of all, in Fig. 7.3 the variation of the frequency for symmetric and antisymmetric modes, and for two different sets of parameters, is shown. From the results in Chapter 6 it can be easily checked that both limits are correctly described, and it is also important to point out that when the fibrils are separated more than twice their width ($l > 4b$) there is no coupling between them, i.e. the sausage and kink modes are equivalent in frequency and correspond to those of a single fibril oscillating alone. When the two fibrils are closer, the interaction is clearly shown and the two modes become separated in frequency, until the limit in which the two fibrils coalesce and form a single one. When the limit $l \to 0$ is approached, the frequency of the kink modes is smaller than that of the sausage mode, and because of the interaction the modes can cross the cut-off frequency. As an example, in Fig. 7.3a, the fourth kink mode, which is under the cut-off frequency for a single fibril having a width of $0.5L$ in Fig. 6.2a (equivalent to the one of the two fibrils together) but is over the cut-off for a single fibril of width $b/L = 0.25$ in the same figure, matches the frequency shown in Fig. 7.3a in the limit $l \to 0$ in Fig. 7.3a, appears for low values of the parameter l and becomes leaky when l is increased.

On the other hand, note the complex interaction of modes shown in Fig. 7.3b. A mode can cross other modes with different type of symmetry due to the coupling, but not modes having the same symmetry. The spacing between the modes is not regular, because there are space

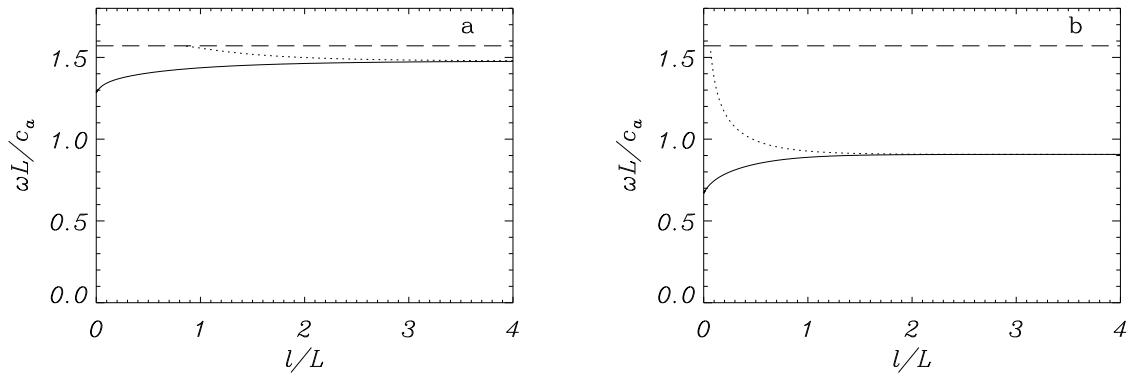

Figure 7.4: Two identical fibrils: variation of frequency with the half-separation for symmetric even modes (solid lines) and antisymmetric even modes (dotted lines) for two realistic sets of parameters **a)** $W/L = 0.1$, $\rho_e/\rho_c = 0.6$, $\rho_p/\rho_c = 200$ and $b/L = 0.01$; **b)** $W/L = 0.1$, $\rho_e/\rho_c = 1$, $\rho_p/\rho_c = 1000$ and $b/L = 0.01$. Now there is only one surviving mode in each symmetry. Notice that the frequency of the antisymmetric mode exceeds the cut-off (dashed line) for low values of b/L.

couplings for this set of parameters (See Chapter 6). It is also noticeable in both Fig. 7.3a and Fig. 7.3b that the higher the order of the mode, the later the interaction starts. The explanation for this behaviour is that even in a single fibril, the modes with higher orders are more spatially confined, so the fibrils must be pushed nearer to start feeling their mutual interaction.

Anyway, the above mentioned features appear when the thickness of the fibrils is far away from the realistic range $b/L \approx 0.001 - 0.01$. For this situation, the behaviour is illustrated in Fig. 7.4. There are few evanescent modes left, and decreasing the parameter b/L, there would be only one with its frequency tending to $\pi/2$ (see Chapter 6). In this case, the first important point to remark is that the influence of both fibrils in the frequency is noticeable even for high values of the separation $2l$ compared with the fibril width $2b$ (in our case, over 500 times), so, in this model two prominence fibrils would always interact. Furthermore, the antisymmetric mode becomes leaky when the two fibrils become closer, as can be clearly seen in Fig. 7.4. Hence, the system is constrained to oscillate in phase if realistic values of the parameters are used.

Spatial profiles

Now we investigate the spatial properties of the modes whose frequencies where calculated before. The dependence along the fibrils was commented in Chapter 4, so we will concentrate on the features concerning the spatial profiles across the fibrils. For sake of clarity, some of the plots will be done with both fibrils, in order to gain a deeper knowledge of the spatial structure of the modes.

First of all, the solution for the x-component of the perturbed velocity is plotted in Fig. 7.5, where the fibrils are wide and the interaction is strong enough to differentiate very well both modes (even in frequency). It can also be checked that the dependence in the z-coordinate is nearly the same as for one fibril alone.

Let us move now to realistic parameter values. Fig. 7.6 displays the evolution of the two surviving modes when the distance between the fibrils is increased. In Fig. 7.6a, only the symmetric

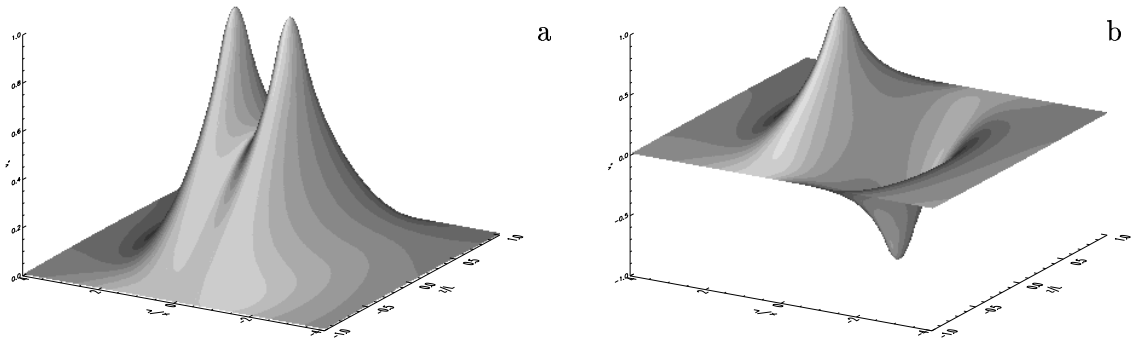

Figure 7.5: Two identical fibrils: **a)** kink and **b)** sausage first mode for two wide fibrils with parameters $W/L = 0.1$, $\rho_e/\rho_c = 0.6$, $\rho_p/\rho_c = 200$, $b/L = 0.5$ and half separation $l/L = 0.5$. Notice that the whole range in the z direction has been plotted, and also that the two fibrils are included in these surface plots.

mode is present, so both fibrils oscillate in spatial phase. In Fig. 7.6b, the antisymmetric mode is also present, but just below the cut-off frequency, and therefore, it extends to long distances far away from the system. In Fig. 7.6c, the two modes become closer in frequency and also in spatial shape, and finally in Fig. 7.6d they are quite similar.

From Fig. 7.6d it is also clear how the modes of a single fibril are recovered. Only adding these modes, the amplitude in the second fibril (that corresponds to $x/L = -5$, not shown in the graph) vanishes, and what is left is just the first one oscillating on its own (with a tiny contribution from the second one). If the second fibril was pushed further away, the single fibril results would be recovered exactly.

7.2.2 Identical fibrils with longitudinal propagation

After having studied the more simple case of $k_y = 0$, now it is time to see how the introduction of this wavenumber changes the properties. It is important to remark that the fibrils in the previous section were influenced by their neighbour because for realistic values of the parameters the perturbation reached long distances from a given fibril. So even when the separation is thousands of times their widths (which is not the case in solar prominences, in which the fibrils are packed closely together) there was influence of the rest of the fibrils in the oscillatory properties of each fibril. However, in Chapter 6 it was stated that these long distances of influence are shortened when longitudinal propagation is included, so some changes might be expected in the results of the previous section.

Now Eqs. (7.3) in their full glory are taken into account. First, the frequency of the dispersion relations is plotted in Fig. 7.7. Effects described in Chapter 6 are also present, namely, the raising of the cut-off frequency and, as a consequence, the trapping of more modes. For a given mode, changing the value of k_y just moves slightly its frequency. Anyway, one important fact from the raising of the cut-off is that now modes that were leaky become trapped, specially the antisymmetric modes. Therefore, the fibrils are no longer constrained to oscillate in phase if k_y is high enough.

The next point is describing the behaviour of the spatial structure when k_y is added. First

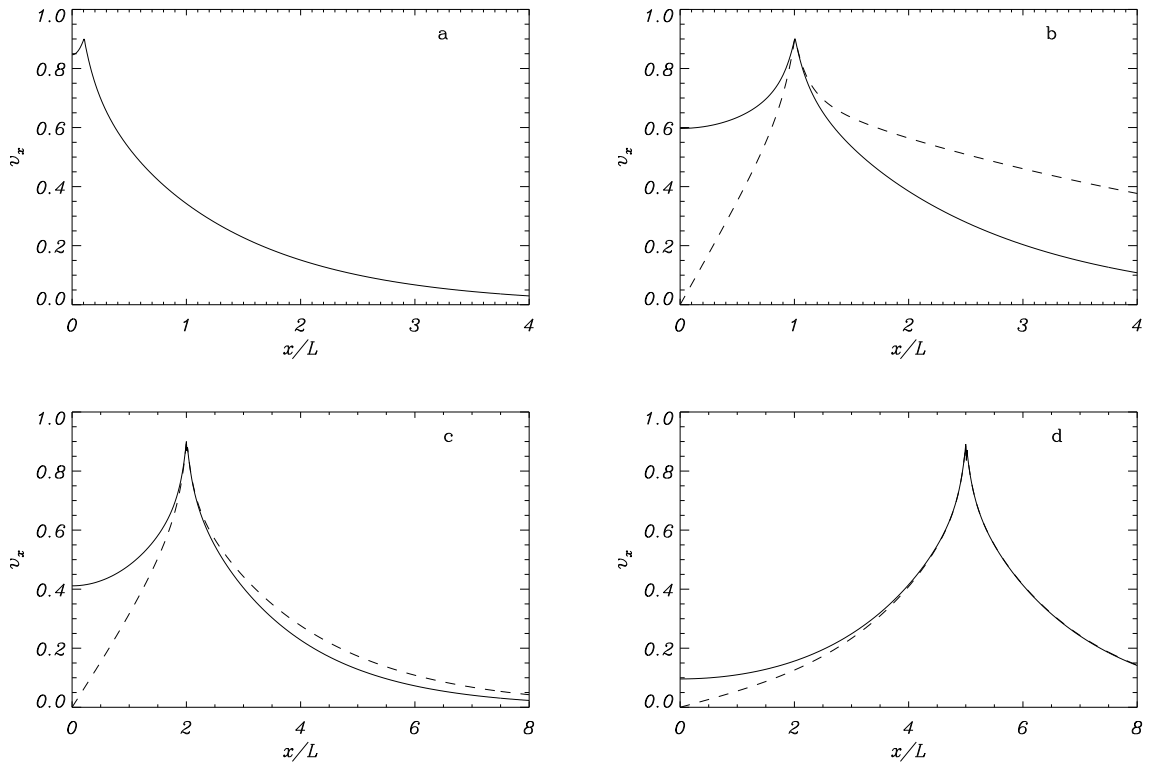

Figure 7.6: Two identical fibrils: cuts in the direction $z/L = 0$ of the first symmetric (solid line) and antisymmetric (dashed line) mode, for the parameters $W/L = 0.1$, $\rho_e/\rho_c = 0.6$, $\rho_p/\rho_c = 200$, $b/L = 0.01$ and **(a)** $l/L = 0.1$, **(b)** $l/L = 1$, **(c)** $l/L = 2$ and **(d)** $l/L = 5$. Notice that the x-scale is changed is the last two panels, while in the first one, the sausage mode has passed through a cut-off (i.e. has become leaky).

of all, in a thick slab (say $b/L = 0.5$), the modes also start their transition to surface modes, similar to what happens for a single fibril. But if we move to the more interesting case of realistic values of $b/L \approx 0.001$, then as a result of the better confinement the interaction is dimished for a fixed set of the other parameters (Fig. 7.8), so the modes look more like the ones of a single fibril when the wavelength is raised. If $k_y L$ reaches values in the order of 100 then these modes also start their transition to surface modes.

In conclusion, the inclusion of the y-direction makes the interaction dimmer, so the fibrils only interact if they are separated a distance comparable with their widths. In solar prominences the fibrils are closely packed, so the coupling is strong even if this effect is taken into account.

7.2.3 Non-identical fibrils

Such as we stated before, there is no reason justifying that all the fibrils of a prominence must share identical physical properties. For this reason, we now investigate the eigenmodes of non-identical fibrils, which will be done numerically in order to avoid cumbersome calculations. The modified parameter is the prominence density which, after all, modifies the Alfvén velocity within the fibril. We have considered the case of two fibrils with different density in the cold

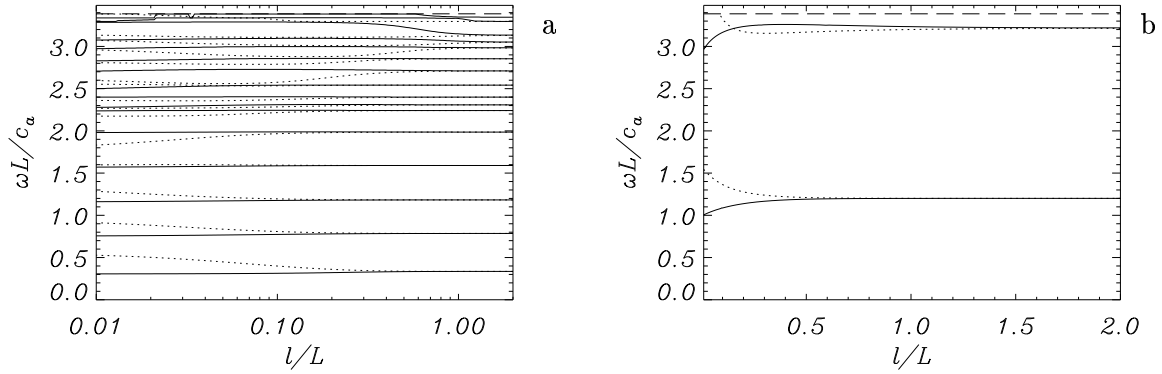

Figure 7.7: Two identical fibrils: variation of frequency with the half-separation for symmetric even (solid lines) and antisymmetric even modes (dotted lines) for the set of parameters $W/L = 0.1$, $\rho_e/\rho_c = 0.6$, $\rho_p/\rho_c = 200$ and **a**) $b/L = 0.5$, **b**) $b/L = 0.01$. These graphs are the counterparts of Fig. 7.3a and Fig. 7.4a for a value of $k_y L = 3$.

part representing the prominence.

The first conclusion is that in the limit of high separation, there are not two degenerate modes (symmetric and antisymmetric), but two fibrils oscillating alone and each fibril having its own eigenfrequency, which was calculated in Chapter 6. As the fibrils come closer the modes interact, and the mode coming from the denser one becomes the one in which both fibrils vibrate in phase, while the mode coming from the less dense fibril becomes the mode in which both fibrils vibrate in opposition of phase. For a realistic value of the fibril thickness, the antisymmetric mode becomes leaky when the fibril separation is reduced, specially for the values that might be expected in solar prominences. This behaviour is illustrated in Fig. 7.9.

Looking at their spatial structure, it can be seen in Fig. 7.10 that for the symmetric mode (Fig. 7.10a) the perturbed velocity is higher in the denser fibril, while for the antisymmetric one (Fig. 7.10b) it is higher in the less dense one. When the fibrils are separated by $l \approx b$, the result is like a single fibril (Fig. 7.11a) oscillating with a frequency slightly smaller than that of the dense fibril, and the spatial profile in and around these non-identical fibrils can be seen in Fig. 7.11b.

Therefore, if the fibrils are not equal, for long separation between them there are important differences: the modes do not tend to a single frequency but to the values corresponding to the fibrils alone, and their spatial structure is also different, with velocity perturbations only in one of the fibrils (mainly because the symmetry of the previous section is lost), but for realistic values of the thickness and separation, the interaction is very strong, so the fibrils end up oscillating in phase with velocity perturbations far away from them, with minor changes from the identical fibrils case.

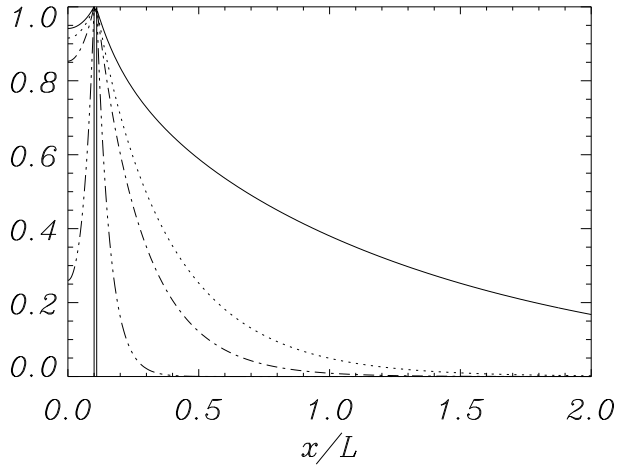

Figure 7.8: Spatial profiles for the fundamental even symmetric mode of a system with two identical fibril and dependence on the y-coordinate. The sets of parameters used are $W/L = 0.1$, $\rho_e/\rho_c = 0.6$, $\rho_p/\rho_c = 200$, $b/L = 0.01$, $l/L = 0.1$ and $k_y L = 0$ (solid line), $k_y L = 3$ (dotted line), $k_y L = 5$ (dotted-dashed line) and $k_y L = 20$ (dotted-dotted-dashed line). The fibril limits are marked by two vertical straight solid lines.

7.3 Numerical analysis of multifibril systems

7.3.1 Homogeneous prominence

The analytical method pointed out before can be extended without any theoretical difficulty to the study of systems with more than two fibrils. However, the system of equations akin to Eq.(7.3) becomes too cumbersome and, therefore, we will solve numerically the partial differential equations for the perturbed velocity components.

For the sake of simplicity, we will study first systems of n_f identically fibrils having thickness $2b$, with a separation $2l$ between all of them. With these conditions, and in the limit of no interaction (l/L big enough) there should be as many modes as fibrils with the same frequency, and for $l \to 0$ there would be a single oscillating fibril with thickness $n_f\, 2b$ (both limits can be calculated with the techniques of Chapter 6).

The resulting dispersion relations for 3 and 4 fibrils can be seen in Fig. 7.12. The main conclusion of these graphs is that for realistic separations of fibrils (that is, $l \approx b$) there is only one non-leaky mode: the first symmetric one in which all the fibrils oscillate in phase, while the modes with fibrils oscillating in phase opposition have become leaky long before. Moreover, the frequency is very close to that of a single fibril with $n_f\, 2b$ width (for the figure, the results in Chapter 6 give $\omega(b/L = 0.03) = 1.132\ c_{Ac}/L$ and $\omega(b/L = 0.04) = 1.019\ c_{Ac}/L$, which are the numerical values of these plots in the limit when $l/L \to 0$).

Regarding the spatial structure, in Fig. 7.6a it is seen that the fibril itself appears as a small spike in the velocity spatial structure. This can be confirmed in Fig. 7.13 for the case under consideration of 3 and 4 fibrils. These plots show the velocity spatial structure in and near the

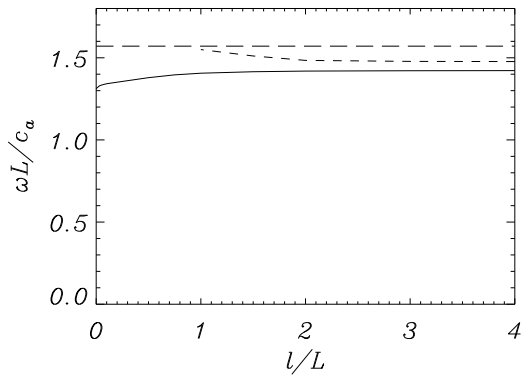

Figure 7.9: Dispersion relations for two non-identical fibrils for the set of parameters $W/L = 0.1$, $\rho_e/\rho_c = 0.6$, $b/L = 0.01$ and $\rho_p/\rho_c = 200$ for one of them and $\rho_p/\rho_c = 150$ for the other. The solid and dashed lines are symmetric and antisymmetric modes respectively.

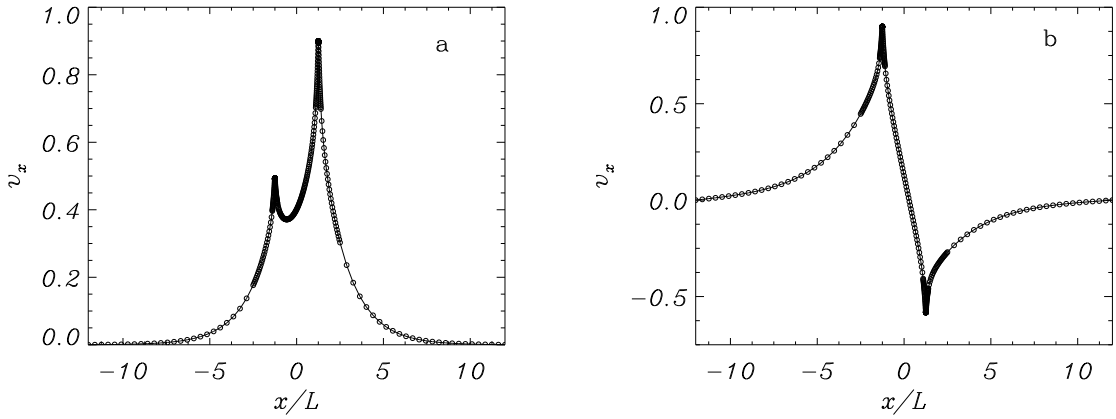

Figure 7.10: Cuts in the direction $z = 0$ for two non-identical fibrils for the set of parameters $W/L = 0.1$, $\rho_e/\rho_c = 0.6$, $b/L = 0.01$, $\rho_p/\rho_c = 200$ for one of them and $\rho_p/\rho_c = 150$ for the other, and half separation $l/L = 1.25$. The panel labelled **(a)** corresponds to the symmetric mode $\omega L/c_{Ac} = 1.412$ and **(b)** to the antisymmetric one $\omega L/c_{Ac} = 1.525$, which is near the cut-off frequency. The denser fibril is placed in the positive x-axis ($l \leq x \leq l + 2b$).

fibrils and, since the interaction is very strong (l/L small), the global shape approaches that for a single fibril having width $n_f\, 2b$. In other words, the overall perturbation is similar to the one in Fig. 7.11a, with a peak in the fibril region and a slow decay away from it, but if we zoom in that region the fibrils are marked, as can be seen in Fig. 7.13, but oscillating with just slightly more amplitude than the surrounding coronal medium.

7.3.2 Non-homogeneous prominence

The above model can be applied to more complex configurations such as those expected to be found in real filaments. As an example, we may study the oscillatory modes of the structure plotted in Fig. 7.14, where all the fibrils are inside flux tubes such as those described in Fig 7.1. The different fibril density ratios represent the inhomogeneity in density of a real prominence, i.e. a different Alfvén velocity for each fibril, and the thickness and separation between fibrils

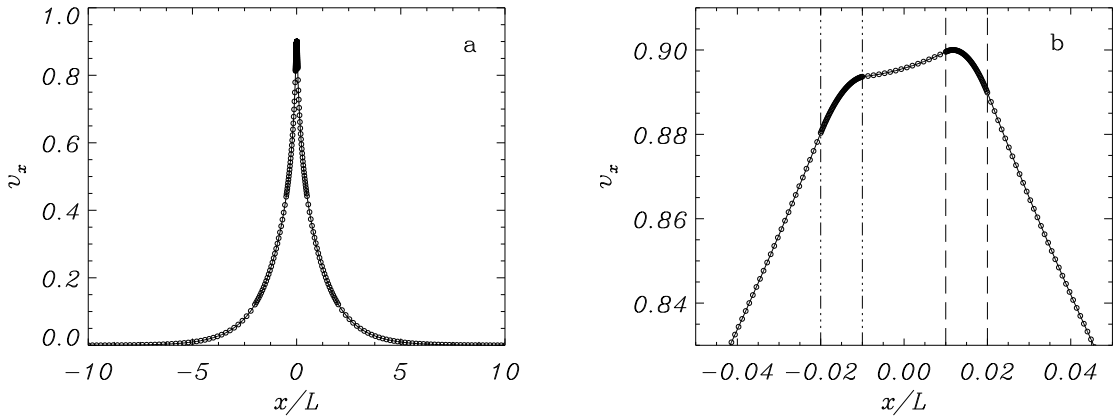

Figure 7.11: **(a)** Cut in the direction $z = 0$ for the symmetric mode ($\omega L/c_{\mathrm{Ac}} = 1.317$) of two non-identical fibrils for the set of parameters $W/L = 0.1$, $\rho_{\mathrm{e}}/\rho_{\mathrm{c}} = 0.6$, $b/L = 0.01$, $\rho_{\mathrm{p}}/\rho_{\mathrm{c}} = 200$ for one of them and $\rho_{\mathrm{p}}/\rho_{\mathrm{c}} = 150$ for the other, and half separation $l/L = 0.01$ (in the range expected in solar prominences). **(b)** Detail of the zone around the fibrils, whose limits are highlighted with vertical dashed lines for the dense one and dashed-dotted lines for the less dense one.

has been chosen randomly within the realistic range.

Now, we can obtain the eigenmodes of this configuration. When the separation between fibrils is the one shown in Fig. 7.14, there is a strong interaction between them since the perturbation can easily overcome the separation and, as a result, there is only one even non-leaky mode: the one with all the fibrils oscillating in phase. The overall structure is like the one in Fig. 7.11a, while the fine structure around the fibrils is plotted in Fig. 7.15. The spatial profile of the velocity is similar to that of the more dense fibril oscillating alone, with small contributions from the less dense fibrils.

The frequency dependence on the fibril separation can be studied, but there are also other parameters which could be modified. We have chosen to increase the fibril separation (named l_{ref}) keeping the widths of the fibrils and the ratios of separation between them as in Fig. 7.15. The results are plotted in Fig. 7.16, and compared with the single dominant fibril oscillating alone (dotted line). In the limit $l_{\mathrm{ref}} \to \infty$, the structure and the frequencies of each fibril oscillating alone are recovered, while for small values of l_{ref} all the non-phase oscillating modes are leaky, and only the mode described before remains having a slightly smaller frequency than in the case of the single dominant fibril mode.

Also, looking at the spatial structure of the modes for separation $l_{\mathrm{ref}} \to \infty$, we find that the spatial structure of each mode tends to be that one of fibrils oscillating alone with its own frequency such as described in Chapter 6. For the first mode, all the fibrils oscillate in phase; for the second mode there are two groups of fibrils oscillating with opposition of phase between them; similarly, for the third mode there are three groups, for the fourth mode only two fibrils oscillate in phase (and the rest in opposition), finally, for the fifth mode all the fibrils vibrate in opposition of phase with its neighbours. However, all these modes, except the fundamental one described in Fig. 7.15, are leaky in the realistic range ($l_{\mathrm{ref}} \approx b$).

Therefore, for realistic values of the separation between fibrils, the multifibril system would oscillate in phase, with similar amplitudes and the same frequency (smaller than the eigen-

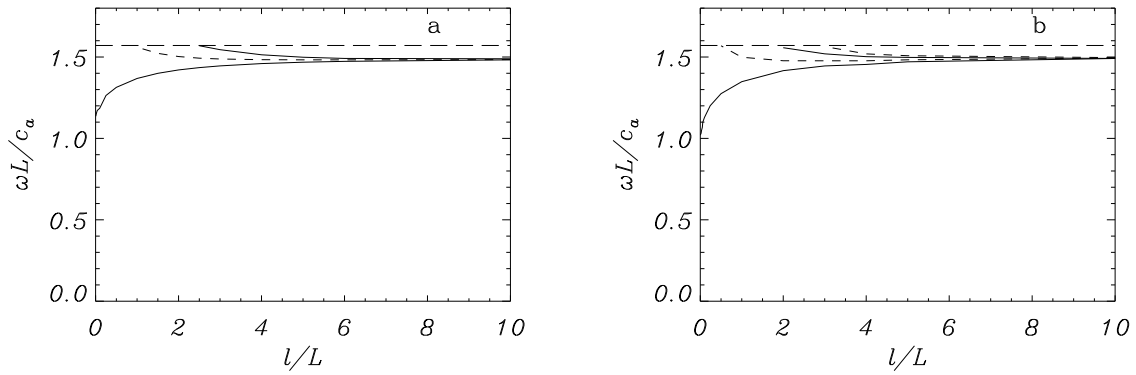

Figure 7.12: Dispersion relations for **a**) three fibrils and **b**) four fibrils for the set of parameters $W/L = 0.1$, $\rho_e/\rho_c = 0.6$, $\rho_p/\rho_c = 200$, $b/L = 0.01$. The solid and dashed lines are symmetric and antisymmetric modes respectively.

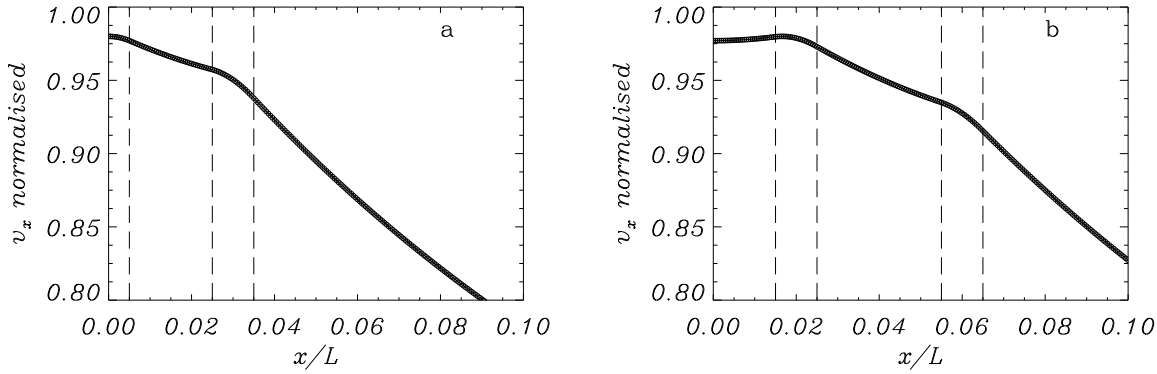

Figure 7.13: Cuts in the direction $z/L = 0$ for the first symmetric mode for the parameters $W/L = 0.1$, $\rho_e/\rho_c = 0.6$, $\rho_p/\rho_c = 200$, $b/L = 0.01$ and $l/L = 0.03 = 3b/L$ for a system with **a**) three fibrils and **b**) four fibrils. The fibril limits are represented by the dashed lines. A small x-range has been selected for a better perception of the structure around the fibrils.

frequency of the more dense fibril), so if we looked at it with a broader scale, we just could see something similar to Fig. 7.11a. Moreover, there would not be any trace of other fibrils eigenmodes, at least in the stationary state.

7.4 Conclusions

Using the analytical and numerical procedure developed in Chapter 4, we have constructed a very simple model to study the interaction between fibrils when fast MHD waves are excited within them. The analytical results have been checked numerically in the simplest case and both results are in a perfect agreement.

With the goal to mimic as accurately as possible real prominences, two different situa-

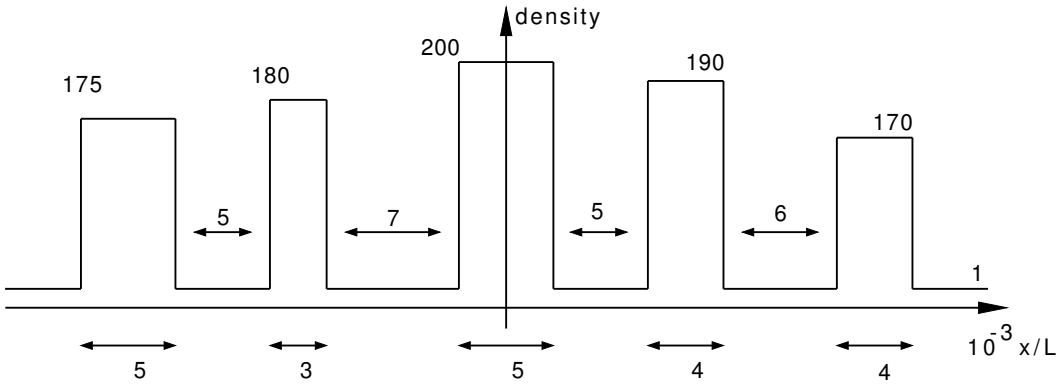

Figure 7.14: Sketch of a cut in the direction $z = 0$ of the normalised density profile (ρ/ρ_c) in the case of an non-homogeneous multifibril system. The normalised numerical values of the density are printed in each fibril, while the coronal medium has a value of 1. The fibril width and the separation between them are also marked.

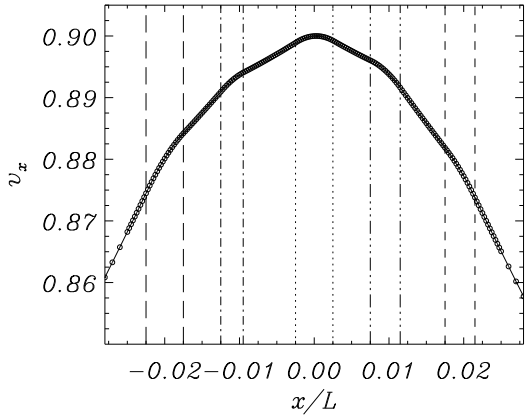

Figure 7.15: Detail of the zone around the fibrils in a cut in the direction $z = 0$ for the symmetric mode ($\omega L/c_{Ac} = 1.316$) of the system of non identical fibrils presented in Fig. 7.14. The fibril limits are marked with vertical lines (each two lines of the same fibril with a different style: long-dashed for the one having $\rho_p/\rho_c = 175$, dotted-dashed for the one with $\rho_p/\rho_c = 180$, dotted for the one with $\rho_p/\rho_c = 200$ and so on).

tions have been studied: homogeneous prominences, composed by fibrils with identical physical properties; and non-homogeneous prominences in which the density of the considered fibrils is different, i.e. the Alfvén velocity is the parameter being modified.

When considering identical fibrils, the symmetric and antisymmetric modes of oscillation have been described, and the general result is that when more than two-fibrils are considered, all the modes except the first symmetric one become leaky for realistic values of the fibril separation. This fact has an important consequence: if a fibril is perturbed and starts to oscillate, only the stationary modes described in Chapter 6 remain after a suitable time scale. However, in a system of fibrils, the symmetric and antisymmetric modes would be excited but, at the end, only the symmetric mode remains, i.e. the fibrils oscillate with the same frequency. Then, extrapolating these results to the whole prominence, after a suitable time scale, the prominence fibrils would oscillate in spatial phase with the same frequency, so the prominence would seem an oscillating slab with fine structure hardly discernible, but with the characteristic frequencies reflecting the fibril presence.

Therefore, a group of these fibrils in a solar prominence would oscillate all together with a

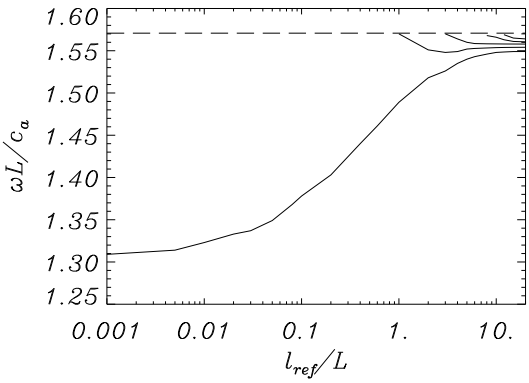

Figure 7.16: Logarithmic plot of the dispersion relation for the multifibril system of Fig. 7.14. The range in the frequency axis has been selected smaller to better display the details. Notice that now we cannot identify modes in phase and in opposition of phase directly (except the fundamental one, which always corresponds to all the fibrils oscillating in phase, see main text).

frequency just slightly different form a slab without structure and width $n_{\rm f}\, 2b$. If we continued this process for bigger values of $n_{\rm f}$, we should tend to a periodic alternance of fibrils and coronal regions that could be studied with similar techniques as the ones used to describe a periodic array of slabs in Berton & Heyvaerts (1987). In that paper the modes of slabs without structure in the z-direction were described, although the low-β assumption was not taken into account, but their conclusions were that there was no qualitative modification of the dispersion relations. Anyway, in our model there is a really high interaction between the fibrils, so a this slight modifications of the single fibril results are not expected for realistic values of the parameters, but the one described in this Chapter.

In the case of non-identical fibrils, i.e. an non-homogeneous prominence, because of the symmetry breaking there are no symmetric or antisymmetric solutions, and the most important conclusion is that when realistic separations between the fibrils of the system are considered, the fibrils oscillate in phase with slightly different amplitudes and with a frequency which is smaller than that of the denser fibril.

It has also been studied the effect of adding a dependence in the y-direction, in a simple example, similar to what was done for a single fibril in Chapter 6. The result is that the interaction is feebler, but for realistic values of the parameters (although it is difficult to make a estimation of the wavelength in this unlimited direction) the are only slight changes. Anyway, if the wavenumber k_y is high enough, the antisymmetric modes could be also trapped. Further work is expected to study this possibility.

On the other hand, there is the possibility to drain some energy from the excited fibril (apart from the leaky modes not studied here) and transfer it to its partners. To study this mechanism a perturbation profile should be assumed and the whole dynamic problem studied (instead of using a Fourier decomposition in the wave equations for the time dependence). Anyway, the results presented here seem to point that after some appropriate time scale all the fibrils of a prominence region (supposed that are closely packed) would be oscillating in phase with the same frequency. This could explain why groups of fibrils seem to oscillate together, but further studies are clearly necessary.

Chapter 8

Fast Magnetohydrodynamic waves in prominence fibrils: cylindrical geometry *

One never notices what has been done; one can only see what remains to be done.
Marie Curie

The most important limitation of the geometry used in Chapter 6 is the consideration of a Cartesian model, with the fibril being infinite in the longitudinal direction of the structure. Then, to make further progress a more realistic model for the prominence fibril structure is needed. The equilibrium we consider here assumes a straight cylindrical flux tube with a cool region representing the prominence, which is confined by two symmetric hot regions. With this geometry the problem becomes three-dimensional, but it can be solved analytically using the mathematical tools developed in Chapter 4.

8.1 Model and basic equations

Then, since in this Chapter we are only interested in the oscillations of a single fibril, our equilibrium model consists of a cylindrically symmetric prominence fibril surrounded by the coronal medium (Fig. 8.1). The configuration consists of a straight flux tube of total length $2L$ made of a cold and dense part (the prominence fibril itself) with length $2W$ and density $\rho_{\rm p}$ and a hotter coronal gas with density $\rho_{\rm e}$ occupying the remainder of the thin loop. The radius of the flux tube is b and this structure is embedded in the coronal environment, with density $\rho_{\rm c}$. The loop is anchored in the photosphere, so its footpoints are subject to line-tying conditions. Furthermore, the plasma is permeated by a uniform magnetic field directed along the prominence fibril and, since gravity has been neglected, all other physical variables (ρ, T and p) are also uniform in each of the three regions.

*This Chapter is based on: Díaz, A. J., Oliver, R. and Ballester, J. L. 2002, "Fast Magnetohydrodynamic oscillations in cylindrical prominence fibrils", ApJ, 580, 550.

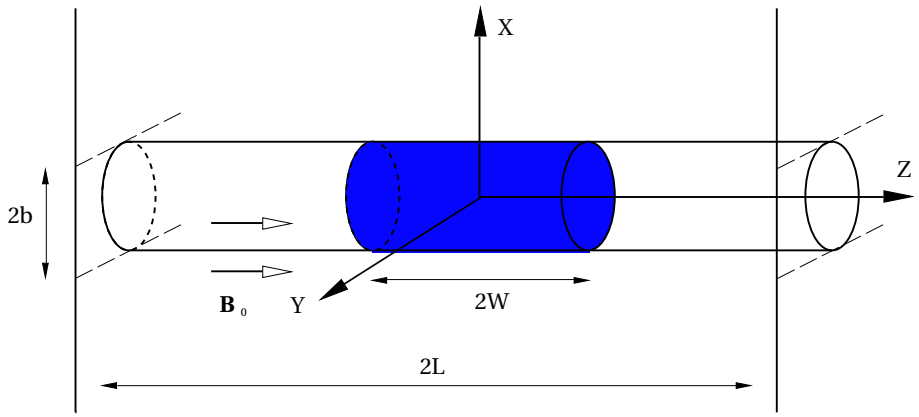

Figure 8.1: Sketch of the equilibrium configuration used in this study. The grey zone represents the cold part of the loop, i. e. the prominence. The density in the prominence region is $\rho_{\rm p}$, in the evacuated (coronal) part of the loop, $\rho_{\rm e}$, and in the coronal environment, $\rho_{\rm c}$. The magnetic field is uniform and parallel to the z-axis, and the whole configuration is invariant in the φ-direction.

As numerical values for the parameters defining the equilibrium model we have considered the same as in Chapter 6, namely the thickness and length of the prominence fibril $2b \simeq 100$–500 km and $2W \simeq 10\,000$ km, respectively, and the total length of magnetic field lines $2L \simeq 50\,000$–$100\,000$ km, so that $b/L \simeq 0.001$–0.01 and $W/L \simeq 0.1$–0.2. Moreover, typical density values are such that $\rho_{\rm c} \simeq \rho_{\rm e}$ and $\rho_{\rm p} \simeq 200\rho_{\rm c}$.

In order to perform the wave analysis, Eqs. (4.22) and (4.23) have to be solved using the techniques developed in Chapter 4. Separation of variables gives us the following expression for the perturbed pressure

$$p_{\rm T}(r,\varphi,z) = \Phi_m(\varphi) \times \begin{cases} \displaystyle\sum_{n=1}^{\infty} u_n^{(\rm l)}(r) h_n^{(l)}(z), & r \leq -b, \\ \displaystyle\sum_{n=1}^{\infty} u_n^{(\rm c)}(r) h_n^{(c)}(z), & r \geq b. \end{cases} \tag{8.1}$$

The resulting equations for the functions $u(r)$, $\Phi(\varphi)$ and $h(z)$ are Eqs. (4.93)–(4.95) We see that the φ-dependent function is simply

$$\Phi_m(\varphi) = e^{im\varphi}, \ m = 0, 1, 2, \ldots, \tag{8.2}$$

and so Φ_m comes in the form of a Fourier decomposition that arises from the original equation after applying the separation of variables technique. The z-dependent basis functions $h_n(z)$ were described in Sect. 4.5.2, as long as the coefficients H_{nm}, while the r-dependent basis functions $u_n(r)$, which result to be Bessel functions from Eq. (4.93), were described in Sect. 4.4.

Putting all together with the boundary conditions, a dispersion relation can be deduced Eq. (4.120), which is repeated here

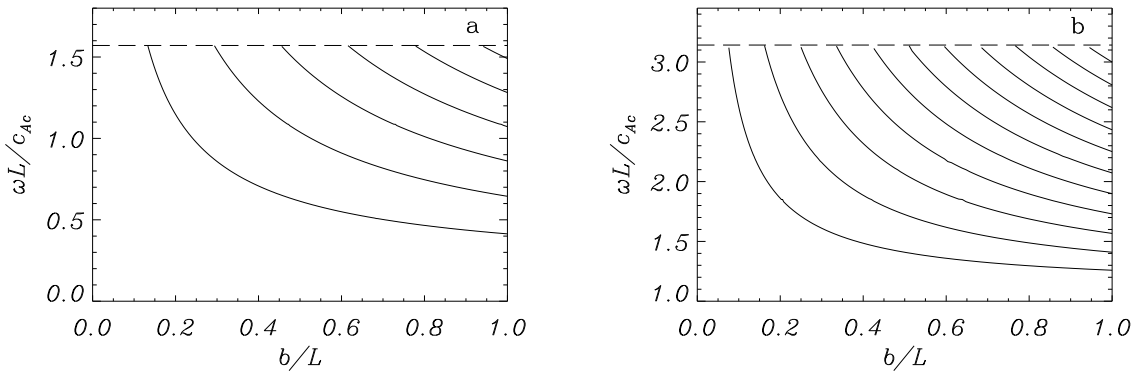

Figure 8.2: Variation of the dimensionless frequency with the fibril half-thickness for sausage ($m = 0$) **a)** even modes and **b)** odd modes ($W/L = 0.1$, $\rho_e/\rho_c = 0.6$ and $\rho_p/\rho_c = 200$). Notice that the fundamental mode and its harmonics have a cut-off frequency (horizontal dashed line) for all values of the fibril thickness.

$$\sum_{s=1}^{c} H_{sn} \left\{ \frac{1}{\lambda_n^{(c)}} J_m(\lambda_s^{*(l)} b) K'_m(\lambda_n^{(c)} b) + \frac{1}{\lambda_s^{*(l)}} K_m(\lambda_n^{(c)} b) J'_m(\lambda_s^{*(l)} b) \right\} B_s^* + \sum_{s=c+1}^{\infty} H_{sn} \left\{ \frac{1}{\lambda_n^{(c)}} I_m(\lambda_s^{(l)} b) K'_m(\lambda_n^{(c)} b) - \frac{1}{\lambda_s^{(l)}} K_m(\lambda_n^{(c)} b) I'_m(\lambda_s^{(l)} b) \right\} B_s = 0. \quad (8.3)$$

The number of imaginary "wavelengths" in the radial direction depends on the values of the parameters of the equilibrium model. One has $c = 1$ for realistic values of the ratios ρ_p/ρ_c and b/L but c can become greater than one for larger values of these two quantities.

8.2 Dependence of the frequency on the fibril thickness

Such as has been pointed out before, the determinant coming from Eq. (8.3) must be truncated by taking into account a finite number of basis functions. For large values of the ratio b/L, a good accuracy in the determination of ω is obtained when $N = 12$ is chosen, but for realistic, i.e. small, values of b/L around $N = 20$ basis functions are needed to achieve the same accuracy.

In Fig. 8.2 the eigenfrequencies of the sausage ($m = 0$) even and odd modes have been plotted in terms of the fibril radius. These modes do not have azimuthal dependence and hence the perturbed velocity is purely radial (see Eq. (4.113)). This figure shows that, in both symmetries, the fundamental modes and their harmonics have a cut-off frequency ($\omega_{cut} = \pi/2$ for even modes and $\omega_{cut} = \pi$ for odd modes, in the dimensionless units used here) and that in thin, realistic fibrils (i.e. for b/L in the range 10^{-3}–10^{-2}) there are no sausage fast modes confined inside the prominence. This is in striking contradiction with our previous findings in Cartesian geometry, in which the fundamental sausage mode is below the cut-off frequency for any thickness of the prominence fibril (see Chapter 6).

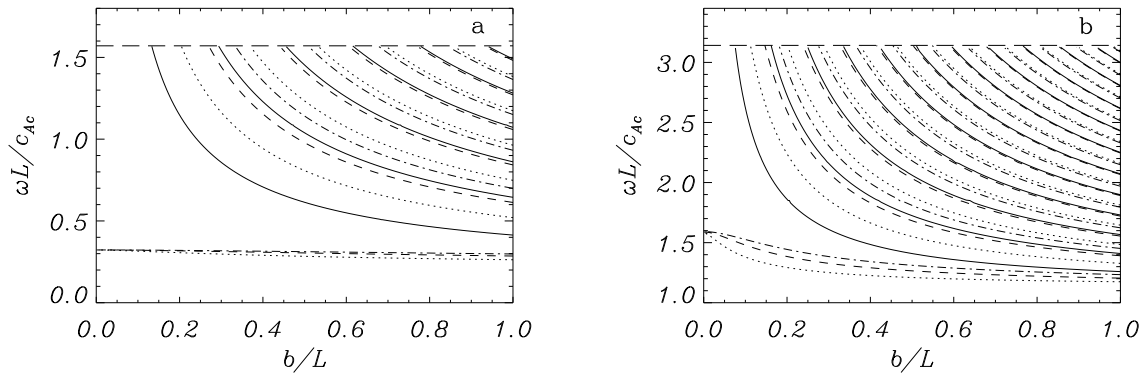

Figure 8.3: Eigenfrequencies for **a)** even and **b)** odd modes with $m = 0$ (solid lines, same ω as in Fig. 8.2), $m = 1$ (dotted lines), $m = 2$ (dashed lines) and $m = 3$ (dash-dotted lines). The equilibrium parameters have the values $W/L = 0.1$, $\rho_e/\rho_c = 0.6$ and $\rho_p/\rho_c = 200$. The horizontal dashed line in each plot gives the cut-off frequency.

We next turn our attention to other eigenmodes having azimuthal dependence ($m \neq 0$). In Fig. 8.3 we have plotted the eigenfrequencies corresponding to $m = 1$ (kink modes) and $m = 2, 3$ (first fluting modes). The most important point is that the fundamental modes for $m \geq 1$ do not have a cut-off frequency and that when $b/L \to 0$ all of them tend to the same value of ω. This behaviour can be more clearly seen in Fig. 8.4, in which, in order to highlight the behaviour for thin tubes, the logarithm of b/L has been used in the horizontal axis. On the other hand, all the harmonics reach the cut-off frequency (and thus become non-oscillatory inside the fibril) for values of b/L much larger than those of physical interest. The above insensitivity of the frequency of fundamental modes on the fibril thickness is of great interest since it reduces the number of free parameters that must be considered when doing prominence seismology. Thus, the observed oscillatory frequency in prominence fibrils can be used to determine the other equilibrium parameters (e.g. ρ_p/ρ_c, W/L), which control the value of ω.

In Fig. 8.5, the behaviour of the frequencies is investigated for values of the equilibrium physical parameters different from those used in Figs. 8.2, 8.3 and 8.4. Such as can be appreciated, the main two effects found in Cartesian geometry, namely mode couplings and decrease of the eigenfrequencies, are also present here. It is also interesting to point out that as the density ratio ρ_p/ρ_c is increased, other modes below the cut-off frequency appear in the range of small b/L. The reason for this behaviour is that for $\rho_p/\rho_c = 200$ the parameter c in Eq. (4.120) is equal to one and so there is just one basis function, namely $u_1(r)h_1(z)$, whose r-dependent part inside the tube is given in terms of an ordinary Bessel function, while all other basis functions inside the fibril are expressed in terms of modified Bessel functions. As a consequence, there is just one mode (whose spatial profile is mostly that of the first basis function) which is confined inside the fibril. On the other hand, for higher values of the ratio ρ_p/ρ_c one finds that c becomes larger than one and so there are more basis functions given in terms of ordinary Bessel functions. In particular, there are two such functions for $\rho_p/\rho_c = 1000$. For each basis function with this behaviour there is one mode that does not show a cut-off for small values of b/L and whose frequency is insensitive to the precise value of this parameter. Finally, we can also see that the fundamental even and odd eigenmodes do not couple to other modes because their spatial

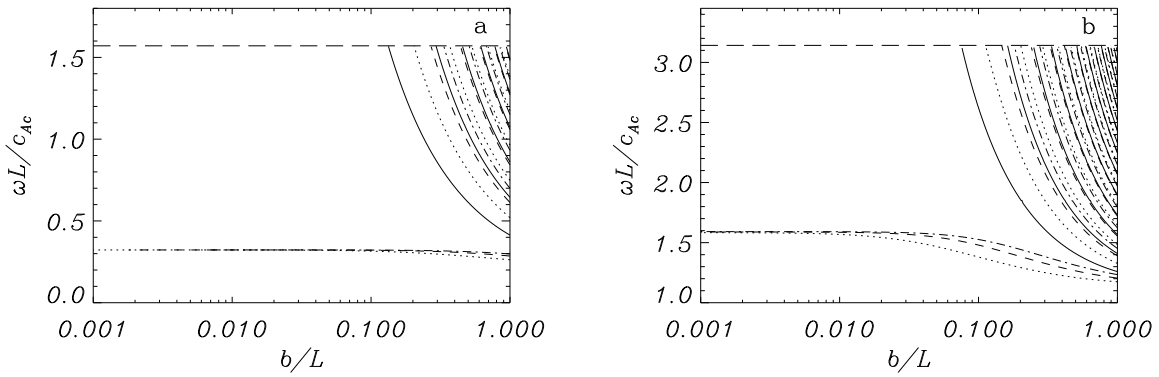

Figure 8.4: Plot of the data in Fig. 8.3 using a logarithmic axis for b/L to highlight that the fundamental kink and fluting modes ($m > 0$) exist for very small (i.e. realistic) values of the fibril thickness and that for $b/L < 0.01$ their frequencies are almost constant. The horizontal dashed line in each plot gives the cut-off frequency.

structure is such that they possess a single extremum and the interchange found in in Cartesian geometry is not possible here.

8.3 Spatial structure of the eigenmodes

Turning our attention to the spatial structure of modes, we find that a larger number of basis functions is required in Eqs. (8.1) and (8.3) to achieve a fine spatial representation of solutions: $N \simeq 60$ for thick fibrils (e.g. $b/L = 0.5$) and $N \simeq 120$ for thin, realistic fibrils ($b/L \simeq 10^{-3}$–10^{-2}).

We start by considering kink modes in a wide prominence fibril ($b/L = 0.5$); sausage modes are not taken into account since they are not relevant for thin, realistic fibrils. The spatial structure of the first three kink even eigenmodes below the cut-off for this fibril radius can be appreciated by means of cuts of the perturbed total pressure along $r = const.$ and $z = const.$ directions (Fig. 8.6) and with the help of surface plots (Fig. 8.7; only the first two modes are displayed). Our previous analytical development indicates that solutions are not separable functions of r and z, but after comparing Figs. 8.6a and b with Fig. 8.7a and Figs. 8.6c and d with Fig. 8.7b it turns out that their shape is well reproduced by cuts in the two directions. This is still true for much thinner tubes and thus, for the sake of clarity, the corresponding solutions will be later shown with the help of cuts along $r = const.$ and $z = const.$ directions.

From Fig. 8.6 it is clear that higher harmonics are associated with a bigger confinement of the mode in the dense part of the fibril, both in the r- and z-directions (note the different range of the horizontal axes in Figs. 8.6a, c and e). On the other hand, it is also evident that the first (i.e. fundamental) mode displays one extremum in r, the second mode has two extrema, etc. and, although it is not readily visible from these plots, the same happens in the z-direction. Nevertheless, this simple scheme does no longer hold when the equilibrium is such that mode couplings appear, as in Fig. 8.5, since modes might have more extrema in the r- and z-directions as a consequence of couplings.

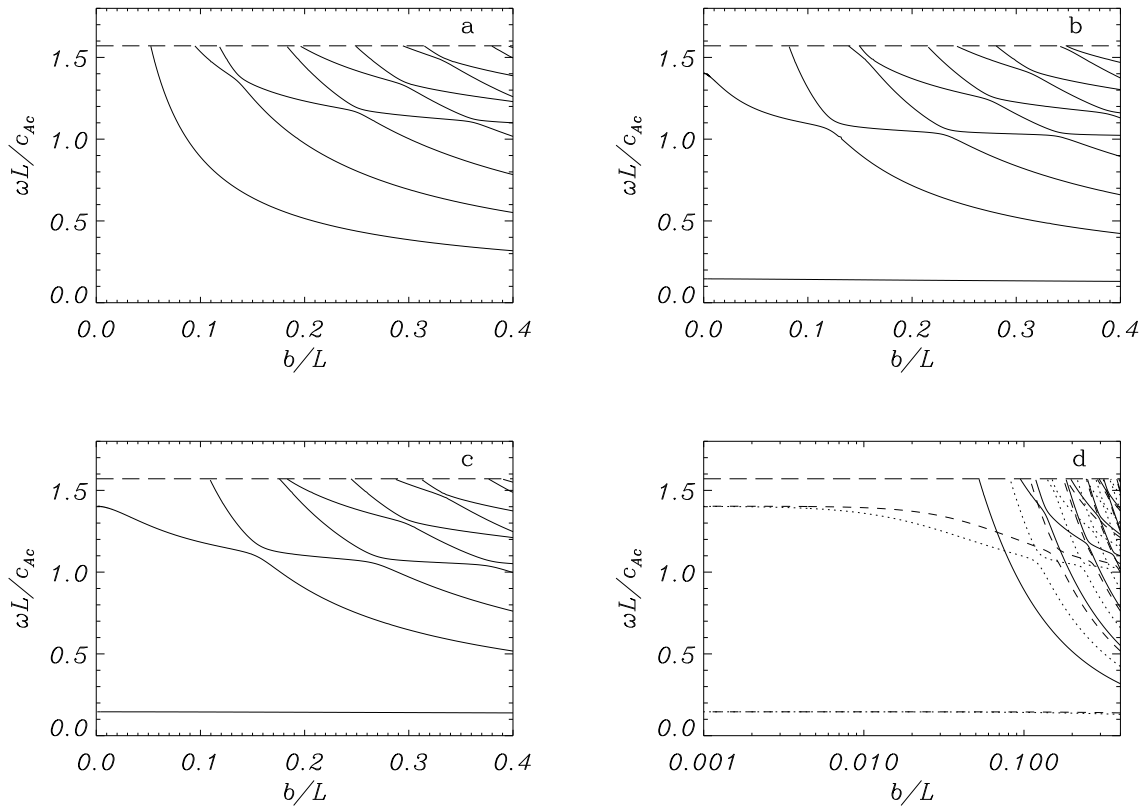

Figure 8.5: Variation of the frequency with the fibril half-thickness for even modes with **a)** $m = 0$, **b)** $m = 1$ and **c)** $m = 2$ for the set of values $W/L = 0.1$, $\rho_e/\rho_c = 1$ and $\rho_p/\rho_c = 1000$. **d)** Logarithmic plot of the curves in **a)** (solid lines), **b)** (dotted lines) and **c)** (dashed lines) to emphasise the behaviour of the modes for thin, realistic fibrils (i.e. b/L in the range 0.001–0.01).

Figs. 8.6a, c and e also show that the derivative of the perturbed total pressure is not continuous at the boundary $r = b$. The boundary conditions at this interface require that both the perturbed total pressure and velocity be continuous at $r = b$ which, in this geometry, does not imply the continuity of the derivative of p_T. This can be checked in Appendix B, where this fact is stressed for the particular case of sausage modes (see Eq. (E.11)).

We next slowly reduce the fibril thickness and observe that as a mode (e.g. any of the two kink harmonics shown in Figs. 8.6c–f) approaches the cut-off frequency it remains confined in the r-direction. This behaviour is completely different from that found in Cartesian geometry, in which as a mode approaches the cut-off frequency, its spatial structure is less confined and it eventually becomes leaky.

We finally concentrate on the structure of modes for small b/L (Fig. 8.8). We here select a larger value of the prominence to coronal density, namely $\rho_p/\rho_c = 1000$, so that instead of just one kink mode below the cut-off there are two of them (compare Figs. 8.4d and 8.5d for $b/L = 0.001$). Now one can appreciate another important difference between solutions in cylindrical and in Cartesian geometry: modes below the cut-off frequency in the small b/L range are confined inside the dense part in a cylindrical fibril. In fact, over 99% of the kinetic energy

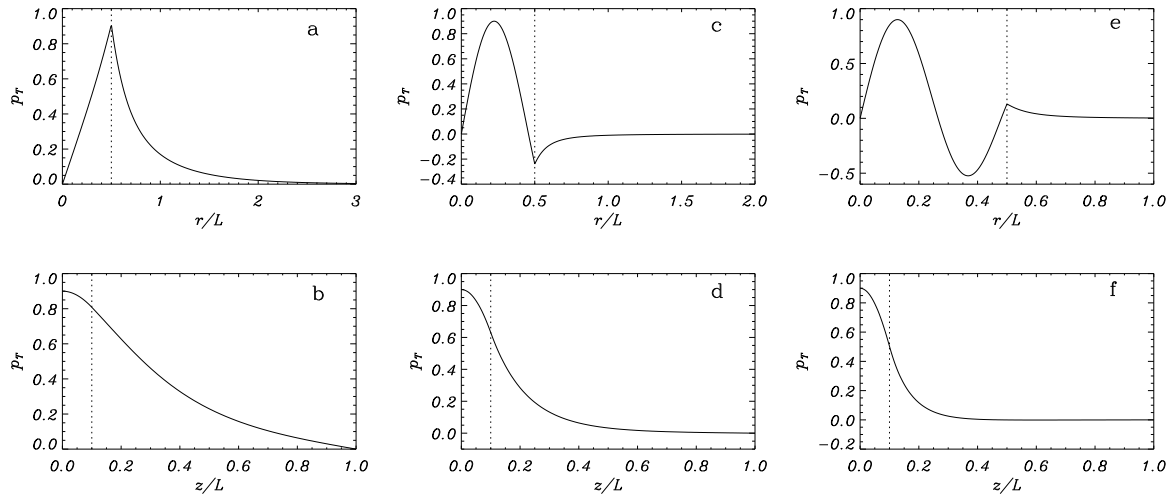

Figure 8.6: Cuts of the perturbed total pressure for the first three kink even modes in a thick fibril ($b/L = 0.5$) with $\rho_e/\rho_c = 0.6$, $\rho_p/\rho_c = 200$ and $W/L = 0.1$. The plots **a)** and **b)** correspond to the fundamental kink mode, **c)** and **d)** to the first harmonic and **e)** and **f)** to the second harmonic. **a)**, **c)** and **e)** Cut of $p_T(r, z)$ in the direction $z = 0$ (note the different horizontal scale used in these three plots); **b)**, **d)** and **f)** cut of $p_T(r, z)$ in the direction $r = b/2$. To compute these solutions, $N = 60$ basis functions have been added. Vertical dotted lines mark the boundary of the cool fibril.

of these two kink modes is located in the dense part of the fibril.

It is also worth to remark that other oscillatory modes having higher values of m exist, their frequencies and spatial structure in the r- and z-directions being similar to those of kink modes shown in Fig. 8.8.

8.4 Spatial velocity profile

We next study the behaviour of the perturbed velocity, a magnitude that can be obtained from observations more easily than the total perturbed pressure and from which prominence oscillations have been detected in most observational reports.

In Fig. 8.10 and 8.11 contour plots and cuts of the perturbed velocity components for the only kink even mode in a thin, realistic fibril are shown. These plots have some similarities to those of the total perturbed pressure. Firstly, the component v_r does not have a continuous derivative at the boundary $r = b$, while the component v_φ is not even continuous on this surface. Moreover, the shape of these functions is the expected one for the fundamental mode of vibration, with a single extremum both in the r- and in the z-directions. Finally, the perturbed velocity components in the present cylindrical configuration are quite confined inside the flux tube, contrary to what is found in Cartesian geometry, in which large perturbed values can be found far from the fibril axis. This can be readily seen by comparing v_x in Cartesian geometry with v_r in cylindrical geometry for the fundamental even kink mode (Fig. 8.12). In both cases the perturbed velocity decays in the direction across the fibril, but in Cartesian geometry a distance $x \approx 10^4 b$ is required to attain a factor 2 reduction in amplitude, while in cylindrical

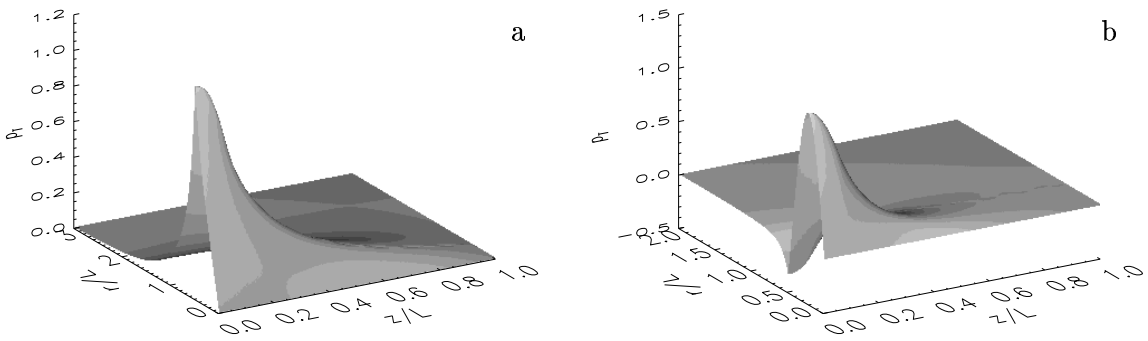

Figure 8.7: Surface plots of the perturbed total pressure corresponding to the kink even modes shown in **a)** Figs. 8.6a and b and **b)** Figs. 8.6c and d.

geometry the same reduction is achieved over a distance $r \approx 2b$ from the tube axis.

8.5 Oscillatory periods

One of the essential results of this Chapter is that the oscillatory frequency is quite insensitive to the exact value of the ratio b/L, i.e. the ratio of the fibril thickness to the total length of magnetic field lines. This is perhaps a surprising result since, given a length L, fibrils with different thickness oscillate with essentially the same frequency, whose dimensionless value depends on two parameters only: the ratios $\rho_{\rm p}/\rho_{\rm c}$ and W/L, because ω is only very weakly influenced by the quantity $\rho_{\rm e}/\rho_{\rm c}$. In addition, three more parameters are required to derive dimensional values of the frequency or the period: the magnetic field strength, B_0, the coronal density, $\rho_{\rm c}$, and the reference length, L.

We start by choosing two typical values of the fibril length, namely $W/L = 0.1$ and $W/L = 0.2$, and plot the frequency of modes below the cut-off as a function of $\rho_{\rm p}/\rho_{\rm c}$ (see Fig. 8.13). In these plots, we keep $b/L = 0.001$ constant, although taking $b/L = 0.01$ only lowers ω slightly. The frequency is seen to decrease with increasing $\rho_{\rm p}/\rho_{\rm c}$ and it can also be appreciated that more oscillatory modes are present for larger values of this quantity. From Fig. 8.13 it is also evident that the value of W/L has a strong influence on the mode frequencies. To compute the corresponding period we consider $L = 5 \times 10^4$ km, $B_0 = 5$ G and $\rho_{\rm c} = 8.37 \times 10^{-13}$ kg/m^3, so that the Alfvén speed in the coronal environment is $c_{Ac} = 488$ km/s. The period obtained from these three quantities is labelled T_0 and corresponds to the right vertical axes in Fig. 8.13 (see also Table 8.1). The period, T, for other values of L, B_0 and $\rho_{\rm c}$ can be calculated from the expression

$$T = T_0 \left(\frac{L}{5 \times 10^4 km}\right) \left(\frac{B_0}{5G}\right)^{-1} \left(\frac{\rho_{\rm c}}{8.37 \times 10^{-13} kg/m^3}\right)^{1/2}. \qquad (8.4)$$

Finally, in Figs. 8.14 and 8.15 contour plots of the non-leaky kink modes (odd and even, respectively) have been plotted. These figures clearly mark that the periods are in a wide range if

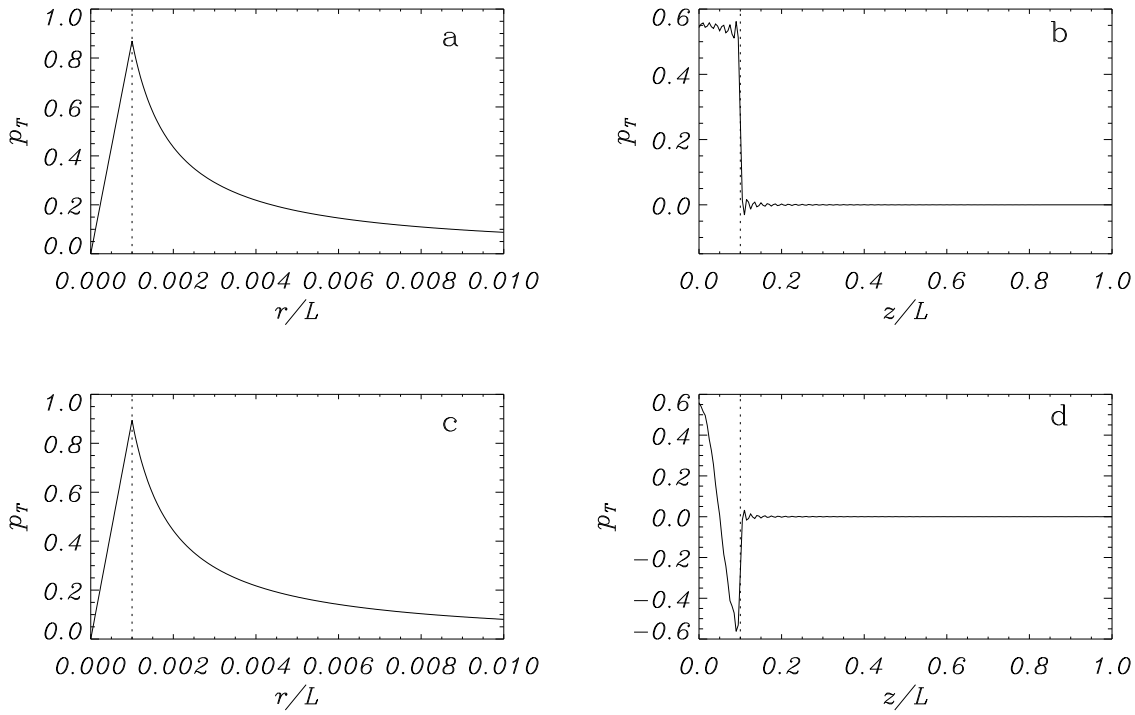

Figure 8.8: Plots of the total perturbed pressure for the two kink even modes below the cut-off frequency for the parameters $\rho_e/\rho_c = 1$, $\rho_p/\rho_c = 1000$, $W/L = 0.1$ and $b/L = 0.001$. **a)** and **b)** Fundamental mode and **c)** and **d)** first harmonic. **a)** and **c)** Cut of $p_T(r,z)$ in the direction $z = 0$; **b)** and **d)** cut of $p_T(r,z)$ in the direction $r = b/2$. Because of the mode coupling that takes place for higher b/L, both modes have a very similar structure, with just one maximum in the r-direction, although the number of extrema in the z-direction is different. The ripples in these plots are numerical and come from the fact that the number ($N = 120$) of basis functions used to compute the solutions is large but still not enough to obtain a fine representation of the small scale details. The global structure is, however, well captured by this solution. Vertical dotted lines mark the boundary of the cool fibril.

the parameter range is not constrained. These figures could be used to do prominence seismology, for example in the following way. The unknown parameters are the length of the supporting magnetic structure, L, the equilibrium magnetic field, B_0, and the prominence density, ρ_p, so we need the periods of three of the eigenmodes of the fibril. Then, the values of these parameters could be adjusted on these plots until the three periods are coherent and thus, we would have estimated the values of these parameters.

The above discussion on the dependence of the fast mode frequency on the various equilibrium parameters not only applies to kink modes but to fluting modes too, since their ω is extremely similar to their counterpart kink modes in the small b/L range (cf. Fig. 8.4).

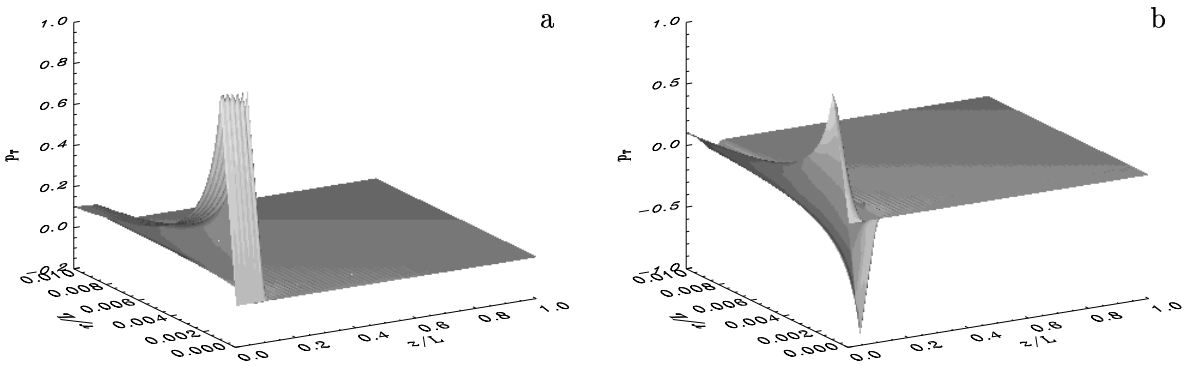

Figure 8.9: 3-D plots of the total pressure for the modes depicted in Fig. 8.8.

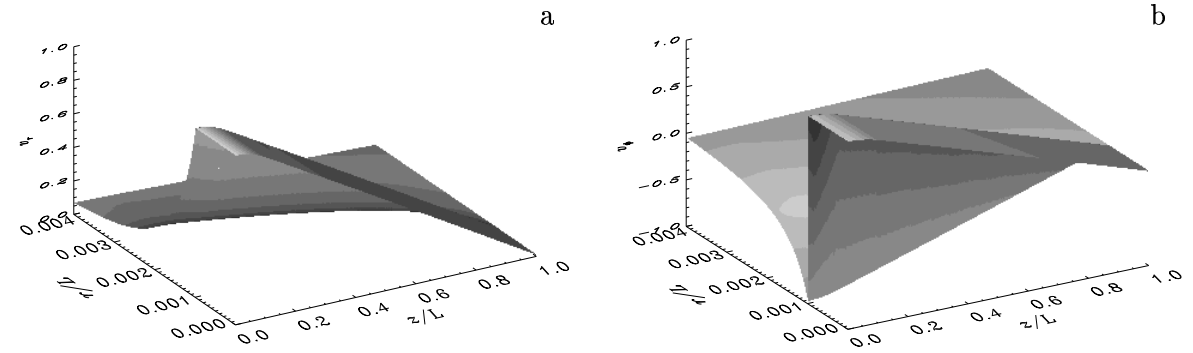

Figure 8.10: Three-dimensional plots of the **a)**r- and **b)** φ-components of the perturbed velocity for the fundamental kink even mode ($m = 1$) in a thin, realistic fibril ($b/L = 0.001$, $\rho_e/\rho_c = 0.6$, $\rho_p/\rho_c = 200$ and $W/L = 0.1$). Cuts of these modes are shown in Fig. 8.10

8.6 Conclusions

Following the analytical procedure presented in Chapter 4, the oscillatory properties of a cylindrical prominence fibril have been studied under the low-β approximation. Several important differences between the solutions obtained in Cartesian and cylindrical geometries must be highlighted. First of all, the solution found in cylindrical geometry is fully three-dimensional, instead of two-dimensional as in the Cartesian case, so one expects that the present results describe more accurately the oscillations of a real prominence fibril. On the other hand, to obtain our analytical solution the partial differential equations governing fast modes have been solved in a different way, with respect to the Cartesian case, and the total perturbed pressure has been used as the main unknown instead of the normal velocity component. In addition, when comparing both solutions, the first important conclusion is that formally they are not very different: the dispersion relations look rather similar, although in cylindrical geometry Bessel functions are involved

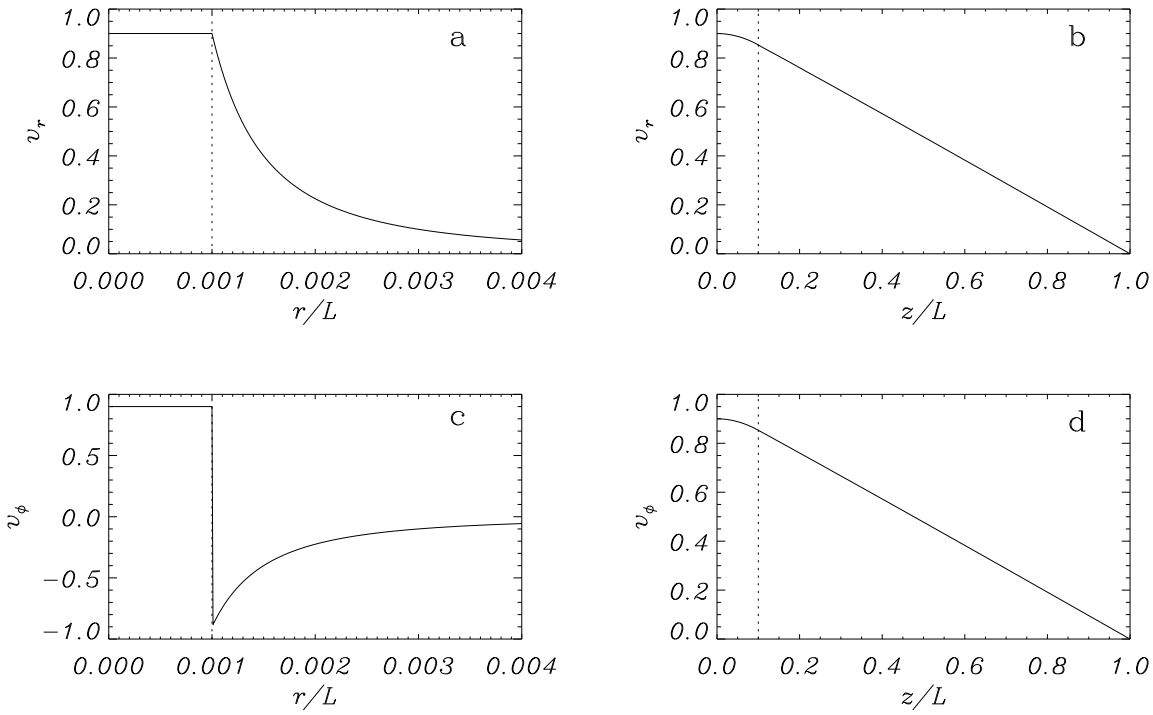

Figure 8.11: Cuts of the r- and φ-components of the perturbed velocity for the fundamental kink even mode ($m = 1$) in a thin, realistic fibril ($b/L = 0.001$). The equilibrium parameters used are $\rho_e/\rho_c = 0.6$, $\rho_p/\rho_c = 200$, $W/L = 0.1$. **a)** and **b)** Cuts of v_r in the directions $z = 0$ and $r = b/2$, **c)** and **d)** cuts of v_φ in the directions $z = 0$ and $r = b/2$. One can appreciate that v_r is continuous at the fibril surface ($r = b$), as requested by the MHD boundary conditions, whereas v_φ is not. Vertical dotted lines mark the boundary of the cool fibril.

instead of trigonometric and exponential functions; furthermore, in both cases the dependence of variables on the z-coordinate is the same, and for a thick, unrealistic fibril thickness the differences between both geometries are only quantitative. For instance, for $b/L \geq 0.1$, say, the eigenfrequencies are only slightly different in both geometries. This can be seen in Table 8.5, in which the frequencies of sausage and kink modes are given for a typical set of parameter values.

However, for a thin, realistic fibril the properties of the eigenfrequencies and eigenmodes found here change completely from those in Chapter 6 The main conclusions which can be drawn from our study are:

1. The fundamental sausage mode ($m = 0$) and its harmonics are always leaky since their frequency does not lie below the cut-off frequency. Therefore, if one of these modes is excited in the prominence fibril, its energy is quickly transferred to the coronal environment and the cold plasma stops oscillating.

2. For all other modes ($m > 0$), i.e. those having angular dependence, at least the fundamental mode lies below the cut-off frequency. Hence, if any of these modes is excited the oscillatory energy in the prominence plasma does not vary in time. Moreover, as the

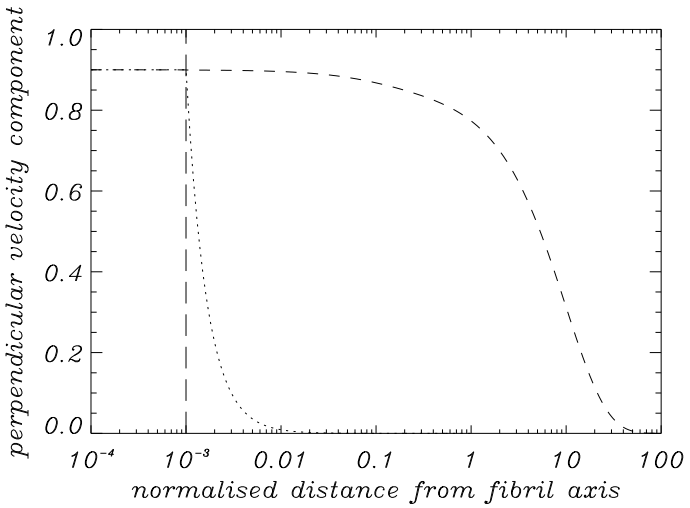

Figure 8.12: Cut of the perturbed velocity component v_x in Cartesian geometry (dashed line) and v_r in cylindrical geometry (dotted line) in the direction across the fibril centre. These solutions correspond to the fundamental kink mode in a prominence fibril with parameters $\rho_e/\rho_c = 0.6$, $\rho_p/\rho_c = 200$, $W/L = 0.1$ and $b/L = 0.01$. The vertical long dashed line marks the fibril boundary.

Table 8.1: Period of kink and fluting modes for $\rho_c = 8.37 \times 10^{-13}$ kg/m^3, $L = 5 \times 10^4$ km and $B_0 = 5$ G, and the parameters $b/L = 0.001$, $\rho_e/\rho_c = 0.6$, $\rho_p/\rho_c = 200$. Entries in the column "Mode No." are 1 and 2 for the fundamental mode and its first harmonic, respectively. The periods for other values of L, B_0 and ρ_c can be obtained from the values of T_0 in this table and Eq. (8.4).

Symmetry	W/L	Mode No.	$\omega L/c_{Ac}$	T_0 (min)
even	0.1	1	0.32288	33.2
odd	0.1	1	1.59153	6.74
even	0.2	1	0.23837	45.0
odd	0.2	1	0.84710	12.7
odd	0.2	2	2.34213	4.58

density ratio between the prominence and the coronal medium (ρ_p/ρ_c) is increased, the frequency of other harmonics may move below the cut-off and so the structure may support a higher number of oscillatory modes.

3. Regarding the spatial structure of perturbations, in cylindrical geometry the modes are always confined in the dense part of the flux tube, this probably being a consequence of the form of the boundary conditions at the prominence-corona interface. Therefore, an oscillating fibril is less likely to induce oscillations in its neighbouring fibrils, unless they are very close. Anyway, this does not diminish the interest of studying interactions between fibrils in multi-fibril systems.

4. Except for sausage solutions, fast modes have r and φ velocity components of the perturbed velocity with more or less the same order of magnitude.

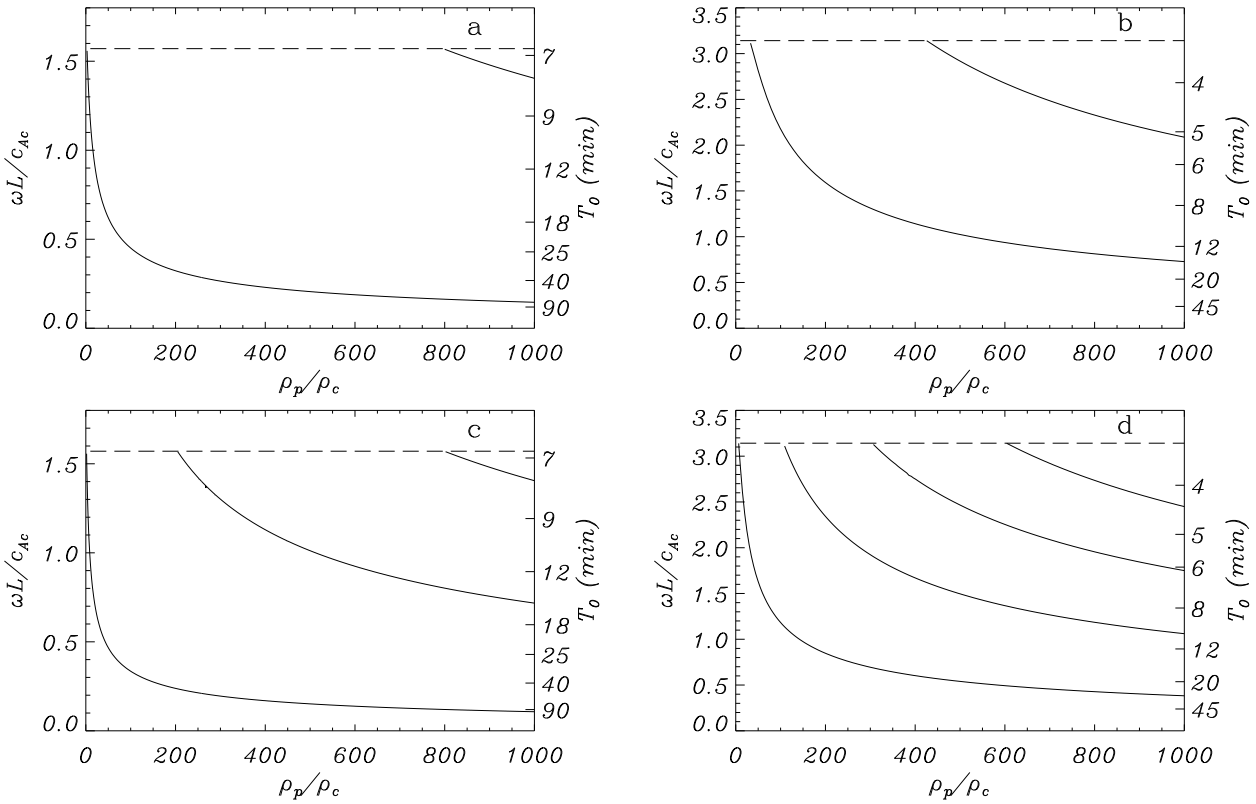

Figure 8.13: Frequency of **a)** and **c)** the kink even modes and **b)** and **d)** the kink odd modes against $\rho_{\rm p}/\rho_{\rm c}$ for the parameters $\rho_{\rm e}/\rho_{\rm c} = 0.6$ and $b/L = 0.001$. In **a)** and **b)** $W/L = 0.1$, while in **c)** and **d)** $W/L = 0.2$. The right axis provides with the period T_0 obtained after assuming the background magnetic field strength, the coronal density and the half-length of field lines are $B_0 = 5$ G, $\rho_{\rm c} = 8.37 \times 10^{-13}$ kg/m^3 and $L = 5 \times 10^4$ km. The horizontal dashed line in each plot gives the cut-off frequency.

5. Although Alfvén modes have not been considered in the present study, it turns out that fast and Alfvén modes are uncoupled for all values of the azimuthal wavenumber, m, and that in the case $m = 0$ the Alfvén mode is a purely torsional one.

In an attempt to allow for comparisons between our theoretical results and those coming from observations of prominence oscillations, the frequency of modes has been plotted for some equilibrium model parameters. Since there is no simple analytical expression for the frequencies, solutions must be plotted against the equilibrium model parameters. In spite of this, the present work is a step forward to understand the complex array of MHD modes present in these structures and indicates that oscillations with many different periods (see Fig. 8.13 and Table 8.1) may correspond to fast MHD stationary waves in prominence fibrils. It is also worth to point out that periods have a dependence on the plasma parameters, like the density or the magnetic field, so two different fibrils in a given prominence may have different characteristic periods. Figs. 8.14 and 8.15 can be used as diagnostic diagrams in prominence seismology, but the models still need refinement to estimate accurately the values of the equilibrium parameters.

On the other hand, in the evacuated part of a curved fibril the dependence of the wave solutions on the coordinate along the loop is constrained by the ratio of the coronal gravitational

Table 8.2: Frequency of fast sausage ($m = 0$) and kink ($m = 1$) even modes for $b/L = 0.5$, $\rho_e/\rho_c = 0.6$, $\rho_p/\rho_c = 200$ and $W/L = 0.1$ both in Cartesian and cylindrical geometry. Note that the fourth kink mode is absent in cylindrical geometry because its frequency lies above the cut-off. Entries in the column "Mode" are 1, 2, ...for the fundamental mode, its first harmonic, etc. and S or K for sausage or kink mode. These values of ω have been obtained by taking $N = 20$ basis functions.

Mode	$\omega_{cartesian}$	$\omega_{cylindrical}$
1S	0.512	0.614
2S	0.938	1.039
3S	1.351	1.453
1K	0.311	0.284
2K	0.728	0.808
3K	1.145	1.234
4K	1.555	—

scale height Λ to the wavelength λ (which is about twice the length of the tube for the fundamental mode). That dependence is roughly sinusoidal, as obtained here, only when $\Lambda/\lambda \gg 1$. This condition is satisfied in the short loops that form the lower part of the prominence, but it is not fulfilled in the long loops that form its higher portion. Then, the z-dependent part of the solutions obtained in our model, in which gravity has been neglected, would be correct for the low-lying prominence loops but only approximate for the high-lying loops.

Finally, one of the most interesting features is that only a few oscillatory modes exist for normal prominence conditions, while the rest are leaky, which offers a mechanism for draining energy away from the fibril. If a fibril is excited by an impulsive disturbance, the resulting perturbation can be decomposed into a weighed sum of the eigenmodes of the structure (both oscillatory and leaky). Therefore, since most of the modes are leaky, after a short time the energy contained in the fibril would be only a fraction of its initial value and would correspond to the energy of the oscillatory modes (i.e. those described in this Chapter). Moreover, if a non-uniform flux tube is considered, even these oscillatory modes can become damped because of couplings with the Alfvén modes (Stenuit et al. 1998, Stenuit et al. 1999), which form a continuous frequency band instead of the discrete eigenvalues of our model. Under such circumstances, the energy of these oscillatory modes would then be dissipated inside the fibril instead of being pumped out into the corona.

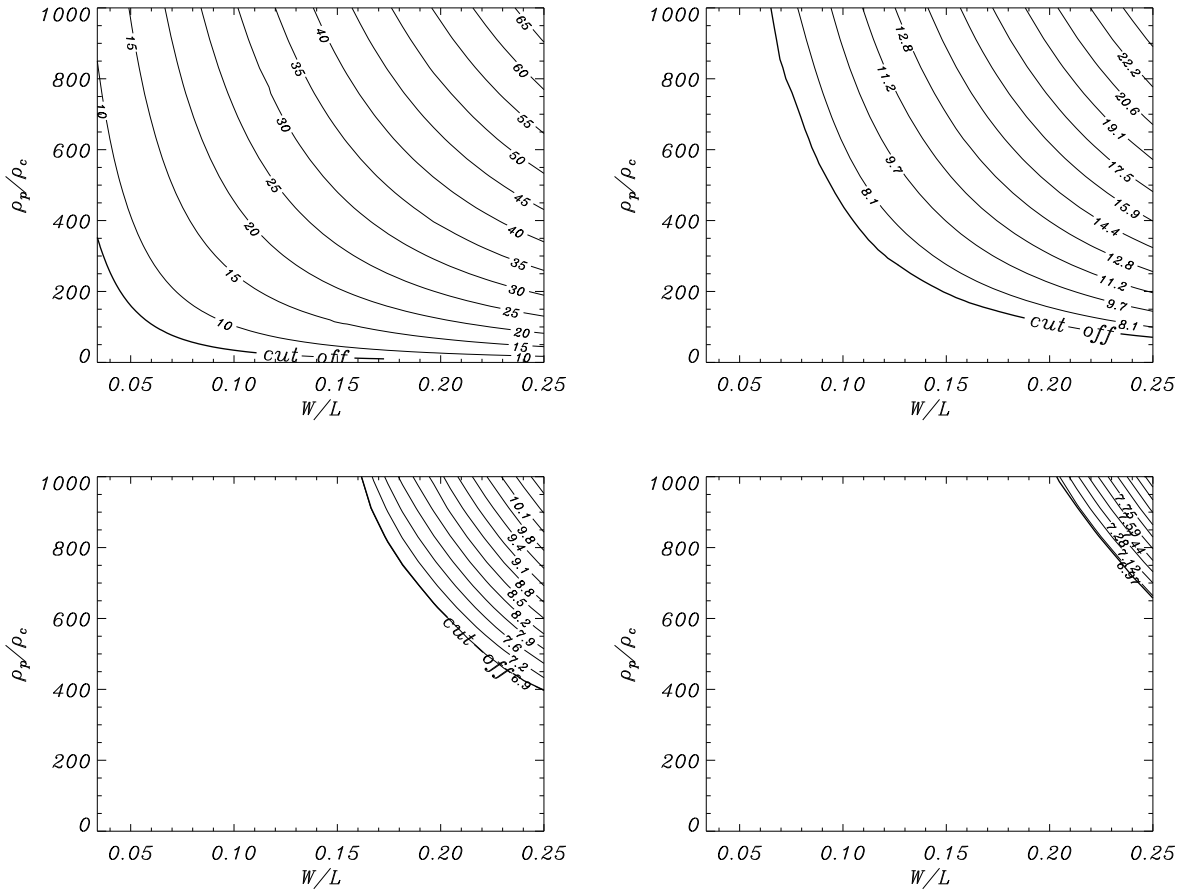

Figure 8.14: Contour plots of the four non-leaky kink odd modes against ρ_p/ρ_c and W/L for the parameters $\rho_e/\rho_c = 0.6$ and $b/L = 0.001$. The number in the isoline provides with the period T_0 obtained after assuming the background magnetic field strength, the coronal density and the half-length of field lines are $B_0 = 5$ G, $\rho_c = 8.37 \times 10^{-13}$ kg/m^3 and $L = 5 \times 10^4$ km. The cut-off is marked with a thick line.

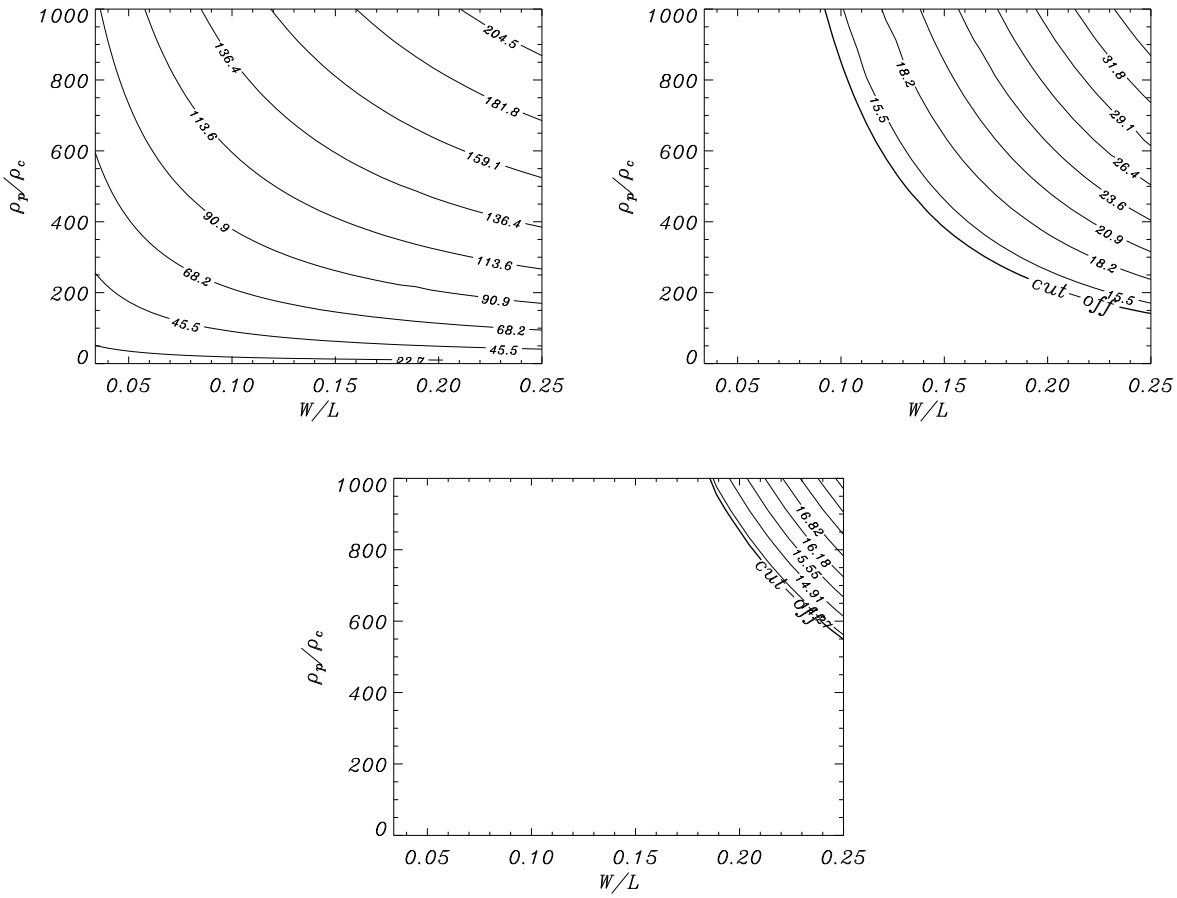

Figure 8.15: Same as Fig. 8.14 for the kink even modes.

Chapter 9

What we have learnt and what we plan to do

Muchas veces me han preguntado si merece la pena estudiar física, ya que al fin y al cabo sólo nos limitamos a intentar explicar y entender fenómenos, y dejamos para ingeniería y otras ramas el crear. Sin embargo, nada me recompensa más que entender un poco mejor lo que nos rodea, aunque sólamente sirva como satisfacción personal. *

First of all I would like to congratulate you, dear reader, for reaching this point. After more than 150 pages of theory we all deserve a rest, so this Chapter is a bit more informal than the rest of the Thesis. I would like to explain what is important of all the previous stuff and to present the new problems that can be studied.

9.1 Conclusions

Solar physics is a very special field in astrophysics, since the object we study is quite close to us. This means that we can obtain quite a lot of information from different channels and literally touch it (at least the solar wind), so you cannot theoretize wildly because some new observations may "put your work in the litter bin". It is quite stimulating that the Sun is the first place in which new theories are checked in their childhood before being applied in other fields, like stellar physics, plasma theory or particle theory. Moreover, there are at least two direct applications: the space weather and the problem of plasma confinement for fusion, so we can always sell our product quite better than other branches of astrophysics.

Coronal loop oscillations is a very active research field nowadays, with many papers pouring every year and with a lot more speakers in solar meetings than in other research areas, although the topic prominence oscillations is not so popular, since prominence structure is quite

*Many times I have been asked if it is worthwhile studying physics, since we just try to understand and explain fenomena but we leave the applications to other branches of science, such as engineering. However, nothing is more rewarding than understanding a bit more what we see, even if it is only for our personal enjoyment.

complicated and not too well understood right now. The reason for the popularity of coronal loop research may be that the new detailed observations have shown many effects that were not expected, but also have confirmed some of the predictions made by the MHD theory. Coronal loops are apparently quite simple, so theoretical and numerical work is encouraged to check the goodness of the current models in equilibrium, dynamics and oscillatory properties

One may wonder what this work has contributed to the present knowledge in solar physics, and in particular in coronal oscillations. Analytical and numerical techniques have been used to investigate the features of fast modes propagating in a thin, cool structure. The analytical solution is quite cumbersome, involving the Stürm-Liouville theory, but on the end it is necessary to solve the dispersion relations numerically, or even find the basis functions by numerical integration (so we often call this approach semi-analytical).

From the theoretical point of view, the well-known system of partial differential equations of linear MHD has been applied to this kind of problems in the low-beta limit, since one of our assumptions is that we work in a low-beta plasma. Then we have obtained a partial differential equation for one of the magnitudes, which allows us to find an analytical solution applying the separation of variables technique. In Cartesian geometry the results have been checked by solving directly the partial differential equations for the perturbed velocity and the agreement is excellent. In fact, this helped to improve the numerical code and we were gratefully surprised when it even proved capable of handling finite discontinuities.

9.1.1 Coronal loop oscillations

Homogeneous coronal loops

Regarding the results for coronal loop oscillations, we first investigated the behaviour of a homogeneous coronal loop when line-tying is added, since we were dissatisfied with the wide use of the results in Edwin & Roberts (1983) without taking into account the differences that arise with the inclusion of this condition. Some of the results are:

1. The introduction of line-tying adds a new characteristic length and a quantization (whose number is labelled as n) in the direction along the flux tube. The plots of the dispersion relation display these features a well as the quantizations in the azimuthal (whose number is labelled as m) and radial (whose number is labelled as l in this particular problem) directions. Therefore, there is a rich array of modes in this problem.

2. In a straight and uniform magnetic cylinder, for values of length, thickness and density of the flux tube in accordance with observations, sausage modes ($m = 0$) are leaky since their frequency lies above the cut-off frequency. If a sausage mode is excited in the loop, its energy is quickly transferred to the coronal environment and the oscillation dies out. For all other modes ($m > 0$) at least the fundamental mode lies below the cut-off frequency. Hence, if any of these modes is excited the oscillatory energy in the loop plasma does not decay. Moreover, as the density ratio between the loop and the coronal medium is increased, the frequency of other harmonics may move below the cut-off and so a dense loop may support a higher number of oscillatory modes.

3. Leaky modes have very short periods and short damping times. If these modes were excited, their energy would be quickly pumped out to the corona, making them difficult to detect (a high cadence would be necessary). Their strong attenuation would also lower their amplitude below the noise level in just a few oscillations.

4. The modes of a homogeneous flux tube with higher values of n, i.e. shorter wavelength along the loop, have periods $T_n = T_0/(n+1)$, where T_0 is the period of the kink or fluting mode with the same numbers l and m, but with $n = 0$. These modes could be detected, since their period is still in the range of the fundamental one and current spatial resolution is high enough. Observational data should contain signatures of these higher harmonics.

5. Currently available observational data does not usually show such short period modes. The suggested explanation is that if some structure is added to the model (for example, the chromospheric layers), the modes having the same m and l are combined to satisfy the MHD boundary conditions on the loop-corona interface. Under such conditions, all the higher order modes become leaky and therefore are undetectable in current observations.

Coronal loops with heating profiles

After this preliminary study, we proceeded to "add more ingredients to the recipe". We investigated the modifications in the solution for homogeneous loops that are introduced when some inhomogeneity along the loop is taken into account. We chose to apply simple equilibrium profiles, well aware that there are other refined models currently available, and the conclusions of that study are:

1. Few modes are trapped under coronal loop conditions. Only the fundamental kink and fluting modes can be sustained, except for very dense coronal loops, in which some higher harmonics might also be trapped.

2. The radius of the loop has very little effect on the oscillatory properties, provided it is small compared with the loop length. Therefore, the oscillatory frequencies would not be modified substantially if the coronal loop was made of filaments with smaller radius (unless collective effects change a lot the description).

3. The frequency of the modes is very sensitive to variations on the heating magnitude and the footpoint density, and the results are far from the ones of a homogeneous tube.

4. However, the frequency is very similar to the one of a homogeneous tube with density equal to the apex density. The reason for this result is that the equilibrium model has a significant density enhancement only near the footpoints, but the MHD oscillatory modes are constrained by the line-tying condition near them, so the amplitude is still small in that region. It must be emphasized that if the homogeneous density flux tube results are applied, the density must be measured near the apex, not in the footpoints, despite being more difficult to estimate.

5. The other studied heating profiles do not introduce too many modifications. It seems quite difficult to estimate the heating profile from the observational periods, although some information might be obtained about the magnitude of the heating term.

6. The addition of a very dense layer in the footpoints simulating the chromosphere only introduces slight corrections (because of the restriction of the amplitude near the footpoints due to the line-tying condition).

9.1.2 Prominence fibril oscillations

Single Cartesian prominence fibril

We then turned our attention to prominence fibril oscillations. We modelled them first as a slab with a density enhancement in the center and independence on the y-coordinate (and no longitudinal propagation). Two are the main conclusions that can be extracted from our results. First, prominence fibrils can only support a few modes of oscillation, those with smaller frequency, since high harmonics cannot be trapped inside the thin loop. Starting from a thick fibril, fast modes increase their frequency as the fibril thickness is reduced and, as soon as they exceed the cut-off frequency corresponding to kink and sausage modes, they become oscillatory. This is not the case, however, with the fundamental even and odd kink modes, whose ω tends asymptotically to $\omega_{\rm cut}$ but never reaches this value. Second, it has been shown that the spatial structure of the fundamental even and odd kink modes is such that the velocity amplitude outside the fibril takes large values over long distances, the reason being that their frequency is so close to $\omega_{\rm cut}$ that they are little confined to the prominence.

A consequence of the above results is that if fast modes were excited in the kind of fibril considered, most of the energy would be pumped out into the corona. Modes are not very well trapped by the fibril structure and, although the density of the coronal environment is very small compared to that of the dense material, the external region is much larger than the fibril and its total energy content can be comparable to the energy contained in the fibril. Therefore, this physical effect can give rise to damping of perturbations by means of energy leakage between fibrils. In addition, from the current view of prominences as made of a large number of thin fibrils packed together, it seems that fibrils would actually oscillate in groups rather than individually and that if a single fibril is disturbed it will excite perturbations in its neighbours, which may help to explain how prominence oscillations are damped in time. Note that the above conclusion about fibrils oscillating in groups rather than individually is not in contradiction with the observations by Yi et al. (1991) and Yi & Engvold (1991) since the spatial resolution in their data is ≥ 1 arcsec.

On the other hand, a solution for the problem with longitudinal propagation was found and in our discussion of the results we emphasized the behaviour of the dispersion relations and the spatial structure of the modes. The inclusion of propagation in the y-direction ($k_y \neq 0$) in the model has two relevant effects with respect to the results with $k_y = 0$:

1. The cut-off frequency now depends on k_y and, as a consequence, more modes become trapped within the fibril for a given set of parameters. However, the frequencies of the modes are only slightly shifted when the value of k_y is increased.

2. The existing modes become more confined, specially the fundamental even and odd ones. Therefore, the effect of the introduction of the third dimension is to weaken the interaction

between neighbouring fibrils. Then, when the separation between fibrils is increased, the probability of groups of fibrils oscillating together by mutual interaction diminishes.

The behaviour of the cut-off frequency with k_y and the possibility of more trapped modes for non-zero values of this parameter seems to be an effect of the addition of a free wave (in this work modes are not trapped in the y-direction). It should be emphasized that if the requirement of trapped modes in the x-direction is dropped, then there are leaky modes with higher frequencies than the cut-off, since the cut-off just separates the ranges of two different kinds of solutions: the leaky and the trapped ones.

Multifibril Cartesian systems

After guessing the oscillatory properties of a bunch of these fibrils from the properties of a single one, we finally attacked the problem of a multifibril system, constructing a very simple model to study the interaction between fibrils. The analytical results were checked numerically in the simplest case and both results are in perfect agreement.

When considering identical fibrils, the symmetric and antisymmetric modes of oscillation were described, and the general result is that when more than two-fibrils are considered, all the modes except the first symmetric one become leaky for realistic values of the fibril separation. This fact has an important consequence: if a fibril is perturbed and starts to oscillate, only the stationary modes remain after a suitable time scale. However, in a system of fibrils, the symmetric and antisymmetric modes would be excited but, at the end, only the symmetric mode remains, i.e. the fibrils oscillate with the same frequency. Then, extrapolating these results to the whole prominence, after a suitable time scale, the prominence fibrils would oscillate in spatial phase with the same frequency, so the prominence would seem an oscillating slab with fine structure hardly discernible, but with the characteristic frequencies reflecting the fibril presence.

Therefore, a group of $n_{\rm f}$ fibrils with thickness $2b$ in a solar prominence would oscillate all together with a frequency just slightly different form a slab without structure and width $n_{\rm f}\,2b$. If we continued this process for bigger values of $n_{\rm f}$, we should tend to a periodic alternance of fibrils and coronal regions that could be studied with similar techniques as the ones used to describe a periodic array of slabs in Berton & Heyvaerts (1987). In that paper the modes of slabs without structure in the z-direction were described, although the low-β assumption was not taken into account, but their conclusions were that there was no qualitative modification of the dispersion relations. Anyway, in our model there is a really high interaction between the fibrils, so these slight modifications of the results of a single fibril are not expected for realistic values of the parameters.

In the case of non-identical fibrils, i.e. a non-homogeneous prominence, because of the symmetry breaking there are no symmetric or antisymmetric solutions, and the most important conclusion is that when realistic separations between the fibrils of the system are considered, the fibrils oscillate in phase with slightly different amplitudes and with a frequency that is smaller than that of the denser fibril. The effect of adding propagation in the y-direction has also been studied in a simple example, similar to what was done for a single fibril. The result is that the interaction between fibrils is feebler, but for realistic values of the parameters the are only slight changes. Anyway, it is difficult to make an estimation of the wavelength in this unlimited

direction and if the wavenumber k_y is high enough, the antisymmetric modes could also be trapped.

Single cylindrical prominence fibril

Finally, we studied a cylindrical prominence fibril. Several important differences between the solutions obtained in Cartesian and cylindrical geometries must be highlighted. First of all, the solution found in cylindrical geometry is fully three-dimensional, instead of two-dimensional as in the Cartesian case, so one expects that the results in cylindrical geometry describe more accurately the oscillations of a real prominence fibril. On the other hand, to obtain our analytical solution the partial differential equations governing fast modes have been solved in a different way with respect to the Cartesian case, and the total perturbed pressure has been used as the main unknown instead of the normal velocity component. In addition, when comparing both solutions, the first important conclusion is that formally they are not very different: the dispersion relations look rather similar, although in cylindrical geometry Bessel functions are involved instead of trigonometric and exponential functions; furthermore, in both cases the dependence of variables on the z-coordinate is the same, and for a large, unrealistic fibril thickness the differences between both geometries are only quantitative. However, for a thin, realistic fibril the properties of the eigenfrequencies and eigenmodes change completely. The main conclusions are:

1. The fundamental sausage mode ($m = 0$) and its harmonics are always leaky since their frequency does not lie below the cut-off frequency. Therefore, if one of these modes is excited in the prominence fibril, its energy is quickly transferred to the coronal environment and the prominence plasma stops oscillating.

2. For all other modes ($m > 0$), i.e. those having angular dependence, at least the fundamental mode lies below the cut-off frequency. Hence, if any of these modes is excited the oscillatory energy in the prominence plasma does not vary in time. Moreover, as the density ratio between the prominence and the coronal medium ($\rho_{\rm p}/\rho_{\rm c}$) is increased, the frequency of other harmonics may move below the cut-off and so the structure may support a higher number of oscillatory modes.

3. Regarding the spatial structure of perturbations, in cylindrical geometry the modes are always confined in the dense part of the flux tube, this probably being a consequence of the form of the boundary conditions at the prominence-corona interface. Therefore, an oscillating fibril is less likely to induce oscillations in its neighbouring fibrils, unless they are very close. Anyway, this does not diminish the interest of studying interactions between fibrils in multifibril systems.

4. Except for sausage solutions, fast modes have r- and φ-components of the perturbed velocity with more or less the same order of magnitude.

5. Although Alfvén modes have not been considered in the present study, it turns out that fast and Alfvén modes are uncoupled for all values of the azimuthal wavenumber, m, and that in the case $m = 0$ the Alfvén mode is a purely torsional one. This is not the case, however, for $m > 0$.

In an attempt to allow for comparisons between our theoretical results and those coming from observations of prominence oscillations, the frequency of modes has been plotted for some equilibrium model parameters. Since there is no simple analytical expression for the frequencies, solutions must be plotted against the equilibrium model parameters. In spite of this, the present work is a step forward to understand the complex array of MHD modes present in these structures and indicates that oscillations with many different periods may correspond to fast MHD stationary waves in prominence fibrils. It is also worth to point out that the period depends on the plasma parameters, like the density or the magnetic field, so two different fibrils in a given prominence may have different characteristic periods. Figs. 8.14 and 8.15 can be used as diagnostic diagrams in prominence seismology, but the models still need refinement to estimate accurately the values of the equilibrium parameters.

In a nutshell, these prominences and non-homogeneous loops do not support too many modes (they only "dance to a few tunes"). These modes depend heavily on the properties of the supporting structure and the plasma parameters, so our results can be applied to coronal seismology and are a step further from classical results. We have found some properties that can help to identify and classify the array of observed eigenmodes in these coronal structures. Also, the relevance of the interaction between these structures has been highlighted and studied in some situations.

9.2 Future developments

It is often valuable not only to answer a question, but also to ask some new others. In that sense, many questions were not fully explained by the work developed in this Thesis and there are many extensions to the results that can be studied. Here we briefly comment on some of them.

Regarding the loop oscillations, here we have studied the effects of a density profile deduced from a stationary heating mechanism, but there are many other features in the equilibrium configuration that can shift the frequency or even change the oscillatory properties and should be included. The numerical code used to find the eigensolutions of a general problem (Sect. 4.5.3) could be applied to other kinds of equilibrium profiles and also be extended easily to work with extrapolations of observational density profiles along a coronal loop. In fact, it is only necessary to impose a density profile to perform the wave analysis, so it would be very interesting to compare the results for oscillating loops in which the density (and temperature) profiles can also be measured, for example, in those studied in Schrijver et al. (2002) and Aschwanden et al. (2002).

It is worthwhile remarking that every well-behaved function can be expanded in a series sum of the basis functions. In fact, we have always expanded the inner basis functions in terms of the outer basis functions (Eq. 4.63) because the outer ones are far simpler, but it could have been done in the opposite way, expanding the outer functions in terms of the inner ones. If all the terms in the sums are taken into account the solution is exactly the same, but if the sums

are truncated very slight differences may appear.

It is quite interesting to investigate how the modes are changed if the assumption of homogeneous coronal medium is relaxed and instead a stratified corona (in the z-direction) is assumed. In this case, the expansion of the inner basis functions in terms of the outer basis functions (Eq. 4.63) is not so straightforward, but it can be calculated numerically. A very important result is that each mode has then its own cut-off frequency which depends on the parameters and many other interesting properties may follow. We are specially interested in the problem in which both the coronal environment and the evacuated part of the fibril loop are stratified, even if gravity is not taken into account in the oscillatory problem.

Another type of dependence that has not been fully explored is the azimuthal one. Loops with lack of symmetry on this coordinate are also possible. A loop with elliptical cross-section can be dealt with the tools of this Thesis, leading to the Mathieu functions, while a tube with azimuthal but not longitudinal dependence can also be studied. In these models new families of modes would appear due to the lack of symmetry. A flux tube with cross-section dependent on position, such as is expected in the solar corona, is a more difficult problem, probably best suited for numerical analysis.

However, there are many other features for which the solution developed in this Thesis are not so straightforward, such as the effect of curvature (Smith et al. 1997), effect of twist in the equilibrium magnetic field (Bennett et al. 1999; Sakai et al. 2000), stratification in a slender flux tube (Hollweg & Roberts 1981), flows in an infinite flux tube (Nakariakov & Roberts 1995; Somasundaram, Venkatraman & Sengottuvel 1999; Homem et al. 2003). In fact, a full theory of coronal loop oscillations should take into account all these features, but for the sake of simplicity they are studied separately. However, it must be stated that the recent observational evidence, specially from *TRACE*, is not easily explained by models with thermal and hydrodynamical equilibrium (Testa, Peres & Reale 2002; Winebarger et al. 2003), so other equilibrium models have been considered by relaxing these hypothesis, for example using time-dependent heating functions (Walsh, Bell & Hood 1994, 1996), random heating pulses simulating nanoevents (Walsh et al. 1994; Walsh & Galtier 2000; Mendoza-Briceño, Erdélyi, Sigalotti 2002; Testa & Peres 2003) or deviations from the thermal equilibrium (Bradshaw & Mason 2003a, 2003b). In fact this is a subject of intense research nowadays, with no definitive conclusions about the true nature of these intriguing objects.

Also, we have just considered evanescent or leaky waves, but the most general solution in the coronal region has both functional dependences that come from a second order ordinary differential equation instead of only one (Eq. (4.73) for the y-coordinate and Eq. (4.76) for the x-coordinate in Cartesian geometry or Eq. (4.107) or (5.22) for the r-coordinate in cylindrical geometry). Using both functions would lead to a scattering problem, which is beyond the scope of this work. On the other hand, if the solution is imposed to be zero on some surface away from the structure then the stationary modes are not allowed to leak, but instead bounce back and forth this artificial boundary, changing the properties of the oscillatory modes. Some numerical calculations have been carried out taking into account this hint (for example De Groof & Goossens (2002) and references therein) and it would be really interesting to investigate how much energy from a propagating perturbation is transferred to the eigenmodes described in this work, or in a similar way, how much energy is pumped out to the coronal environment if some energy is released inside the loop (for example by reconnection or mode conversion). These

situations are linked with the leaky solutions, a problem which must be studied allowing the full temporal dependence instead of Fourier-analyzing the time component.

Regarding the Cartesian prominence fibrils, the inclusion of k_y in the Cartesian model has the effect of a better confinement of modes. The present work provides with a model of fast MHD oscillations with dependence on the three spatial coordinates in Cartesian fibrils, but it cannot be regarded as a three-dimensional model, since modes are not bounded in the y-direction. The next step could be to consider an orthogonal fibril (truly three-dimensional), leading to trapped modes in the x- and y-directions with a fixed cut-off frequency, such as happens in a cylindrical prominence fibril. Moreover, a comparison shows that the inclusion of k_y in the Cartesian model has the effect of a better confinement of modes, with their spatial structure across the fibril tending to that of the modes in a cylindrical structure. These conclusions must be checked by solving the orthogonal fibril. Preliminary results for a homogeneous line-tied orthogonal structure point out the existence of the same cut-off frequencies and the appearance of arrays of modes with different extrema in the x- and y-directions, results that probably can be extended to orthogonal prominence fibrils.

It is also interesting to mention that previous works based on the plasma slab (Edwin & Roberts 1988; Nakariakov and Roberts 1995) show that the simple step profile along the long axis is a good approximation and that more complicated shapes of inhomogeneities do not lead to important differences. This is also confirmed in Oliver & Ballester (1996), whose results suggest that a smooth discontinuity profile is only relevant for modes with large wavenumber in the direction of the discontinuity and since our evanescent modes have much larger scales, the use of a step profile is not expected to be relevant. Therefore, results for the slab are of wider validity and likely to be applicable to solar structures, even though they are an idealisation. Although this is not fully developed in this work, it is also possible with minor modifications of the proposed solution to study that kind of effects.

One of the most interesting features is that only a few oscillatory modes exist for normal prominence conditions, while the rest are leaky, which offers a mechanism for draining energy away from the fibril. If a fibril is excited by an impulsive disturbance, the resulting perturbation can be decomposed into a weighed sum of the eigenmodes of the structure (both oscillatory and leaky). Therefore, since most of the modes are leaky, after a short time the energy contained in the fibril would be only a fraction of its initial value and would correspond to the energy of the oscillatory modes. Then, there is the possibility to drain some energy from the excited fibril and to transfer it to its partners. To study this mechanism a perturbation profile should be assumed and the whole dynamic problem studied (instead of using a Fourier decomposition in the wave equations for the time dependence). Anyway, the results presented here seem to point out that after some appropriate time scale all the fibrils of a prominence (assuming they are closely packed) would be oscillating in phase with the same frequency. Moreover, if a non-uniform flux tube is considered, even these oscillatory modes can become damped because of couplings with Alfvén modes (Stenuit et al. 1998, 1999), which form a continuous frequency band instead of the discrete eigenvalues of our model. Under such circumstances, the energy of these oscillatory modes would then be dissipated inside the fibril instead of being pumped out into the corona.

We also plan to carry out prominence seismology on observed data, which is an improvement on the current estimations based on oscillatory properties that simply assume a value for some of the unknown parameters to tune the remaining ones until the resulting period matches the observed one. We stated that we need at least the frequencies of three modes to obtain values for the unknown equilibrium parameters and this calculation can be done even with the data in Yi & Engvold (1991) and Yi et al. (1991), which reported more than one characteristic period for a single object.

We mentioned the existence of flows in loops, but these flows are also detected in prominences. The modes are affected by these flows (Homem et al. 2003), but one must be careful when looking for this kind of solution, since only the flow-trough line-tying boundary condition makes sense. One may expect the features to be dragged by these equilibrium flows, but some stationary state coherent with the line-tying may be reached.

Another extension of the present work would be to investigate the properties of a periodic array of Cartesian prominence fibrils in a similar way as Berton & Heyvaerts (1987) studied an array of infinite slabs. This would be an extension of the results in the homogeneous multifibril section, leading to frequency shifts and some other strange effects such as the apparition of bands, for example.

Last but not least, an additional reason for taking a single cylindrical fibril is based in an attempt to simplify our study as much as possible, leaving the investigation of multifibril systems open for further work. A first step is to study the interaction of two identical cylindrical fibrils, which can be dealt with bicylindrical coordinates and the addition theorem for cylindrical harmonics. For such a system of two fibrils, the modes of a single fibril would be shifted and a new array of modes would appear due to the lack of symmetry in the azimuthal direction. Then, the collective behaviour exhibited by packed cylindrical flux tubes could be considered and thus the results of the multifibril Cartesian systems studied in this Thesis could be extended, for example following Bogdan and Zweibel (1985) (and related references).

Appendix A

Derivation of the MHD equations

MHD can be viewed basically as a combination of the electromagnetic equations (Maxwell equations and Ohm's law) and fluid mechanics equations (the Navier-Stokes equations). In this appendix the equations are introduced from general theories in Physics and the manipulations that lead to the MHD equations are presented.

A.1 Electromagnetic equations

Consider Maxwell equations describing the evolution of the electric $\mathbf{E}(\mathbf{r},t)$ and magnetic field $\mathbf{B}(\mathbf{r},t)$ in response to current density $\mathbf{j}(\mathbf{r},t)$ and charge density $\rho^*(\mathbf{r},t)$ (where the star is used to distinguish the charge density from the mass density in the following),

$$\nabla \times \mathbf{E} = -\frac{\partial \mathbf{B}}{\partial t}, \tag{A.1}$$

$$\nabla \times \mathbf{B} = \mu \mathbf{j} + \frac{1}{c^2}\frac{\partial \mathbf{E}}{\partial t}, \tag{A.2}$$

$$\nabla \cdot \mathbf{E} = \frac{\rho^*}{\epsilon}, \tag{A.3}$$

$$\nabla \cdot \mathbf{B} = 0, \tag{A.4}$$

respectively Faraday's law, Ampere's law, Coulomb's law and the solenoidal condition. In this equations the charge density is $\rho^* = e(n^+ - n^-)$ with n^+ and n^- the density of positive and negative charges. In many processes in the solar atmosphere the plasma is *electrically neutral* to a high degree of approximation, that is $n^+ - n^- \ll n$, with n the electron density. In practice, a local charge imbalance produces an electrical field with a spatial range given by the *Debye length* $\lambda_D = (kT/(4\pi n e^2))^{1/2}$, which is a measure of the distance in which the charge density fluctuations are important enough to deviate the value of the density appreciably. In fact, a

plasma may be defined as an ionised gas for which λ_D is much smaller than all other scales of interest.

If it is assumed that L is a typical length scale over which fields vary and T the associated time scale, the typical velocity in the MHD approximation satisfies $V = L/T \ll c$. Faraday's law shows that $E/L \sim B/T$ and substituting the electric field order of magnitude in Ampere's law,

$$\mu j \sim O\left(\frac{B}{L}\right) + O\left(\frac{V^2}{c^2}\frac{B}{L}\right). \tag{A.5}$$

As a consequence, the displacement current can be neglected compared with the current density (since we are not interested in electromagnetic waves). Under these conditions, Ampere's law just reduces to

$$\mathbf{j} = \frac{1}{\mu}\nabla \times \mathbf{B}. \tag{A.6}$$

Now the current density can be regarded as a derived quantity from the magnetic field instead of its source (although the latter interpretation is still physically valid).

There is another electromagnetical equation that should be introduced here, namely Ohm's law,

$$\mathbf{j} = \sigma(\mathbf{E} + \mathbf{v} \times \mathbf{B}), \tag{A.7}$$

where σ is the electric conductivity and $\mathbf{v}$ the fluid velocity. We have to note here that Ohm's law lacks the universality of Maxwell equations, since comes from equilibrium assumptions in Boltzmann equations. It can be extended to take into account the differences between ions and electrons (and neutrals, that still exist in a very small proportion), but this is not necessary except in extremely thin regions of high current concentration. Notice that Ohm's law provides a link between the electromagnetic and dynamic equations.

The electric field can also be considered now a response of the existing magnetic field because it is totally determined by $\mathbf{v}$ and $\mathbf{B}$. It is convenient to eliminate $\mathbf{E}$ between Faraday's law (Eq. A.1), the modified Ampere's law (Eq. A.6) and Ohm's law (Eq. A.7) to obtain the so-called *induction equation*,

$$\frac{\partial \mathbf{B}}{\partial t} = \nabla \times (\mathbf{v} \times \mathbf{B}) - \nabla \times (\eta \nabla \times \mathbf{B}), \tag{A.8}$$

where $\eta = 1/\mu\rho$ is the magnetic diffusivity, which is usually constant, so by virtue of the solenoidal condition the equation can be cast in the form

$$\frac{\partial \mathbf{B}}{\partial t} = \nabla \times (\mathbf{v} \times \mathbf{B}) + \eta \nabla^2 \mathbf{B}. \tag{A.9}$$

It is capital to compare the order of magnitude of the two terms in last equation,

$$\frac{\nabla \times (\mathbf{v} \times \mathbf{B})}{\eta \nabla^2 \mathbf{B}} \sim \frac{VB/L}{\eta B/L^2} = \frac{VL}{\eta} = R_{\rm m}, \tag{A.10}$$

with $R_{\rm m}$ the magnetic Reynolds number. If $R_{\rm m} \ll 1$ then Eq. (A.9) reduces to a simple diffusion equation. On the other hand, if $R_{\rm m} \gg 1$ Eqs. (A.9) and (A.7) take the form

$$\frac{\partial \mathbf{B}}{\partial t} = \nabla \times (\mathbf{v} \times \mathbf{B}), \tag{A.11}$$

$$0 = \mathbf{E} + \mathbf{v} \times \mathbf{B}. \tag{A.12}$$

Under these conditions, Alfvén's *frozen-flux theorem* holds: *in a perfectly conducting plasma, magnetic field lines behave as if they move with the plasma* (by the vorticity-magnetic field analogy this is directly comparable with the classical *vorticity theorem of Helmholtz and Kelvin*). Therefore, the magnitude of the magnetic Reynolds number ($R_{\rm m}$) is very important. In the solar corona it is of order 10^8, so only in phenomena having very small scales the magnetic diffusion might be relevant. Moreover, magnetic field structures dissipate much faster that the diffusive limit predictions, so other mechanisms must be involved. In general, Eqs. (A.11) and (A.12) are used in coronal MHD applications.

A.2 Fluid mechanics equations

We next consider the gas dynamic equations for the evolution of the plasma parameters, such as density ρ, pressure p or the velocity field $\mathbf{v}$. Our first equation comes from the mass continuity (conservation of mass in the fluid motion), which can be written in two equivalent forms,

$$\frac{\partial \rho}{\partial t} + \nabla \cdot (\rho \mathbf{v}) = 0, \tag{A.13}$$

$$\frac{D\rho}{Dt} + \rho \nabla \cdot \mathbf{v} = 0, \tag{A.14}$$

where $D/Dt = \partial/\partial t + \mathbf{v} \cdot \nabla$ is the Lagrangian time-derivative (moving with the fluid).

The next equation comes from Newton's second law (momentum conservation),

$$\rho \frac{D\mathbf{v}}{Dt} = -\nabla p + \mathbf{j} \times \mathbf{B} + \rho^* \mathbf{E} + \mathbf{F}. \tag{A.15}$$

Any other force not being the pressure gradient or the electromagnetic one, such as the viscous forces or gravity, appears in the last term, but since these other forces are not be relevant in this deduction we set $\mathbf{F} = \mathbf{0}$. Moreover, in a magnetised plasma like the coronal one the Lorentz force $\mathbf{j} \times \mathbf{B}$ dominates over the electric force, that can be neglected as it is shown in the following dimensional analysis (using Coulomb's law and Eq. (A.5)),

$$\frac{\rho^* E}{jB} \approx \frac{\epsilon E^2}{L}\frac{\mu L}{B^2} = \mu\epsilon\frac{E^2}{B^2} = \frac{V^2}{c^2} \ll 1. \tag{A.16}$$

In fact, this reflects that there are not important charge imbalances in the plasma, so the electric force is not relevant. Therefore, the equation of motion is cast in the form

$$\rho\frac{D\mathbf{v}}{Dt} = -\nabla p + \mathbf{j}\times\mathbf{B}, \tag{A.17}$$

It is worthwhile having a deeper look into the Lorentz force. By means of Eq. A.6 and a vector identity it can be rewritten as

$$\mathbf{j}\times\mathbf{B} = (\mathbf{B}\cdot\nabla)\frac{\mathbf{B}}{\mu} - \nabla\left(\frac{B^2}{2\mu}\right). \tag{A.18}$$

The first term on the right hand side of this equation represents the effect of a tension parallel to the magnetic field and the second one the gradient of a scalar magnetic pressure. The Lorentz force has therefore two effects on the plasma: to shorten magnetic field lines through the tension force and also to compress the plasma through the pressure term. It is often convenient to rearrange Eq. (A.17) taking into account this decomposition,

$$\rho\frac{D\mathbf{v}}{Dt} = -\nabla p_{\mathrm{T}} + (\mathbf{B}\cdot\nabla)\frac{\mathbf{B}}{\mu}, \tag{A.19}$$

where the quantity $p_{\mathrm{T}} = p + B^2/(2\mu)$ is called the total pressure.

There are still other necessary equations to close the system. First of all a perfect gas law (equation of state) is necessary

$$p = \frac{R}{\tilde{\mu}}\rho T = nk_B T, \tag{A.20}$$

where R is the gas constant, T is the plasma temperature, $\tilde{\mu}$ the mean atomic weight (the average mass per particle in units of the proton mass, which for fully ionised hydrogen takes the value 0.5, while in many coronal applications is taken as 0.6), n the particle density and k_B the Boltzmann constant.

Finally, we also need an energy equation, which in a general form can be cast as

$$\rho T\frac{Ds}{Dt} = -\mathcal{L}, \tag{A.21}$$

where s is the entropy per unit mass of the plasma and $\mathcal{L}$ the energy loss function. By using thermodinamical relations and the equation of state Eq. (A.20), Eq. (A.21) can be expressed in terms of the set of variables that are being used in the form

$$\frac{Dp}{Dt} + \gamma p \nabla \cdot \mathbf{v} = -\mathcal{L}. \tag{A.22}$$

The energy loss function $\mathcal{L}$ has contributions from heat flux due particle conduction, radiation, ohmic dissipation and any other sources or sinks (such as viscous dissipation, wave heating in the corona or nuclear energy generation in the solar interior). In ideal MHD it is set to zero, which corresponds to the adiabatic approximation. In any case, this energy loss function is small compared with the other terms when the time-scale changes in p, ρ and T are much smaller than the time scales for radiation, conduction or heating; this is often valid for rapid changes associated with wave motions or instabilities.

However, it is convenient to work with some form of the energy loss function $\mathcal{L}$ for searching suitable equilibrium models. This magnitude can be written in the form

$$\mathcal{L} = \nabla \cdot (\kappa \nabla T) - L_r - j^2/\sigma + H \tag{A.23}$$

where κ is the thermal conduction tensor, L_r is the radiation term, j^2/σ stands for the ohmic dissipation and H groups together other terms of heating, such as viscous dissipation or heating by waves or reconnection. Regarding the thermal conduction term, it can be split in two parts,

$$\nabla \cdot (\kappa \nabla T) = \nabla_{\parallel} \cdot (\kappa_{\parallel} \nabla T) + \nabla_{\perp} \cdot (\kappa_{\perp} \nabla T), \tag{A.24}$$

where the subscripts $\parallel$ and $\perp$ refer to values along and across magnetic field. In general, the thermal conduction is strongly prevented across the magnetic field lines. Therefore, in typical coronal conditions the magnetic field is strong enough to make $\kappa_{\parallel} \gg \kappa_{\perp}$, so the conduction across the magnetic field direction can be neglected and Eq. (A.23) reduces to

$$\mathcal{L} = \nabla_{\parallel} \cdot (\kappa_{\parallel} \nabla T) - H(s) = \frac{1}{A(s)} \frac{d}{ds} \left(\kappa_{\parallel} A(s) \frac{dT}{ds} \right) + H(s), \tag{A.25}$$

where s is a coordinate along magnetic field lines and radiation and dissipation have been neglected. Finally, the parallel component of the thermal conduction tensor depends on the temperature in the form

$$\kappa_{\parallel} = \kappa_0 T^{5/2}, \tag{A.26}$$

with $\kappa_0 = 9.24 \times 10^{-12}$ Jm^{-1}s^{-1}, so the energy equation becomes

$$\rho T \frac{Ds}{Dt} = -\frac{1}{A(s)} \frac{d}{ds} \left(\kappa_0 T^{5/2} A(s) \frac{dT}{ds} \right) - H(s). \tag{A.27}$$

Appendix B

Derivation of the boundary conditions in Magnetohydrodynamics

In this Appendix to obtain the boundary conditions on a surface separating two plasmas of different properties. At these boundaries the MHD model breaks down inside a layer of infinitesimal thickness δ, because the gradients are increasingly large. As a consequence, non-linear terms and dissipative effects become important. But across the layer, the momentum, mass or energy should be continuous and that is the main reason for deriving these "jump" conditions. In the limit $\delta \to 0$ the variables may jump across this layer, but the magnitude of this jump is determined by the conservation of these and other quantities.

It is necessary then to write the MHD equations in a conservative form, that is

$$\frac{\partial g}{\partial t} + \nabla \cdot \mathbf{f} = 0. \tag{B.1}$$

This equation can be integrated across the layer of thickness δ from the region labelled 1 to the region labelled 2 and then the limit $\delta \to 0$ can be taken. After using Gauss's theorem the second term in Eq. (B.1) gives

$$\lim_{\delta \to 0} \int_1^2 \nabla h dl = \hat{\mathbf{n}} \int_1^2 \frac{\partial h}{\partial l} dl = \hat{\mathbf{n}}(h_2 - h_1) = \hat{\mathbf{n}}\,[h], \tag{B.2}$$

where the convention $[a] = a_2 - a_1$ has been used and dl is the line element perpendicular to the layer. Hence,

$$\hat{\mathbf{n}} \cdot [\mathbf{f}] = \lim_{\delta \to 0} \int_\delta dl \frac{\partial g}{\partial t}. \tag{B.3}$$

This partial time derivative must be computed carefully, because in the Eulerian description it is not calculated on the boundary (which is moving with the fluid), so using the Lagrangian description:

$$\frac{\partial g}{\partial t} = \frac{Dg}{Dt} - \mathbf{v}\cdot\nabla g = \frac{Dg}{Dt} - v_n\frac{\partial g}{\partial l} - v_t\frac{\partial g}{\partial s}, \tag{B.4}$$

where the subscripts n and t stand for the normal and tangential components (with ds the line element in the tangential direction). Therefore, integrating over dl and taking the limit $\delta \to 0$ we have

$$\hat{\mathbf{n}}\cdot[\mathbf{f}] = -v_n[g]. \tag{B.5}$$

The next step is to express the MHD equations in a conservative form which involves the use of vector and tensor identities. It is convenient to rewrite the energy equation (Eq. 2.3) using the internal energy e of the plasma,

$$e = \frac{p}{(\gamma-1)\,\rho}, \tag{B.6}$$

which transforms Eq. (2.3) in

$$\frac{\partial e}{\partial t} + (\gamma-1)e\nabla\cdot\mathbf{v} + \mathbf{v}\cdot\nabla e = 0. \tag{B.7}$$

Using Eq. (B.7) as the energy equation the MHD system Eqs. (2.1)–(2.5) can be written in the following way

$$\frac{\partial \rho}{\partial t} + \nabla\cdot(\rho\mathbf{v}) = 0, \tag{B.8}$$

$$\frac{\partial(\rho\mathbf{v})}{\partial t} + \nabla\cdot\{\rho\mathbf{v}\mathbf{v} + (p + B^2/(2\mu))\overset{\Rightarrow}{I} - \mathbf{B}\mathbf{B}/\mu\} = 0, \tag{B.9}$$

$$\frac{\partial \mathbf{B}}{\partial t} + \nabla\cdot\{\mathbf{B}\mathbf{v} - \mathbf{v}\mathbf{B}\} = 0, \tag{B.10}$$

$$\frac{\partial}{\partial t}\left(\frac{1}{2}\rho v^2 + \rho e + \frac{1}{2\mu}B^2\right) + \nabla\cdot\left\{(\rho v^2/2 + \rho e + p + B^2/\mu)\mathbf{v} - (\mathbf{v}\cdot\mathbf{B})\,\mathbf{B}\right\} = 0, \tag{B.11}$$

plus the condition $\nabla\cdot\mathbf{B} = 0$. The symbol $\overset{\Rightarrow}{I}$ denotes the identity tensor and $\mathbf{a}_1\mathbf{a}_2$ the dyadic product of the vectors $\mathbf{a}_1$ and $\mathbf{a}_2$.

Now Eq. (B.5) might be applied, but it still has to be demanded that the normal velocity across the boundary is zero to guarantee coherence in the fluid (just like in fluid physics),

$$\hat{\mathbf{n}}\cdot[\mathbf{v}] = 0. \tag{B.12}$$

Eqs. (B.8)–(B.11) then become

$$-v_n[\rho] + \hat{\mathbf{n}}\cdot[\rho\mathbf{v}] = 0, \tag{B.13}$$

$$-v_n[\rho\mathbf{v}] + \hat{\mathbf{n}}\cdot\left[\rho\mathbf{v}\mathbf{v} + (p + B^2/(2\mu))\ \overrightarrow{I} - \mathbf{B}\mathbf{B}/\mu\right] = 0, \tag{B.14}$$

$$-v_n[\mathbf{B}] - \hat{\mathbf{n}}\cdot[\mathbf{B}\mathbf{v} - \mathbf{v}\mathbf{B}] = 0, \tag{B.15}$$

$$-v_n[\rho v^2/2 + \rho e + B^2/(2\mu)] + \hat{\mathbf{n}}\cdot\left[(\rho v^2/2 + \rho e + p + B^2/\mu)\mathbf{v} - (\mathbf{v}\cdot\mathbf{B})\,\mathbf{B}\right] = 0. \tag{B.16}$$

Rearranging terms and taking the components along and across the boundary in vector identities and also taking into account that by Eq. (B.12) $[\hat{\mathbf{n}}\cdot\mathbf{v}\ f] = \hat{\mathbf{n}}\cdot\mathbf{v}\ [f]$ we have

$$(\hat{\mathbf{n}}\cdot\mathbf{v} - v_n)\ [\rho] = 0, \tag{B.17}$$

$$(\hat{\mathbf{n}}\cdot\mathbf{v} - v_n)(\hat{\mathbf{n}}\cdot\mathbf{v})\,[\rho] + [p + B^2/(2\mu)] - [\hat{\mathbf{n}}\cdot\mathbf{B}\ \hat{\mathbf{n}}\cdot\mathbf{B}] = 0, \tag{B.18}$$

$$(\hat{\mathbf{n}}\cdot\mathbf{v} - v_n)\ [\rho\hat{\mathbf{n}}\times\mathbf{v}] + [\hat{\mathbf{n}}\cdot\mathbf{B}\ \hat{\mathbf{n}}\times\mathbf{B}] = 0, \tag{B.19}$$

$$(\hat{\mathbf{n}}\cdot\mathbf{v} - v_n)\ [\hat{\mathbf{n}}\cdot\mathbf{B}] - \hat{\mathbf{n}}\cdot\mathbf{v}[\hat{\mathbf{n}}\cdot\mathbf{B}] = 0, \tag{B.20}$$

$$(\hat{\mathbf{n}}\cdot\mathbf{v} - v_n)\ [\hat{\mathbf{n}}\times\mathbf{B}] - [\hat{\mathbf{n}}\cdot\mathbf{v}\hat{\mathbf{n}}\times\mathbf{B}] = 0, \tag{B.21}$$

$$(\hat{\mathbf{n}}\cdot\mathbf{v} - v_n)\ [\rho v^2/2 + \rho e + B^2/(2\mu)] + \hat{\mathbf{n}}\cdot\mathbf{v}\ [p + B^2/(2\mu)] - [\hat{\mathbf{n}}\cdot\mathbf{B}\ \ \mathbf{v}\cdot\mathbf{B}] = 0, \tag{B.22}$$

and also $\hat{\mathbf{n}}\cdot[\mathbf{B}] = 0$ coming from the solenoidal condition. Many terms in these equations vanish, since $\hat{\mathbf{n}}\cdot\mathbf{v} - v_n = 0$ (in a general development, one should distinguish between the boundary speed u and the fluid motion v, but since we are not interested in shocks this has not been done for the sake of simplicity). Putting the remaining non-vanishing identities together,

$$\begin{aligned}
\hat{\mathbf{n}}\cdot[\mathbf{v}] &= 0, && \text{(B.23)}\\
\hat{\mathbf{n}}\cdot[\mathbf{B}] &= 0, && \text{(B.24)}\\
[p + B^2/(2\mu)] &= 0, && \text{(B.25)}\\
\hat{\mathbf{n}}\cdot\mathbf{B}\ [\hat{\mathbf{n}}\times\mathbf{B}] &= 0, && \text{(B.26)}\\
\hat{\mathbf{n}}\cdot\mathbf{B}\ [\hat{\mathbf{n}}\times\mathbf{v}] &= 0, && \text{(B.27)}\\
\hat{\mathbf{n}}\cdot\mathbf{v}\ [p + B^2/(2\mu)] - \hat{\mathbf{n}}\cdot\mathbf{B}\ [\mathbf{v}\cdot\mathbf{B}] &= 0. && \text{(B.28)}
\end{aligned}$$

Now, there are two different possibilities for contact discontinuities, depending on whether the magnetic field is normal to the boundary or not, so we have

- $\boxed{\hat{\mathbf{n}}\cdot\mathbf{B} \neq 0.}$ The only possibility left is

$$[\mathbf{v}] = [\mathbf{B}] = [p] = 0. \tag{B.29}$$

- $\boxed{\hat{\mathbf{n}}\cdot\mathbf{B} = 0.}$ In this case the resulting boundary conditions are

$$\hat{\mathbf{n}}\cdot[\mathbf{v}] = \hat{\mathbf{n}}\cdot[\mathbf{B}] = [p + B^2/(2\mu)] = 0, \tag{B.30}$$

Appendix C

Finite-difference numerical solution and discretization of first and second order derivatives

In the main text Eq. (4.23) has been solved using analytical techniques, but this partial differential equation can also be solved numerically by a finite differences algorithm. There are mainly two reasons for doing so: a numerical solution is useful as an independent check of the cumbersome numerical calculations and it is also valuable because in more complicated models the analytical solution might be too difficult to handle, so it is convenient to introduce and test this kind of techniques in this relatively simple problem. Moreover, when some of the assumptions used to derive Eq. (4.23) are dropped, the analytical solution developed no longer holds, but the numerical programs can still be modified. Besides, it will be necessary to apply numerical techniques to find solutions from the dispersion relations, so it is worthwhile having something to compare with (in fact, the technique described in the previous Chapter should be regarded as a semi-numerical solution instead of completely analytical).

For these reasons, the numerical code described in Oliver, Hood & Priest (1996) has been used. It solves the resulting partial differential wave equations for the perturbed velocity (Arregui, Oliver & Ballester 2001), although the perturbed pressure can also be obtained as an output. This program gives, among other information, the frequency and spatial structure of the fast and slow magnetoacoustic modes of any two-dimensional, y-invariant equilibrium with $B_y = 0$. Since we are concerned with solving Eq. (4.34), obtained under the $\beta = 0$ assumption, it is necessary to set the sound speed to zero to eliminate the slow mode.

However, that code was modified in Arregui, Oliver & Ballester (2003) to take into account plane wave propagation in the y-direction and also a sheared magnetic field ($B_y \neq 0$) in the low-beta limit. In the context of this work that modification is also useful to check the three-dimensional solution by setting the y-component of the magnetic field to zero in the program. Nevertheless, it turns out that the numerical code requires extra modifications because it displays spurious numerical oscillations in the direction across the field, which become even more pronounced if the step is taken shorter. To avoid this problem a staggered grid is used, so v_x and v_y are computed in interlaced space intervals (see Arregui, Oliver & Ballester (2003) and cites

therein for a deeper discussion on this subject). Then, the program can also be used to check our solutions of Sect. 6.2. It should be remarked that the agreement is unexpectedly extremely good, since the numerical program reproduces even the step discontinuities in the solution due to the MHD boundary conditions, although in the code only finite discretization is implemented.

Nevertheless, before applying the numerical code to the present problem it had to be modified so that the thin fibril and the much wider coronal environment can be adequately represented by a computational mesh with non-uniform spacing. Previous versions of the code are not suitable for this task since they make use of a grid with two different but constant spacings in the x- and z-directions. Hence, to obtain a fine spatial representation of the velocity inside the fibril it would have been necessary to use an excessively small grid spacing, with the associated enormous computational cost.

Our use of the non-uniform grid consists essentially of taking a uniform mesh (although with different spacing in the x- and z-directions) covering the whole prominence fibril. The fibril is then surrounded by a coarser mesh which is in turn embedded in one or more even coarser grids that span the rest of the system. Therefore, the finite difference formulas for the derivatives of the velocity components are second order accurate in each of the regions, but are only first order accurate at the interfaces between regions. Since the number of points in these interfaces is much smaller than the total number of points used, almost second order accuracy of the eigensolutions is ensured.

Finally, we turn to the boundary conditions that must be imposed on v_x. Such as we mentioned before, this velocity component must vanish at $z = \pm L$ because of photospheric line-tying explained in Sect. 4.2. On the other hand, v_x must also vanish as $|x| \to \infty$ (Eq. 4.38) and it is expected that solutions will decay exponentially in the x-direction. It is also important to remark that this boundary condition can be difficult to implement in a numerical computation; to sort out that problem we demand the perturbations to vanish on a surface at long distance from the structure (though finite, say H from the fibril axis), and then check the results by pushing that artificial surface further and making sure that the calculated mode did not change significantly. Hence, we place two horizontal boundaries sufficiently far from the thin loop (at $x = \pm H$, say) and impose $v_x = 0$ there, that is

$$v_x(\pm H) = 0 \tag{C.1}$$

for a value $H \gg b$ (a condition more suitable for the numerical simulations than Eq. (4.38)). If these boundaries have been put far enough from the loop, the frequency and spatial structure of v_x remain unaltered when H is increased. It turns out that it is necessary to set H some orders of magnitude larger than the thickness of the fibril in order to correctly reproduce the exponential decay in the x-direction (e.g. Fig. 6.7c).

To discretize the derivatives, let us consider a two-dimensional mesh of points (ψ_i, χ_j) (following Oliver et al. (1996) we use the names ψ and χ for the variables in the plane perpendicular to the y-direction. In the present case, $\psi = z$ and $\chi = x$.) We define the grid spacings in the two directions as,

$$h_i = \psi_i - \psi_{i-1}, \qquad i = 2, 3, \ldots, N_\psi, \tag{C.2}$$

$$g_j = \chi_j - \chi_{j-1}, \qquad j = 2, 3, \ldots, N_\chi, \tag{C.3}$$

with N_ψ and N_χ the number of grid points in the ψ- and χ-directions. Next, consider a function $f(\psi, \chi)$ whose derivatives are to be approximated by finite difference formulas at a point (ψ_i, χ_j). We now expand the function f in Taylor series around this point to calculate its value at the eight mesh points around (ψ_i, χ_j) and obtain expressions of the form

$$f_{i+1,j} = f_{i,j} + h_{i+1}\frac{\partial f}{\partial \psi} + \frac{1}{2}h_{i+1}^2\frac{\partial^2 f}{\partial \psi^2} + \frac{1}{6}h_{i+1}^3\frac{\partial^3 f}{\partial \psi^3} + O(h_{i+1}^4), \tag{C.4}$$

$$\begin{aligned} f_{i+1,j-1} &= f_{i,j} + h_{i+1}\frac{\partial f}{\partial \psi} - g_j\frac{\partial f}{\partial \chi} + \frac{1}{2}h_{i+1}^2\frac{\partial^2 f}{\partial \psi^2} - h_{i+1}g_j\frac{\partial^2 f}{\partial \psi \partial \chi} + \frac{1}{2}g_j^2\frac{\partial^2 f}{\partial \chi^2} \\ &+ \frac{1}{6}h_{i+1}^3\frac{\partial^3 f}{\partial \psi^3} - \frac{1}{2}h_{i+1}^2 g_j\frac{\partial^3 f}{\partial \psi^2 \partial \chi} + \frac{1}{2}h_{i+1}g_j^2\frac{\partial^3 f}{\partial \psi \partial \chi^2} - \frac{1}{6}g_j^3\frac{\partial^3 f}{\partial \chi^3} \\ &+ O(\max\{h_{i+1}^4, h_{i+1}^3 g_j, h_{i+1}^2 g_j^2, h_{i+1}g_j^3, g_j^4\}), \end{aligned} \tag{C.5}$$

where $f_{i,j} = f(\psi_i, \chi_j)$, $f_{i+1,j} = f(\psi_{i+1}, \chi_j)$, etc., and all partial derivatives are evaluated at the point (ψ_i, χ_j).

Now, approximate formulas for the partial derivatives can be determined by combining some or all of the above series expansions to eliminate unwanted partial derivatives. Then we have

$$\frac{\partial f}{\partial \psi} = \frac{1}{h_i + h_{i+1}}\left[p_i f_{i+1,j} + (q_i - p_i)f_{i,j} - q_i f_{i-1,j}\right] + O(h_i h_{i+1}), \tag{C.6}$$

where $p_i = h_i/h_{i+1} \equiv q_i^{-1}$. Notice that this expression, which is second order accurate in the mesh size, reduces to the well-known formula for equally spaced points after setting $h_i = h_{i+1} = h$.

Next, second-order derivatives are approximated by

$$\begin{aligned} \frac{\partial^2 f}{\partial \psi^2} &= \frac{2}{h_{i+1}(h_i + h_{i+1})}f_{i+1,j} - \frac{2}{h_i h_{i+1}}f_{i,j} \\ &+ \frac{2}{h_i(h_i + h_{i+1})}f_{i-1,j} + O\left(\frac{h_{i+1}^2 - h_i^2}{h_i + h_{i+1}}\right). \end{aligned} \tag{C.7}$$

This expression is first order accurate in h, but it becomes second order accurate for uniform spacing ($h_i = h_{i+1}$). There are other finite-difference formulas to compute this derivative using other combinations of $f_{i,j}$, $f_{i+1,j}$, etc., but none of them achieves second order accuracy.

Finally, the second order, cross derivative is also needed,

$$\frac{\partial^2 f}{\partial \psi \partial \chi} = \frac{\alpha_1}{h_{i+1}g_{j+1}}(f_{i+1,j+1} + f_{i,j} - f_{i,j+1} - f_{i+1,j})$$

$$+ \quad \frac{\alpha_2}{h_i g_{j+1}}(f_{i-1,j} + f_{i,j+1} - f_{i-1,j+1} - f_{i,j})$$
$$+ \quad \frac{\alpha_3}{h_i g_j}(f_{i,j} + f_{i-1,j-1} - f_{i-1,j} - f_{i,j-1})$$
$$+ \quad \frac{\alpha_4}{h_{i+1} g_j}(f_{i+1,j} + f_{i,j-1} - f_{i,j} - f_{i+1,j-1}). \tag{C.8}$$

In order to get second order accuracy, the quantities α_1, α_2, α_3 and α_4 must satisfy the following conditions *at each point* (ψ_i, χ_j)

$$\alpha_2 = \frac{1}{s_j + 1} - \alpha_1, \tag{C.9}$$

$$\alpha_3 = \frac{1}{p_i + 1} - \alpha_2, \tag{C.10}$$

$$\alpha_4 = \frac{1}{q_i + 1} - \alpha_1, \tag{C.11}$$

where $s_j = g_{j+1}/g_j$ and α_1 is a free parameter here taken equal to 0.25. This choice is not arbitrary, but arises from the fact that a possible set of values for a uniform mesh is $\alpha_1 = \alpha_2 = \alpha_3 = \alpha_4 = 0.25$.

So we are left with finite difference expressions for the first and second order derivatives of a function with respect to ψ and χ (the last ones are not given here and are similar to Eqs. (C.6) and (C.7)). This function can be either the normal or parallel velocity component (respectively v_x and v_z in the present configuration). Upon substituting the approximations for derivatives into the linearized MHD equations, one gets an algebraic eigenvalue system which is solved using the procedure described in Oliver et al. (1996).

Appendix D

Special coefficients for a structure with density enhancement

This appendix is devoted to calculating the expresions of the inner solution when the wavelengths are purely imaginary. The expresions involve different mathematical functions, but are similar to the ones presented in Sections. 4.3.3 and 4.5.2.

It has been mentioned in Chapter 3 that $\kappa_{\rm e}^2 < 0$ holds for the first basis function $h_1^{(1)}$. For this function Eqs. (4.139)–(4.140) are not valid and must be replaced by

$$h_1^{(1)}(z) = \Lambda_{\rm ev}^* \begin{cases} \cos(\kappa_{\rm p} W)\sinh[\kappa_{\rm e}^*(L+z)], & -L < z < -W, \\ \sinh[\kappa_{\rm e}^*(L-W)]\cos(\kappa_{\rm p} z), & -W < z < W, \\ \cos(\kappa_{\rm p} W)\sinh[\kappa_{\rm e}^*(L-z)], & W < z < L, \end{cases} \tag{D.1}$$

and

$$h_1^{(1)}(z) = \Lambda_{\rm od}^* \begin{cases} -\sin(\kappa_{\rm p} W)\sinh[\kappa_{\rm e}^*(L+z)], & -L < z < -W, \\ \sinh[\kappa_{\rm e}^*(L-W)]\sin(\kappa_{\rm p} z), & -W < z < W, \\ \sin(\kappa_{\rm p} W)\sinh[\kappa_{\rm e}^*(L-z)], & W < z < L, \end{cases} \tag{D.2}$$

where $\kappa_{\rm e}^* = i\kappa_{\rm e}$. Taking this into account and with the corresponding normalisation condition the coefficients are now

$$\begin{aligned} (\Lambda_{\rm ev}^*)^{-2} &= (L-W)\cos^2(\kappa_{\rm p} W) - W\sinh^2[\kappa_{\rm e}^*(L-W)] \\ &- \frac{1}{2\kappa_{\rm e}^*}\cos^2(\kappa_{\rm p} W)\sinh[2\kappa_{\rm e}^*(L-W)] - \frac{1}{2\kappa_{\rm p}}\sinh^2[\kappa_{\rm e}^*(L-W)]\sin(2\kappa_{\rm p} W), \end{aligned} \tag{D.3}$$

$$\begin{aligned} (\Lambda_{\rm od}^*)^{-2} &= (L-W)\sin^2(\kappa_{\rm p} W) - W\sinh^2[\kappa_{\rm e}^*(L-W)] \\ &- \frac{1}{2\kappa_{\rm e}^*}\sin^2(\kappa_{\rm p} W)\sinh[2\kappa_{\rm e}^*(L-W)] + \frac{1}{2\kappa_{\rm p}}\sinh^2[\kappa_{\rm e}^*(L-W)]\sin(2\kappa_{\rm p} W). \end{aligned} \tag{D.4}$$

In addition, some coefficients in Eqs. (4.145) and (4.146) are also different,

$$
\begin{aligned}
H^*_{1,2m-1} &= \Lambda^*_{\rm od} L^{-1/2} \left\{ \sin[\kappa^*_{\rm e}(L-W)] \left(\frac{\sin[(\kappa_{\rm p}-\kappa_{\rm c}^{\rm ev})W]}{\kappa_{\rm p}-\kappa_{\rm c}^{\rm ev}} + \frac{\sin[(\kappa_{\rm p}+\kappa_{\rm c}^{\rm ev})W]}{\kappa_{\rm p}+\kappa_{\rm c}^{\rm ev}} \right) \right. \\
&+ 2\frac{\cos(\kappa_{\rm p}W)}{\kappa^{*2}_{\rm e}+\kappa^{\rm ev\,2}_{\rm c}} \left(\kappa^*_{\rm e} \cosh[\kappa^*_{\rm e}(L-W)] \cos(\kappa_{\rm c}^{\rm ev} W) \right. \\
&- \left. \left. \kappa_{\rm c}^{\rm ev} \sinh[\kappa^*_{\rm e}(L-W)] \sin(\kappa_{\rm c}^{\rm ev} W) \right) \right\}, \qquad \text{(D.5)}
\end{aligned}
$$

$$
\begin{aligned}
H^*_{2,2m} &= \Lambda^*_{\rm ev} L^{-1/2} \left\{ \sin[\kappa^*_{\rm e}(L-W)] \left(\frac{\sin[(\kappa_{\rm p}-\kappa_{\rm c}^{\rm od})W]}{\kappa_{\rm p}-\kappa_{\rm c}^{\rm od}} - \frac{\sin[(\kappa_{\rm p}+\kappa_{\rm c}^{\rm od})W]}{\kappa_{\rm p}+\kappa_{\rm c}^{\rm od}} \right) \right. \\
&+ 2\frac{\sin(\kappa_{\rm p}W)}{\kappa^{*2}_{\rm e}+\kappa^{\rm ev\,2}_{\rm c}} \left(\kappa^*_{\rm e} \cosh[\kappa^*_{\rm e}(L-W)] \sin(\kappa_{\rm c}^{\rm ev} W) \right. \\
&+ \left. \left. \kappa_{\rm c}^{\rm ev} \sinh[\kappa^*_{\rm e}(L-W)] \cos(\kappa_{\rm c}^{\rm ev} W) \right) \right\}. \qquad \text{(D.6)}
\end{aligned}
$$

Eqs. (4.87) and (4.88) must be modified. If the first c values satisfy $\kappa_{\rm e}^2 < 0$, the dispersion relations for kink and sausage modes become (with $\lambda^{({\rm l})*} = i\lambda^{({\rm l})}$)

$$
\begin{aligned}
&\sum_{m=1}^{c} H^*_{mn} B^{\cos *}_m \left[\frac{-\lambda^{({\rm l})*}_m}{{\lambda^{({\rm l})*}_m}^2 + k_y^2} \cos(\lambda^{({\rm l})*}_m b) + \frac{\lambda^{({\rm c})}_n}{{\lambda^{({\rm c})}_n}^2 - k_y^2} \sin(\lambda^{({\rm l})*}_m b) \right] = 0 + \\
&\sum_{m=c+1}^{\infty} H_{mn} B^{\cos}_m \left[\frac{\lambda^{({\rm l})}_m}{{\lambda^{({\rm l})}_m}^2 - k_y^2} \cosh(\lambda^{({\rm l})}_m b) + \frac{\lambda^{({\rm c})}_n}{{\lambda^{({\rm c})}_n}^2 - k_y^2} \sinh(\lambda^{({\rm l})}_m b) \right] = 0, \qquad \text{(D.7)}
\end{aligned}
$$

$$
\begin{aligned}
&\sum_{m=1}^{c} H^*_{mn} B^{\sin *}_m \left[\frac{\lambda^{({\rm l})*}_m}{{\lambda^{({\rm l})*}_m}^2 + k_y^2} \sin(\lambda^{({\rm l})*}_m b) + \frac{\lambda^{({\rm c})}_n}{{\lambda^{({\rm c})}_n}^2 - k_y^2} \cos(\lambda^{({\rm l})*}_m b) \right] = 0 + \\
&\sum_{m=c+1}^{\infty} H_{mn} B^{\sin}_m \left[\frac{\lambda^{({\rm l})}_m}{{\lambda^{({\rm l})}_m}^2 - k_y^2} \sinh(\lambda^{({\rm l})}_m b) + \frac{\lambda^{({\rm c})}_n}{{\lambda^{({\rm c})}_n}^2 - k_y^2} \cosh(\lambda^{({\rm l})}_m b) \right] = 0, \qquad \text{(D.8)}
\end{aligned}
$$

The rest of the work has been done by numerical computations. First of all we need to solve Eqs. (4.138) and (4.137) numerically to obtain the set of eigenvalues. Then we can calculate the $\kappa' s$ and the H_{nm} from Eqs. (D.5) and (D.6). Finally one can write down the determinant coming from Eqs. (D.8) and (D.7) and solve it to find out the characteristic frequencies of our model.

Appendix E

Derivation of the dispersion relation using the perturbed velocity in cylindrical geometry as the dependent variable (sausage mode)

The main dependent variable used in Díaz et al. (2001a) is the perturbed velocity component across the fibril (equivalent to v_r here). One may wonder whether it is necessary to modify this point of view in the cylindrical geometry and it will next be shown that the dispersion relation can be also derived by keeping v_r as our dependent variable, although only for sausage modes.

We start by using Eq. (4.18) to eliminate $p_{\rm T}$ in Eq. (4.22), which reduces to Eq. (4.29). The r- and φ-components of this equation are the following coupled partial differential equations,

$$\frac{\partial^2 v_r}{\partial t^2} = c_{\rm A}^2 \left\{ \frac{\partial}{\partial r} \left[\frac{1}{r} \left(\frac{\partial}{\partial r}(r\, v_r) + \frac{\partial v_\varphi}{\partial \varphi} \right) \right] + \frac{\partial^2 v_r}{\partial z^2} \right\}, \tag{E.1}$$

$$\frac{\partial^2 v_\varphi}{\partial t^2} = c_{\rm A}^2 \left\{ \frac{1}{r^2} \left[\frac{\partial^2}{\partial r \partial \varphi}(r\, v_r) + \frac{\partial^2 v_\varphi}{\partial \varphi^2} \right] + \frac{\partial^2 v_\varphi}{\partial z^2} \right\}. \tag{E.2}$$

It is worth remarking that the φ-dependence of v_r and v_φ is responsible for the coupling of these equations and, as a consequence, fast modes have motions in the radial and azimuthal directions as long as solutions possess such a φ-dependence. Just like in Cartesian geometry, one must assume independence with respect to the angular variable to decouple the two equations, which reduce to

$$\frac{\partial^2 v_r}{\partial t^2} = c_{\rm A}^2 \left\{ \frac{\partial}{\partial r} \left[\frac{1}{r} \frac{\partial}{\partial r}(r\, v_r) \right] + \frac{\partial^2 v_r}{\partial z^2} \right\}, \tag{E.3}$$

$$\frac{\partial^2 v_\varphi}{\partial t^2} = c_{\rm A}^2 \frac{\partial^2 v_\varphi}{\partial z^2}, \tag{E.4}$$

and so the equations for v_r and v_φ decouple exclusively for sausage modes. This is the reason why the variable $p_{\rm T}$ has been used throughout the Thesis as dependent variable.

Since Eq. (E.3) is similar to the one solved in previous Chapters, the analysis carried out there can be used again. First of all, the time dependent part is Fourier analysed in the form $v_r(r,z,t) = v_r(r,z)\, e^{-i\omega t}$. The solution is then written as

$$v_r^{(\rm j)}(r,z) = \sum_{n=1}^{\infty} u_n^{(\rm j)}(r)\, h_n^{(\rm j)}(z), \tag{E.5}$$

where the superscript j stands for internal (l) or external (c) solution. Substitution of this expression into Eq. (E.3) gives us two uncoupled ordinary differential equations,

$$\frac{d^2 h_n^{(\rm j)}}{dz^2} + \frac{\omega^2}{c_{\rm A}^{(\rm j)2}} h_n^{(\rm j)} = -\lambda_n^{(\rm j)2} h_n^{(\rm j)}, \tag{E.6}$$

$$\frac{d}{dr}\left[\frac{1}{r}\frac{d}{dr}\left(r\, u_n^{(\rm j)}\right)\right] - \lambda_n^{(\rm j)2} u_n^{(\rm j)} = 0, \tag{E.7}$$

where $c_{\rm A}^{(j)}$ must be substituted by the corresponding value of the Alfvén speed. The solutions to these equations have been discussed in Chapter 4, so it will suffice to mention that, when $\lambda_n^{(\rm j)2} > 0$, Eq. (E.7) is the modified Bessel's equation of first order. Therefore, the functions $u_n(r)$ which are regular at $r = 0$ and evanescent as $r \to \infty$ are given by

$$\begin{aligned} u_n^{(\rm c)}(r) &= A_n K_1(\lambda_n^{(\rm c)} r), \\ u_n^{(\rm l)}(r) &= B_n I_1(\lambda_n^{(\rm l)} r). \end{aligned} \tag{E.8}$$

We next turn our attention to the boundary conditions that must be imposed at the various interfaces between uniform regions. Following our discussion in Section 4.2, it turns out that some conditions, e.g. the photospheric line-tying at $z = L$ or the continuity of the perturbed velocity and its derivative at $z = W$, are exactly the same as in Chapter 4. However, the boundary $r = b$, where the set of conditions given by Eq. (4.40) must be applied, should be treated carefully. The first of these conditions implies

$$v_r^{(\rm l)}(b) = v_r^{(\rm c)}(b). \tag{E.9}$$

To impose $[p_{\rm T}] = 0$ we first use Eq. (4.18) to derive the following expression,

$$p_{\rm T} = -\rho_0 c_{\rm A}^2 \frac{1}{r}\frac{\partial}{\partial r}(r v_r), \tag{E.10}$$

and in conclusion the continuity of the total pressure yields

$$\frac{\partial}{\partial r}\left(rv_r^{(\mathrm{l})}\right)\Big|_{r=b^-} = \frac{\partial}{\partial r}\left(rv_r^{(\mathrm{c})}\right)\Big|_{r=b^+}. \tag{E.11}$$

It is important to stress that this equation does not involve the continuity of the derivative of v_r across the boundary, but the continuity of the derivative of rv_r. Finally, applying the boundary conditions given by equations (E.9) and (E.11) one has the following sets of equations for $n = 1, 2, \ldots$

$$A_n K_1(\lambda_n^{(\mathrm{c})} b) = \sum_{s=1}^{\infty} H_{sn} B_s I_1(\lambda_n^{(\mathrm{l})} b), \tag{E.12}$$

$$-A_n \lambda_n^{(\mathrm{c})} K_0(\lambda_n^{(\mathrm{c})} b) = \sum_{s=1}^{\infty} H_{sn} B_s \lambda_n^{(\mathrm{l})} I_0(\lambda_n^{(\mathrm{l})} b), \tag{E.13}$$

where some properties of the derivatives of Bessel functions have been used. Eliminating the coefficients A_n between these equations yields an infinite system of algebraic equations for the coefficients B_n and again using some properties of the Bessel functions this system can be cast in the form

$$\sum_{s=1}^{\infty} H_{sn} \left\{ \lambda_n^{(\mathrm{c})} I_0'(\lambda_s^{(\mathrm{l})} b) K_0(\lambda_n^{(\mathrm{c})} b) - \lambda_s^{(\mathrm{l})} K_0'(\lambda_n^{(\mathrm{c})} b) I_0(\lambda_s^{(\mathrm{l})} b) \right\} B_s = 0, \tag{E.14}$$

for $n = 1, 2, \ldots$ This expression is very similar to Eq. (4.117) with $m = 0$, except that $\lambda_n^{(\mathrm{c})}$ and $\lambda_s^{(\mathrm{l})}$ are now multiplying instead of dividing. Nevertheless, we next show that the same dispersion relation, which comes from setting the determinant of the system of equations to zero, is obtained. By dividing the n-th row of the determinant by $\lambda_n^{(\mathrm{c})}$ and the s-th column by $\lambda_s^{(\mathrm{l})}$, the original dispersion relation is indeed recovered. Also note that since v_r is a function of Bessel functions of first order, Eq. (E.10) implies that p_{T} depends on Bessel functions of zeroth order, so the original solution (eq. (8.1)) for the total pressure is obtained.

Appendix F

Line-tied homogeneous Cartesian slabs

Coronal loops are more appropriately modelled as cylindrical flux tubes than as slabs, but it is nonetheless useful to have some results in Cartesian geometry to compare with the cylindrical ones. Moreover, magnetic slabs are commonly used to model fibril structures in prominences (see, for example, Joarder & Roberts (1992a); Oliver et al. (1992); Díaz et al. (2001a)). Here we briefly develop expressions for slabs similar to those obtained for cylindrical geometry in the main part of this Thesis. The equilibrium model is similar (homogeneous dense region, uniform magnetic field parallel to the z-axis), but with no structure in the y-direction (see Fig F.1). We consider perturbations with no dependence on the y-coordinate, although the results can easily be extended to allow dependence on this coordinate if necessary.

The starting point is Eq. (4.23) for the total pressure. Separation of variables in the form

$$p_{\mathrm{T}}(x,z) = u(x)h(z), \tag{F.1}$$

in which the z-dependent part, $h(z)$, is exactly the same as for the cylindrical geometry, namely Eqs. (5.7) and (5.8). The resulting ordinary differential equation for the x-dependent part is

$$\frac{d^2}{dx^2}u(x) = \lambda^2 u(x), \tag{F.2}$$

whose solution can be written in the coronal and loop regions as

$$u(x) = \begin{cases} A\cosh\lambda^{(\mathrm{l})}x, & 0 \le x \le b, \\ Be^{-\lambda^{(\mathrm{c})}(x-b)}, & x > b. \end{cases} \tag{F.3}$$

Here we have taken an even solution in the x-direction; a similar form can be written for the odd modes (substituting the cosh function by a sinh function). Using the jump conditions of Eq. (4.40), the slab dispersion relations are

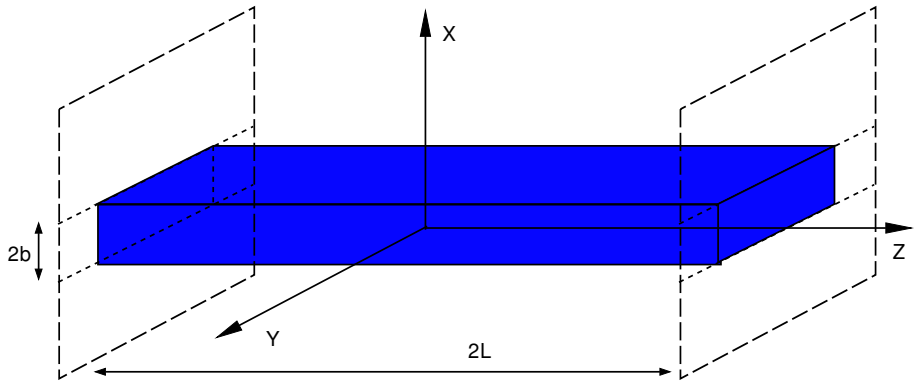

Figure F.1: Sketch of the equilibrium configuration of the line-tied homogeneous slab. The slab length is $2L$ and its width is $2b$. The whole configuration is invariant in the y-direction.

$$\lambda^{(\mathrm{l})}\coth\lambda^{(\mathrm{l})}b+\lambda^{(\mathrm{c})}=0 \tag{F.4}$$

for the sausage (perturbed velocity odd with respect to $x=0$) modes and its counterpart

$$\lambda^{(\mathrm{l})}\tanh\lambda^{(\mathrm{l})}b+\lambda^{(\mathrm{c})}=0 \tag{F.5}$$

for the kink (perturbed velocity even with respect to $x=0$) modes. These dispersion relations have been widely discussed for unbounded slabs (see, for example, Edwin & Roberts (1982)). As in the cylindrical case, these dispersion relations can also be obtained from the most general form of Eqs. (4.87) and (4.88) taking into account that the z-dependent functions are the same inside and outside the slab, so we can use Eq. (4.126) to simplify and therefore every basis function (labelled as "n" in these equations) has its own dispersion relation in the form of Eqs. (F.4) and (F.5).

The next feature to be studied is the thin slab limit ($b/L\to 0$). Since $\tanh z\sim z$ for $z\ll 1$, Eq.(F.4) for the sausage modes yields

$$\frac{\lambda^{(\mathrm{l})}}{\lambda^{(\mathrm{l})}b}+\lambda^{(\mathrm{c})}=0. \tag{F.6}$$

This equation cannot be satisfied for any value of the frequency ($\lambda^{(\mathrm{c})}$ should go to infinity, and there is no finite value of ω in Eq. (5.9) that can satisfy that condition); thus, the sausage mode cannot propagate in very thin slabs. For the kink modes (Eq. F.5) in the limit $b/L\to 0$ gives

$$\lambda^{(\mathrm{l})}(\lambda^{(\mathrm{l})}b)+\lambda^{(\mathrm{c})}=0, \tag{F.7}$$

requiring $\lambda^{(\mathrm{c})}=0$. From Eqs. (5.9) and (5.10) this leads to

$$\frac{\omega}{c_{\mathrm{Ac}}}L=\kappa L=\frac{(n+1)\pi}{2L},\quad n=0,1,..., \tag{F.8}$$

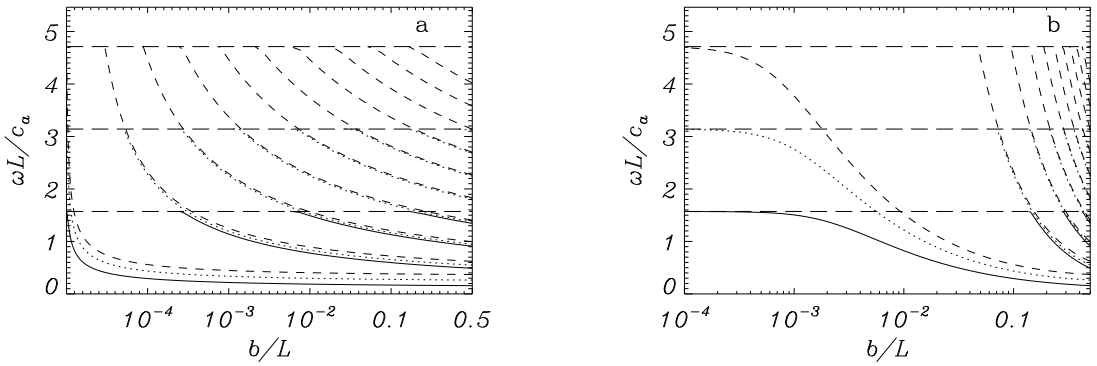

Figure F.2: **a)** Variation of the dimensionless frequency with the slab half-thickness for the lowest ten kink modes of a slab with high density ratio $\rho_{\rm l}/\rho_{\rm c} = 200$ (typical of prominence plasmas). The solid lines are modes with $\kappa L = \pi/2$ ($n = 0$, even modes), the dotted ones with $\kappa L = \pi$ ($n = 1$, odd modes) and the dashed ones with $\kappa L = 3\pi/2$ ($n = 2$, even modes). The cut-off frequencies are marked with horizontal long dashed lines. **b)** Logarithmic plot of panel **a)**, showing the structure for small b/L.

It is important to notice that there are non-vanishing amplitudes far away from the fibril, since the exponential decrease in Eq. (F.3) is very slow when $\lambda^{(\rm c)} \to 0$, in contrast with the cylindrical geometry, in which the perturbation is always confined around the density inhomogeneity (see Eq. (5.17)).

Our next aim is to plot the dispersion relation, Eq. (F.4). However, $\lambda^{(\rm c)}$ has to be real to have trapped modes, so there are the same cut-off frequencies for each value of κ as in a cylindrical geometry (Eq. (5.19)). The dispersion relations are plotted in Fig. F.2 for modes with $n = 0$, 1 and 2, for a very dense slab. The reason for selecting such a high density ratio is that this kind of model applies much better to prominences as a whole than to coronal tubes. Each family has its own cut-off frequency, $\omega_{\rm cut}$, given by Eq. (5.19), and in the limit $b/L \to 0$ only one mode is trapped for each value of n, with a frequency tending to $\omega_{\rm cut}$; see Fig. F.2b. Moreover, the perturbations of the surviving trapped modes in the thin slab limit reach large distances from the slab, so they can hardly be considered trapped solutions! These figures are quite similar to their cylindrical counterparts (Fig. 5.2) for large values of the tube radius, but for values in the realistic range they differ markedly.

Fig. F.2 can be compared with Fig. 4 of Edwin & Roberts (1982) (corrected in Edwin & Roberts (1983)) taking into account that their plot is drawn using ω/κ as the dependent variable, while here $\omega L/c_{\rm Ac}$ is used, so each family of solutions has a different vertical (and also horizontal) scale. The plots are exactly the same for fast modes (note that Edwin & Roberts also gave the slow modes in their figure).

Having discussed the trapped modes, we can also study the leaky modes in a Cartesian slab, a problem that was also discussed by Roberts & Webb (1979). The results are plotted in Fig. F.3, for a high density slab. The damping times of the modes can be quite low. For example, for a prominence modelled as a slab (Joarder & Roberts (1992a)) of length $2L \approx 200,000$ km and width $2b \approx 5000$ km we have $\omega_i L/c_{\rm Ac} \approx -0.2$; for a typical coronal Alfvén speed $c_{\rm Ac} \approx 1000$ km s^{-1}, this gives a damping time $\tau = 8.3$ min. It can be appreciated in Fig. F.3b that higher

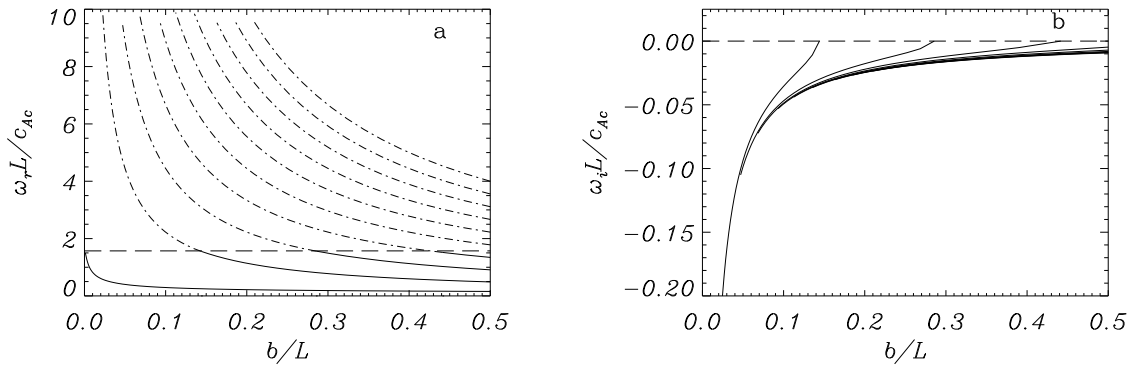

Figure F.3: Variation of **a)** the real and **b)** the imaginary part of the dimensionless frequency with the slab half-thickness for the $n = 0$ kink even modes of a slab with density ratio $\rho_1/\rho_c = 200$. The cut-off frequency is marked with a horizontal long dashed line. In panel **a)** the trapped modes are plotted with solid lines (and correspond to the solid lines in Fig. F.2), and the leaky modes with dash-dotted lines, while in panel **b)** only the values different from zero are plotted. Notice that when a mode becomes leaky (i.e. passes above the cut-off frequency in panel **a)**), its imaginary part is shown in panel **b)**.

harmonics have almost the same damping times τ, although their oscillatory period is rather short ($T_{l=1} = 2\pi/\omega_r = 1.19$ min and $T_{l>1} < T_{l=1}$) compared with that of the corresponding standing modes, $T_{l=0} = 19.04$ min. However, the fundamental mode is not damped at all. This simple calculation points to the fact that leakage to the surrounding coronal medium can be a very important mechanism for draining energy away from a structure.

Bibliography

Abramowitz, M. & Stegun, I. A. 1967, *Handbook of Mathematical Functions*, Dover.

Arfken, G. 1985, "Mathematical methods for Physicists", Academic Press (3rd ed.).

Arregui, I., Oliver, R., & Ballester, J. L. 2001, A&A, 369, 1122.

Arregui, I. 2003. Ph. D. Thesis, Universitat de les Illes Balears.

Arregui, I., Oliver, R., & Ballester, J. L. 2003, A&A, 402, 1129.

Aschwanden, M. J., Fletcher, L., Schrijver, C. J., & Alexander, D. 1999, ApJ, 520, 880.

Aschwanden, M. J., Schrijver, C. J., & Alexander, D. 2001, ApJ, 550, 1036.

Aschwanden, M. J. 2002, in Proc. of the Magnetic Coupling of the Solar Atmosphere Euroconference and IAU Colloquium 188, ESA publications division, SP-505, 191.

Aschwanden, M. J.m & Schrijver, C. J. 2002, ApJSS, 142, 269.

Aschwanden, M. J., De Pontieu, B., Schrijver, C. J., & Title, A. M. 2002, Solar Phys., 206, 99.

Aschwanden, M. J., Nakariakov, V. M., & Melnikov, V. F. 2004, ApJ, 600, 458.

Balthasar, H., Wiehr, E., Schleicher, H. & Wöhl, H. 1993, A&A, 277, 635.

Balthasar, H., & Wiehr, E. 1994, A&A, 204, 286.

Ballester, J. L., & Priest, E. R. 1989, A&A, 225, 213.

Ballester, J. L. 2003, in *Turbulence, Waves and Instabilities in the Solar Plasma*, R. Erdélyi (eds.), Kluwer Academic Publishers, 193.

Bashkirtsev, V. S., & Mashnich, G. P. 1984, Solar Phys., 91, 93.

Bennett, K., Roberts, B., & Narain, U. 1999, Solar Phys., 185, 41.

Berghmans, D., & Clette, F. 1999, Solar Phys., 186, 207.

Berton, R. & Heyvaerts, J. 1987, Solar Phys., 109, s201.

Bogdan, T. J., & Zweibel, E. G. 1985, ApJ, 298, 867.

Bogdan, T. J., & Zweibel, E. G. 1987, ApJ, 312, 444

Bogdan, T. J. 1987, ApJ, 318, 888

Bogdan, T. J. 1987, ApJ, 318, 896

Bradshaw, S. J., & Mason, H. E. 2003, A&A, 401, 699.

Bradshaw, S. J., & Mason, H. E. 2003, A&A, 407, 1127.

Bray, R. J., & Loughhead, R. E. 1974, *The Solar Cromosphere*, The international astrophysics series, Chapman and Hall.

Cally, P. S. 1986, Solar Phys., 103, 277.

Cally, P. S. 2003, Solar Phys., 217, 95.

Chae, J., Poland, A. I., & Aschwanden, M. J. 2002, ApJ, 581, 726.

Degenhardt, U., & Deinzer, W. 1993, A&A, 278, 288.

De Groof, A., & Goossens, M. 2002, A&A, 386, 691.

De Moortel, I., Ireland, J., Walsh, R. W., & Hood, A. W. 2002, Solar Phys., 209, 61.

De Moortel, I., Hood, A. W., Ireland, J., & Walsh, R. W. 2002, Solar Phys., 209, 89.

Demoulin, P., Raadu, M., Malherbe, J. M., & Schmieder, B. 1987, A&A, 183, 142.

Díaz, A. J., Oliver, R., Erdélyi, R., & Ballester, J.L. 2001a, A&A, 379, 1083.

Díaz, A. J., Oliver, R. and Ballester, J. L. 2002, ApJ, 580, 550.

Díaz, A. J., Oliver, R. and Ballester, J. L. 2003, A&A, 402, 781.

Díaz, A. J., Oliver, R., Ballester, J. L., & Roberts, B. 2003, A&A, submitted.

Díaz, A. J. 2003, in preparation (corrected bh87)

Dunn, R. B. 1960, Ph. D. Thesis, Harvard University.

Edwin, P. M., Roberts, B. 1982, Solar Phys., 76, 239.

Edwin, P. M., & Roberts, B. 1983, Solar Phys, 88, 179.

Edwin, P. M., Roberts, B., & Benz, A. O. 1984, ApJ, 279, 857.

Edwin, P. M., Roberts, B. 1983, Solar Phys., 88, 179.

Engvold, O. 1976, Solar Phys., 49, 283.

Engvold, O. 2001, in INTAS Workshop on MHD Waves in Astrophysical Plasmas, eds. Ballester, J. L. & Roberts, B., Universitat de les Illes Balears, Spain, in press.

Engvold, O., Kjeldseth-Moe, O., Bartoe, J. D. F., & Brueckner, G. 1987, in Proceedings of the 21st ESLAB Symposium, ESA SP-275, 21.

Engvold, O., Hansteen, V., Kjeldseth-Moe, O., & Brueckner, G. E. 1990 in V. Ruždjak & E. Tandberg-Hanssen (eds), Dynamics of Quiescent Prominences, IAU Colloq., 117, 250.

Engvold, O., Hirayama, T., Leroy, J. L., Priest, E. R., & Tandberg-Hanssen, E. 1989, in Dynamics of Quiescent Prominences, IAU Colloq. 117, eds. Ruždjak, V. & Tandberg-Hanssen, E., Springer-Verlag, 296.

Erdélyi, R., & Goossens, M. 1996, A&A, 313, 664.

Goedbloed, J. P. 1983, Lecture Notes on Ideal Magnetohydrodynamics, Rijnhuizen Report, 76–83.

Goossens, M., Andries, J., & Aschwanden, M. J. 2002, A&A, 394, L39.

Goossens, M. 2003, *An introduction to plasma astrophysics and magnetohydrodynamics*, Kluwer Academic Publishers.

Hain, K., & Lüst, R. 1958, Z. Naturforsch., 13a, 936.

Heyvaerts, J., & Priest, E. R. 1983, A&A, 117, 220.

Hollweg, J. V., & Roberts, B. 1981, ApJ, 250, 398.

Homem, M. T., Erdélyi, R., & Ballai, I. 2003, Solar Phys., 217, 199.

Hood, A. W.,& Priest, E. R. 1979, A&A, 77, 233.

Hood, A. W. 1986, Solar Phys., 105, 307.

Hood, A. W., Priest, E. R., & Anzer, U. 1992, Solar Phys., 138, 331.

Jensen, E, & Wijk, J. E. 1990 in V. Ruždjak & E. Tandberg-Hanssen (eds), 'Dynamics of Quiescent Prominences', IAU Colloq., 117, 298.

Joarder, P. S., & Roberts, B. 1991, A&A, 256, 264.

Joarder, P. S., & Roberts, B. 1991, A&A, 261, 625.

Joarder, P. S., & Roberts, B. 1993, A&A, 277, 225.

Joarder, P. S., Nakariakov, V., & Roberts, B. 1997, Solar Phys., 173, 81.

Karami, K., Nasiri, S., & Sobouti, Y. 2002, A&A, 396, 993.

Katsiyannis, A. C., Williams, D. R., McAteer, R. T. J., Gallagher, P. T., Keenan, F. P., & Murtagh, F. 2003, A&A, 406,709.

Leroy, J. L. 1989, in E. R. Priest (ed.), *Dynamics and Structure of Quiescent Solar Prominences*, Kluwer Academic Publishers, Dordrecht, Holland, p. 49.

Lin, Y., Engvold, O., Martin, S. F., Wiik, J. E., & Zirker, J. B. 2002, (to be submitted to Solar Phys.).

Lin, Y., Engvold, O. 2002 (submitted to Solar Phys.).

Mashnich, G. P., & Bashkirtsev, V. S. 1990, A&A, 235, 428.

Mein, P. 1994, in V. Rušin, P. Heinzel and J.C. Vial (eds.), 'Solar Coronal Structures, IAU Colloq., 144, 289.

Mendoza-Briceño, C. A., Erdélyi, R., & Sigalotti, L. G. 2002, ApJ, 579, 49.

Menzel, D. H., & Evans, J. W. 1953, Convegno Volta, 11, 119.

Molowny-Horas, R., Oliver, R., Ballester, J. L., & Baudin, F. 1997, Solar Phys., 172, 181.

Nagata, S., Hara, H., Kano, R., Kobayashi., Sakao, T., Shimizu, T., Tsuneta, S., Yoshida, T., Gurman, J. B. 2003, ApJ, 590, 1095.

Nakariakov, V. M., & Roberts, B. 1995, Solar Phys. Letters, 159, 399.

Nakariakov, V. M., Ofman, L., DeLuca, E. E., Roberts, B., & Davila, J. M. 1999, Science, 285, 862.

Nakariakov, V. M., & Ofman, L. 2001, A&A, 372, 53.

Nakariakov, V. M., Melnikov, V. F., & Reznikova, V. E. 2003, A&A, 412, 7.

Ofman, L., & Wang, T. J. 2002, ApJ, 279, 857.

Oliver, R., & Ballester, J. L. 2002, Solar Phys., 206, 45.

Oliver, R., Ballester, J. L., Hood, A. W., & Priest, E. R. 1992, ApJ, 400, 369.

Oliver, R., Ballester, J. L., Hood, A. W., & Priest, E. R. 1993, ApJ, 409, 809.

Oliver, R., & Ballester, J. L. 1996, ApJ, 456, 393.

Oliver, R., Hood, A. W., & Priest, E. R. 1996, ApJ, 461, 424.

Poedts, S., & Goossens, M. 1991, Solar Phys., 133, 281.

Priest, E. R. & Hood, A. W. (eds.), *Advances in Solar System Magnetohydrodynamics*, Cambridge Press.

Priest, E. R. 2000, Solar Magnetohydrodynamics, Kluwer Academic Publishers.

Priest, E. R., Foley, C. R., Heyvaerts, J., Arber, T. D., Mackay, D., Culhane, J. L., & Acton, L. W. 2000, ApJ, 539, 1002.

Roberts, B., & Webb, A. R. 1979, Solar Phys. 64, 77.

Roberts, B. 1981, Solar Phys. 69, 27.

Roberts, B., Edwin, P. M., & Benz, A. O. 1984, ApJ, 279, 857.

Roberts, B. 2002, in 'Solar variability: from core to outer frontiers. The 10th European Solar Physics Meeting', ESA Publications Division, 506, 481.

Rosner, R., Tucker, W. H., & Vaiana, G. S. 1978, ApJ, 220, 643.

Ruderman, M. S., & Roberts, B. 2002, ApJ, 577, 475.

Sakai, J. I., Yawata, T., Yoshida, K., Furusawa, K., & Cramer, N. F. 2000, ApJ, 537, 1063.

Sakurai, T., Ichimoto, K., Raju, K. P., & Singh, J. 2002, Solar Phys., 209, 265.

Schmieder, B., & Mein, P. 1989 Hvar Obs. Bulletin 13, IAU Colloq. 119, 31.

Schmieder, B., Raadu, M., & Wijk, J.,E. 1991, A&A, 252, 353.

Schmitt, D., & Degenhardt, U. 1996, in Rev. Mod. Astron., ed. Klare, G., Springer-Verlag.

Schrijver, C. J., Aschwanden, M. J., & Title, A. M. 2002, Solar Phys. 206, 69.

Serio, S., Peres, G., Vaiana, G. S., Golub, L., & Rosner, R. 1981, ApJ, 243, 288.

Smith, J. M., Roberts, B., & Oliver, R. 1997, A&A, 317, 752.

Somasundaram, K., Venkatraman, S., & Sengottuvel, M. P. 1999, Plasma Phys. Control Fusion, 41, 1421.

Steele, C. D. C. 1996, A&A, 308, 219.

Steele, C. D. C., & Priest, E. R. 1992, Solar Phys., 140, 289.

Stenuit, H., Keepens, R., & Goossens, M. 1998, A&A, 331, 392.

Stenuit, H., Tirry, W. J., Keepens, R., & Goossens, M. 1999, A&A, 342, 863.

Suematsu, Y., Yoshinaga, R., Terao, N., & Tsubaki, T. 1990, Publ. Astron. Soc. Japan, 42, 187.

Sütterlin, P., Wiehr, E., Bianda, M., & Küveler, G. 1997, A&A, 321, 921.

Tandberg-Hanssen, E. 1995, *The Nature of Solar Prominences*, Kluwer Academic Publishers.

Terradas, J., Molowny-Horas, R., Wiehr, E., Balthasar, H., Oliver, R., & Ballester, J. L. 2002, A&A, 393, 637.

Testa, P., Peres, G., Reale, F.,& Orlando, S. 2002, ApJ, 580, 1159.

Testa, P., & Peres, G. 2003, in American Astronomy Society SPD meeting #34, 1702.

Thompson, W. T., & Schmieder, B. 1991, A&A, 243, 501.

Tsubaki, T., & Takeuchi, A. 1986, Solar Phys., 104, 313.

Tsubaki, T., Toyoda, M., Suematsu, Y., & Gamboa, G. A. R. 1988, Publ. Astron. Soc. Japan, 40, 121.

Van der Linden, R. A. M., Hood, A. W., & Goedbloed, J. P. 1994, Solar Phys., 154, 69.

Vaiana, G., S., Krieger, A. S., & Timothy, A. F. 1973, Solar Phys., 32, 81.

Walsh, R. W., Bell, G. E.. & Hood, A. W. 1995, Solar Phys., 161, 83.

Walsh, R. W., Bell, G. E.. & Hood, A. W. 1996, Solar Phys., 169, 33.

Walsh, R. W.,& Galtier, S. 2000, Solar Phys., 197, 57.

Wang, T., J., Solanki, S. K., Curdt, W., Innes, D. E., & Dammasch, I. E. 2002, ApJ, 574, 101.

Wang, T. J., Solanki, S. K., Innes, D. E., Curdt, W., & Marsch, E. 2003, A&A, 402, 17.

Wang, T. J., Solanki, S. K., Curdt, W., Innes, D. E., Dammasch, I. E., & Kliem, B. 2003, A&A, 406, 1105.

Webb, D. F., Schmieder, B. & Rust, D. M. 1998, in ASP Conf. Ser. 150, New Perspectives on Solar Prominences, IAU Colloq. 167.

Wiehr, E. 2003, in SOHO 13; Waves, oscillations and small scale transient events in the solar atmosphere, Palma, Spain.

Wijk, J. E., Schmieder, B., & Noëns, J. C. 1994, Solar Phys., 125, 277.

Williams, D. R.; Mathioudakis, M.; Gallagher, P. T.; Phillips, K. J. H.; McAteer, R. T. J.; Keenan, F. P.; Katsiyannis, A. C. 2002, in Proc. of the Magnetic Coupling of the Solar Atmosphere Euroconference and IAU Colloquium 188, ESA publications division, SP-505, 615.

Winebarger, A. R., Warren, H. P., & Mariska, J. T. 2003, ApJ, 587, 439.

Yi, Z., Engvold, O. 1991, Solar Phys., 134, 275.

Yi, Z., Engvold, O., & Keil, S. L. 1991, Solar Phys., 132, 63.

Zweibel, E. G., & Bogdan, T. J. 1986, ApJ, 308, 401

List of Figures